PHD THESIS

To obtain the degree of doctor in **Micro and Nanotechnologies, acoustics and telecommunications**

Specialization: Electronics and photonics

From the University of Lille

SPI doctoral school

Elias AKIKI

Integrated SOI photoacoustic gas sensor at THz frequencies for food quality control application

Prepared at IEMN, THz Photonics group

Defended on June 25, 2021

Jury:

Reviewers:	Pr. Frédéric Garet	IMEP-LAHC. University of Savoie Mont-Blanc
	Dr. Yanko Todorov	LPENS, University of Paris Sciences et lettres
Supervisor:	Pr. Guillaume Ducournau	IEMN. University of Lille
Co-Supervisor:	Dr. Mathias Vanwolleghem	IEMN, University of Lille
President:	Pr. Frédéric Garet	IMEP-LAHC. University of Savoie Mont-Blanc
Examinators:	Pr. Delphine Marris-Morini	C2N, University of Paris Saclay
	Dr. Marc Faucher	IEMN, University of Lille

THÈSE DE DOCTORAT

Pour obtenir le grade de docteur en **Micro et Nanotechnologies, Acoustiques et télécommunications**

Spécialité: Electronique et photonique

De l'Université de Lille

École doctorale SPI

Elias AKIKI

Capteur à gaz intégrée sur SOI pour la détéction photoacoustique aux fréquences THz, appliqué au contrôle de qualité alimentaire

Preparé à l'IEMN, équipe photonique THz

Soutenue le 25 Juin 2021

Jury:

Rapporteurs:	Pr. Frédéric Garet	IMEP-LAHC. Université Savoie Mont-Blanc
	Dr. Yanko Todorov	LPENS, Université Paris Sciences et lettres
Directeur:	Pr. Guillaume Ducournau	IEMN. Université de Lille
Encadrant:	Dr. Mathias Vanwolleghem	IEMN, Université de Lille
Président:	Pr. Frédéric Garet	IMEP-LAHC. Université Savoie Mont-Blanc
Examinateurs:	Pr. Delphine Marris-Morini	C2N, Université Paris Saclay
	Dr. Marc Faucher	IEMN, Université de Lille

To my parents
Youssef and Rima Akiki

“Some people want it to happen, some wish it would happen, others make it happen”

-Michael Jordan

Acknowledgement

This thesis work was undertaken as part of the Terafood project, which is financially supported by the European Regional Development Fund and the province Oost-Vlaanderen (INTERREG V FR-WA-VL 1.1.11).

First of all, I would like to thank my supervisors Pr. Guillaume Ducournau and Dr. Mathias Vanwolleghem for accepting to guide me during these years of my PhD. The Assistance, knowledge, and kindness of Pr. Guillaume Ducournau were most helpful. He was always ready to teach me and help me to solve scientific and technical problems.

I am extremely grateful to Dr. Mathias Vanwolleghem for giving me this opportunity to be part of the Terafood project team and for trusting me to work independently on this project. His continuous encouragement and moral support were my precious motivation. The completion of my dissertation would not have been possible without his valuable linguistic and scientific remarks. I will never forget the good times we shared during the conferences and presentations. Thank you Mathias for everything you have taught me on the professional and personal aspects.

My special thanks to Dr. Jean-François Lampin who guided me during the experiments of the gas spectroscopy. I have enriched my scientific background thanks to his enormous knowledge and experience. I would also like to thank all the permanent members of the THz photonics group especially Dr. Stefano Barbieri who was my first contact at the IEMN and who believed in my potential.

I would like to express my deepest appreciation to my committee members Pr. Frédéric Garet, Dr. Yanko Todorov, Pr. Delphine Marris-Morini and Dr. Marc Faucher. Thank you for your insightful remarks that helped improve the quality of this manuscript.

Also thanks to all the IEMN members and engineers in particular Sophie, Sylvie, Vanessa, Etienne, Jean-Michel, David, Christophe, Nora, Andy and Valérie.

I would also like to thank all the collaborators and members of the Terafood project. I am grateful to the staff of Vmicro, Benjamin, Marc, Fuanki, Estelle, and Edouard who did the fabrication of the components. I also had great pleasure working with Mattias and Bart from the University of Ghent, and Marie, Gaël, Robin, Frank, Arnaud, and Meriem from the LPCA.

During these years at the IEMN, I met many colleagues and friends that I want to thank them all for sharing good moments. My deep thanks belong to Jawad, Alexandre, Mohammed, Charbel, Théo, Mélanie, Kévin, Cybelle, Kathia, Ali, Mehdi, Wijden, Guiseppe, Haitham, Hugo.

My special thanks to my second family in France, Nassif, Mimo, Elie, Sandy, Stephy, and Toni. Thank you for making me feel at home. Also thanks to all my friends Charbel, Michel, Elie-Joe, Carlos, Lara, Amanda, Rana, Sylia, Salim and all the people with whom I spent pleasant moments and good barbecues in Lille. I would also like to thank all my friends in Lebanon who stayed in contact with me even after all these years and despite the long distances. I especially thank my friend but also my brother Nicolas for having been at my side all these last years.

Meeting you, Vanessa, was one of the best things that happened to me during my stay in France. I am so grateful to you for allowing me to enjoy all the moments, even the hard ones. Thank you for your endless love and support. I will also not forget to thank you for the most delicious food you prepared for me when I was writing this thesis.

Finally, I want to thank my father, mother, and sisters because without them nothing was possible. Mom and dad, there are no words that can describe how grateful I am to you. Lea and Lara, you are both the best sisters in the world, thank you for your love and support, thank you for being my inspiration. I will not forget the two angels that have almost the age of this thesis, my beautiful nieces Sama and Marina, you are my happiness, I love you. And I want also to thank my brothers in law Ziad and Avo.

I thank God and Jesus Christ for giving me the strength and faith to finish this work.

Résumé et contenu de la thèse

Le gaspillage alimentaire est un problème économique et social qui prend de plus en plus d'ampleur, notamment avec la production massive des aliments emballés. En Europe, 90 milliards de kilos de nourriture sont jetés chaque année. Une grande partie de ces pertes est due à l'élimination d'aliments emballés dont la date de péremption est dépassée mais qui sont parfois encore parfaitement consommables. C'est également le cas pendant la production, où des paquets d'échantillons alimentaires sont prélevés aléatoirement et ouverts quotidiennement pour mesurer l'intégrité des produits. La détérioration de produits alimentaires hautement périssables tels que le poisson frais est généralement due à une activité microbienne qui entraîne la production de composés organiques volatiles (COV). Ces composés pourraient être utilisés comme indicateurs de détérioration et donc pour la surveillance de la qualité de produits alimentaires emballés.
Le but de cette thèse est de proposer une technique qui permet de suivre l'évolution de ces COV dans les paquets alimentaires sans les détruire afin de pouvoir déterminer l'état de fraîcheur de l'aliment emballés. Ces COVs se présentent sous forme des molécules de gaz comme le sulfate d'Hydrogène (H_2S), méthanol (CH_3OH), éthanol (C_2H_5OH), ammoniac (NH_3) … La plupart de ces gaz sont des molécules polaires qui présentent des raies d'absorption intenses aux fréquences THz. Cela fait de la spectroscopie THz un outil intéressant pour la détection de ces molécules de gaz et donc le contrôle de qualité des aliments emballés. En plus, les paquets alimentaires sont constitués de matériaux transparents aux ondes THz tels que le polystyrène, polyéthylène, polypropylène, ce qui permet aux faisceaux THz d'interagir avec les molécules de gaz sans détruire l'emballage alimentaire.

Par conséquent et grâce à tous les avantages des ondes THz mentionnés précédemment, nous proposons le design et la conception d'un capteur de gaz photoacoustique aux fréquences THz. La spectroscopie photoacoustique est une technique qui permet de transformer l'énergie du faisceau de lumière absorbé par les molécules en une onde acoustique qui peut être simplement détectée avec un microphone. L'avantage de cette technique par rapport aux autres méthode de spectroscopie est qu'elle se base sur un système de détection mécanique simple, sensible, pas cher et, surtout, qui ne nécessite pas une correction de la ligne de base (baseline). Dans les années précédentes, plusieurs capteurs de gaz photoacoustique ont été proposés. La haute sensibilité d'un capteur de gaz est toujours nécessaire surtout pour des applications comme le contrôle de qualité

des aliments qui nécessite la détection de faibles concentrations de l'ordre de 100's de ppb. La sensibilité des capteurs existants dépend fortement de la puissance de la source THz, de la longueur d'interaction entre le faisceau THz et les molécules ainsi que de la sensibilité du microphone utilisé pour la détection de l'onde acoustique. Dans ce travail, le design proposé intègre trois résonateurs : mécanique, acoustique et photonique. Le résonateur photonique est formé par une cavité crystal photonique intégré dans un guide HR-Si aux fréquences THz. Cette cavité permet d'exalter localement la puissance THz et d'augmenter la longueur effective d'interaction lumière-molécule. L'un des trous cylindriques de la cavité crystal photonique se comporte comme un résonateur acoustique. Finalement ce résonateur est recouvert par une membrane en Poly-Si qui agit comme un microphone et un résonateur mécanique. Ces résonateurs acousto-mécaniques permettent d'amplifier l'amplitude des ondes acoustiques générées par les molécules après l'interaction avec la lumière THz et ainsi d'augmenter la sensibilité du capteur.

Le premier chapitre introduit de manière détaillée le sujet de la thèse. Il débute par la présentation des ondes THz et leur application dans le contrôle de qualité alimentaires. Ensuite, une comparaison entre la spectroscopie d'absorption et la spectroscopie photoacoustique est présentée. Cela est suivi d'un développement analytique et d'une interprétation de la théorie photoacoustique. Une comparaison entre les différents capteurs à gaz photoacoustique est aussi effectuée. Enfin, ce chapitre se conclut par une présentation de l'état de l'art des guides d'ondes et cavités cristaux photoniques aux fréquences THz. Ces derniers constituent une partie principale du capteur et sont étudiées en détail dans ce travail.

Dans le chapitre 2, le concept du capteur à gaz proposé est illustré en présentant les détails du fonctionnement de ses trois différentes parties. La partie principale de ce chapitre se concentre sur les travaux numériques effectués pour optimiser le design du guide d'onde et de la cavité THz. D'abord, nous présentons une analyse numérique du comportement modal d'un guide d'onde en Silicium haute résistivité. Les différentes pertes liées à la propagation dans le guide d'onde choisi sont ensuite étudiées. La deuxième partie de ce chapitre présente les différentes analyses numériques utilisées pour optimiser le design de la cavité crystal photonique. Cette cavité est optimisée pour confiner la lumière THz aux fréquences d'absorption de la molécule H_2S (610 et 650 GHz) qui est considérée comme un indicateur important de la dégradation alimentaire.

Le chapitre 3 explique brièvement le processus technologique utilisé pour la fabrication des composants THz et du capteur de gaz. Ensuite nous introduisons les différentes méthodes expérimentales et techniques de mesure utilisées pour la caractérisation des guides d'ondes, cavités THz et les membranes en Poly-Si qui constituent le résonateur mécanique du capteur de gaz.

Le chapitre 4 présente les résultats des mesures expérimentales afin de caracteriser le fonctionnement correct des différentes parties du capteur. Au début nous présentons les mesures effectuées pour extraire les pertes de propagation dans le guide HR-Si. Les pertes d'insertion liées au couplage du faisceau THz de la source dans le guide HR-Si sont ensuite discutées. Une interprétation expérimentale du comportement modal du guide d'onde est également présentée. Nous présentons aussi dans cette partie les mesures des bandgap et des fréquences de résonance des cavités cristaux photoniques proposées dans le chapitre 2.
La deuxième partie de ce chapitre illustre les mesures de résonances mécaniques de la membrane PolySi utilisée comme microphone résonnant pour la détection des ondes acoustiques dans le capteur à gaz.

Le chapitre 5 est le dernier chapitre de cette thèse. Il présente les mesures d'une détection photoacoustique du gaz H_2S. Ces mesures ont été effectuées avec une simple membrane Poly-Si (donc sans couplage aux autres éléments résonnants du nouveau concept : la cavité crystal photonique et le résonateur acoustique). Ceci est dû à la complexité de l'assemblage des différentes parties du capteur qui n'est pas encore finalisé. Avant l'illustration de ces résultats nous présentons la chambre à gaz utilisé pour effectuer ces mesures. Cette chambre à gaz a été spécialement conçue pour permettre la transition guidée des faisceaux THz dans un milieu à pression contrôlé et étanche.

Une dernière partie de ce manuscrit reprend en conclusion les résultats principaux de cette recherche doctorale et présente plusieurs pistes de recherche intéressantes pour la suite de ce projet.

Summary and thesis content

Food waste is an economic and social problem that is becoming more and more important, especially with the massive production of packaged food. In Europe, 90 million tons of food are thrown away every year. A large part of this loss is due to the disposal of packaged food that has passed its expiration date but is sometimes still perfectly consumable. This is also the case during production, where packages of food samples are randomly taken and opened daily to measure product integrity. Spoilage of highly perishable food products such as fresh fish is usually due to microbial activity that results in the production of volatile organic compounds (VOCs). These compounds can be used as indicators of spoilage and therefore for monitoring the quality of packaged food products.

This thesis proposes a technique to monitor the evolution of these VOCs in food packages without destroying them in order to be able to determine the freshness state of the packaged food. These VOCs are represented by gas molecules such as hydrogen sulfate (H_2S), methanol (CH_3OH), ethanol (C_2H_5OH), ammonia (NH_3) ... Most of these gases are polar molecules that possess intense absorption lines at THz frequencies. This makes THz spectroscopy an interesting tool for the detection of these gas molecules and thus the quality control of packaged foods. Moreover, food packages are made of materials transparent to THz waves such as polystyrene, polyethylene, polypropylene, which allows THz beams to interact with the molecules without destroying the food package.

Therefore, and due to all the advantages of THz waves mentioned above, we propose the design and conception of a photoacoustic gas sensor at THz frequencies. Photoacoustic spectroscopy is a technique that transforms the energy of the light beam absorbed by the molecules into an acoustic wave which can be simply detected with a microphone. The advantage of this technique over other spectroscopy methods is that it is based on a simple, sensitive, low cost and most importantly a zero background measurement system. In previous years several photoacoustic gas sensors have been proposed. The high sensitivity of a gas sensor is always necessary especially for applications like food quality control which requires the detection of low concentrations in the order of 100's of ppb. The sensitivity of existing sensors depends strongly on the power of the THz source, the interaction length between the THz beam and gas molecules, and the sensitivity of the microphone used for the detection of the acoustical wave. In this work, the proposed design integrates three

resonators: mechanical, acoustic, and photonic. The photonic resonator is represented by a photonic crystal cavity integrated on a suspended HR-Si guide at THz frequencies. This cavity allows to locally enhance the THz power and increase the effective length of light-molecule interaction. One of the cylindrical holes of the photonic crystal cavity behaves like an acoustic resonator (acoustic pipe). Finally, this resonator is covered by a Poly-Si membrane which acts as a microphone and a mechanical resonator. These acousto-mechanical resonators allow amplifying the amplitude of the acoustic waves generated by the molecules after the interaction with the THz light and thus increase the sensitivity of the sensor.

Chapter 1 is a detailed introduction to the main topic and the different subjects addressed in this thesis. It begins with the presentation of the THz waves and their application for food quality control. Then, a comparison between the absorption spectroscopy and photoacoustic spectroscopy is illustrated. This is followed by an analytical development and interpretation of the photoacoustic theory. A review of the different available photoacoustic gas sensors is also presented. Finally, this chapter is concluded by the presentation of the state of art on the waveguides and photonic crystal cavities at THz frequencies. The latter constitutes a main part of the sensor and is studied in detail in this work.

In chapter 2, the concept of the proposed gas sensor is illustrated by presenting the operational mechanism of its three different parts. This chapter focuses on the numerical calculation performed to optimize the design of the THz waveguide and photonic crystal cavity. First, we present a numerical modal analysis of a high resistivity silicon waveguide. The different loss mechanisms of the proposed waveguide design are numerically calculated. The second part of this chapter presents the different numerical calculations performed to properly design a high Q photonic crystal cavity. This cavity is optimized to confine THz light at the absorption frequencies of the H_2S molecule (610 and 650 GHz) which is considered an important indicator of food spoilage.

Chapter 3 briefly explains the technological process used in the fabrication of the THz components and gas sensor. Then we introduce the different experimental methods and measurement techniques used for the characterization of the THz waveguides and cavities and the Poly-Si membranes which constitute the mechanical resonator of the gas sensor.

Chapter 4 presents the results of the experimental measurements related to the characterization of the different parts of the sensor. It starts out by presenting the measurements performed to extract the propagation losses in the HR-Si guide. The insertion losses related to the coupling of the THz energy from the source into the HR-Si waveguide are then discussed. An experimental interpretation of the waveguide's modal behavior is also presented. This part includes also the characterization of the bandgap and the resonances of the photonic crystal cavities proposed in chapter 2.
The second part of this chapter concentrates on the mechanical resonance measurements of the PolySi membrane used as a resonant microphone for the detection of the acoustic waves in the gas sensor.

Chapter 5 is the last chapter of this thesis. It presents for the first time photoacoustic detection of low concentrations H_2S gas molecule in trace amounts at THz frequencies. These measurements are performed with a Poly-Si membrane in the absence of the photonic crystal cavity and the acoustic resonator. This is due to the complexity of the assembly of the different parts of the sensor which is not yet finalized. Before illustrating the results, we present the gas chamber used to perform these measurements. This gas chamber is specially designed to allow the transition of guided THz waves inside a pressure controlled and sealed medium.

A last part of this manuscript summarizes the most important results of this doctoral research and sketches several interesting directions for future work.

Table of contents

List of abbreviations

THz	Terahertz
EM	Electromagnetic
PhC	Photonic Crystal
HR-Si	High Resistivity Silicon
PA	PhotoAcoustic
VOC	Volatile Organic Compounds
UV	Ultraviolet
CW	Continuous Wave
THz-TDS	THz - Time Domain Spectroscopy
PAS	Photoacoustic Spectroscopy
FWHM	Full Width Half Maximum
CEPAS	Cantilever Enhanced Photoacoustic Spectroscopy
MEMS	Microelectromechanical Systems
NNEA	Normalized Noise Equivalent Absorption
MDL	Minimum Detection Limit
QEPAS	Quartz Enhanced Photoacoustic Spectroscopy
QTF	Quartz Tuning Forks
TF	Tuning Forks
Si	Silicon
Poly-Si	Polycrystalline Silicon
LDV	Laser Doppler Vibrometer
MWG	Metallic Waveguide
DRIE	Deep Reactive Ion Etching
SB	Supporting Beams
SOG	Silicon-On-Glass
mmW	millimeter Wave
IR	Infrared
1D	One-Dimensional
2D	Two-Dimensional

3D	Three-Dimensional
SNR	Signal to Noise Ratio
Q	Quality Factor
ppm	part per million
SOI	Silicon On Insulator
AMC	Amplifier Multiplier Chain
FDE	Finite Difference Eigensolver
TE	Transverse Electric
FDTD	Finite-Difference Time-Domain
VNA	Vector Network Analyzer
VDI	Virgina Diode Incorporated
NA	Numerical Aperture
PML	Perfectly Matched Layer
TIR	Total Internal Reflection
DM	Dielectric Mode
AM	Air Mode
MSB	Mini Stop Band
FT	Fourier Transform
PEC	Perfect Electric Conductor
HRFZ	High Resistivity Float-Zone
SEM	Scanning Electron Microscope
FIB	Focused Ion Beam
PCA	Photoconductive Antenna
DC	Direct Current
EOM	Electro-Optic Modulator
PT	Photothermal
HVA	High Voltage Amplifier
SM	Single Mode
NEMS	Nanoelectromechanical System
RF	Radio Frequency
TTL	Transistor-Transistor-Logic

LPF	Low-Pass Filter
OAP	Operational Amplifier
CVD	Chemical Vapor Deposition
PVD	Physical Vapor Deposition
MBE	Molecular Beam Epitaxy
GIS	Gas Injection System
TPX	Polymethylpentene
VNAX	Vector Network Analyzer Extender
PE	Polyethylene
PP	Polypropylene
EFL	Effective Focal Length
Pt	Platinum
Cr	Chromium
Au	Gold
BW	Bandwidth
H_2S	Hydrogen Sulfide
N_2	Nitrogen
H_2O	Water
RMS	Root Mean Square
CH_3CN	Methyl cyanide
CH_3OH	Methanol
QCL	Quantum Cascade Laser
ppt	Part per trillion
ppb	Part per billion
PLA	Polylactic acid
MIR	Mid Infrared
W	Tungsten

List of Figures

List of tables

Chapter I:

Introduction

CONTENTS

I.1. INTRODUCTION ON TERAHERTZ (THZ) WAVES:

From the electronics to the photonics world, a range of electromagnetic (EM) waves are classified in an electromagnetic spectrum. This spectrum shown in figure I.1.1 starts with the long wavelength and low frequency EM waves where the electronics dominate and ends by very short wavelength and extremely high frequency in the photonics world. These waves can be represented by a wavelength (mm, µm, nm), mainly in the photonic world (infrared (IR), visible), a wavenumber (cm^{-1}) for spectroscopy, a frequency (Hz) for electronic telecommunication world, and sometimes by an energy (eV or Joules). The 0.1-10 THz (3000-30 µm) frequency band of this spectrum, lying between micro-and millimetric- waves (< 0.1THz) in electronics and infrared (> 10THz) in photonics is called today THz region or THz gap.

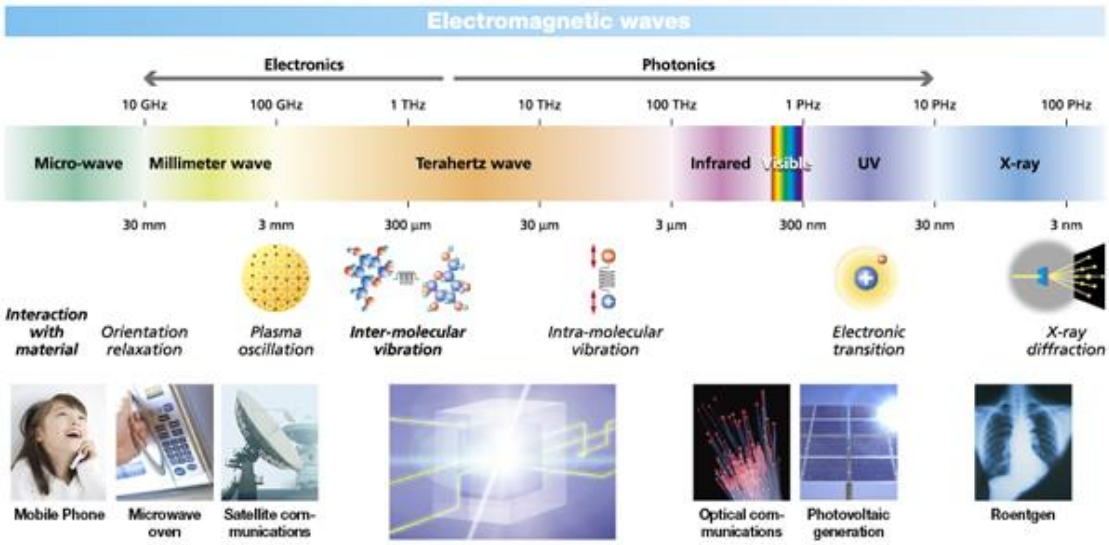

Figure I.1.1 Electromagnetic waves spectrum [1]

The discovery of those waves started at the end of 19th century, and it was called obscure radiation in the study published by Nicholas[2]. It took 80 years more for the term Terahertz to appear in the first scientific publications[3]–[6]. Referring to this region as a "gap" in the spectrum finds its origin in the limited scientific discoveries in this frequency range and the initial difficulty to produce efficient passive and active components operating at these frequencies.

Owing to the unique properties of THz waves and their multiple applications in several fields, researchers have over the past decades put tremendous efforts to fill this “gap”. The non-ionizing property due to the low energy (0.41-41.5 meV) of THz waves and their capability of penetrating

different types of materials including some opaque ones in the visible range, make them helpful for medicine, biosensors, and imaging [7]–[10]. The presence of several molecules with vibrational and rotational transitions in this frequency region allows THz waves to act as a unique spectroscopic tool [11]–[15]. Besides the mentioned ones a large variety of other applications exists, where THz waves fulfill a crucial role: food examination and quality control [16]–[19], communication [20], [21], astronomy [22]–[24]…

For many of these applications, the availability of efficient passive and active THz components (sensors, sources, detectors, waveguides, resonators, …), is essential. As such this PhD research has as an ultimate goal to add another important element to the rich THz toolbox: an ultra-low loss integrated platform for spectroscopic applications. In this work we present, a low loss suspended high resistivity Silicon (HR-Si) waveguide and a high Q photonic crystal (PhC) resonator. The presented components are useful for any application in the THz domain but are specifically designed here to operate as an integrated photoacoustic (PA) gas sensor for food spoilage examination and quality control. As discussed earlier, many molecules and components present vibrational and rotational transitions at the THz energy level. THz sources and detectors are necessary for such sensing applications. High sensitivity with a sufficient dynamic range, therefore, requires a source providing sufficient power on the one hand and a sufficiently sensitive detection mechanism on the other hand. This work concentrates on the detection mechanism. We propose a gas sensor that uses the photoacoustic technique combined with a triple resonator design to enhance the signal using only 100's of µW of THz source power.

I.2. THz FOR FOOD

Food waste is a major societal problem today, especially with the large production of packaged food. Food packaging is a way to conserve and transport food for the consumer. But after that and until now, there is no way to check the freshness of the food in real time and without destroying the packaging. As a result, for safety reasons and due to limited information on the biochemical degradation mechanisms of packaged food, huge quantities of packaged food are disposed of. The histogram of figure I.2.1, published by the food and agriculture organization of the united nations, shows that food waste per capita in Europe is estimated at 280 Kg/year. Furthermore, almost 40% of this waste happens at retail and consumer levels which means after packaging [25].

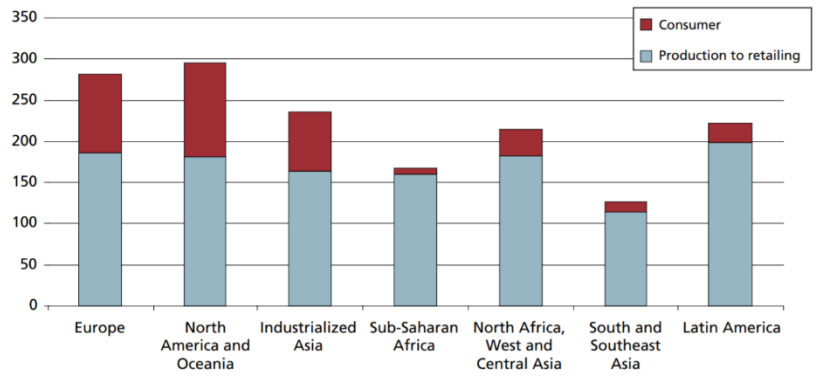

Figure I.2.1 Food waste per capita before and after consumer level [25]

The food spoilage process is related to a microbiological activity. A large number of different volatile organic compounds (VOCs) are emitted by the packaged food during its storage period. The concentration evolution of some molecules is responsible for color and odor change and finally for food spoilage. Several studies on food safety and VOCs analysis for packaged vegetables and fish, present different molecules as food spoilage indicators such as hydrogen sulfide (H_2S), ethyl acetate ($C_4H_8O_2$), ethanol (C_2H_5OH), ammonia (NH_3) … [26]–[31]. The production of H_2S by other food types such as beef meat [32]–[34] and cheddar cheese [35] was also reported. Many of these molecules can be detected by THz spectroscopic techniques due to their high absorption peaks in this frequency region. The detection of H_2S inside a salmon food package has been reported by F.Hindle et al. [36] in the framework of this project, using THz absorption spectroscopy.

The advantage of THz waves is limited not only to its ability to detect these compounds but it also possible to do that without destroying the package. The plastics that make up the food package, like polystyrene, polyethylene, polypropylene … are transparent for THz waves unlike other regions such as the visible.

As previously mentioned, several studies have shown the existence and evolution of H_2S concentrations inside different types of food packages. It has also been proven that this gas can be used as a food spoilage indicator. Since this polar molecule presents several strong rotational absorption peaks in the THz spectrum, we propose within the framework of the Interreg Terafood project a THz gas sensor dedicated to the detection of low concentrations of H_2S for food quality control. This sensor is based on the THz photoacoustic spectroscopic technique. Before describing

the working of this sensor we will first introduce the difference between the THz absorption and photoacoustic spectroscopies.

I.3. THz ABSORPTION SPECTROSCOPY

Absorption spectroscopy is an old well-known technique, that studies the interaction between electromagnetic waves and matter. This interaction allows discovering the optical, electronic, and chemical properties of a material, such as refractive index, conductivity, and energy levels. While microwave, infrared, UV, and visible spectroscopy are commercially used for a long time, THz spectroscopy is only starting to emerge as a result of recent improvements in the availability of power sources and better detection techniques. The THz low energy (0.41-41.5 meV) is able to probe the rotational energy levels of polar molecules or low energy vibrational levels of flexible molecules (figure I.3.1). These molecular excitations are represented by a specific resonance frequency which is unique to each molecule and called its "fingerprint". This technique is used to measure the transmitted signal intensity of a broadband or a tunable monochromatic source through a test sample.

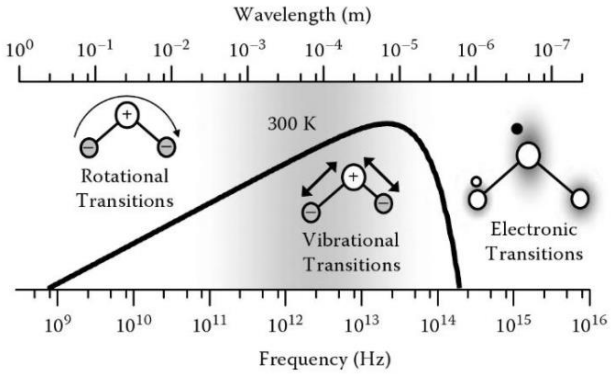

Figure I.3.1 Atomic and molecular transitions represented on the electromagnetic wave spectrum [12]

I.3.1. Molecular absorption

The attenuated signal intensity is considered to be related to the absorbance by the molecules or atoms contained in a test sample according to the Lambert-Beer law:

$$I(\upsilon)_T = I_0 e^{-\alpha(\upsilon)L} \qquad \text{(I.3.1)}$$

where $I(\upsilon)_T$ $\left(\frac{W}{cm^2}\right)$ represents the transmitted signal intensity, I_0 $\left(\frac{W}{cm^2}\right)$ the source emitted signal intensity, $\alpha(\upsilon)$ (cm^{-1}) the molecule's or sample's absorbance, L (cm) the sample length and υ the resonance frequency defined by:

$$\upsilon = \frac{E_j - E_i}{h}. \tag{I.3.2}$$

$h = 6.626 \times 10^{-34}$ $\frac{m^2 Kg}{s}$ corresponds to Planck's constant and $E_j - E_i$ is the energy difference between the upper and lower state related to the absorbed photon energy at a frequency υ. Figure I.3.2 shows a schematic of the THz absorption spectroscopy. The THz signal traveling through a gas cell of a length L is attenuated due to the molecular absorption and then detected by a sensitive THz detector.

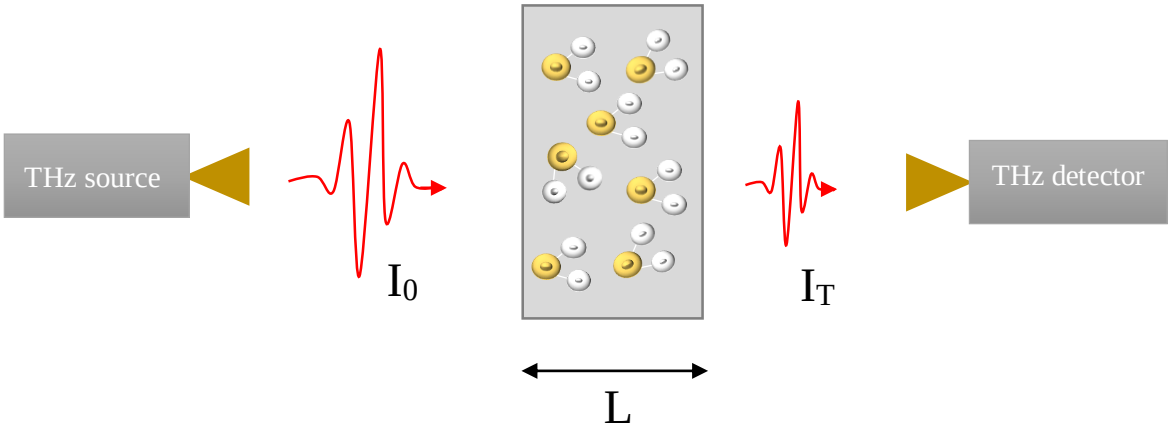

Figure I.3.2 A schematic of the THz absorption spectroscopy

For low absorption approximation equation I.1.1 gives:

$$I(\upsilon)_T = I_0 e^{-\alpha(\upsilon)L} = I(\upsilon)_T = I_0(1 - \alpha(\upsilon)L) \tag{I.3.3}$$

$$\alpha(\upsilon) = \frac{1}{L}\frac{\Delta I}{I_0} \tag{I.3.4}$$

The absorbance $\alpha(\upsilon)$ is also represented as a function of gas density N $\left(\frac{mol}{cm^3}\right)$ and molecules absorption cross section $\sigma(\upsilon)$ $\left(\frac{cm^2}{mol}\right)$

$$\alpha(\upsilon) = N\sigma(\upsilon) \tag{I.3.5}$$

Using equations I.3.4 and I.3.5, equation I.3.6 gives the relationship between the gas density N and the measured or transmitted signal intensity:

$$N = \frac{1}{\sigma(\upsilon)L}\frac{\Delta I}{I_0} \tag{I.3.6}$$

and thus the gas concentration given by $C = \frac{N}{N_{total}}$ where $N_{total} = N_L \frac{296}{T} P_0$ and $N_L = 2.479 \times 10^{19}\, mol.cm^{-3}.atm^{-1}$ the Loschmidt number can be obtained from equation I.3.6. Therefore, the minimum detectable concentration and the sensitivity of the spectroscopic technique is related to molecules absorption cross section $\sigma(\upsilon_i)$, molecules-electromagnetic waves interaction length L , source power, and detector sensitivity.

The frequency-integrated molecule absorption cross section $\varsigma(\upsilon)$ defined as

$$\varsigma(\upsilon) = \int_{-\infty}^{+\infty} \sigma(\upsilon) d\upsilon \tag{I.3.7}$$

is also expressed by the product between the linestrength S and the lineshape function $\varphi(P,T)$ at certain pressure P and temperature T

$$\varsigma(\upsilon) = S\, \varphi(P,T) \tag{I.3.8}$$

The linestrength $S\left(\frac{cm}{mol}\right)$ depends on $P_j = \frac{N_j}{N}, P_i = \frac{N_i}{N}$ the probability of density of states for E_j and E_i energy levels respectively, following the Boltzmann distribution and Einstein absorption coefficient $B_{ji} = \frac{8\pi^3}{3h^2c}\mu_{ji}^2 \left(\frac{cm^2}{J.s}\right)$ with μ_{ji}^2 the electric dipolar momentum:

$$S = h\upsilon_{ji} B_{ji}\left(P_j - P_i\right) \tag{I.3.9}$$

$$S = h\upsilon_{ji} B_{ji} \frac{N_j}{N}\left(1 - e^{-\frac{h\upsilon_{ji}}{KT}}\right) \tag{I.3.10}$$

$$S = \frac{h\upsilon_{ji} B_{ji}}{Q_T}\left(e^{-\frac{E_j}{KT}} - e^{-\frac{E_i}{KT}}\right) \tag{I.3.11}$$

where $N_i = N_j e^{-\frac{h\upsilon_{ji}}{KT}}$ and $N_j = \frac{N}{Q_T} e^{-\frac{E_j}{KT}}$, with Q_T the total partition function. The linestrength S of certain molecules can be found in the HITRAN database[37].

Not only sensitivity is important in gas absorption spectroscopy, but selectivity and resolution are also desired as many molecules with very close absorption lines at low temperature exists. Self or natural, Doppler, and collisional broadening are the three processes that could affect the absorption lineshape $\varphi(P,T)$. High resolution spectroscopic techniques are needed to allow discriminating closely spaced lines. Several THz spectroscopies have been reported such as Time domain THz spectroscopy (THz-TDS) [38]–[42], continuous wave (CW) THz spectroscopy [43]–[52], THz comb spectroscopy [53]–[56]. Although fast and covering a broad spectral range, THz-TDS suffers from its poor spectral resolution limited by the mechanical delay stage precision. In contrast, CW and frequency comb THz spectroscopy benefit from narrow linewidth sources, such as QCL [43]–[46], photomixing [47]–[50], and multiplied microwave sources [51], [52], but these sources have limited bandwidth and low power at room temperature. To increase the sensitivity of such techniques, large gas cells allowing to increase the light-molecules interaction length and high sensitivity detectors often needing cryogenic cooling are highly required.

On the other hand, another spectroscopic technique called photoacoustic spectroscopy (PAS) allows to detect gas molecules' concentrations with high sensitivity, fast response and low cost will be presented in the next section

I.4. THz PHOTOACOUSTIC SPECTROSCOPY

Before being used in spectroscopic techniques, the photoacoustic (PA) effect was discovered in 1880 by Bell when he demonstrates the first optical telecommunication system the photophone [57]. The schematic of Bell's photophone experiment is illustrated in figure I.4.1. He uses a thin glass metalized disk to reflect the sunlight toward a selenium cell connected to a telephone receiver. The thin disk would bend and vibrate under the effect of the speaker's sound wave. The sunlight reflected on the disk surface is then modulated in response to the vibrations of the disk. A telephone receiver allows finally to hear the voice from the modulated light collected by the selenium cell.

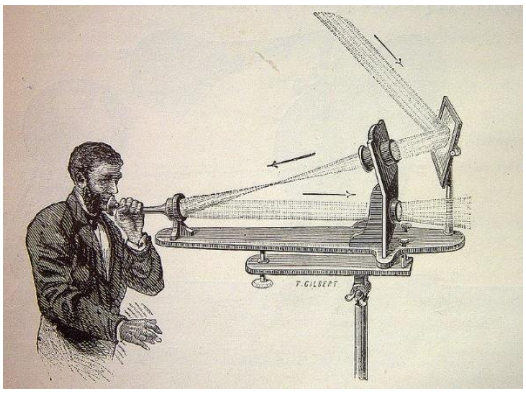

Figure I.4.1 Illustration of Bell's discovery: the photophone

It took almost 90 more years for this discovery to find its true potential as a spectroscopic tool. Thanks to the demonstration of laser sources in 1960 [58], that photoacoustic was applied for the detection of water vapor and CO_2 gas molecules in 1968 [59].

As described previously in section I.3 an atomic or molecular system is excited, by going from the ground (E_i) to a higher energy state (E_j) following the interaction with an electromagnetic wave of $h\upsilon_{ji}$ photon energy. This excitation phenomenon is followed by two principal relaxation processes, radiative and non-radiative relaxation. The radiative relaxation is related to stimulated or spontaneous emission, while the non-radiative one is mainly manifesting itself as heat generation caused by molecular collisions. THz energy corresponds to the excitation of rotational and vibrational energy levels. At these energy levels, the non-radiative relaxation process is dominant. When the light interacting with molecules is modulated, a pressure acoustic wave is generated resulting from the periodic heat dissipation of the relaxation process. Therefore, in contrast to the direct absorption spectroscopy, which measures the intensity of light absorbed by the excited molecules, this technique with zero background measures the pressure wave created by the molecules' response. In absorption spectroscopy, the attenuation of the transmitted light isn't only limited by the molecular absorbance, but it is also the result of the experimental setup absorption and reflection losses, such as the one caused by the cell windows. In addition to this, a direct measurement of the transmitted light is sometimes accompanied by the detection of black body radiations. Therefore, to eliminate all these undesired effects a background correction is necessary, by measuring the transmitted signal in absence of gas molecules. However, the detection of the acoustical signal in the PAS technique is only attributed to the molecular absorption resulting in a zero background measurement.

The THz photoacoustic spectroscopy is illustrated in figure I.4.2. A modulated THz light is absorbed by the gas molecules, followed by a nonradiative relaxation process leading to the generation of periodic heat waves. The produced heat is then detected as an acoustic wave using a microphone.

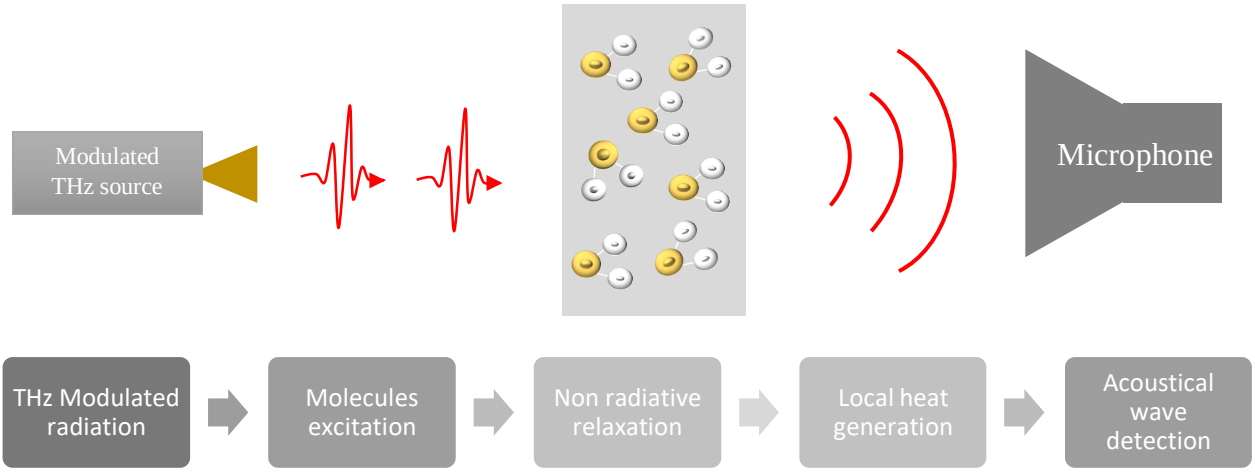

Figure I.4.2 A schematic of the THz photoacoustic spectroscopy

I.4.1. Molecular relaxation and heat production

Similarly to the absorption spectroscopy, the excitation process of a molecule with density N is presented by two-level states E_i and E_j with densities $N_i = N - N_j$ and N_j respectively after the absorption of photon energy $h\upsilon_{ji}$. The excitation process is followed by the relaxation process and the density exchange $\frac{dN_j}{dt}$ of the excited state j is expressed by the following equation:

$$\frac{dN_j}{dt} = (N - N_j)\sigma\psi - N_j\left(\sigma\psi + \frac{1}{\tau}\right) \qquad \text{(I.4.1)}$$

with σ the molecular cross section, $\psi\left(\frac{cm^{-2}}{s}\right)$ function representing the incident photon flux and $\tau\ (s)$ the relaxation lifetime. The first part of this equation corresponds to the excitation process however the second one represents the radiative (spontaneous and stimulated emission) and non-radiative relaxation process. Considering a low incident light power, the stimulated emission can be neglected due to the low population density in the excited state ($N_j \ll N$). Equation I.4.1 become:

$$\frac{dN_j}{dt} = N\sigma\psi - N_j\frac{1}{\tau} \tag{I.4.2}$$

The inverse relaxation lifetime $\left(\frac{1}{\tau}\right)$ is expressed by the sum of radiative $\left(\frac{1}{\tau_r}\right)$ and non-radiative$\left(\frac{1}{\tau_{nr}}\right)$ inverse lifetime

$$\frac{1}{\tau} = \frac{1}{\tau_r} + \frac{1}{\tau_{nr}} \tag{I.4.3}$$

At THz frequencies the non-radiative process is dominant and this is due to the very short non-radiative lifetime ($\tau_{nr} \approx 10^{-12}s$) compared to the radiative one ($\tau_r \approx 10^{-6}s$) [60]. Therefore the relaxation lifetime τ is considered to be limited by τ_{nr} and $\tau \approx \tau_{nr}$. For a sinusoidal modulated incident EM wave, the photon flux function can be written as follows:

$$\psi = \psi_0\left(1 + e^{i\omega t}\right) \tag{I.4.4}$$

where ψ_0 correspond to the non-modulated part, and $\psi_0 e^{i\omega t}$ is time dependent with $\omega = 2\pi f$ the angular modulation frequency of the EM wave source. Since the photoacoustic response is governed by the modulation signal, it suffices to consider the time dependent part of the equation (I.4.2):

$$\frac{dN_j}{dt} = N\sigma\psi_0 e^{i\omega t} - N_j\frac{1}{\tau} \tag{I.4.5}$$

Searching for a solution of type,

$$N_j = N_{j0}e^{i\omega t} \tag{I.4.6}$$

for the differential equation (I.4.5) type $\left(y' + ay = f(t)\right)$ gives:

$$N_{j0} = \frac{N\sigma\psi_0\tau}{\sqrt{1 + (\omega\tau)^2}}\, e^{-i\varphi} \tag{I.4.7}$$

with

$$\varphi = \tan^{-1}(\tau\omega) \tag{I.4.8}$$

The final solution of the excited state population is then:

$$N_j = \frac{N\sigma\psi_0\tau}{\sqrt{1+(\omega\tau)^2}}\, e^{i(\omega t-\varphi)} \tag{I.4.9}$$

The heat generation caused by the periodic relaxation process is then proportional to the population density of the excited state N_j, and the probability of transition $\frac{1}{\tau}$. This relation is expressed by:

$$H = \frac{N_j h\nu}{\tau} \tag{I.4.10}$$

with $h\nu$ the thermal energy, where ν corresponds to the absorption frequency or also light source frequency. The final expression of heat is given by the combination of equation I.4.9 and I.4.10

$$H = H_0 e^{i(\omega t-\varphi)} \tag{I.4.11}$$

where $H_0 = \frac{N\sigma I_0}{\sqrt{1+(\omega\tau)^2}}$ represents the heat amplitude and $I_0 = \psi_0 h\nu$ the light source intensity.

For low modulation frequency $\omega\tau \ll 1$, the approximation of heat amplitude is then:

$$H_0 = N\sigma I_0 \tag{I.4.12}$$

$$H_0 = \alpha(\upsilon) I_0 \tag{I.4.13}$$

The generated heat energy is directly proportional to the absorbance $\alpha(\upsilon)$ and the light source intensity I_0. This linearity is only valid for slow modulation frequencies ($\omega\tau \ll 1$) and low light intensity to prevent optical saturation. At these conditions, the generated heat is then proportional to molecule concentration. Therefore, the lowest detected concentration using this technique depends on the sensitivity of the thermal wave detection

I.4.2. Local heat production into acoustic wave generation

The relation between generated heat and acoustic pressure wave was presented by Morse and Ingrad in 1968 [61] using thermodynamics and fluid mechanics laws. This model is described by the momentum (Navier Stokes in absence of viscosity losses) (I.4.14), and mass conservation equations (I.4.15), thermodynamic equation of state for density change (I.4.16) and entropy change (I.4.17), and the equation of heat flow continuity (I.4.18)

$$\frac{\partial \mathrm{v}}{\partial t} = -\frac{1}{\rho_0}\nabla p(r,t) \tag{I.4.14}$$

$$\frac{\partial \delta(r,t)}{\partial t} + \rho_0 \nabla . \mathrm{v_l} = 0 \tag{I.4.15}$$

$$\delta(r,t) = \left(\frac{\partial \rho}{\partial P}\right)_{T_0} p(r,t) + \left(\frac{\partial \rho}{\partial T}\right)_{P_0} \theta(r,t) = \gamma \rho \kappa_s \big(p(r,t) - \alpha\theta(r,t)\big) \tag{I.4.16}$$

$$\sigma_s(r,t) = \left(\frac{\partial S}{\partial P}\right)_{T_0} p(r,t) + \left(\frac{\partial S}{\partial T}\right)_{P_0} \theta(r,t) = \frac{C_P}{T}\left(\theta(r,t) - \frac{\gamma-1}{\gamma} p(r,t)\right) \tag{I.4.17}$$

$$T\frac{\partial \sigma_s}{\partial t} \approx K\nabla^2\theta \tag{I.4.18}$$

In the previous equations, v correspond to the fluid (gas) velocity, while $\mathrm{v_l}$ represent it longitudinal part that contributes to the pressure variation. ρ_0, P_0 and T_0 correspond respectively to the medium initial mass density, pressure, and temperature at equilibrium. However, their variations are defined by δ for mass density, p for pressure, and θ for temperature. Similarly σ_s is for the entropy variation. The thermal physical coefficients κ_s, κ_T, β, and K describe respectively, the adiabatic and isothermal compressibility, thermal expansion, and conductivity. With $\alpha = \frac{\beta}{\kappa_T}$ the rate of increase of pressure with the temperature at constant volume. And finally $\gamma = \frac{C_p}{C_v}$ the specific heat at constant pressure and volume ratio.

To solve this complex model another approximation is used by considering a small variation of temperature T, pressure P, mass density ρ and entropy S of the system and written by:

$$\begin{aligned} P(r,t) &= P_0 + p(r,t) \\ \rho(r,t) &= \rho_0 + \delta(r,t) \\ T(r,t) &= T_0 + \theta(r,t) \end{aligned} \tag{I.4.19}$$

$$S(r,t) = S_0 + \sigma_s(r,t)$$

Without going into further detail in the calculation presented in [61], by eliminating the temperature T, mass density ρ, gas velocity v and entropy S dependency from the previous equations, the relation between pressure wave and generated heat is expressed by the following linear wave equation:

$$\nabla^2 p(r,t) - \frac{1}{c_s^2}\frac{\partial^2 p(r,t)}{\partial t^2} = -\frac{\gamma - 1}{c_s^2}\frac{\partial H(r,t)}{\partial t} \tag{I.4.20}$$

with $c_s = 343\ m/s$ speed of the sound in the air and $H(r,t)$ the heat source presented in equation (I.4.11).

I.4.3. Acoustical signal amplitude and PA sensitivity

The acoustical signal of the PAS technique is determined by the solution of equation I.4.20. This inhomogeneous wave equation is solved by taking its Fourier transformation

$$\left(\nabla^2 + \frac{\omega^2}{c_s^2}\right) p(r,\omega) = i\omega\left(\frac{\gamma - 1}{c_s^2}\right) H(r,\omega) \tag{I.4.21}$$

where

$$\begin{aligned} p(r,t) &= \int p(r,\omega)\, e^{-i\omega t}\, d\omega \\ H(r,t) &= \int H(r,\omega)\, e^{-i\omega t}\, d\omega \end{aligned} \tag{I.4.22}$$

and searching for a solution of the type

$$p(r,\omega) = \sum_j A_j(\omega) p_j(r) \tag{I.4.23}$$

corresponding to the sum of $p_j(r)$ modes solution of the homogenous equation with amplitude $A_j(\omega)$. The solution of the homogenous equation

$$\left(\nabla^2 + \frac{\omega_j^2}{c_s^2}\right) p_j(r) = 0 \tag{I.4.24}$$

depends on the acoustic cell geometry and boundary conditions that will be discussed in the next section with a particular solution of the cylindrical acoustic resonator. Inserting (I.4.23) in (I.4.21) with the use of equation (I.4.24) and the normalization condition (I.4.25):

$$\int p_i^* p_j = V_c \delta_{ij} \tag{I.4.25}$$

gives the mode amplitude:

$$A_j(\omega) = -\frac{i\omega}{\omega_j^2}\frac{\gamma - 1}{V_c}\frac{\int p_j^* H \, dV}{1 - \left(\frac{\omega}{\omega_j}\right)^2} \tag{I.4.26}$$

For a modulation angular frequency ω equivalent to the mode resonance frequency ω_j, the resonant mode amplitude A_j goes to ∞, this has no physical sense because of the absence of loss which is not considered here. To include losses, the term Q_j is added to the equation (I.4.26) giving:

$$A_j(\omega) = -\frac{i\omega}{\omega_j^2}\frac{\gamma - 1}{V_c}\frac{\int p_j^* H \, dV}{1 - \left(\frac{\omega}{\omega_j}\right)^2 - \frac{i\omega}{\omega_j Q_j}} \tag{I.4.27}$$

Q_j is a dimensionless factor called quality factor and represents the losses of a physical resonator. It is defined by $Q_j = 2\pi \frac{Accumulated\ energy}{Energy\ lost\ per\ cycle}$ representing the energy losses of a wave after a round trip inside a cavity. It could be also written as $Q_j = \frac{f_0}{\Delta f}$, where f_0 corresponds to the resonance frequency and Δf to its full width half maximum (FWHM).

Using equations (I.4.13) and (I.4.27), a representation of the acoustical signal amplitude $A_j(\omega)$ as a function of light intensity I_0 and the molecules' absorption $\alpha(\upsilon)$ can be written using the following expression:

$$A_j(\omega) = -\frac{i\omega\alpha(\upsilon)}{\omega_j^2}\frac{\gamma - 1}{V_c}\frac{\int p_j^* I_0 \, dV}{1 - \left(\frac{\omega}{\omega_j}\right)^2 - \frac{i\omega}{\omega_j Q_j}} \tag{I.4.28}$$

The light intensity I_0 and power P_0 are related by a function $g(r)$ representing the spatial distribution of the light beam (i.e. Gaussian distribution, optical cavity mode …)

$$I_0 = P_0 g(r) \tag{I.4.29}$$

Considering the case of perfect resonance $\omega = \omega_j$, the final expression for the acoustical signal amplitude at the resonant frequency is expressed by:

$$A_j(\omega_j) = \frac{\alpha(\upsilon) P_0 Q_j (\gamma - 1) L}{\omega_j V_c} \frac{1}{L} \int p_j^* \, g(r) \, dV \tag{I.4.30}$$

Where L represents the cell length , and the integration $\frac{1}{L} \int p_j^* \, g(r) \, dV$ defines the overlap between acoustical and optical modes.

Finally, the expression (I.4.30), shows the dependence of the acoustical signal on molecules absorbance $\alpha(\upsilon)$, light (EM wave) power P_0, acoustic cell geometry: volume V_c, length L and quality factor Q_j, acoustic resonance frequency (light modulation frequency) ω_j and finally, the light and acoustic modes overlap $\vartheta = \frac{1}{L} \int p_j^* \, g(r) \, dV$.

Therefore, to increase the sensitivity of PAS techniques, a resonant cell such as a Helmholtz resonator, cavity resonator, or cylindrical resonator with high quality factor is necessary. The next section describes one of the most used resonant cells in PAS: the cylindrical one.

I.4.4. Cylindrical acoustical resonators

In resonant PAS, the gas cell is not limited by the container role, but it also serves as an acoustic resonator to enhance the acoustic signal and increase the sensitivity. The most commonly used shape cells are cylindrical ones with open or closed ends. Taking one particular case of a gas cell (namely a cylindrical open end cell), the homogenous wave equation (I.4.24) can be solved by applying the boundary conditions for this case. Using the cylindrical coordinates equation (I.4.24) becomes:

$$\frac{1}{r} \frac{\partial}{\partial r} \left(r \frac{\partial}{\partial r} + \frac{1}{r^2} \frac{\partial^2}{\partial \varphi^2} + \frac{\partial^2}{\partial z^2} \right) p_j(r, \varphi, z, \omega) \; + k_j^2 p_j(r, \varphi, z, \omega) = 0 \tag{I.4.31}$$

With $k_j = \frac{\omega_j}{c}$ the eigenvalues of the eigenfunctions $p_j(r, \varphi, z, \omega)$. Separating the variables $p_j(r, \varphi, z) = R(r)\emptyset(\varphi)Z(z)$, and finding solution for $R(r), \emptyset(\varphi)$ and $Z(z)$, gives the general solution of equation (I.4.31):

$$p_j(r, \varphi, z, \omega) = \cos(m\varphi)\sin(k_z z) J_m(k_r r) \tag{I.4.32}$$

With $m = k_\varphi r$, $k = \sqrt{k_r^2 + k_\varphi^2 + k_z^2}$ and J_m the Bessel function of m[th] order. At the cell walls and closed ends, the normal fluid velocity vanishes resulting in a boundary condition with no pressure variation $\nabla p_{wall} = 0$, while at open boundaries, the pressure vanishes and satisfies the condition $p = 0$. Thus the final solution with these boundary conditions is the following:

$$p_j(r, \varphi, z, \omega) = \cos(m\varphi)\sin\left(\frac{l\pi z}{2L}\right) J_m\left(\frac{\alpha_{mn} r}{R_0}\right) \tag{I.4.33}$$

and

$$f_{lmn} = \frac{c_s}{2}\sqrt{\left(\frac{l}{2L}\right)^2 + \left(\frac{\alpha_{mn}}{\pi R_0}\right)^2} \tag{I.4.34}$$

With f_{lmn} the resonance frequency of the different acoustical modes. l, m, and n are the indexes of the longitudinal, azimuthal, and radial modes respectively. R_0 corresponds to the cylinder radius and L to its length. The first values of α_{mn} that corresponds to the n[th] solution of the equation $\frac{dJ_m}{dr} = 0$ at $r = R_0$ are represented in table I.4.1. The fundamental resonance frequency of longitudinal, azimuthal, and radial mode corresponds respectively to $f_{100} = \frac{c_s}{4L}$, $f_{010} = \frac{\alpha_{10} c_s}{2\pi R} = \frac{1.84\, c_s}{2\pi R}$, $f_{001} = \frac{\alpha_{01} c_s}{2\pi R} = \frac{3.83\, c_s}{2\pi R}$. Therefore, the longitudinal resonance frequency is defined by the length of the cylinder, while the azimuthal and radial ones are adjusted by its radius. Figure I.4.3 shows the propagation of a longitudinal pressure wave mode inside a one open end cylinder. The pressure is maximal at the close end and vanishes at the open side. However, for a both open sides cylinder, the pressure wave with a resonant frequency $f_{100} = \frac{Lc_s}{2}$ vanishes at the two sides edges and achieves its maximum at the cell center. Similarly, for a two closed ends cylinder with $f_{100} = \frac{Lc_s}{2}$, the wave has maxima and minima at the ends and vanishes in the cell center. Differently, the radial and azimuthal modes behave independently from the cell ends.

α_{mn}	n / m	0	1	2	3
0		0	3.832	7.016	10.173
1		1.841	5.331	8.526	11.706
2		3.054	6.706	9.969	13.170
3		4.201	8.015	11.346	14.586

Table I.4.1 Some of the values of α_{mn}

While longitudinal and radial modes are highly investigated in PAS for acoustic signal amplification, the azimuthal modes are less used due to their lower quality factor and off axis excitation.

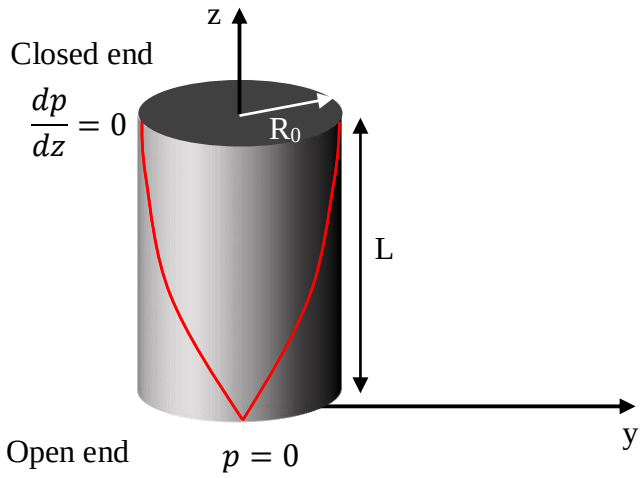

Figure I.4.3 One open end cylinder cell with radius R_0 and length L. The red lines represent the pressure wave of the fundamental longitudinal mode

Such type of cell is well known and has been highly used with different modes and several detections and excitation mechanisms. Adjusted designs by adding buffers to the cell's ends, or by using a parallel cylinder to reduce the acoustic impedance and noise are also investigated.

I.4.5. Pressure wave detection: microphones, cantilevers, and quartz tuning forks

The previous sections describe the generation and enhancement of pressure waves in PAS. The next and final regarding the detection of sound wave detection is presented here. PAS usually uses

microphones for the detection of sound waves. Therefore, the sensitivity of this technique is also related to the microphones' responsivity.

In classical PAS condenser microphones are usually used. Such microphones are formed by two electrodes with distance d and surface A to form a capacitance. One of these electrodes is a vibrating metalized membrane, the membrane displacement of this membrane varies the capacitance C:

$$p \propto \Delta C = \frac{\varepsilon A}{3d^2} w_0 \tag{I.4.35}$$

Where ε correspond to the permittivity of the medium between electrodes, p, ΔC and w_0 pressure, capacitance variation, and membrane displacement. The pressure variation is proportional to the capacitance variation, which increases by increasing the distance d between electrodes and their surface A. However, the most sensitive commercial microphones with optimized d and A are limited by a damping factor called breathing effect due to the presence of the second electrode.

In an attempt to increase the microphone sensitivity some techniques, such as cantilever enhanced photoacoustic spectroscopy (CEPAS) [62]–[66], propose the use of optical methods for microphone displacement detection. In these techniques, the condenser microphone is replaced by microelectromechanical systems (MEMS) such as a thin membrane or a microcantilever. The second electrode used in a condenser microphone to form the capacitance is not necessary here as the mechanical displacement is optically and not electrically detected. Similarly, to a condenser microphone, when a pressure wave hits the MEMS, it starts to vibrate. The displacement of the vibrating object is detected by a laser beam focused on its back, and using an interferometer to detect an optical path difference and phase mismatch giving information about the object displacement. The amplitude A of a vibrating cantilever is expressed by:

$$A = \frac{F_0}{m\sqrt{(\omega_0^2 - \omega^2)^2 + \left(\frac{\omega\beta}{m}\right)^2}} \tag{I.4.36}$$

where F_0 correspond to the external force produced by the pressure wave, β a damping constant, ω the light modulation angular frequency, m and $\omega_0 = 2\pi f_0$ are respectively the cantilever's mass and angular resonance frequency. The sensitivity of these detection techniques is then limited

by the cantilever's resonance frequency and the sensitivity of the optical system used for the detection.

At THz frequencies, the demonstrations of CEPAS have been little studied. The detection of methyl cyanide (CH_3CN) absorption lines between 300 and 500 GHz was achieved by [67] and [68] with a normalized noise equivalent absorption (NNEA) of 1.39×10^{-9} and 4.28×10^{-10} cm^{-1} W $Hz^{-1/2}$ respectively. These NNEA values correspond to a minimum detection limit (MDL) of 100 and 80 ppm. The NNEA and MDL are two factors used to describe the sensitivity of a gas sensor. NNEA is expressed by:

$$NNEA = \alpha_{min} P_0 \sqrt{t} \tag{I.4.37}$$

where α_{min} correspond to the minimal detectable absorption coefficient, P_0 the THz power and t the integration time. While the MDL represents the minimal detected concentration for a unity signal to noise ratio (SNR).

In 2002, the quartz enhanced photoacoustic spectroscopy (QEPAS) was proposed by Kosterev et al. [69] as another approach for the detection of weak photoacoustic signals. For the QEPAS shown in figure I.4.4, the resonant acoustic cell and sensitive microphones are replaced by the use of high Q resonant transducer tuning fork. Quartz tuning forks (QTF) are being employed for a long time already in watches since the late 1960s. Their shape is well known and formed by two prongs connected at one end, that oscillate together. An approximate solution of the fundamental resonant angular frequency $\omega = 2\pi f$ of a tuning fork is defined by:

$$\omega = \frac{1.76a}{l^2}\sqrt{\frac{E}{\rho}} \tag{I.4.38}$$

Its working frequency is determined by the prong length l, thickness a, quartz Young modulus E, and its mass density ρ. The traditional QTF has a prong length $l = 3.2\ mm$, thickness $a = 0.33\ mm$ and a gap of $0.3mm$ in between the prongs, where a laser beam is focused and excites the molecules that allow generating the heat causing the tuning fork (TF) motion. The high Q factor of such an oscillator (in the order of 10^3 at atmospheric pressure which is at least 10 times higher than a traditional acoustic resonant cell), allows to store and enhance the acoustic signal which is finally transformed into an electrical signal due to the piezoelectric properties of quartz.

To prevent high noise, the laser beam has to be well focused between the prong without touching them. Several techniques have been proposed to achieve this: tapered optical fibers, off axis excitation… However, when working at THz frequencies the gap in between the prongs is in the order of the beam wavelength (1 THz ≈ 0.3 mm). Therefore, for the use in THz PAS, an adjusted larger design of QTF ($l = 17.7mm$, $a = 1.3mm$, and a gap of $0.8mm$) with a resonant frequency of $f = 4.246\ kHz$ and a $Q = 9330$ was proposed by Borri et al.[70].

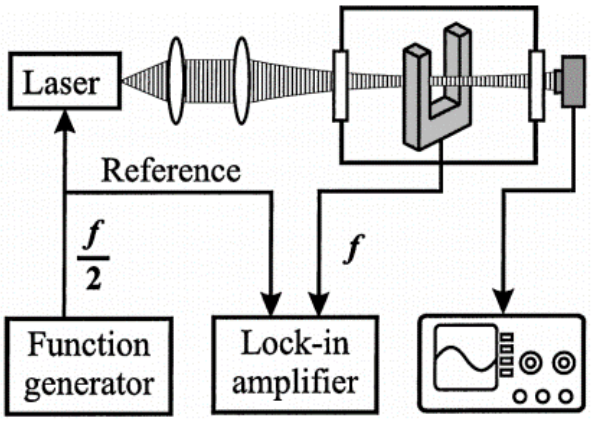

Figure I.4.4 Experimental setup of the first QEPAS by [69]

After this first successful demonstration, the THz QEPAS has observed rapid growth. In the past few years, several THz QEPAS with high sensitivity was reported. An MDL of 7 ppm for the detection of methanol (CH_3OH) was presented by [71]. The detection of 13 ppm and a record of 360 ppb of H_2S was demonstrated in [72] and [73] respectively. However, most of these demonstrations rely on the use of THz QCL (Quantum cascade laser) which requires cryogenic cooling. Due to the very high Q factors of the TF these sensors require a long integration time. In addition to the slow acquisition and the low working temperatures, these sensors suffer from the small light molecules interaction lengths due to the small distance between the TF prongs. To increase the interaction length, some work in the MIR have proposed to combine a QEPAS or CEPAS with optical cavities [74]–[76]. However, such demonstration in the THz is still missing.

The photoacoustic spectroscopy has shown several interests in IR as in THz region for the detection of gas molecules, due to its high sensitivity and zero background measurements. Several versions have been proposed and discussed in this chapter such as PAS, resonant PAS, CEPAS, and QEPAS. A performance comparison between several THz sensors based on different PA

techniques is illustrated in table I.4.2. Each of these techniques has a minimal detected signal defined by several parameters, such as cell geometry, resonators quality factors, optical power, interaction length, microphones sensitivity…

PAS technique	CEPAS [67]	CEPAS [68]	QEPAS [71]	QEPAS [72]	QEPAS [73]
THz source & power (mw)	AMC VDI 0.6-1.4 mW	AMC VDI 25 µW	QCL 40 µW	QCL 0.24 mW	QCL 150 mW
Detected gas	CH_3CN	CH_3CN	CH_3OH	H_2S	H_2S
THz emission frequency	312 GHz	400 GHz	3.93 THz	2.91 THz	2.87 THz
Integration time	0.5s	0.5s	4s	30s	10s
Pressure	170 µbar	200 µbar	13 mbar	26 mbar	80 mbar
NNEA	1.39×10^{-9}	4.28×10^{-10}	2×10^{-10}	4.4×10^{-10}	3.1×10^{-8}
MDL	**100 ppm**	**80 ppm**	**7 ppm**	**13 ppm**	**360 ppb**

Table I.4.2 Table summarizing the performances of different THz PAS gas sensors

In this work, we will present a new integrated gas sensor based on the photoacoustic spectroscopy, and combine three different resonators to enhance the detected signal and to increase the sensitivity. The gas sensor shown in figure I.4.5 is integrated on a low-loss THz HR-Si guiding platform. A THz Photonic crystal (PhC) cavity is created by making circular etched holes in the core of a Si suspended waveguide. This cavity uses to confine a THz light inside an etched air hole at the absorption frequency of the target gas with high Q factors. The effective interaction length between the THz light and the gas present inside the cavity hole will increase by a factor proportional to the cavity Q factor. The same hole of the THz cavity behaves as an acoustical cylinder (similar to the one presented in I.4.4). The acoustical signal is then enhanced inside this acoustical resonator. The bottom of the cylinder is covered by a Poly-Si membrane representing a MEMS microphone. The latter corresponds to the third resonator that enhances the detected mechanical signal. A laser Doppler vibrometer (LDV) is finally used to optically read out the displacement of the Poly-Si mechanical resonator. More details on the sensor design will be presented in chapter II.

In the next sections, we will introduce and present the state of the art of THz waveguides and PhC cavities. These THz components represent the main electromagnetic parts of the designed gas sensor.

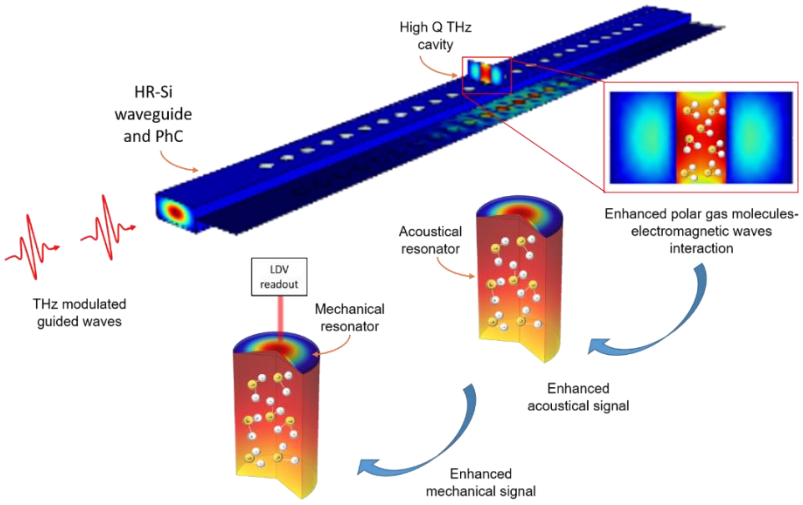

Figure I.4.5 Sensor design based on triple resonators

I.5. THz COMPONENTS

In addition to spectroscopy, THz waves are investigated in many more applications such as communication, medicine, imaging, astronomy… For the use in such applications, THz components such as sources, detectors, waveguides, cavities, modulators are necessary. In this work, we are not concentrating on the detection side, since the designed sensor is based on the PA technique that uses to convert the THz signal into mechanical energy. The sensitive detection of the THz signal is thus replaced by optical detection of a mechanical displacement. Powerful sources aren't either the subject of this work due to the original idea of the triple resonators sensor design that allows detecting low signals without the necessity of high THz power. One of the main reasons behind the signal enhancement is the presence of a high Q PhC cavity that strongly confines the THz light and increases its interaction with gas molecules. However, all of this depends crucially on the availability of a low loss THz platform in order to be able to work at low power. This low loss platform is represented by a HR-Si suspended waveguide. The design of the low loss Si suspended waveguide and the high Q PhC crystal cavity are presented in chapter II.

In this section, we discuss the different types and performances of the existing waveguide at the THz frequencies. Then, a brief introduction to the historical discovery of the PhC is presented. Finally, the state of the art of available THz PhC cavities is reported.

I.5.1. THz waveguides

In integrated circuits, low-loss waveguides are essential to transmit the EM waves between all passive and active components. They are also necessary to ensure the transition from off- to on-chip. The available THz waveguide can be classified into two different categories: Metallic and dielectric waveguides.

I.5.1.1 Metallic THz waveguide

Metallic waveguides (MWG) are well known in the microwave and millimeter wave bands. The same design of hollow metallic waveguides is scaled with smaller dimensions to work in the THz frequency band. The main disadvantage of these waveguides is their high ohmic loss, due to the finite conductivity of their metallic walls. The ohmic loss originates from the small skin depth of metal at high frequencies defined by:

$$\delta_s = \sqrt{\frac{2}{\omega\mu(\omega)\sigma}} \tag{I.5.1}$$

where $\omega = 2\pi f$ is the wave angular frequency, $\mu(\omega)$ the permeability, and σ metal conductivity. The cut-off frequency of a rectangular metallic waveguide is related to its cross section dimensions via the relation below:

$$f_{cmn} = c\sqrt{\left(\frac{m}{2a}\right)^2 + \left(\frac{n}{2b}\right)^2} \tag{I.5.2}$$

where $c = 3 \times 10^8\ m/s$ corresponds to the speed of light, a, and b the horizontal and vertical dimensions of the guiding channel, and m, n the modes index. For a single-mode operation at high frequencies, waveguides with very small dimensions are necessary. Because of their small dimensions, the fabrication of these waveguides requires a complex process and complicated assembly. Despite the fabrication complexity, these types of waveguides are fabricated and commercially used for frequencies up to 3 THz [77]. Figure I.5.1(b) shows a schematic of the VDI

WR-1.5 MWG covering the 500-750 GHz frequency range. The reported propagation losses of this WR-1.5 waveguide vary between 0.73 and 1.05 dB/cm. The bulky size of these commercial waveguides, prevent their use in integrated circuits. A miniaturized MWG was proposed by [78], [79] thanks to the Deep Reactive Ion Etching (DRIE) technique. The waveguide channel is etched inside a Si wafer using the DRIE technique, then a metal layer is added by sputter coating. A photograph and a schematic of the micromachined WR-1.5 MWG are presented in figure I.5.1 (a). The propagation loss measured by [78] and [79] corresponds respectively to 1.5 and 4 dB/cm at 570 and 380 GHz. These micromachined designs still suffer from high ohmic losses despite the use of thin reflective metal layers.

Figure I.5.1 (a) Micromachined metallic WR-1.5 waveguide [78], (b) schematic of the VDI WR-1.5 waveguide [77]

I.5.1.1 Dielectric THz waveguide

As opposed to metallic waveguides, dielectric ones do not depend on metallic reflectivity, but rather on the total internal reflection between two dielectric materials with different refractive indices $n = \sqrt{\mu_R \varepsilon_R}$. Dielectric waveguides were first used in the optical domain, then extended for the first time to mmW in 1958 [80]. The investigations of dielectric waveguides in the mmW region continue in the 1970s and 1980s [81]–[83], until the 1990s when the THz region was reached for the first time [84]. The main advantage of dielectric waveguide over metallic ones is obviously the absence of conduction losses. The propagation losses in such structures are governed by material absorption loss and radiative loss. For high modal confinement and low loss propagation THz waveguide, materials with large refractive index contrast and low losses are necessary to form the core and cladding of the waveguide. At THz frequencies, the available material systems that combine high index, transparency, and planar processing are limited. In

recent years the use of HR-Si for THz applications has attracted considerable interest, due to its very low absorption coefficient and large non-dispersive refractive index [85], [86]. The Silicon-on-glass waveguides shown in figure I.5.2 (a), presented by Ranjkesh et al. [87], use the refractive index contrast between Si and glass which are bonded together in order to create the guiding channel for mm-waves. The extracted propagation loss of this design was found to be 0.63, 0.28, and 0.53 dB/cm, for 55-65, 90-110, and 140-170 GHz bands. At frequencies beyond 400 GHz, the absorption of the glass substrate material increases dramatically [86], [88] and it becomes useless for guiding purposes. To avoid material losses, [89] proposes a layout where the glass is locally etched and the guiding layer is suspended by Silicon supporting beams (SB). A schematic of this suspended Si waveguide on a glass substrate is presented in figure I.5.2(b). An average loss of 0.54 dB/cm over 440-550 GHz frequency band is reported for this suspended waveguide. The process is laborious and the large number of SB increases the scattering losses due to roughness at the SB edges, adding to that a bonding of HR-Si/Glass followed by glass etching steps is still required.

Other types of dielectric waveguides known as line defect PhC or slab waveguides were also reported. The guiding principle of a line defect PhC waveguide is quite similar to the previously presented ridge waveguide. However, instead of only using the refractive index contrast between two different materials such as air/HR-Si or glass/HR-Si, it also uses the bandgap properties of a PhC for guiding purposes. Periodic holes are etched in the HR-Si on both sides of the guiding channel to create a cladding with an effective index lower than the refractive index of the HR-Si representing the core of the waveguide. The PhC and PhC cavities will be the main topics of the discussion in the following section. Figure I.5.2 (c) shows the schematic of a line defect PhC waveguide design proposed by [90].

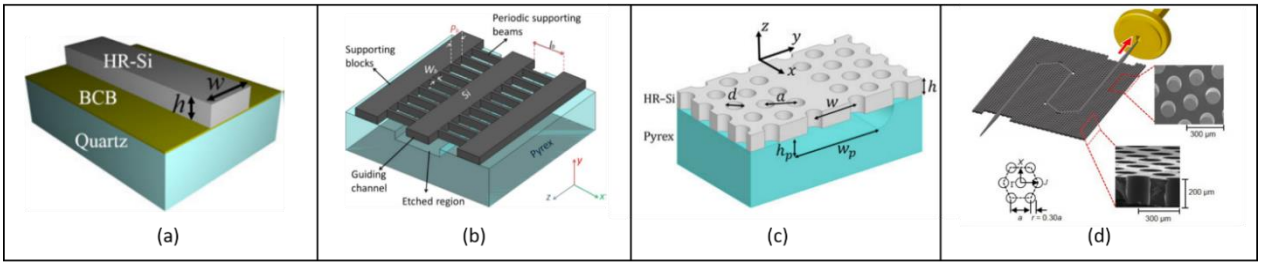

Figure I.5.2 Schematics of the different available designs of HR-Si waveguides. (a) silicon on glass waveguide [87], (b) silicon suspended waveguide [89], (c) Photonic crystal line defect waveguide [90], (d) Fully suspended Photonic crystal line defect waveguide [91]

Very large propagation losses of 4 dB/cm are measured in this work at the 540-630 GHz frequency range. These high losses are mainly the result of the large number of etched holes that greatly increase the scattering losses. In addition to the very high losses, the fabrication of this waveguide requires several technological steps: etching the glass, etching the HR-Si, and bonding the two parts. Another fully suspended line defect PhC waveguide design (see figure I.5.2 (d)) with fewer technological steps and lower propagation losses was presented in [91]. The disadvantage of this design is that the very low measured propagation losses of 0.1 dB/cm cover a very short frequency band region 326-331 GHz.

We presented in this section some of the several waveguides reported in the past few years at THz frequencies. Table I.5.1, summarizes and compares the performances of the existing THz waveguides discussed in this section. While the MWG suffers from high ohmic losses and bulky size, the HR-Si dielectric waveguides remain the best solution for an integrated compact guiding channel with low propagation losses.

Waveguide design	Propagation loss (average) (dB/cm)	Frequency (GHz)	Propagation loss (average) (dB/λ_0)
VDI WR-1.5 [92]	0.73-1.05 (min-max)	500-750	0.042-0.0438
Micromachined WR-1.5 [78]	1.5	500-750	0.072
Micromachined (band pass filter) [79]	4	325-440	0.28
Silicon-on-glass (SOG) [87]	0.53	140-170	0.1
Suspended SOG [89]	0.54	440-550	0.0346
Line defect PhC [90]	4	540-630	0.208
Suspended Line defect PhC [91]	0.1	326-331	0.009

Table I.5.1 A comparative table showing the performances of several THz waveguides

In this thesis work, we present the design, fabrication, and characterization of a fully suspended HR-Si waveguide with low propagation losses. The demonstrated THz low loss HR-Si platform is then used to create high Q photonic crystal cavities and finally develop an integrated THz gas sensor.

I.5.2. Photonic crystal

Photonic crystals are periodic structures, designed in a way to control the propagation of electromagnetic waves similar to a solid-state crystal that naturally control the electronic waves propagation. In 1987 Eli Yablonovitch was the first to make the approach between solid crystal

and 3D periodic refractive index structure and defined the photonic band gap inside a photonic crystal [93]. Since that day "photonic crystal" has become the attributed name for 1D,2D, and 3D periodic structures. However, 100 years before in 1887, the idea of a band gap in a 1D periodic structure was derived by Lord Rayleigh [94]. The photonic "band gap" originates from the periodic variation, on the wavelength scale, of the refractive index in a structure. The electromagnetic waves propagating through these structures scatter at the interfaces of the periodic materials. A region of forbidden frequency, called the band gap, is therefore the result of constructive and destructive interference between these waves. The complete photonic band gap has been demonstrated experimentally in 3D PC structures for mmW [95]. The term "complete" refers to the ability to control the propagation of light in the three spatial dimensions. At higher frequencies in the THz, IR, and visible domain the fabrication of such structure becomes more complicated due to the necessity for micro- and nanometric resolution 3D fabrication techniques. Meanwhile, 2D and 1D PCs geometries have been extensively studied and used in several applications. 2D structures called also slab photonic crystals can be created by etching air holes inside a dielectric membrane, or by the growth of periodically separated dielectric rods (see figure I.5.3).

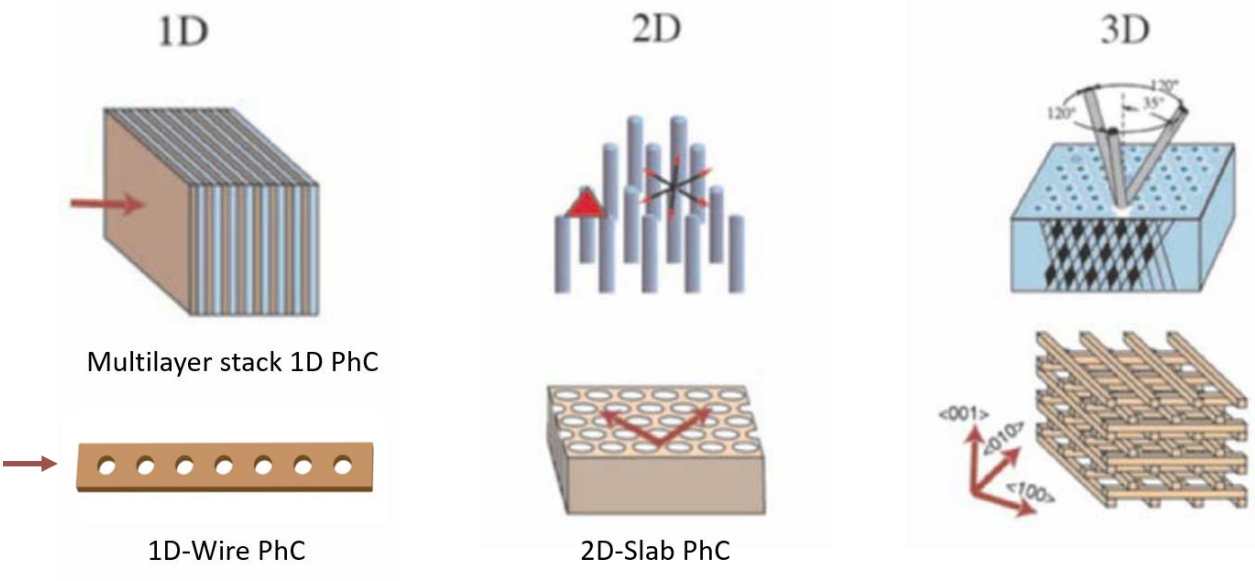

Figure I.5.3 1D,2D, and 3D photonic crystal structures [96]

While the simplest case of 1D PhC consists of a multilayer stack deposition and has been used to form Bragg reflectors. Another type of 1D PhC is formed by creating a periodic etched hole inside the core of a ridge waveguide. Figure I.5.3 shows the different geometries of 1D, 2D, and 3D PhCs

(this figure was taken from [96] and modified). The interest in using photonic crystals to control electromagnetic waves is not limited to the perfect periodic structure. Creating defects inside such structures has shown several interests to form cavities with high Q factors where the light is trapped, or to form guiding channels such as the one presented earlier in the dielectric waveguide section (Figure I.5.2 (c) and (d)). In this work are interested in designing high Q cavities to confine the THz light and increase the interaction with the gas molecules. Therefore in the next part, we discuss the different designs of PhC cavities proposed in the THz region.

I.5.2.1 Photonic crystal THz cavities

One of the greatest advantages of a PhC is its ability to behave like an optical cavity and traps photon at a precise energy for very long times. A PhC cavity is the result of a point defect introduced into the geometry of a perfect periodic PhC. The defect can be created in several ways as removing a hole from the periodic structure, shifting the position of the holes, changing the filling material of the holes… By breaking the periodicity of the structure, a resonant cavity mode appears inside the photonic bandgap. Such characteristics make the PhC useful for many applications: lasing, light-matter strong coupling, sensing … In this work we are interested in designing a PhC cavity on top of a HR-Si waveguide to confine the THz energy at the absorption peak of a gas molecule for very long time. This allows to increase the light-molecule effective length interaction and thus increase the sensitivity of the designed gas sensor. The trapped photon lifetime τ_p is described by the cavity quality factor expressed by:

$$Q = \omega_0 \tau_p \tag{I.5.3}$$

with $\omega_0 = 2\pi f_0$ the angular frequency of the resonant trapped mode. For a long photon lifetime, it is then necessary to design cavities with a high Q factor. 2D slab (etched membrane) and 1D wire (etched waveguide) photonic crystal cavities are highly studied in the visible, near, and mid-infrared [97]–[109]. Because of the fabrication simplicity at the millimetric wavelength scale, 2D and 3D PhC cavities were reported in the 10-110 GHz frequency range [110]–[114]. At THz frequencies, high Q PhC cavities are less explored and this is due to the limited availability of low loss material in this frequency range. 2D metal-coated dielectric slab photonic crystal cavities were reported in [115], [116]. These structures suffer from high metal ohmic losses and present low quality factors less than 140. Thanks to the low loss of high resistivity silicon several 2D slab PhC

cavities with highest quality factors up to Q≈10800 were presented in [117]–[120]. Aside from [121], 1D wire photonic crystal cavities were very little investigated in the THz region. In [121] a Q of 11900 was measured for a resonant defect mode at a frequency of 100 GHz. A review of some available THz photonic crystal cavities and their performances is presented in table I.5.2.

In this work, we present a 1D-wire PhC cavity with ultra-high Q factors for a resonant defect mode trapped in an air hole of the PhC. The frequency of the confined mode is adjusted to overlap with an absorption peak of a gas molecule. Therefore, the interaction between the gas molecules and the THz light is enhanced to finally increase the sensitivity of the proposed gas sensor.

PhC cavity design	Q	Frequency (GHz)
Au coated Si 2D PhC [116]	20	914
Au coated Su-8 2D PhC [115]	133	1460
HR-Si 2D PhC [120]	1000	1000
HR-Si 2D PhC [117]	5800	100
HR-Si 2D PhC [119]	9000	100
HR-Si 2D PhC [118]	10800	318
HR-Si 1D wire PhC [121]	11900	100

Table I.5.2 A comparative table showing the different quality factors obtained for some of the available THz PhC cavities

I.6. CONCLUSION OF THIS CHAPTER

In this chapter, we have introduced the THz waves and their unique properties that make them very useful for several applications. Food quality control is one of these many applications where the THz can contribute to resolving a societal problem by reducing food and money waste. For that purpose, we proposed a THz gas sensor based on the photoacoustic spectroscopy technique to monitor food spoilage. A comparison between two principals spectroscopic techniques: absorption and photoacoustic spectroscopy was illustrated. A detailed theoretical analysis of the PA theory was also developed. A review of the available PA gas sensors and their performances at the THz frequencies was reported. To improve the sensitivity of the PA detection, we proposed a sensor's design with triple resonators for the enhancement of the signal. This design is fabricated on a low-loss THz HR-Si waveguide where a high Q THz PhC cavity has been created. Therefore, in the

second part of this chapter, we presented the state of the art of available THz waveguides. Finally, we briefly introduced the PhC crystals and discussed the existing THz PhC cavities.

I.7. REFERENCES

[1] "About Terahertz Waves - Advantest." https://www.advantest.com/products/terahertz-spectroscopic-imaging-systems/about-terahertz-waves.

[2] E. F. Nichols, "A Study of the Transmission Spectra of Certain Substances in the Infra-Red," *Phys. Rev. Ser. I*, vol. 1, no. 1, pp. 1–18, Jul. 1893, doi: 10.1103/PhysRevSeriesI.1.1.

[3] J. R. Ashley and F. M. Palka, "Transmission Cavity and Injection Stabilization of an X-Band Transferred Electron Oscillator," in *1973 IEEE G-MTT International Microwave Symposium*, Jun. 1973, pp. 181–182, doi: 10.1109/GMTT.1973.1123140.

[4] J. W. Fleming, "High-Resolution Submillimeter-Wave Fourier-Transform Spectrometry of Gases," *IEEE Trans. Microw. Theory Tech.*, vol. 22, no. 12, pp. 1023–1025, Dec. 1974, doi: 10.1109/TMTT.1974.1128419.

[5] A. J. Kerecman, "The Tungsten - P Type Silicon Point Contact Diode," in *1973 IEEE G-MTT International Microwave Symposium*, Boulder, CO, USA, 1973, pp. 30–34, doi: 10.1109/GMTT.1973.1123080.

[6] D. H. Auston and M. C. Nuss, "Electrooptical generation and detection of femtosecond electrical transients," *IEEE J. Quantum Electron.*, vol. 24, no. 2, pp. 184–197, Feb. 1988, doi: 10.1109/3.114.

[7] E. Pickwell-MacPherson and V. P. Wallace, "Terahertz pulsed imaging—A potential medical imaging modality?," *Photodiagnosis Photodyn. Ther.*, vol. 6, no. 2, pp. 128–134, Jun. 2009, doi: 10.1016/j.pdpdt.2009.07.002.

[8] S. J. Oh, Y.-M. Huh, J.-S. Suh, J. Choi, S. Haam, and J.-H. Son, "Cancer Diagnosis by Terahertz Molecular Imaging Technique," *J. Infrared Millim. Terahertz Waves*, vol. 33, no. 1, pp. 74–81, Jan. 2012, doi: 10.1007/s10762-011-9847-9.

[9] T. Hasebe, S. Kawabe, H. Matsui, and H. Tabata, "Metallic mesh-based terahertz biosensing of single- and double-stranded DNA," *J. Appl. Phys.*, vol. 112, no. 9, p. 094702, Nov. 2012, doi: 10.1063/1.4761966.

[10] X. Yang *et al.*, "Biomedical Applications of Terahertz Spectroscopy and Imaging," *Trends Biotechnol.*, vol. 34, no. 10, pp. 810–824, Oct. 2016, doi: 10.1016/j.tibtech.2016.04.008.

[11] L. Ho, M. Pepper, and P. Taday, "Signatures and fingerprints," *Nat. Photonics*, vol. 2, no. 9, Art. no. 9, Sep. 2008, doi: 10.1038/nphoton.2008.174.

[12] S. L. Dexheimer, *Terahertz Spectroscopy: Principles and Applications*. CRC Press, 2017.

[13] M. C. Kemp, "Explosives Detection by Terahertz Spectroscopy—A Bridge Too Far?," *IEEE Trans. Terahertz Sci. Technol.*, vol. 1, no. 1, pp. 282–292, Sep. 2011, doi: 10.1109/TTHZ.2011.2159647.

[14] J. B. Baxter and G. W. Guglietta, "Terahertz Spectroscopy," *Anal. Chem.*, vol. 83, no. 12, pp. 4342–4368, Jun. 2011, doi: 10.1021/ac200907z.

[15] M. Theuer, S. S. Harsha, D. Molter, G. Torosyan, and R. Beigang, "Terahertz Time-Domain Spectroscopy of Gases, Liquids, and Solids," *ChemPhysChem*, vol. 12, no. 15, pp. 2695–2705, Oct. 2011, doi: 10.1002/cphc.201100158.

[16] F. Hindle *et al.*, "Monitoring of food spoilage by high resolution THz analysis," *Analyst*, vol. 143, no. 22, pp. 5536–5544, Nov. 2018, doi: 10.1039/C8AN01180J.

[17] A. Redo-Sanchez *et al.*, "Assessment of terahertz spectroscopy to detect antibiotic residues in food and feed matrices," *Analyst*, vol. 136, no. 8, pp. 1733–1738, Mar. 2011, doi: 10.1039/C0AN01016B.

[18] G. Ok, H. J. Kim, H. S. Chun, and S.-W. Choi, "Foreign-body detection in dry food using continuous sub-terahertz wave imaging," *Food Control*, vol. 42, pp. 284–289, Aug. 2014, doi: 10.1016/j.foodcont.2014.02.021.

[19] G. Ok, K. Park, H. J. Kim, H. S. Chun, and S.-W. Choi, "High-speed terahertz imaging toward food quality inspection," *Appl. Opt.*, vol. 53, no. 7, pp. 1406–1412, Mar. 2014, doi: 10.1364/AO.53.001406.

[20] T. Nagatsuma, G. Ducournau, and C. C. Renaud, "Advances in terahertz communications accelerated by photonics," *Nat. Photonics*, vol. 10, no. 6, Art. no. 6, Jun. 2016, doi: 10.1038/nphoton.2016.65.

[21] G. Ducournau *et al.*, "THz Communications using Photonics and Electronic Devices: the Race to Data-Rate," *J. Infrared Millim. Terahertz Waves*, vol. 36, no. 2, pp. 198–220, Feb. 2015, doi: 10.1007/s10762-014-0112-x.

[22] C. K. Walker, *Terahertz Astronomy*. CRC Press, 2015.

[23] A. V. Smirnov *et al.*, “Space mission Millimetron for terahertz astronomy,” in *Space Telescopes and Instrumentation 2012: Optical, Infrared, and Millimeter Wave*, Sep. 2012, vol. 8442, p. 84424C, doi: 10.1117/12.927184.
[24] C. Kulesa, “Terahertz Spectroscopy for Astronomy: From Comets to Cosmology,” *IEEE Trans. Terahertz Sci. Technol.*, vol. 1, no. 1, pp. 232–240, Sep. 2011, doi: 10.1109/TTHZ.2011.2159648.
[25] J. Gustavsson, C. Cederberg, and U. Sonesson, *Global food losses and food waste: extent, causes and prevention ; study conducted for the International Congress Save Food! at Interpack 2011, [16 - 17 May], Düsseldorf, Germany*. Rome: Food and Agriculture Organization of the United Nations, 2011.
[26] L. Kuuliala *et al.*, “Microbiological, chemical and sensory spoilage analysis of raw Atlantic cod (Gadus morhua) stored under modified atmospheres,” *Food Microbiol.*, vol. 70, pp. 232–244, Apr. 2018, doi: 10.1016/j.fm.2017.10.011.
[27] L. Kuuliala *et al.*, “Spoilage evaluation of raw Atlantic salmon (Salmo salar) stored under modified atmospheres by multivariate statistics and augmented ordinal regression,” *Int. J. Food Microbiol.*, vol. 303, pp. 46–57, Aug. 2019, doi: 10.1016/j.ijfoodmicro.2019.04.011.
[28] B. Noseda *et al.*, “Microbiological spoilage of vacuum and modified atmosphere packaged Vietnamese Pangasius hypophthalmus fillets,” *Food Microbiol.*, vol. 30, no. 2, pp. 408–419, Jun. 2012, doi: 10.1016/j.fm.2011.12.025.
[29] S. Medina, J. A. Pereira, P. Silva, R. Perestrelo, and J. S. Câmara, “Food fingerprints – A valuable tool to monitor food authenticity and safety,” *Food Chem.*, vol. 278, pp. 144–162, Apr. 2019, doi: 10.1016/j.foodchem.2018.11.046.
[30] B. Noseda *et al.*, “Effect of O2CO2 enriched atmospheres on microbiological growth and volatile metabolite production in packaged cooked peeled gray shrimp (Crangon crangon),” *Int. J. Food Microbiol.*, vol. 160, no. 1, pp. 65–75, Nov. 2012, doi: 10.1016/j.ijfoodmicro.2012.09.018.
[31] W.-Y. Chung, G. T. Le, T. V. Tran, and N. H. Nguyen, “Novel proximal fish freshness monitoring using batteryless smart sensor tag,” *Sens. Actuators B Chem.*, vol. 248, pp. 910–916, Sep. 2017, doi: 10.1016/j.snb.2017.01.134.
[32] L. H. Almy, “A METHOD FOR THE ESTIMATION OF HYDROGEN SULFIDE IN PROTEINACEOUS FOOD PRODUCTS [1],” *J. Am. Chem. Soc.*, vol. 47, no. 5, pp. 1381–1390, May 1925, doi: 10.1021/ja01682a024.
[33] M. O. Hanna, J. W. Savell, G. C. Smith, D. E. Purser, F. A. Gardner, and C. Vanderzant, “Effect of Growth of Individual Meat Bacteria on pH, Color and Odor of Aseptically Prepared Vacuum-Packaged Round Steaks,” *J. Food Prot.*, vol. 46, no. 3, pp. 216–221, Mar. 1983, doi: 10.4315/0362-028X-46.3.216.
[34] B. J. Shay and A. F. Egan, “Hydrogen sulphide production and spoilage of vacuum-packaged beef by a Lactobacillus,” *Psychrotrophic Microorg. Spoilage Pathog. Ed. TA Roberts Al*, 1981, Accessed: Mar. 23, 2021. [Online]. Available: https://agris.fao.org/agris-search/search.do?recordID=US201302612979.
[35] T. Kristoffersen and F. E. Nelson, “The Relationship of Serine Deamination and Hydrogen Sulfide Production by Lactobacillus casei to Cheddar Cheese Flavor,” *J. Dairy Sci.*, vol. 38, no. 12, pp. 1319–1325, Dec. 1955, doi: 10.3168/jds.S0022-0302(55)95114-6.
[36] F. Hindle *et al.*, “Monitoring of food spoilage by high resolution THz analysis,” *Analyst*, vol. 143, no. 22, pp. 5536–5544, Nov. 2018, doi: 10.1039/C8AN01180J.
[37] I. E. Gordon *et al.*, “The HITRAN2016 molecular spectroscopic database,” *J. Quant. Spectrosc. Radiat. Transf.*, vol. 203, pp. 3–69, Dec. 2017, doi: 10.1016/j.jqsrt.2017.06.038.
[38] T. Yasui *et al.*, “Enhancement of spectral resolution and accuracy in asynchronous-optical-sampling terahertz time-domain spectroscopy for low-pressure gas-phase analysis,” *Opt. Express*, vol. 20, no. 14, pp. 15071–15078, Jul. 2012, doi: 10.1364/OE.20.015071.
[39] D. M. Mittleman, R. H. Jacobsen, R. Neelamani, R. G. Baraniuk, and M. C. Nuss, “Gas Sensing using Terahertz Time-Domain Spectroscopy,” *Appl. Phys. B*, vol. 67, no. 3, pp. 379–390, Jan. 1998, doi: http://dx.doi.org/10.1007/s003400050520.
[40] R. M. Smith and M. A. Arnold, “Selectivity of Terahertz Gas-Phase Spectroscopy,” *Anal. Chem.*, vol. 87, no. 21, pp. 10679–10683, Nov. 2015, doi: 10.1021/acs.analchem.5b03028.
[41] H. Harde, N. Katzenellenbogen, and D. Grischkowsky, “Terahertz coherent transients from methyl chloride vapor,” *JOSA B*, vol. 11, no. 6, pp. 1018–1030, Jun. 1994, doi: 10.1364/JOSAB.11.001018.
[42] H. Harde and D. Grischkowsky, “Coherent transients excited by subpicosecond pulses of terahertz radiation,” *JOSA B*, vol. 8, no. 8, pp. 1642–1651, Aug. 1991, doi: 10.1364/JOSAB.8.001642.
[43] L. Consolino, S. Bartalini, H. E. Beere, D. A. Ritchie, M. S. Vitiello, and P. De Natale, “THz QCL-Based Cryogen-Free Spectrometer for in Situ Trace Gas Sensing,” *Sensors*, vol. 13, no. 3, pp. 3331–3340, Mar. 2013, doi: 10.3390/s130303331.

[44] T. Hagelschuer *et al.*, “Terahertz gas spectroscopy through self-mixing in a quantum-cascade laser,” *Appl. Phys. Lett.*, vol. 109, no. 19, p. 191101, Nov. 2016, doi: 10.1063/1.4967435.
[45] H.-W. Hübers *et al.*, “High-resolution gas phase spectroscopy with a distributed feedback terahertz quantum cascade laser,” *Appl. Phys. Lett.*, vol. 89, no. 6, p. 061115, Aug. 2006, doi: 10.1063/1.2335803.
[46] H.-W. Hübers, R. Eichholz, S. G. Pavlov, and H. Richter, “High Resolution Terahertz Spectroscopy with Quantum Cascade Lasers,” *J. Infrared Millim. Terahertz Waves*, vol. 34, no. 5, pp. 325–341, Jun. 2013, doi: 10.1007/s10762-013-9973-7.
[47] F. Hindle, A. Cuisset, R. Bocquet, and G. Mouret, “Continuous-wave terahertz by photomixing: applications to gas phase pollutant detection and quantification,” *Comptes Rendus Phys.*, vol. 9, no. 2, pp. 262–275, Mar. 2008, doi: 10.1016/j.crhy.2007.07.009.
[48] D. Bigourd *et al.*, “Detection and quantification of multiple molecular species in mainstream cigarette smoke by continuous-wave terahertz spectroscopy,” *Opt. Lett.*, vol. 31, no. 15, pp. 2356–2358, Aug. 2006, doi: 10.1364/OL.31.002356.
[49] G. Mouret *et al.*, “Anomalous dispersion measurement in terahertz frequency region by photomixing,” *Appl. Phys. Lett.*, vol. 88, no. 18, p. 181105, May 2006, doi: 10.1063/1.2200393.
[50] F. Hindle *et al.*, “Widely tunable THz synthesizer,” *Appl. Phys. B*, vol. 104, no. 4, p. 763, Aug. 2011, doi: 10.1007/s00340-011-4690-1.
[51] F. Hindle *et al.*, “Monitoring of food spoilage by high resolution THz analysis,” *Analyst*, vol. 143, no. 22, pp. 5536–5544, Nov. 2018, doi: 10.1039/C8AN01180J.
[52] J. C. Pearson *et al.*, “Demonstration of a room temperature 2.48–2.75 THz coherent spectroscopy source,” *Rev. Sci. Instrum.*, vol. 82, no. 9, p. 093105, Sep. 2011, doi: 10.1063/1.3617420.
[53] S. Yokoyama, R. Nakamura, M. Nose, T. Araki, and T. Yasui, “Terahertz spectrum analyzer based on a terahertz frequency comb,” *Opt. Express*, vol. 16, no. 17, pp. 13052–13061, Aug. 2008, doi: 10.1364/OE.16.013052.
[54] M. M. Assefzadeh *et al.*, “Terahertz trace gas spectroscopy based on a fully-electronic frequency-comb radiating array in silicon,” in *2016 Conference on Lasers and Electro-Optics (CLEO)*, Jun. 2016, pp. 1–2.
[55] Y.-D. Hsieh *et al.*, “Terahertz Comb Spectroscopy Traceable to Microwave Frequency Standard,” *IEEE Trans. Terahertz Sci. Technol.*, vol. 3, no. 3, pp. 322–330, May 2013, doi: 10.1109/TTHZ.2013.2250333.
[56] T. Yasui *et al.*, “Real-time monitoring of continuous-wave terahertz radiation using a fiber-based, terahertz-comb-referenced spectrum analyzer,” *Opt. Express*, vol. 17, no. 19, pp. 17034–17043, Sep. 2009, doi: 10.1364/OE.17.017034.
[57] E. Lüscher, “Photoacoustic Effect in Condensed Matter — Historical Development,” in *Photoacoustic Effect Principles and Applications: Proceedings of the First International Conference on the Photoacoustic Effect in Germany*, E. Lüscher, P. Korpiun, H.-J. Coufal, and R. Tilgner, Eds. Wiesbaden: Vieweg+Teubner Verlag, 1984, pp. 1–20.
[58] T. H. Maiman, “Stimulated Optical Radiation in Ruby,” *Nature*, vol. 187, no. 4736, pp. 493–494, Aug. 1960, doi: 10.1038/187493a0.
[59] E. L. Kerr and J. G. Atwood, “The Laser Illuminated Absorptivity Spectrophone: A Method for Measurement of Weak Absorptivity in Gases at Laser Wavelengths,” *Appl. Opt.*, vol. 7, no. 5, pp. 915–921, May 1968, doi: 10.1364/AO.7.000915.
[60] L. Consolino, S. Bartalini, and P. De Natale, “Terahertz Frequency Metrology for Spectroscopic Applications: a Review,” *J. Infrared Millim. Terahertz Waves*, vol. 38, no. 11, pp. 1289–1315, Nov. 2017, doi: 10.1007/s10762-017-0406-x.
[61] P. M. Morse and K. U. Ingard, *Theoretical Acoustics*. Princeton University Press, 1986.
[62] H. Moser and B. Lendl, “Cantilever-enhanced photoacoustic detection of hydrogen sulfide (H2S) using NIR telecom laser sources near 1.6 μm,” *Appl. Phys. B*, vol. 122, no. 4, Apr. 2016, doi: 10.1007/s00340-016-6355-6.
[63] J. Kauppinen, K. Wilcken, I. Kauppinen, and V. Koskinen, “High sensitivity in gas analysis with photoacoustic detection,” *Microchem. J.*, vol. 76, no. 1–2, pp. 151–159, Feb. 2004, doi: 10.1016/j.microc.2003.11.007.
[64] V. Koskinen, J. Fonsen, K. Roth, and J. Kauppinen, “Progress in cantilever enhanced photoacoustic spectroscopy,” *Vib. Spectrosc.*, vol. 48, no. 1, pp. 16–21, Sep. 2008, doi: 10.1016/j.vibspec.2008.01.013.
[65] C. B. Hirschmann, J. Lehtinen, J. Uotila, S. Ojala, and R. L. Keiski, “Sub-ppb detection of formaldehyde with cantilever enhanced photoacoustic spectroscopy using quantum cascade laser source,” *Appl. Phys. B*, vol. 111, no. 4, pp. 603–610, Jun. 2013, doi: 10.1007/s00340-013-5379-4.
[66] K. Chen, Q. Yu, Z. Gong, M. Guo, and C. Qu, “Ultra-high sensitive fiber-optic Fabry-Perot cantilever enhanced resonant photoacoustic spectroscopy,” *Sens. Actuators B Chem.*, vol. 268, pp. 205–209, Sep. 2018, doi: 10.1016/j.snb.2018.04.123.

[67] N. E. Glauvitz, R. A. Coutu, I. R. Medvedev, and D. T. Petkie, “Terahertz Photoacoustic Spectroscopy Using an MEMS Cantilever Sensor,” *J. Microelectromechanical Syst.*, vol. 24, no. 1, pp. 216–223, Feb. 2015, doi: 10.1109/JMEMS.2014.2327916.
[68] R. A. Coutu, I. R. Medvedev, and D. T. Petkie, “Improved Sensitivity MEMS Cantilever Sensor for Terahertz Photoacoustic Spectroscopy,” *Sensors*, vol. 16, no. 2, Art. no. 2, Feb. 2016, doi: 10.3390/s16020251.
[69] A. A. Kosterev, Yu. A. Bakhirkin, R. F. Curl, and F. K. Tittel, “Quartz-enhanced photoacoustic spectroscopy,” *Opt. Lett.*, vol. 27, no. 21, p. 1902, Nov. 2002, doi: 10.1364/OL.27.001902.
[70] S. Borri *et al.*, “Terahertz quartz enhanced photo-acoustic sensor,” *Appl. Phys. Lett.*, vol. 103, no. 2, p. 021105, Jul. 2013, doi: 10.1063/1.4812438.
[71] P. Patimisco *et al.*, “A quartz enhanced photo-acoustic gas sensor based on a custom tuning fork and a terahertz quantum cascade laser,” *Analyst*, vol. 139, no. 9, pp. 2079–2087, Apr. 2014, doi: 10.1039/C3AN01219K.
[72] V. Spagnolo *et al.*, “THz Quartz-enhanced photoacoustic sensor for H_2S trace gas detection,” *Opt. Express*, vol. 23, no. 6, pp. 7574–7582, Mar. 2015, doi: 10.1364/OE.23.007574.
[73] A. Sampaolo *et al.*, “H2S quartz-enhanced photoacoustic spectroscopy sensor employing a liquid-nitrogen-cooled THz quantum cascade laser operating in pulsed mode,” *Photoacoustics*, vol. 21, p. 100219, Mar. 2021, doi: 10.1016/j.pacs.2020.100219.
[74] S. Borri *et al.*, “Intracavity quartz-enhanced photoacoustic sensor,” *Appl. Phys. Lett.*, vol. 104, no. 9, p. 091114, Mar. 2014, doi: 10.1063/1.4867268.
[75] P. Patimisco *et al.*, “High finesse optical cavity coupled with a quartz-enhanced photoacoustic spectroscopic sensor,” *Analyst*, vol. 140, no. 3, pp. 736–743, 2015, doi: 10.1039/C4AN01158A.
[76] T. Tomberg, T. Hieta, M. Vainio, and L. Halonen, “Cavity-enhanced cantilever-enhanced photo-acoustic spectroscopy,” *Analyst*, vol. 144, no. 7, pp. 2291–2296, 2019, doi: 10.1039/C9AN00058E.
[77] “Virginia Diodes, Inc - Your Source for Terahertz and mm-Wave Products.” https://www.vadiodes.com/en/.
[78] K. M. K. H. Leong *et al.*, “WR1.5 Silicon Micromachined Waveguide Components and Active Circuit Integration Methodology,” *IEEE Trans. Microw. Theory Tech.*, vol. 60, no. 4, pp. 998–1005, Apr. 2012, doi: 10.1109/TMTT.2012.2184296.
[79] J. Hu, S. Xie, and Y. Zhang, “Micromachined Terahertz Rectangular Waveguide Bandpass Filter on Silicon-Substrate,” *IEEE Microw. Wirel. Compon. Lett.*, vol. 22, no. 12, pp. 636–638, Dec. 2012, doi: 10.1109/LMWC.2012.2228179.
[80] J. C. Wiltse, “Some Characteristics of Dielectric Image Lines at Millimeter Wavelengths,” *IRE Trans. Microw. Theory Tech.*, vol. 7, no. 1, pp. 65–69, Jan. 1959, doi: 10.1109/TMTT.1959.1124625.
[81] K. Solbach and I. Wolff, “The Electromagnetic Fields and the Phase Constants of Dielectric Image Lines,” *IEEE Trans. Microw. Theory Tech.*, vol. 26, no. 4, pp. 266–274, Apr. 1978, doi: 10.1109/TMTT.1978.1129363.
[82] K. Ogusu, “Numerical Analysis of the Rectangular Dielectric Waveguide and its Modifications,” *IEEE Trans. Microw. Theory Tech.*, vol. 25, no. 11, pp. 874–885, Nov. 1977, doi: 10.1109/TMTT.1977.1129235.
[83] W. V. McLevige, T. Itoh, and R. Mittra, “New Waveguide Structures for Millimeter-Wave and Optical Integrated Circuits,” *IEEE Trans. Microw. Theory Tech.*, vol. 23, no. 10, pp. 788–794, Oct. 1975, doi: 10.1109/TMTT.1975.1128684.
[84] A. G. Engel and L. P. B. Katehi, “Low-loss monolithic transmission lines for submillimeter and terahertz frequency applications,” *IEEE Trans. Microw. Theory Tech.*, vol. 39, no. 11, pp. 1847–1854, Nov. 1991, doi: 10.1109/22.97485.
[85] J. Dai, J. Zhang, W. Zhang, and D. Grischkowsky, “Terahertz time-domain spectroscopy characterization of the far-infrared absorption and index of refraction of high-resistivity, float-zone silicon,” *JOSA B*, vol. 21, no. 7, pp. 1379–1386, Jul. 2004, doi: 10.1364/JOSAB.21.001379.
[86] D. Grischkowsky, S. Keiding, M. van Exter, and C. Fattinger, “Far-infrared time-domain spectroscopy with terahertz beams of dielectrics and semiconductors,” *JOSA B*, vol. 7, no. 10, pp. 2006–2015, Oct. 1990, doi: 10.1364/JOSAB.7.002006.
[87] N. Ranjkesh, M. Basha, A. Taeb, A. Zandieh, S. Gigoyan, and S. Safavi-Naeini, “Silicon-on-Glass Dielectric Waveguide—Part I: For Millimeter-Wave Integrated Circuits,” *IEEE Trans. Terahertz Sci. Technol.*, vol. 5, no. 2, pp. 268–279, Mar. 2015, doi: 10.1109/TTHZ.2015.2399693.
[88] M. Naftaly and R. E. Miles, “Terahertz Beam Interactions with Amorphous Materials,” in *Terahertz Frequency Detection and Identification of Materials and Objects*, Dordrecht, 2007, pp. 107–122.
[89] N. Ranjkesh, M. Basha, A. Taeb, and S. Safavi-Naeini, “Silicon-on-Glass Dielectric Waveguide—Part II: For THz Applications,” *IEEE Trans. Terahertz Sci. Technol.*, vol. 5, no. 2, pp. 280–287, Mar. 2015, doi: 10.1109/TTHZ.2015.2397279.

[90] H. Amarloo and S. Safavi-Naeini, "Terahertz Line Defect Waveguide Based on Silicon-on-Glass Technology," *IEEE Trans. Terahertz Sci. Technol.*, vol. 7, no. 4, pp. 433–439, Jul. 2017, doi: 10.1109/TTHZ.2017.2708505.
[91] K. Tsuruda, M. Fujita, and T. Nagatsuma, "Extremely low-loss terahertz waveguide based on silicon photonic-crystal slab," *Opt. Express*, vol. 23, no. 25, pp. 31977–31990, Dec. 2015, doi: 10.1364/OE.23.031977.
[92] "Straight Waveguides, Tapers, Horn Antennae." https://www.vadiodes.com/en/products/straight-waveguides-tapers-horn-antenna-directional-couplers.
[93] E. Yablonovitch, "Inhibited Spontaneous Emission in Solid-State Physics and Electronics," *Phys. Rev. Lett.*, vol. 58, no. 20, pp. 2059–2062, May 1987, doi: 10.1103/PhysRevLett.58.2059.
[94] Lord Rayleigh, "XVII. *On the maintenance of vibrations by forces of double frequency, and on the propagation of waves through a medium endowed with a periodic structure*," *Lond. Edinb. Dublin Philos. Mag. J. Sci.*, vol. 24, no. 147, pp. 145–159, Aug. 1887, doi: 10.1080/14786448708628074.
[95] E. Yablonovitch, "Photonic band structure: the face-centered-cubiccase," p. 9.
[96] J.-M. Lourtioz, H. Benisty, V. Berger, J.-M. Gerard, D. Maystre, and A. Tchelnokov, *Photonic Crystals: Towards Nanoscale Photonic Devices*, 2nd ed. Berlin Heidelberg: Springer-Verlag, 2008.
[97] P. B. Deotare, M. W. McCutcheon, I. W. Frank, M. Khan, and M. Lončar, "High quality factor photonic crystal nanobeam cavities," *Appl. Phys. Lett.*, vol. 94, no. 12, p. 121106, Mar. 2009, doi: 10.1063/1.3107263.
[98] Y. Akahane, T. Asano, B.-S. Song, and S. Noda, "High- Q photonic nanocavity in a two-dimensional photonic crystal," *Nature*, vol. 425, no. 6961, pp. 944–947, Oct. 2003, doi: 10.1038/nature02063.
[99] W. Xie *et al.*, "High-Q Photonic Crystal Nanocavities on 300 mm SOI Substrate Fabricated With 193 nm Immersion Lithography," *J. Light. Technol.*, vol. 32, no. 8, pp. 1457–1462, Apr. 2014.
[100] D. Yang, X. Chen, X. Zhang, C. Lan, and Y. Zhang, "High-Q, low-index-contrast photonic crystal nanofiber cavity for high sensitivity refractive index sensing," *Appl. Opt.*, vol. 57, no. 24, pp. 6958–6965, Aug. 2018, doi: 10.1364/AO.57.006958.
[101] P. Lalanne, C. Sauvan, and J. P. Hugonin, "Photon confinement in photonic crystal nanocavities," *Laser Photonics Rev.*, vol. 2, no. 6, pp. 514–526, 2008, doi: 10.1002/lpor.200810018.
[102] Q. Quan, P. B. Deotare, and M. Loncar, "Photonic crystal nanobeam cavity strongly coupled to the feeding waveguide," *Appl. Phys. Lett.*, vol. 96, no. 20, p. 203102, May 2010, doi: 10.1063/1.3429125.
[103] D. Yang, C. Wang, and Y. Ji, "Silicon on-chip 1D photonic crystal nanobeam bandstop filters for the parallel multiplexing of ultra-compact integrated sensor array," *Opt. Express*, vol. 24, no. 15, pp. 16267–16279, Jul. 2016, doi: 10.1364/OE.24.016267.
[104] E. Kuramochi, H. Taniyama, T. Tanabe, K. Kawasaki, Y.-G. Roh, and M. Notomi, "Ultrahigh-Q one-dimensional photonic crystal nanocavities with modulated mode-gap barriers on SiO_2 claddings and on air claddings," *Opt. Express*, vol. 18, no. 15, pp. 15859–15869, Jul. 2010, doi: 10.1364/OE.18.015859.
[105] D. Englund *et al.*, "Deterministic Coupling of a Single Nitrogen Vacancy Center to a Photonic Crystal Cavity," *Nano Lett.*, vol. 10, no. 10, pp. 3922–3926, Oct. 2010, doi: 10.1021/nl101662v.
[106] A. Faraon, E. Waks, D. Englund, I. Fushman, and J. Vučković, "Efficient photonic crystal cavity-waveguide couplers," *Appl. Phys. Lett.*, vol. 90, no. 7, p. 073102, Feb. 2007, doi: 10.1063/1.2472534.
[107] Y. Akahane, T. Asano, B.-S. Song, and S. Noda, "High-Q photonic nanocavity in a two-dimensional photonic crystal," *Nature*, vol. 425, no. 6961, pp. 944–947, Oct. 2003, doi: 10.1038/nature02063.
[108] G. Manzacca, D. Paciotti, A. Marchese, M. S. Moreolo, and G. Cincotti, "2D photonic crystal cavity-based WDM multiplexer," *Photonics Nanostructures - Fundam. Appl.*, vol. 5, no. 4, pp. 164–170, Nov. 2007, doi: 10.1016/j.photonics.2007.03.003.
[109] Z. Zhang and M. Qiu, "Compact in-plane channel drop filter design using a single cavity with two degenerate modes in 2D photonic crystal slabs," *Opt. Express*, vol. 13, no. 7, p. 2596, Apr. 2005, doi: 10.1364/OPEX.13.002596.
[110] F. Gadot, A. de Lustrac, J.-M. Lourtioz, T. Brillat, A. Ammouche, and E. Akmansoy, "High-transmission defect modes in two-dimensional metallic photonic crystals," *J. Appl. Phys.*, vol. 85, no. 12, pp. 8499–8501, Jun. 1999, doi: 10.1063/1.370634.
[111] M. Bayindir, E. Cubukcu, I. Bulu, T. Tut, E. Ozbay, and C. M. Soukoulis, "Photonic band gaps, defect characteristics, and waveguiding in two-dimensional disordered dielectric and metallic photonic crystals," *Phys. Rev. B*, vol. 64, no. 19, p. 195113, Oct. 2001, doi: 10.1103/PhysRevB.64.195113.
[112] A. Serpenguzel, "Transmission characteristics of metallodielectric photonic crystals and resonators," *IEEE Microw. Wirel. Compon. Lett.*, vol. 12, no. 4, pp. 134–136, Apr. 2002, doi: 10.1109/7260.993292.

[113] S. Lin, V. M. Hietala, S. K. Lyo, and A. Zaslavsky, “Photonic band gap quantum well and quantum box structures: A high-Q resonant cavity,” *Appl. Phys. Lett.*, vol. 68, no. 23, pp. 3233–3235, Jun. 1996, doi: 10.1063/1.116558.
[114] E. Özbay, B. Temelkuran, M. Sigalas, G. Tuttle, C. M. Soukoulis, and K. M. Ho, “Defect structures in metallic photonic crystals,” *Appl. Phys. Lett.*, vol. 69, no. 25, pp. 3797–3799, Dec. 1996, doi: 10.1063/1.117002.
[115] Y. Zhao and D. R. Grischkowsky, “2-D Terahertz Metallic Photonic Crystals in Parallel-Plate Waveguides,” *IEEE Trans. Microw. Theory Tech.*, vol. 55, no. 4, pp. 656–663, Apr. 2007, doi: 10.1109/TMTT.2007.892798.
[116] A. L. Bingham and D. Grischkowsky, “Terahertz two-dimensional high-Q photonic crystal waveguide cavities,” *Opt. Lett.*, vol. 33, no. 4, pp. 348–350, Feb. 2008, doi: 10.1364/OL.33.000348.
[117] S. M. Hanham, C. Watts, W. J. Otter, S. Lucyszyn, and N. Klein, “Dielectric measurements of nanoliter liquids with a photonic crystal resonator at terahertz frequencies,” *Appl. Phys. Lett.*, vol. 107, no. 3, p. 032903, Jul. 2015, doi: 10.1063/1.4927242.
[118] K. Okamoto, K. Tsuruda, S. Diebold, S. Hisatake, M. Fujita, and T. Nagatsuma, “Terahertz Sensor Using Photonic Crystal Cavity and Resonant Tunneling Diodes,” *J. Infrared Millim. Terahertz Waves*, vol. 38, no. 9, pp. 1085–1097, Sep. 2017, doi: 10.1007/s10762-017-0391-0.
[119] W. J. Otter, S. M. Hanham, N. M. Ridler, G. Marino, N. Klein, and S. Lucyszyn, “100GHz ultra-high Q-factor photonic crystal resonators,” *Sens. Actuators Phys.*, vol. 217, pp. 151–159, Sep. 2014, doi: 10.1016/j.sna.2014.06.022.
[120] C. M. Yee and M. S. Sherwin, “High-Q terahertz microcavities in silicon photonic crystal slabs,” *Appl. Phys. Lett.*, vol. 94, no. 15, p. 154104, Apr. 2009, doi: 10.1063/1.3118579.
[121] S. M. Hanham, M. M. Ahmad, S. Lucyszyn, and N. Klein, “LED-Switchable High-Q Packaged THz Microbeam Resonators,” *IEEE Trans. Terahertz Sci. Technol.*, vol. 7, no. 2, pp. 199–208, Mar. 2017, doi: 10.1109/TTHZ.2016.2634547.

Chapter II:

Design of low loss suspended Silicon waveguide and high Q photonic crystal cavity for use as a photoacoustic THz gas sensor

CONTENTS

II.1. TRIPLE RESONATOR PHOTOACOUSTIC GAS SENSOR

In sensing applications, and especially in food quality control the detection of volatile organic compounds (VOC's) and gas molecules at very low concentrations is very important for safety reasons. We presented in chapter I some of the VOC's that can be considered as food spoilage indicators. Tens ppm of H_2S gas molecule is observed inside several packages of spoiled food. The sub-ppm detection of H_2S concentrations is, therefore, necessary to ensure the consumption safety of a packaged food. For that purpose, we propose in this work the design of a photoacoustic gas sensor intended for the detection of H_2S inside food packaging. The design concept is represented in figure II.1.1. It is based on the implementation of three resonators in order to achieve a triple enhancement of the signal and thus to increase its sensitivity for the detection of very low concentrations in the sub-ppm range. The proposed sensor design is composed of three main parts:

1. **THz HR-Si suspended waveguide and PhC cavity**
2. **Cylindrical acoustical resonator**
3. **Poly-Si thin membrane mechanical resonator.**

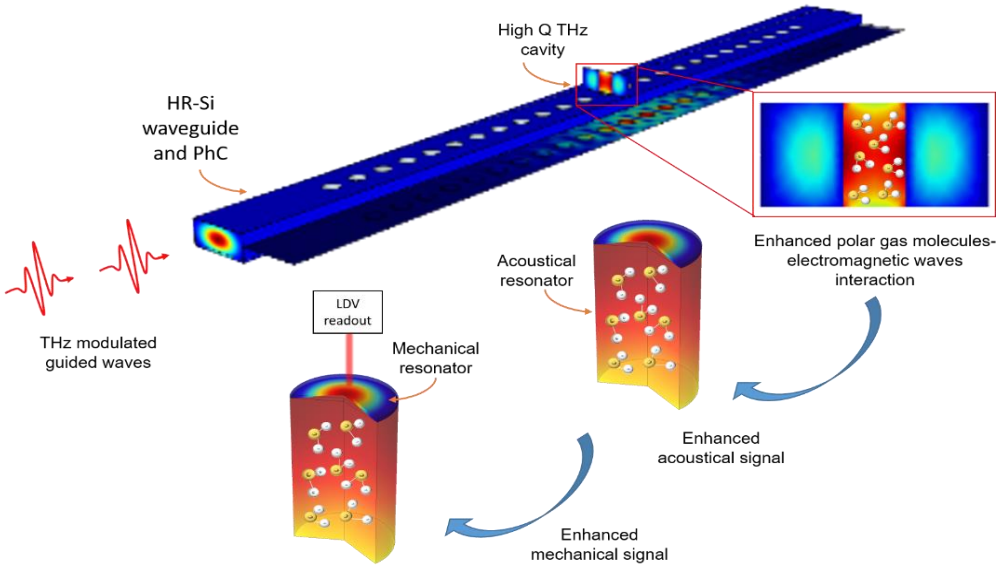

Figure II.1.1 Sensor design based on triple resonators

In this chapter, we present the numerical and theoretical calculation of the THz electromagnetic part of this sensor (waveguide and photonic crystal cavities). But first, we will briefly describe its

three different parts, and resolve analytically the acousto-mechanical system. More details and numerical calculations on the acousto-mechanics can be found in our collaborators' work [1].

1- **THz waveguide and resonator**: THz waves used for the excitation of molecules are guided inside a low loss HR-Si waveguide, where they are trapped in a high Q-factor cavity formed by a defect air hole of a photonic crystal. The resonant profile of the THz cavity is adjusted to overlap the absorption frequency of the targeted gas molecules (H_2S) present in the air hole. The THz light-molecules interaction length inside the cavity is increased by a factor proportional to the quality factor Q. For the photoacoustic phenomenon to occur, the THz light is modulated resulting in the generation of heat by the molecular non-radiative relaxation. The released heat energy propagates in the form of acoustic pressure waves. From equation I.4.30, the amplitude of the pressure wave is proportional to the light-molecules interaction length. Therefore, inside the THz cavity, the amplitude of the acoustic signal increases proportionally to the cavity quality factor Q. In this chapter, we will discuss the design and adjustments of several THz waveguides and cavities.

2- Cylindrical acoustic resonator: The THz cavity is formed by creating a defect inside a 1D photonic crystal. This PhC is built on a suspended HR-Si waveguide by introducing cylindrical etched holes inside its core. This cylindrical shape of the THz cavity is also used here as an acoustical cylindrical cavity. On the bottom of the cylinder, a Poly-Silicon membrane is deposited that will serve as a mechanical resonator to detect a pressure wave. The behavior of this membrane will be discussed next.

The cylinder is considered as a one open-end acoustical resonator. One end is open to the air where the gas freely moves and the other end is closed by the membrane. From equation I.4.34 for an open-end cylinder, the acoustic resonant frequency is expressed by $f_{lmn} = \frac{c_s}{2}\sqrt{\left(\frac{l}{2L}\right)^2 + \left(\frac{\alpha_{mn}}{\pi R_0}\right)^2}$.

The fundamental longitudinal mode is defined by the cylinder height L, where $f_{100} = \frac{c_s}{2}\sqrt{\left(\frac{1}{2L}\right)^2} = \frac{c_s}{4L}$. The waveguide thickness, which defines the cavity height, is chosen to be $T = L = 90\ \mu m$ in order to maintain single mode behavior for the THz cavity and to achieve a reasonable acoustical resonance frequency $f_{100} = 953\ kHz$. The approximations used leading to equation I.4.34 don't take into consideration the air inertia outside the cylinder, where the pressure does not really vanish at the open end. For that an "end correction" [2] has to be considered increasing the cylinder's effective length:

$$L_{eff} = L + 2\delta \tag{II.1.1}$$

with δ a correction factor of the order of the cylinder radius R. Using these corrections the resonance frequency of the acoustical cylinder becomes $f_{100} = 710\ kHz$. Modulating the THz light at the acoustic resonance frequency allows the enhancement of the acoustic wave by a factor Q_{ac} corresponding to the acoustical quality factor. Q_{ac} is the result of three dominant energy dissipations[1], [3]: firstly, sound power radiation at the open end represented by $Q_1 = \frac{Lc_s}{\pi R^2 f}$, secondly the viscous drag at the sidewalls with $Q_2 = \sqrt{\frac{\rho\pi R^2}{\eta_d}}$, and finally thermal boundary effects originate from the fact that the surrounding solid has a much higher heat conductivity than the fluid and has a $Q_3 = \sqrt{\frac{\rho f C_p \pi R^2}{\kappa}}\left(\frac{C_v}{C_p - C_v}\right)$. L represents the cylinder height, R its radius, f the resonant frequency and c_s the speed of sound. η_d, ρ, κ, c_v and c_p are respectively the air (or gas) dynamic viscosity, density, thermal conductivity, specific heat capacity at a constant volume, and specific heat capacity at constant pressure.

Thus the final acoustical resonator quality factor is $Q_{ac} = \frac{1}{Q_1^{-1} + Q_2^{-1} + Q_3^{-1}} = 5.2$ and the acoustical signal amplitude presented in equation I.4.30 is then enhanced by a factor $Q_j = Q_{ac}$.

3- **<u>Mechanical membrane resonator:</u>** Membranes are usually used as microphones for the detection of pressure waves. In the proposed design the Poly-Silicon membrane covering the closed end of the acoustical resonator is used for pressure wave detection, but it is also used as a mechanical resonator to realize a third enhancement of the detected signal.

The wave equation for the displacement $w(r, \varphi, t)$ of a circular membrane evolution over a time t is represented by[4]:

$$\nabla^2 w = \frac{1}{c^2}\frac{\partial^2 w}{dt^2} \tag{II.1.2}$$

with $c = \sqrt{\frac{T}{\sigma}}$ where $\sigma\left(\frac{kg}{m^2}\right)$ corresponds to the areal mass density and $T\left(\frac{N}{m}\right)$ the tension force of a stretched string. Using polar coordinates, the equation II.1.13 becomes:

$$\frac{1}{r}\frac{\partial}{\partial r}\left(r\frac{\partial w}{\partial r}\right) + \frac{1}{r^2}\frac{\partial^2 w}{\partial \varphi^2} = \frac{1}{c^2}\frac{\partial^2 w}{dt^2} \tag{II.1.3}$$

Considering $w = R(r)\emptyset(\varphi)e^{-i\omega t}$ and searching for solutions for $R(r)$ and $\emptyset(\varphi)$ separately, the final solution for the displacement function is then presented by:

$$w(r,\varphi,t) = \cos(m\varphi - \alpha) J_m\left(\frac{\omega r}{c}\right)\cos(\omega t - \Omega) \quad \text{(II.1.4)}$$

With J_m the Bessel function of mth order. The allowed mode resonance frequencies are found by applying the following boundary conditions to equation II.1.4

$$w(r,\varphi) = w(r,\varphi) + 2\pi \quad \text{(II.1.5)}$$

$$w(R_0,\varphi) = 0 \;\rightarrow\; J_m\left(\frac{\omega r}{c}\right)_{r=R_0} = J_m\left(\frac{\omega R_0}{c}\right) = 0 \quad \text{(II.1.6)}$$

The membrane borders are fixed leading to have zero amplitude at the edges (II.1.6). The resonant frequencies of the vibrating membrane are given by:

$$f_{mn} = \frac{c}{2\pi R_0}\beta_{mn} \quad \text{(II.1.7)}$$

β_{mn} m \ n	0	1	2	3
0	0	2.405	5.520	8.654
1	3.832	7.016	10.173	13.3237
2	5.136	8.417	11.620	13.170
3	6.380	9.761	13.015	16.223

Table II.1.1 Some of the βmn values

with β_{mn} represent the n[th] root of the m[th] order Bessel function, where m and n describe the resonant mode number. The first values of β_{mn} are represented in table II.1.1.

The membrane resonance frequency depends then on the material mass density $\rho = \frac{\sigma}{h}$, internal stress tension $\sigma_i = \frac{T}{h}$ and radius R_0. The radius of the membrane is related to the hole size of the PhC cavity. To keep a compromise between lowering the impedance mismatch in the THz cavity (this will be discussed in section II.3) and decreasing the mechanical resonance frequency of the

membrane (for a low modulation in the PA application), the radius size is optimized to be on the order of 28 µm. Since the membrane covers the THz guiding channel and to avoid the Poly-Si THz losses, the membrane has to be very thin. Therefore, for a radius R_0=28 µm and a thickness h=100 nm the membrane's mechanical resonance is adapted to the acoustical one by adjusting its internal stress to $\sigma_i \approx 6.2$ MPa $\left(T = 62 \times 10^{-2}\,\frac{N}{m}\right)$. The analytical resolution of this problem is based on several approximations by neglecting the effect of the membrane's boundaries and without considering nonlinear effects. To take those into account, numerical methods are necessary. However, these calculations are not discussed here.

II.2. WAVEGUIDE DESIGN

The designed THz waveguide is based on index guiding between two materials with high refractive index contrast. HR-Si is a perfect candidate for the core material of the waveguide due to its large, and frequency independent (nondispersive) refractive index (n_{Si}= 3.42) at Terahertz (THz) frequencies [5], [6]. High resistivity float zone (HRFZ) silicon is moreover quasi-lossless at THz frequencies. While such core material is ideally loss-less, cladding materials with a sufficiently lower refractive index than Si such as silica, borosilicate, crystal quartz, or other glasses have important absorption losses that moreover increase dramatically at frequencies beyond 500 GHz [6], [7]. Thus the proposed design shown in figure II.2.1 (a), is composed of a HRFZ Silicon channel surrounded by air. The high refractive index contrast between Si and air defined as $\Delta = \frac{n_1^2 - n_2^2}{2n_1^2} = 45\%$ [8], allows to strongly confine modes with respect to the guiding channel dimensions. However, in reality the waveguide cannot be floating in air, and it needs anchors to suspend its core (see figure II.2.1 (c)). The fabrication technology allowing to create such suspended structures (and which will be discussed later in chapter III) uses DRIE etching techniques to etch high resistivity silicon on insulator wafer (SOI). In this chapter the modal analysis and waveguide dimensions are discussed. Subsequently, the anchors used to suspend these structures are also adjusted in order to minimize their impact on the propagation losses. The fabrication of a compact and long waveguide is also necessary. To achieve this, bent waveguides are required. Numerical simulations studying radiation losses in 90° bend are therefore also considered. It is not only important to have a low loss waveguide but also to be able to feed it with

minimal insertion loss. For that purpose, we propose the design of an inverted taper (presented in figure II.2.1 (b)) allowing a highly efficient transition from a metallic waveguide to the designed Si waveguide. The metallic waveguide (MWG) represents the output of the VDI AMC (Amplifier multiplier chain) THz electronic source (presented in chapter III) used to feed the gas senor. It is also the output of the VNA (Vector network analyzer) frequency extenders used for the waveguides and cavities characterization.

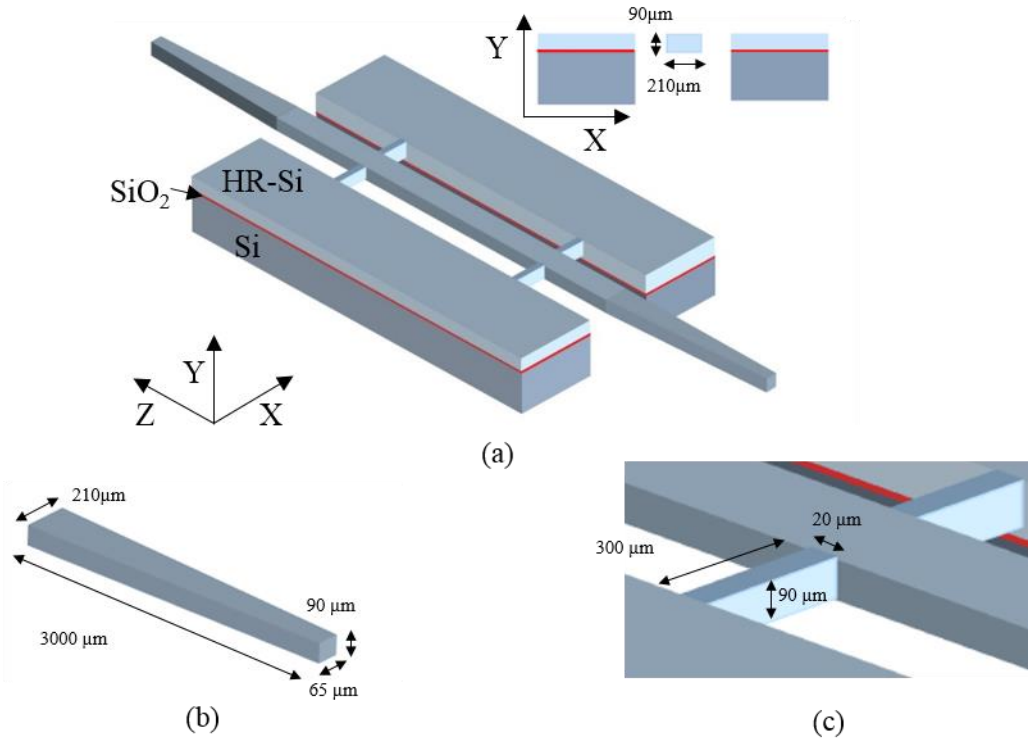

Figure II.2.1 (a) Schematic of the suspended waveguide inset: transversal cross section of the waveguide. b) Taper dimensions. c) supporting anchors dimensions

II.2.1 Modal analysis

The analysis of modal propagation inside a waveguide is described by the solution of the wave equations for electric $\boldsymbol{E}$ and magnetic $\boldsymbol{H}$ field vectors:

$$\nabla^2 \boldsymbol{E}(x,y,z,t) + \frac{\varepsilon_r}{c^2}\frac{\partial^2 \boldsymbol{E}(x,y,z,t)}{\partial t^2} = 0 \qquad \text{(II.2.1)}$$

$$\nabla^2 \boldsymbol{H}(x,y,z,t) + \frac{\varepsilon_r}{c^2}\frac{\partial^2 \boldsymbol{H}(x,y,z,t)}{\partial t^2} = 0 \qquad \text{(II.2.2)}$$

which are derived from Maxwell's equations [9] represented by

$$\nabla . \boldsymbol{E} = \frac{\rho}{\varepsilon_0} \tag{II.2.3}$$

$$\nabla . \boldsymbol{B} = 0 \tag{II.2.4}$$

$$\nabla \times \boldsymbol{E} = -\frac{\partial \boldsymbol{B}}{\partial t} \tag{II.2.5}$$

$$\nabla \times \boldsymbol{H} = \boldsymbol{j} + \frac{\partial \boldsymbol{D}}{\partial t} \tag{II.2.6}$$

where $\boldsymbol{D} = \varepsilon \boldsymbol{E}$ and $\boldsymbol{B} = \mu_0 \boldsymbol{H}$ are respectively the electric displacement and magnetic flux density, with $\varepsilon = \varepsilon_r \varepsilon_0$ and μ the respective permittivity and permeability of an isotropic non-magnetic medium. $\boldsymbol{j}$ corresponds to the electric current density, ρ the volumic electric charge density and $c = \frac{1}{\sqrt{\varepsilon_0 \mu_0}}$ the speed of light in vacuum. The electric and magnetic field of a wave propagating in **Z** direction is represented by

$$\boldsymbol{E}(x, y, z, t) = \boldsymbol{E}(x, y) e^{i(\omega t - \beta z)} \tag{II.2.7}$$

$$\boldsymbol{H}(x, y, z, t) = \boldsymbol{H}(x, y) e^{i(\omega t - \beta z)} \tag{II.2.8}$$

with ω the angular frequency, $\beta = \frac{\omega n_{eff}}{c}$ the propagation constant proportional to the modal effective index n_{eff}. At interfaces between two media and in absence of surface current and surface charge densities, $\boldsymbol{E}$ and $\boldsymbol{H}$ must fulfill the following boundary conditions:

$$\boldsymbol{n} \times (\boldsymbol{E}_{1t} - \boldsymbol{E}_{2t}) = 0 \tag{II.2.9}$$

$$\boldsymbol{n} \times (\boldsymbol{H}_{1t} - \boldsymbol{H}_{2t}) = 0 \tag{II.2.10}$$

$$\boldsymbol{n} . (\boldsymbol{H}_{1n} - \boldsymbol{H}_{2n}) = 0 \tag{II.2.11}$$

$$\boldsymbol{n} . (\varepsilon_1 \boldsymbol{E}_{1n} - \varepsilon_2 \boldsymbol{E}_{2n}) = 0 \tag{II.2.12}$$

These conditions mean that the tangential components of $\boldsymbol{E}$ and $\boldsymbol{H}$ are continuous, however only the normal component of $\boldsymbol{H}$ is continuous while the normal component of $\boldsymbol{E}$ is discontinuous. By applying the previous boundary conditions and using equations II.2.1, II.2.2, II.2.7, II.2.8 an analytical solution of the mode propagation can be found. To do that several analytical methods

such as Marcatili's method [10] and effective index method[11], have been proposed using some approximations. The development of many numerical calculation methods makes the resolution of these types of problems simpler and moreover avoids the need for approximations. The modal analysis simulations of this design are solved using the commercial Lumerical mode solver software [12] based on the finite difference method. The finite difference method approximates the exact refractive index profile by making a cross sectional spatial discretization (mesh) of the guiding structure. The derivative forms of Maxwell's equations are then replaced by their finite difference representation. The simulation region is defined by a box with Perfectly Matched Layer (PML) or metallic boundaries, where the electric and magnetic field are supposed to vanish. In a Finite Difference Eigensolver (FDE), two main factors have to be taken into consideration in order to reduce the calculations error: first the mesh size has to be small enough and secondly the simulation box region should be large enough for the fields to vanish at the simulation edges.

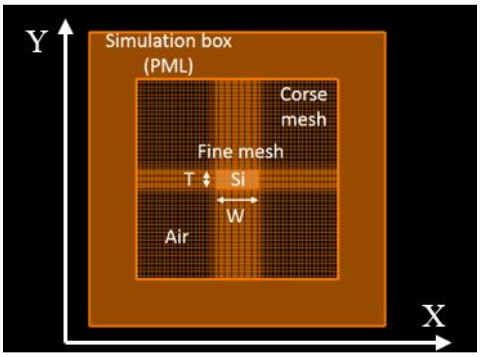

Figure II.2.2 FDE Lumerical mode solver simulation box

The waveguide formed by High resistivity Silicon core and an air clad, is represented by a rectangular shape of HR-Si material (n = 3.4174), with a width (W) in the **X** direction, thickness (T) in **Y** direction, and length (L) in the propagation direction **Z**, surrounded by an air box (figure II.2.2). The HR-Si is considered as a lossless and non-dispersive material by applying a constant real value for its refractive index (n_{Si} =3.4174, κ_{Si}=0). Modes with an effective index $n_{eff} = \frac{\beta}{k_0}$ lying between $n_{clad} = n_{air} = 1$ and $n_{core} = n_{Si} = 3.4174$ ($n_{air} < n_{eff} < n_{Si}$) are guided and propagate along the Si guiding channel. These modes are separated into quasi TE-mode denoted by E_x^{mn} where the dominant component of the electric field $\boldsymbol{E}$ is oriented along the **X**-axis (long side which is the waveguide width in our case) and quasi TM-mode denoted by E_y^{mn} with its dominant component oriented along the **Y**-axis (short side or thickness here). m and n, are the

mode indices representing the number of maxima and minima in the **X** direction for m and **Y** direction for n. The modal behavior is adjusted by the geometrical dimensions of the silicon channel. Starting from an analytical solution, for an infinite width waveguide the maximal thickness allowing single mode guiding is given by $T = \frac{\lambda_0}{2\sqrt{n_2^2 - n_1^2}} \approx 76\ \mu m$ (at 650GHz). For a finite width waveguide, the modal propagation constants are obtained numerically for different waveguide widths and thicknesses using a numerical sweep. The waveguide's width is chosen to be larger than its thickness W > T, for E_x^{mn} to be favored. Starting from large dimensions W= 500 µm and T= 150 µm, to support the largest number of modes at the frequency of interest (650 GHz), and looping the width and the thickness, the modal propagation constants are calculated for several thicknesses and plotted as a function of the waveguide width in figure II.2.3.

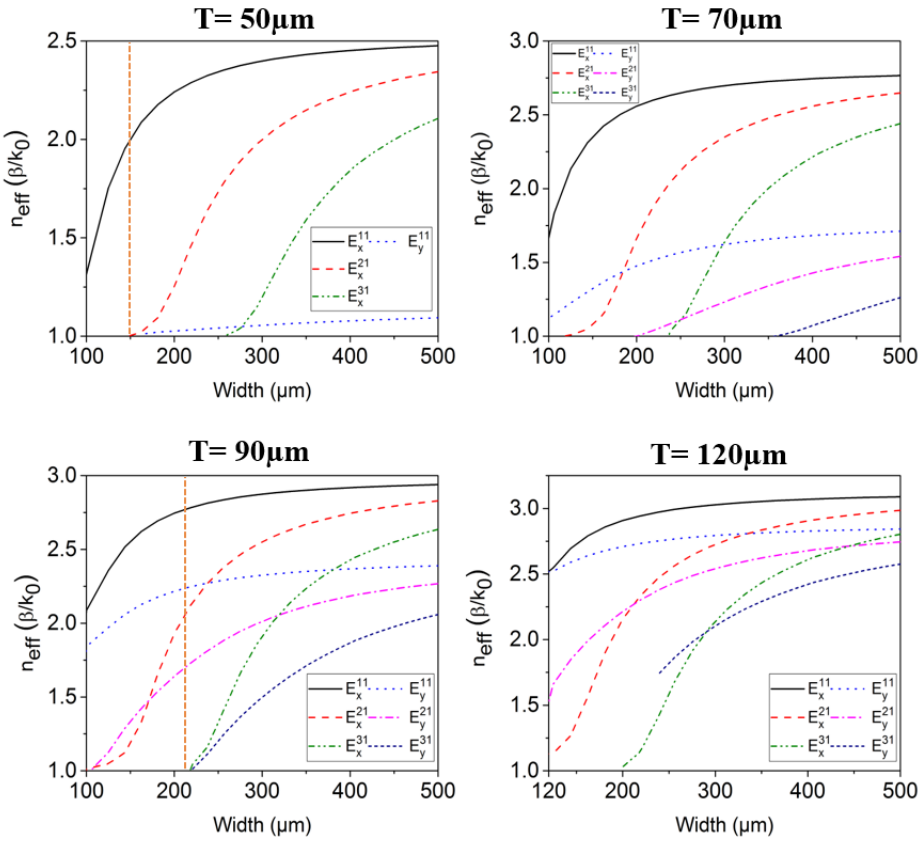

Figure II.2.3 First modes normalized propagation phase constant function of waveguide width for several particular thicknesses

The simulation region (1.5 mm x 1.5 mm) is at least three times larger than the largest geometrical feature and the wavelength, guaranteeing a sufficiently decreased field strength at the

mathematical boundaries. To reduce the simulation time, boundaries are chosen to be metallic instead of PML, however, the result is still converging. The mesh size is also adjusted to 5µm in all directions, in order to reduce the simulation time while maintaining the accuracy of the calculations. As represented in figure II.2.3 by the orange dashed vertical line, a width (W) of 150 µm and a thickness (T) of 50 µm represents the dimensions of a single mode waveguide. At such dimensions however the modal confinement in the silicon layer is rather poor (58%) (see figure II.2.5) and the guided mode is highly dispersive. As mentioned earlier the thickness of the waveguide define also the height of the acoustical resonator of the gas sensor. To reduce the acoustic resonant frequency and thus the modulation frequency for the PAS application a long acoustic resonator is required. Therefore, a thicker waveguide is necessary. However, the disadvantage of a very thick waveguide (i.e. 120µm) is that higher order vertical modes appear (i.e. E_x^{12} which is not represented in figure II.2.3) that are not immune to excitation even under symmetric injection (figure II.2.5). Our choice finally falls on a design with a width (W) and thickness (T) of 210x90 µm. With such dimensions, the waveguide allows sufficiently strong confinement of the fundamental mode E_x^{11} inside the core (89%) (figure II.2.5), while the propagation of the second symmetric mode E_x^{31} remains prevented (figure II.2.3). This choice is not only limited by the modal behavior of the waveguide and the confinement factor, but is also related to the THz photonic crystal cavity, and acoustic resonator geometry of the designed sensor. The propagation phase constant dispersion diagrams of these two waveguides are represented in figure II.2.4.

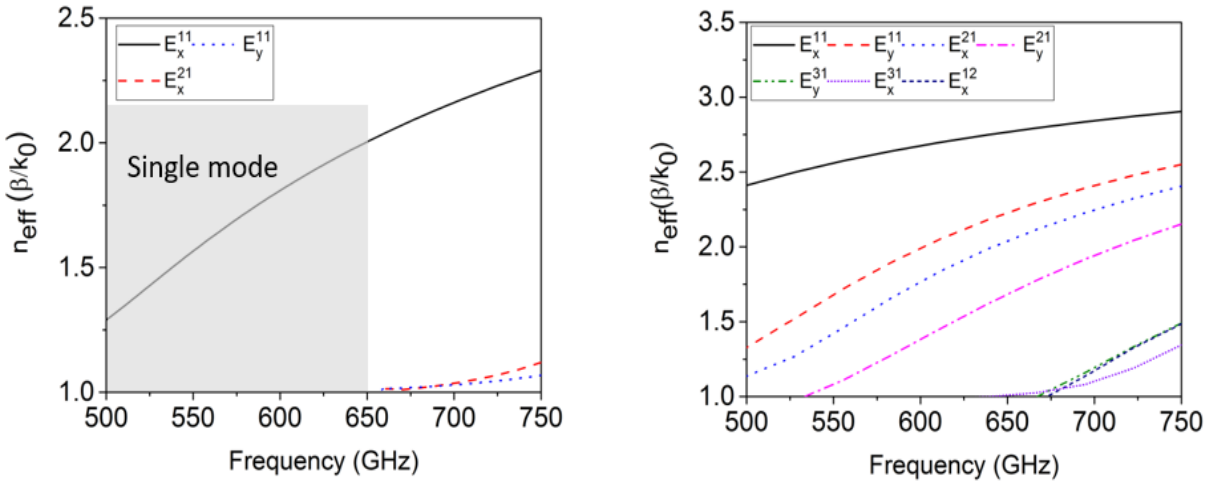

Figure II.2.4 Normalized propagation phase constant dispersion diagram for the waveguide structure 150(W) x 50(T) µm on the left and the 210(W) x 90(T) µm structure on the right

The 150x50 µm has a single mode behavior over the entire frequency band 500-650 GHz. However, the 210x90 µm design is a multimode waveguide in this region, but with respect to the polarization (Quasi TE polarization E_x^{mn}) and the modal symmetry, it can operate in the single mode regime.

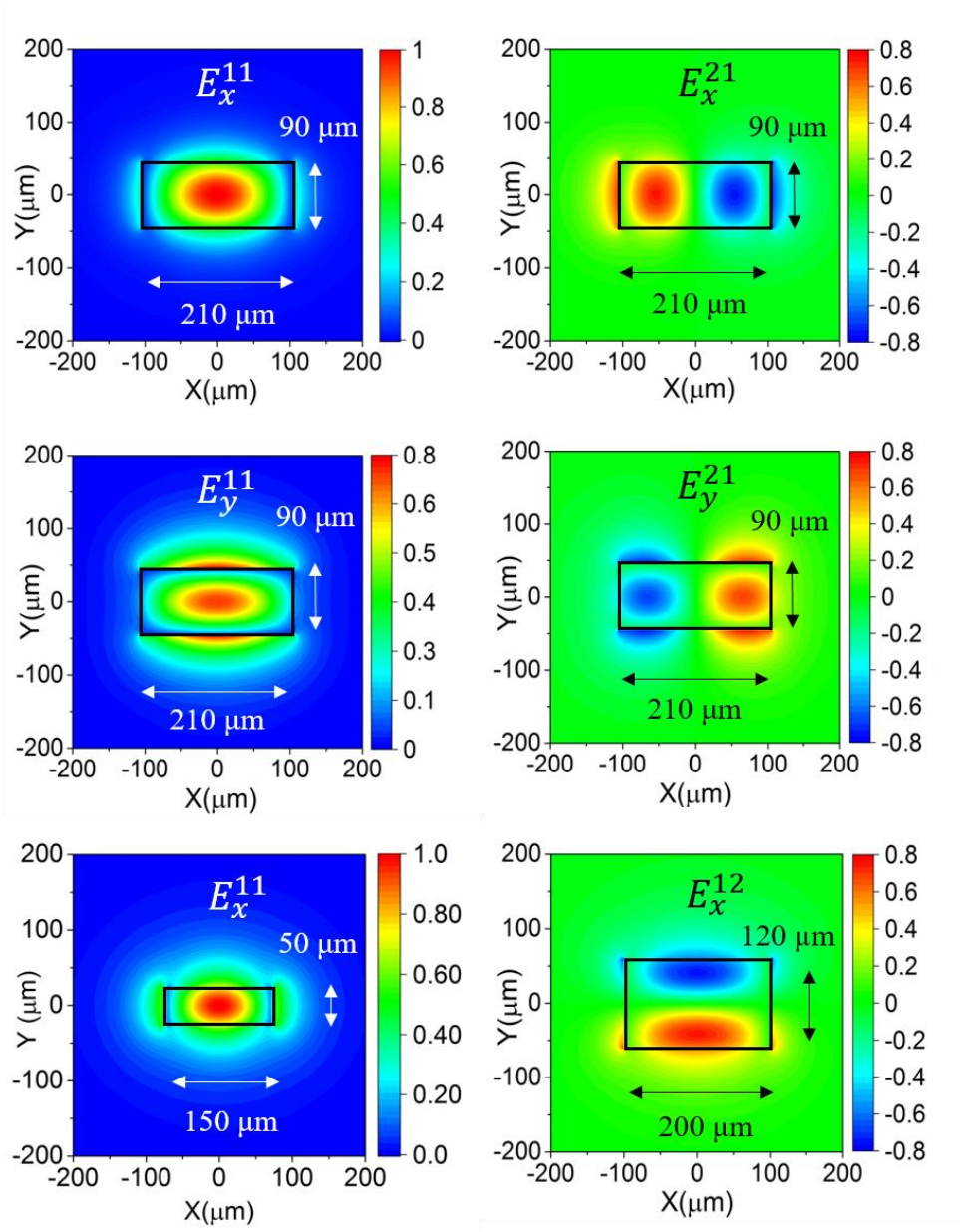

Figure II.2.5 Cross section distribution of electric field components for the first modes of several waveguide dimensions at 650 GHz with E_x real component for E_x^{mn} modes and E_y real one for E_y^{mn}modes

Figure II.2.5, represents components of the electric field distribution of E_x^{mn} and E_y^{mn} modes at 650 GHz for different waveguide sizes. E_x represent the dominant component of the electric field

for E_x^{mn} modes while the E_y^{mn} ones are represented by the dominant component E_y. The low confinement factor of the fundamental E_x^{11} mode for the 50 µm thick waveguide is represented by the large part of the evanescent field in the air, which is not the case for the 90 µm one where the field is highly oscillating inside the Silicon.

Besides its low loss and single mode behavior, the modal dispersion of a waveguide is another important characteristic, governing the expansion and spreading of time pulses. Dispersion is the result of the frequency dependence of the propagation constant (β). This dependence is described by the group index:

$$n_g = \frac{c}{v_g} = c\frac{\partial \beta}{\partial \omega} \tag{II.2.13}$$

Where v_g represents the group velocity, that defines the speed at which the energy is propagating and $c = 3 \times 10^8 m/s$ the vacuum speed of light. Several phenomena are at the origin of the dispersion in a waveguide [9]:

- Material refractive index change (material dispersion)
- Waveguide geometry and propagating wave frequency (wavelength) (waveguide dispersion)
- Multimode dispersion (Intermodal dispersion)

The main advantage of this design is the use of HR-Si as a guiding channel which, besides being low loss material, is also non-dispersive at these THz working frequencies [13], [14]. Therefore, the material dispersion does not contribute here. However, it is clear from figure II.2.4, how the propagation constant is rapidly changing with frequency for the 150x50 µm structure while for the 210x90 µm this variation is less important. Modal dispersion is obviously stronger for geometries with lower confinement with important contributions from evanescent fields. Therefore, the 210x90 µm structure presents an additional advantage over the 150x50 µm one as it is less dispersive. This dispersion phenomenon is known by the waveguide dispersion which depends only on the waveguide geometry. The waveguide dispersion is represented by the group velocity variation. Figure II.2.6 shows the normalized group velocity of the first 7 modes supported by the 210x90 µm waveguide. The modal group velocity near the cut-off frequency approach to the speed of light in the air. At higher frequency where the mode becomes highly confined inside the Si, the

group velocity approach to that of the bulk material ($v_g/c=0.29$). The quasi-constant group velocity at high frequencies, confirms the absence of material dispersion.

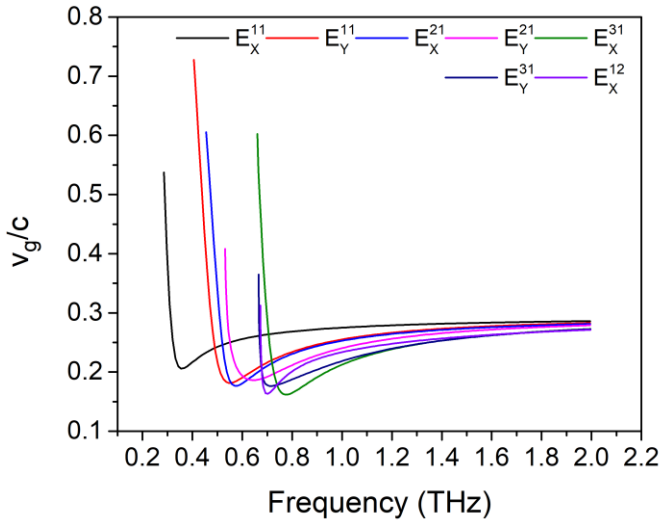

Figure II.2.6 Group velocity of the first 7 modes propagating in the 210x90 µm cross-section waveguide

When multiple modes are propagating inside the waveguide an additional dispersion mechanism called intermodal dispersion contributes to the time pulse chirp. This is due to the propagation of the several modes at different group velocities. For the frequencies below 650 GHz, and for a symmetric E_x polarization the waveguide can be considered in the single mode regime, and therefore the dispersion mechanism will be limited by the waveguide dispersion.

We presented in this part the numerical modal analysis of HR-Si suspended waveguides with different geometries. The waveguide with the 210x90 µm cross section dimensions will be used in the fabrication of the PhC cavities and finally the PA gas sensor. Therefore, in the following, we only discuss the numerical simulations related to this waveguide design.

The waveguide is suspended using Si anchor beams as shown in figure II.2.1. The impact of these anchor beams on the waveguide propagation losses is simulated and discussed in the next section. This is followed by a numerical study of the bends radiative losses.

II.2.2 Anchors and bends losses

THz waveguides with very low propagation losses are necessary for many applications. The propagation losses can be divided into three loss mechanisms: material absorption, scattering and

radiation losses. While the absorption losses are related to the resistivity of the Si wafer, scattering and radiation losses are caused by non-perfect guiding. Therefore, the addition of anchor beams and bends to the guiding structure increase the scattering and radiation losses. To minimize the impact of the anchor losses, FDTD (Finite-difference time-domain) numerical simulations using Lumerical were performed for waveguides with different anchor beam sizes. The bend losses were also calculated for different 90˚bends radius with Lumerical FDTD and FDE.

II.2.2.1 Anchors losses

As represented in the schematic of figure II.2.1, in order to fabricate a suspended waveguide, anchors are needed to connect the waveguide to the Si supporting platforms. Such an addition to the waveguide produces a modal perturbation and could potentially increase the waveguide scattering and radiation losses. To minimize the impact of these beams on the waveguide losses, 3D FDTD simulations are conducted on several structures with the same number of beams (4 pairs) at identical positions, varying only the beam's size. All structures are simulated using a guided fundamental E_x^{11} mode of a broadband source (500-750 GHz) inside a waveguide of 1.5 cm length, 210 µm width, and 90 µm thick. The waveguide material is defined by the real part refractive index of Silicon n_{Si} = 3.4174, in order to isolate purely the scattering loss. The waveguide edges cross PML boundaries of the simulation box, to prevent reflections at the finite edges (Figure II.2.7). However, to reduce the simulation time and memory, symmetric and anti-symmetric boundary conditions are used in the X and Y plane respectively. Transmission and reflection monitors are used to collect the transmitted field after propagating inside the waveguide, and the returned field caused by reflections. The simulation time is set to 10ns and a mesh size of 5,4,3 µm in X, Y, and Z directions is chosen. The anchor beams' size shown in figure II.2.8 is fixed in X and Y to 300 and 90 µm respectively, while its sizes change along the propagation direction between each simulation going from 10 µm thick to 50 µm with a 10µm step size. To only detect the guided transmitted power, the modal expansion monitor calculates the overlap integrals between the detected fields and the modal fields:

$$T = \frac{P_i}{P_{in}} = Re\left[\frac{(\int \boldsymbol{E}_i \times \boldsymbol{H}_{in}^*.\, d\boldsymbol{S}).(\int \boldsymbol{E}_{in} \times \boldsymbol{H}_i^*.\, d\boldsymbol{S})}{\int \boldsymbol{E}_i \times \boldsymbol{H}_i^*.\, d\boldsymbol{S}}\right]\frac{1}{Re(\int \boldsymbol{E}_{in} \times \boldsymbol{H}_{in}^*.\, d\boldsymbol{S})} \qquad \text{(II.2.14)}$$

where T represent the modal transmitted power, P_i, $\boldsymbol{E}_i$ and $\boldsymbol{H}_i$ the modal power, electric and magnetic field respectively, while P_{in}, $\boldsymbol{E}_{in}$ and $\boldsymbol{H}_{in}$ corresponds to the monitor input wave.

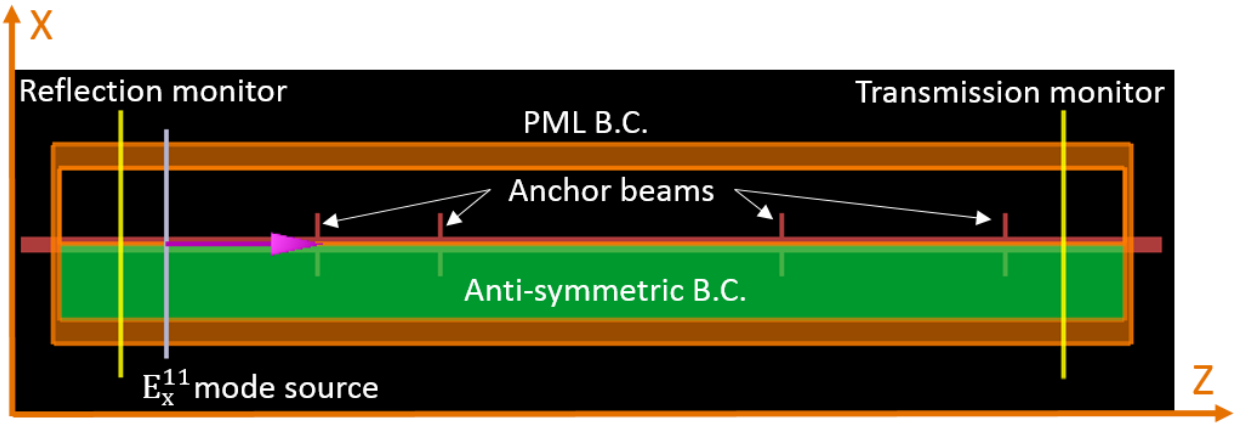

Figure II.2.7 FDTD simulation region of a waveguide with anchors

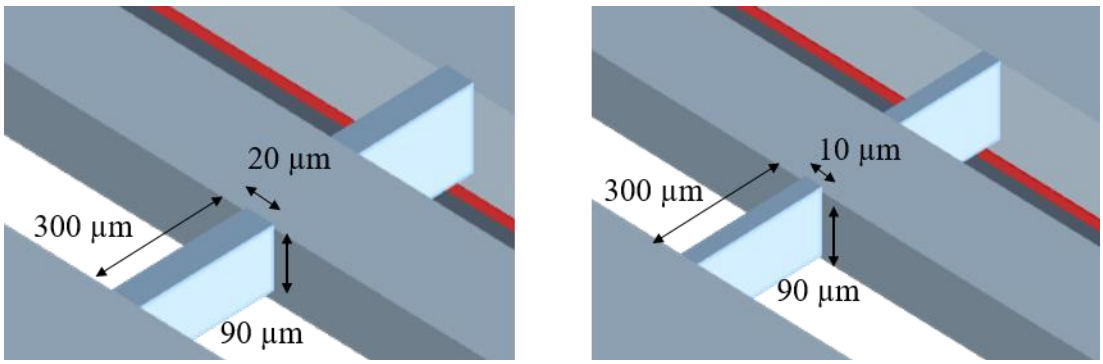

Figure II.2.8 Schematic of anchors suspending the waveguide with 20µm thick on the left and 10 µm on the right

Since the simulation is a time-domain method, the source is defined by a time pulse and its Fourier transform in the frequency domain does not have a flat response. Therefore, normalization with the spectrum has to be applied. For that, a simulation with the same parameters and without anchors is performed. The extracted loss is then defined by:

$$\alpha_{anchor}(dB) = 10\log\left(\frac{T}{T_0}\right) \qquad \text{(II.2.15)}$$

with T_0 the normalization factor corresponding to the transmitted power for a structure without anchors. Assuming that each anchor pair contributes the same loss, the loss per anchor pair can be expressed by the relation:

$$\alpha_{anchor\ pair} = \frac{\alpha_{anchor}}{4} \quad \text{(II.2.16)}$$

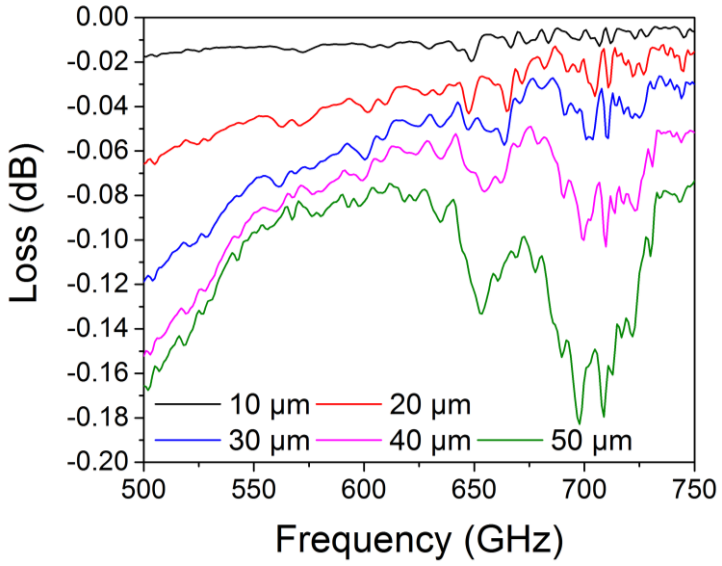

Figure II.2.9 Simulated losses per anchor pair for different anchors size

Figure II.2.9 represents the simulated losses of anchors per pair. It is clear for all the sizes that the losses are higher at low frequencies, where the evanescent field is larger and waves scatter more at the beams' side edge. Having a very thick anchor beam on the other hand can create high losses especially at high frequencies where the wave could escape the waveguide and propagate inside the anchor beam. Therefore, the impact of the anchors decreases with their width. In order to maintain a compromise between mechanical stability and low scattering loss the dimensions of the anchors are chosen to be 20x300x90 µm (Figure II.2.8).

II.2.2.2 90° bend loss

Bends are necessary for integrated compact circuits. However, waveguide modes in bends are intrinsically only lossless in the limit of infinite radius. In this section radiation losses in bent waveguides are studied as a function of bend radius. In a bent waveguide, the wavefront at the outer side of the bend travels faster than its central part. Therefore, at a critical distance $r_{critical}$, the phase front reaches the speed of light in the cladding and couples to radiative modes. This loss mechanism is described in figure II.2.10 by the representation of the index profile in a bent and straight waveguide. The horizontal dashed line represents the effective index of the guided mode, while the critical distance $r_{critical}$ is represented by the vertical dashed line, where the mode will

cross the barrier and couple to radiative modes by tunneling effect. This loss phenomenon is mainly dependent on the bend radius and modal confinement factor.

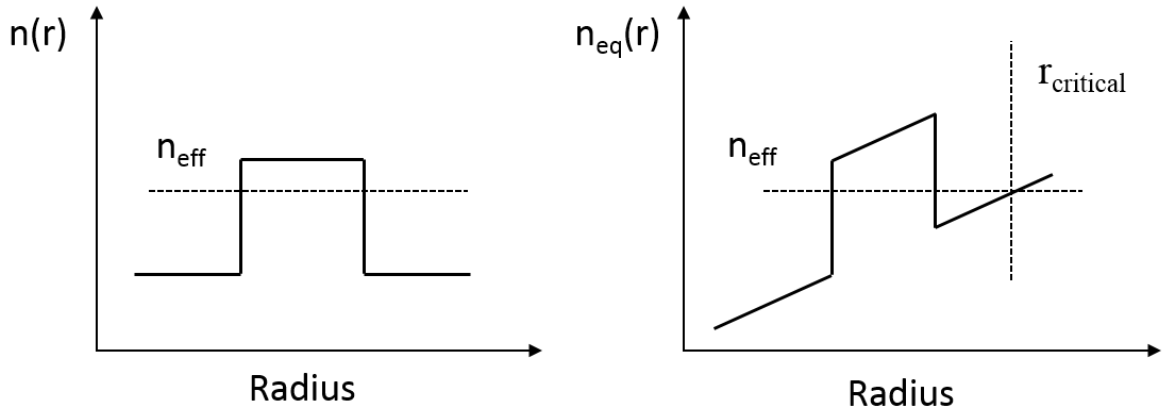

Figure II.2.10 Index profile of bent waveguide on the right and straight waveguide on the left

In the proposed design, the combined HR-Si/air high index contrast and high modal confinement allow reducing bend losses. However, very short bends would increase the radiative losses as they are exponentially proportional to the bending radius[15]:

$$\alpha_{bend} \propto e^{-R} \tag{II.2.17}$$

To estimate the bend losses, numerical calculations are performed using both the FDE (Finite Difference eigenvalue) and the FDTD (Finite Difference Time Domain) method from Lumerical software. In FDE, the bend loss is deduced from a modal overlap calculation between modes in a straight and bent waveguide and expressed in dB by:

$$\alpha_{bend} = 2 \times 10 \times \log(Re\left[\frac{(\int \boldsymbol{E}_b \times \boldsymbol{H}_s^*.d\boldsymbol{S}).(\int \boldsymbol{E}_s \times \boldsymbol{H}_b^*.d\boldsymbol{S})}{(\int \boldsymbol{E}_b \times \boldsymbol{H}_b^*.d\boldsymbol{S}).(\int \boldsymbol{E}_s \times \boldsymbol{H}_s^*.d\boldsymbol{S})}\right]) \tag{II.2.18}$$

where 2 represents the number of the waveguide straight/bend interfaces at the in- and output of the bend. The bracketed term represents the modal overlap. Figure II.2.11, shows the bend losses of a 90° bent waveguide for different bending radius at 400, 500, 650, and 750 GHz frequencies. As expected, losses increase with decreasing radius. At higher frequencies, increasing modal confinement should lead to lower losses. This seems to be the case up to 500 GHz (red curve in II.2.11). However, beyond this frequency, contrary to what is expected, bend losses start increasing again (blue and pink curves in II.2.11). It is assumed that this is counterintuitive behavior is caused

by coupling to the second antisymmetric mode before being coupled to radiative modes. To be more accurate, FDTD simulations were also performed (figure II.2.12).

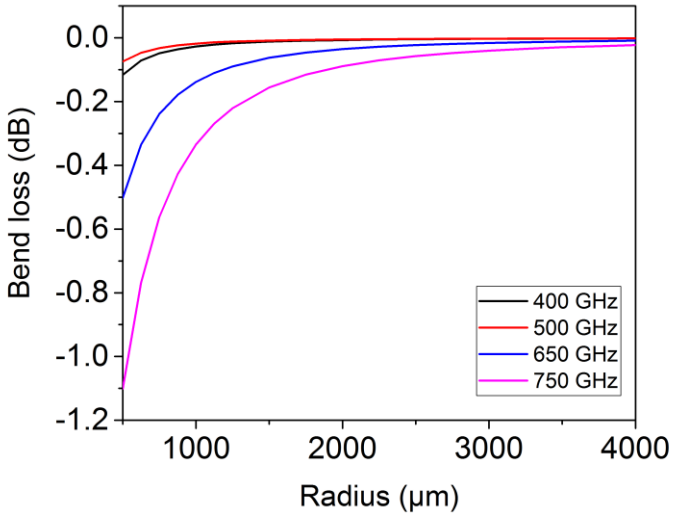

Figure II.2.11 Simulated bend loss with FDE method for several bending radii at 4 particular frequencies

The corresponding simulations are time and memory consuming, therefore losses are calculated for only 0.5 and 3 mm bending radius structures and represented in figure II.2.13. Simulations confirm the possibility of having very short bends down to 0.5 mm with acceptable losses. In our designs, we choose to fabricate structures with 3 mm bend radius, where losses are expected to be lower than 0.1 dB.

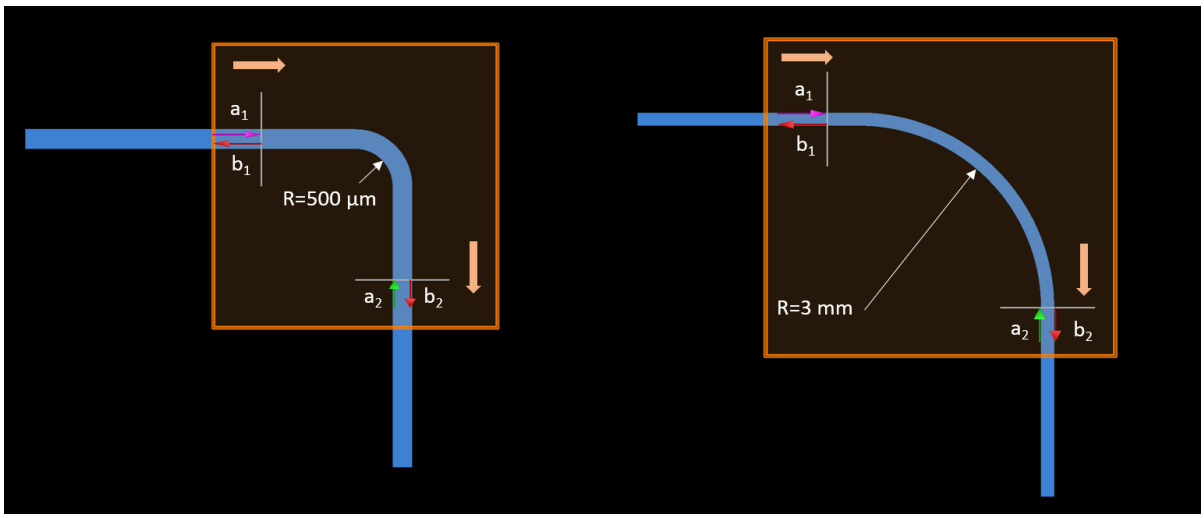

Figure II.2.12 FDTD simulation region of a 90° bend waveguide with a 3 mm radius on the right and a 500 µm one on the left

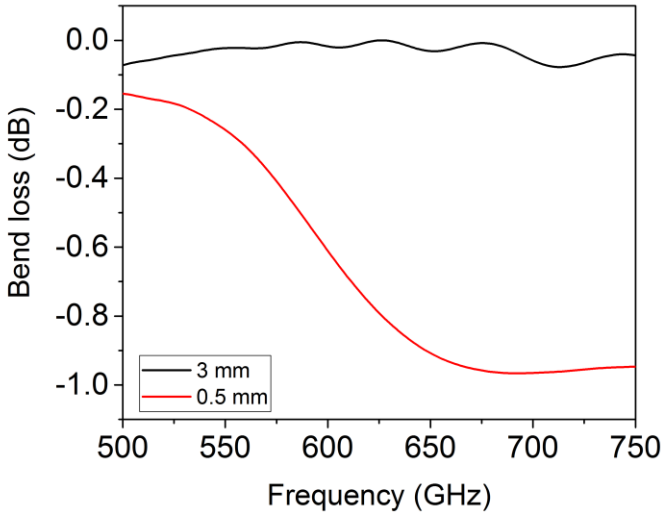

Figure II.2.13 Simulated bend loss using FDTD method for 3 and 0.5 mm bending radius

II.2.3 Coupling and Insertion losses

The VDI THz AMC source and the VNA frequency extender used for feeding and characterizing the designed gas sensor and waveguide are both equipped by a WR-1.5 metallic waveguide at their outputs. In this part, we study the transition of the THz waves from these WR-1.5 metallic waveguides to the Si waveguide.

To achieve smooth injection and good transition from MWG ports to the silicon waveguide, adiabatic tapers are added at the in- and output sides of the suspended waveguide. Wave impedance is represented by [16]

$$Z_{MWG} = \frac{\eta_0}{\sqrt{1 - \left(\frac{f_c}{f}\right)^2}} \qquad \text{(II.2.19)}$$

for an air filled MWG and,

$$Z_{Si} = \frac{\eta_0}{\sqrt{\epsilon_{eff}}} \qquad \text{(II.2.20)}$$

for Si waveguide with $\eta_0 = \sqrt{\frac{\mu_0}{\epsilon_0}}$ the free space impedance, f_c the MWG cutoff frequency which is $f_c = 393\ GHz$ for WR-1.5 MWG, f working frequency and $\epsilon_{eff} = n_{eff}^2$ effective permittivity of the propagating mode inside Si waveguide. To reduce the mismatch between these two impedances, the Si taper edge should be small enough, for the fundamental mode to still be guided but weakly confined in the Si with the lowest n_{eff}. A taper edge section of 65x90 µm slightly confines the fundamental mode with an $n_{eff} = 1.03$ at 650 GHz and therefore presents the smallest impedance mismatch with a guided wave inside MWG, before E_x^{11} goes to cut-off (see figure II.2-14). A larger section leads to stronger Si confinement, resulting in a higher effective index and therefore deeper reflection dips, especially at higher frequencies. Once the mode at the taper's edge is excited, a gentle variation of the taper dimension is necessary to prevent that the fundamental mode couples to higher order radiative or guided modes, before reaching the Si waveguide. For that, the taper length L_t has to be much longer than the beat length L_b corresponding to the coupling length between the fundamental mode and the second symmetric mode.

L_b and L_t are defined by [17]

$$L_b = \frac{2\pi}{\beta_1 - \beta_2} \tag{II.2.21}$$

$$L_t = \frac{\Delta W}{2\tan\theta} \gg L_b \tag{II.2.22}$$

where $\beta_1 = n_{eff1} k_0$ and $\beta_2 = n_{eff2} k_0$ are the propagation constant of the two first symmetric modes, where $k_0 = \frac{2\pi}{\lambda_0}$ is the free space propagation constant. $\Delta W = W_1 - W_2 = 145$ µm, the width difference between the taper's edges and θ the taper's variation angle. So according to the adiabaticity criterion, the variation angle θ has to be smaller than θ_{min}

$$\theta \ll \theta_{min} = \frac{\Delta W(\beta_1 - \beta_2)}{4\pi} \tag{II.2.23}$$

In our design, the width of the waveguide is tapered and reduced down to 65 µm over a length of 3000 µm, while its height remains constant (90 µm). This slow variation with a very small angle of 0.048 rad << θ_{min}, allows an adiabatic transition of modes and prevents any energy exchange

with higher order guided or radiative modes. Longer tapers with 4000 µm length and a slope angle of merely 0.036 rad, are also simulated. The 4000 µm taper presents almost the same performance as the 3000 µm one, which means that the taper is adiabatic enough. Therefore, only the results of the 3000 µm taper are discussed and represented here.

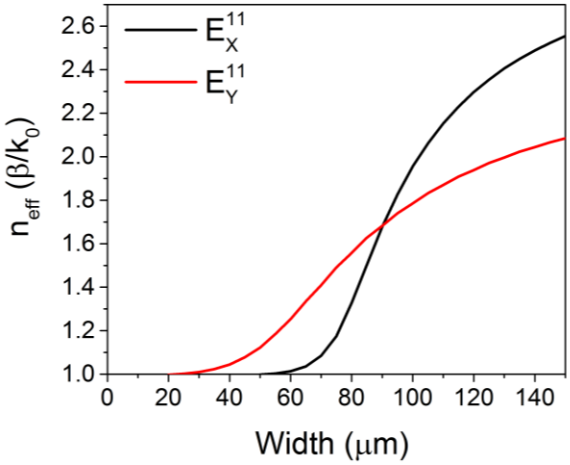

Figure II.2.14 Normalized propagation constant function of taper width variation at 650 GHz

In a MWG the electric field $\vec{E}$ of the fundamental TE mode is oriented along the smallest side of the waveguide, while in the dielectric one $\vec{E}$ is oriented along the long side for the fundamental E_x mode. In order to have the best overlap between these two modes the MWG is rotated by 90°, as it usually has its long side oriented horizontally. The numerical aperture of such a waveguide at 500 GHz is N.A.= sinθ = 0.79 and 0.53 at 750 GHz so strong diffraction occurs at the output of this MWG especially at lower frequencies (ie 500GHz). Placing the taper outside the MWG, presents high coupling losses. To estimate the insertion and return losses caused by the transition of a wave from the MWG to the Si waveguide through the taper, a FDTD simulation has been done. The simulated structure is composed of two metallic waveguides (WR-1.5) of 191x381 µm air guiding channel, surrounded by a PEC (perfect electrical conductor) layer to form the metallic boundaries, and 2 Si (n_{Si}=3.42) tapers in between. The whole structure is surrounded by PML (perfectly matched layer) boundaries, while symmetric and anti-symmetric boundary conditions are used to reduce the simulation time and memory (Figure II.2.15). For several depths of insertion of the taper inside the MWG (starting at perfect butt-coupling 0mm), the simulated insertion (S_{21}) and return (S_{11}) loss are represented in figures II.2.16 and II.2.17. In figure II.2.16 the taper is

considered to be perfectly centered at the MWG ports, and the effect of its position inside the MWG along the propagation direction (Z) is presented.

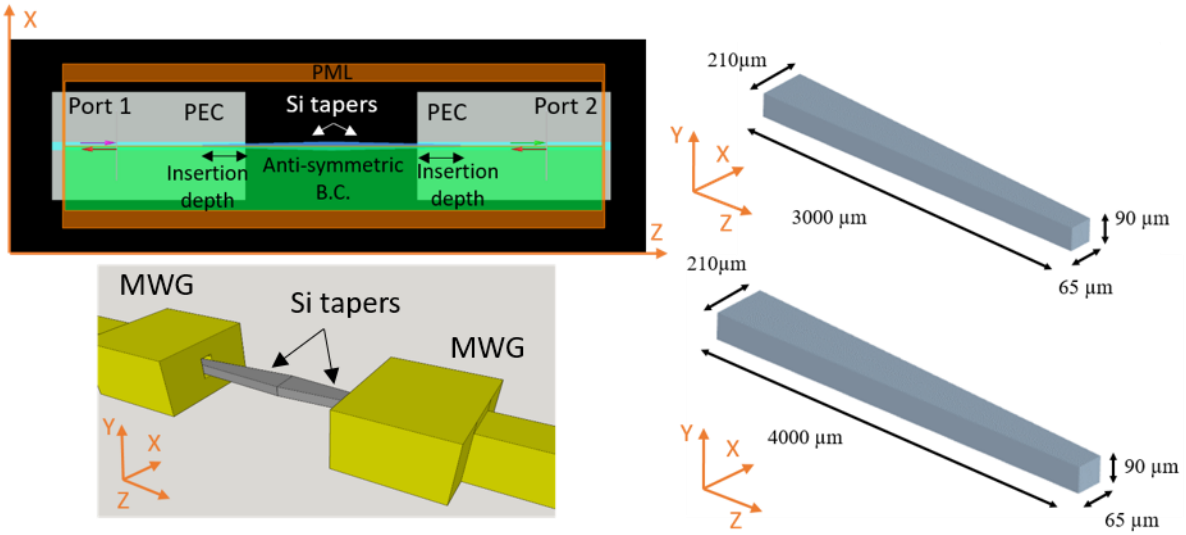

Figure II.2.15 FDTD simulation region of the insertion loss calculation (top left). 3D drawing of insertion loss simulation (bottom left). Schematics of the tapers with 2 different lengths: 3 and 4 mm (right)

For different positions of taper, the return losses are below -10 dB (below the red dashed line) except for perfect butt coupling, which confirms the low impedance mismatch. However, the best coupling and the lowest insertion loss are achieved for the positions where the taper is well inserted inside the MWG. For positions below 1mm, the taper cross section at the output of MWG does not exceed 100x90µm. For these dimensions, the fundamental mode at low frequencies is slightly confined with low $n_{eff} = 1.1$ at 500 GHz, which increases the insertion loss due to the coupling with radiative modes. Insertion losses are very low (0.15 dB at 600 GHz), for positions above 1mm. The simulated results of insertion losses show also some oscillations that correspond to a Fabry-Pérot cavity effect between the two MWG ports with a free spectral range ~5-7 GHz, corresponding to a cavity effect of about 5-6 mm for a group index of ~4.5. This is precisely twice the taper length. The low ripple reconfirms the strong coupling. In figure II.2.18 the magnitude of $\vec{E}$ at the transition between the MWG and the taper is represented for three different frequencies at 1mm insertion well centered inside. The large radiative field part at 500 GHz corresponds to the high insertion losses represented in figure II.2.16 at low frequencies. Experimentally, it is not easy to be perfectly aligned, so it is important to study the effect of misalignment. Figure II.2.17 represents the insertion losses, for a X and Y off axis displacement and rotation. A Y displacement

perpendicularly to $\vec{E}$ direction (X direction) doesn't show a big effect on the insertion and return losses, while a misalignment in the direction of $\vec{E}$ or an angular deviation breaks the modal symmetry, and some dips appear in S_{21} at certain frequencies where the higher order anti-symmetric mode is excited, while S_{11} remains low. In conclusion, the designed taper allows feeding the Si waveguide, from WR-1.5 MWG ports with very low losses.

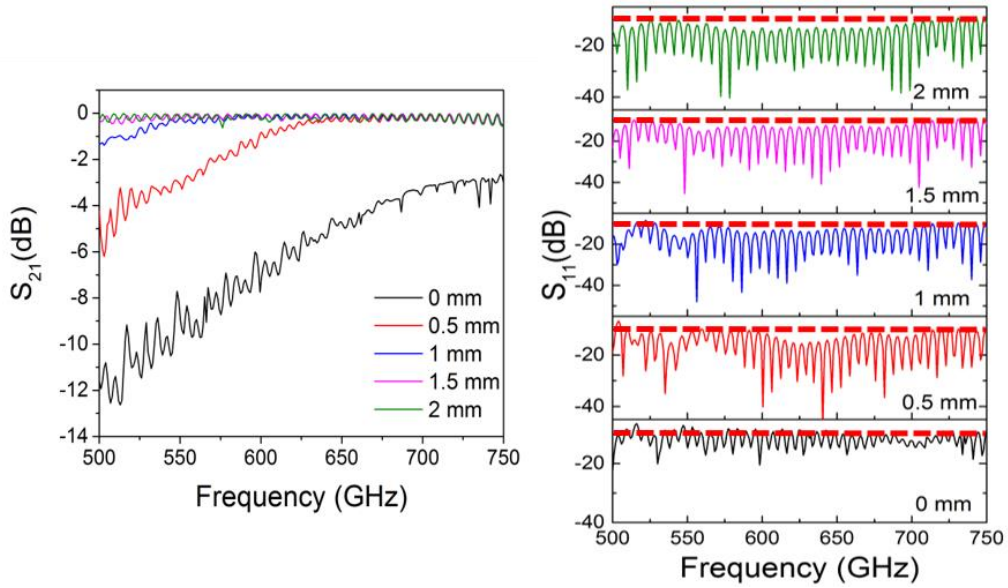

Figure II.2.16 Simulated insertion losses for different positions of taper inside. S_{21} parameter (transmittance) on the left, and S_{11} parameter (Reflectance) on the right MWG with the red dashed horizontal line indicating the 10 dB level

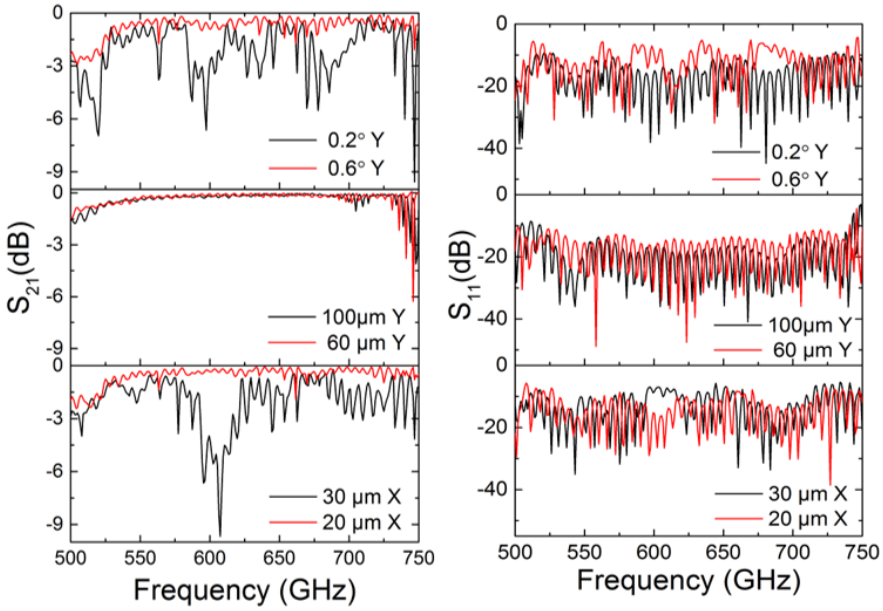

Figure II.2.17 Simulated insertion losses for the different misaligned positions of taper at 1 mm inside MWG. S_{21} parameter (transmittance) on the left, and S_{11} parameter (Reflectance) on the right

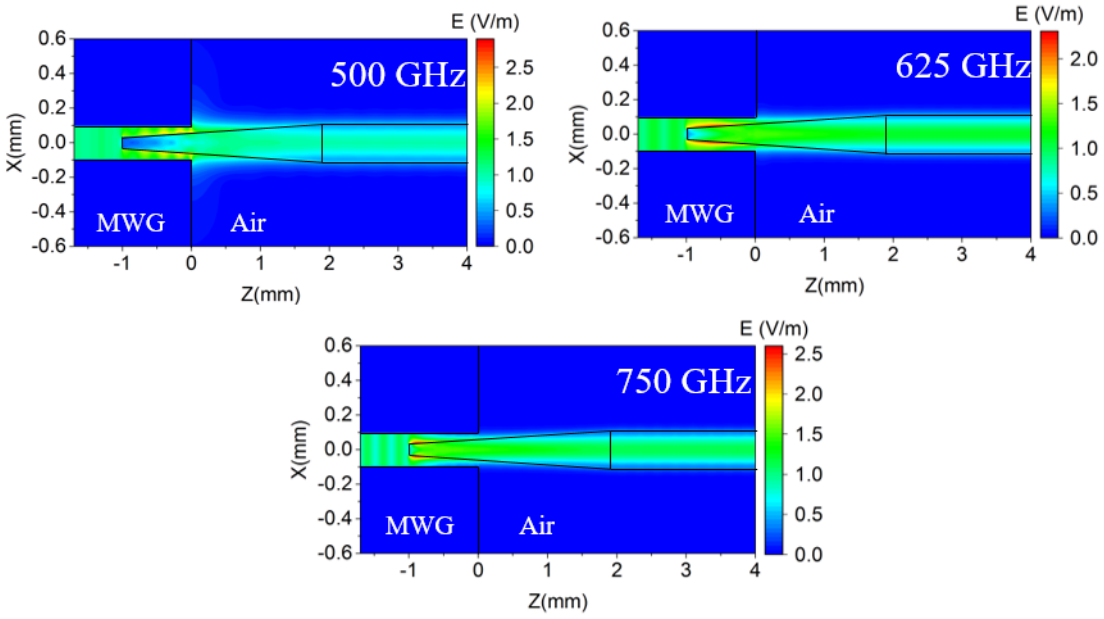

Figure II.2.18 Electric field transition from MWG to the dielectric waveguide taper at 3 different frequencies 500, 625, and 750 GHz

II.3. PHOTONIC CRYSTAL CAVITY DESIGN

In the previous parts, we presented the design of a suspended low-loss Silicon waveguide. Such a platform can be used for different applications in the THz integrated systems. In this part, we mainly focus on the design of photonic crystals and photonic crystal cavities on top of this Si waveguide. The proposed PhC cavities designs are adjusted to overlap with the absorption peaks of H_2S gas molecules, ultimately serving as a high-Q resonator in the PA gas sensor.

II.3.1 Solid/photonic crystal approach and photonic band gap

Photonic crystals in all their types (1D-2D-3D) are engineered in a way to control the propagation of electromagnetic waves. In the same way, as the atomic periodicity of a solid crystal controls the electronic energy states, the periodic permittivity in a photonic crystal determines the permitted and forbidden photon energy. This approach can be understood from the analogy between Schrödinger's equation [18]

$$-\frac{\hbar^2}{2m}\nabla^2\psi(r) + V(r) = E\,\psi(r) \qquad \hat{H}\psi(r) = E\,\psi(r) \tag{II.3.1}$$

and Maxwell's master equations:

$$\frac{1}{\varepsilon_r(r)}\nabla \times \left(\nabla \times \boldsymbol{E}(r)\right) = \frac{\omega^2}{c^2}\boldsymbol{E}(r)$$
$$\hat{O}\,\boldsymbol{E}(r) = \frac{\omega^2}{c^2}\boldsymbol{E}(r) \qquad \text{(II.3.2)}$$

$$\nabla \times \left(\frac{1}{\varepsilon_r(r)}\nabla \times \boldsymbol{H}(r)\right) = \frac{\omega^2}{c^2}\boldsymbol{H}(r)$$
$$\hat{\theta}\,\boldsymbol{H}(r) = \frac{\omega^2}{c^2}\boldsymbol{H}(r) \qquad \text{(II.3.3)}$$

Similarly, to the periodic potential variation V(r) in Schrödinger's equation, periodic variation of the permittivity $\varepsilon_r(r)$ (refractive index $n(r) = \sqrt{\varepsilon_r(r)}$) creates the photonic band gap. The permittivity $\varepsilon_r(r)$ in a photonic crystal is represented by a periodic function which is invariant under translation operator operator $\hat{T}$:

$$\hat{T}\varepsilon_r(r) = \varepsilon_r(r+R) = \varepsilon_r(r) \qquad \text{(II.3.4)}$$

In a 1D periodic structure, R represents the lattice constant a. The Bloch-Floquet theorem dictates that the solution of an equation which is invariant under the translational operator $\hat{T}$ is a periodic function multiplied by e^{ikr}. Since $\boldsymbol{H}(r)$ and $\boldsymbol{E}(r)$ are the eigenfunctions of the operator $\hat{T}$, therefore, the solution of equations II.3.2 and II.3.3 can be determined by the Bloch-Floquet theorem as a Bloch wave modes satisfying the equations below:

$$\boldsymbol{E_k}(r) = e^{ikr}u_k(r) \qquad \boldsymbol{E_k}(r+R) = e^{ikR}\boldsymbol{E_k}(r) \qquad \text{(II.3.5)}$$

$$\boldsymbol{H_k}(r) = e^{ikr}u'_k(r) \qquad \boldsymbol{H_k}(r+R) = e^{ikR}\boldsymbol{H_k}(r) \qquad \text{(II.3.6)}$$

where $u_k(r)$ and $u'_k(r)$ are periodic functions having the same periodicity as ε_r and k the wave vector. The periodicity of $u_k(r)$ and $u'_k(r)$ allows the restriction of the wavevector k to the first Brillouin zone. For any wavevector k' exist a wavevector k in the first Brillouin zone where $k'=k+G$, with $G=\frac{2\pi}{a}$ the reciprocal lattice basis vector. Using equations II.3.5-II.3.2 and II.3.6-II.3.3, the modal eigenvalues $\omega(k)$ can be determined and represented in the first Brillouin zone of the

dispersion diagram. The first Brillion zone is defined by the primitive cell in the reciprocal space. In a 1D photonic crystal, it corresponds to the range of *k* between:

$$-\frac{\pi}{a} < k < \frac{\pi}{a} \qquad \text{(II.3.7)}$$

with a the primitive lattice period that corresponds to the refractive index variation period. The spatial symmetry in a 1D PhC allows reducing the study of the band structure to the irreducible Brillouin zone $\left(0 < k < \frac{\pi}{a}\right)$.

Considering the example of a suspended waveguide (represented in a 2D schematic in figure II.3.1.a), the electromagnetic waves are confined in X and Y directions by index guiding and propagating in Z direction. In this structure a continuous translational symmetry is imposed by the constant permittivity along the propagation direction Z. Its dispersion diagram is represented in figure II.3.2.a with E_x^{mn} and E_y^{mn} the guided modes below the light line $\omega \geq ck$. The representation of the band structure here is shown for the region $0 < k < \frac{\pi}{a}$, however, for such structures *k* is unrestricted and the Brillouin zone is infinite because of the continuous translational symmetry.

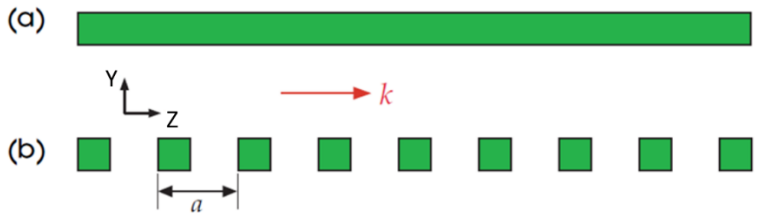

Figure II.3.1 2D illustration of a) a dielectric waveguide b) a photonic crystal with period "a" [19]

For a similar structure with periodic permittivity variation in the Z propagation direction (figure II.3.1.b), the discrete translational symmetry guarantees the conservation of *k*, and thus the reconstruction of the light line and guided modes in the finite periodic Brillouin zones. The range $-\frac{\pi}{a} < k < 0$ is equivalent to the $\frac{\pi}{a} < k < \frac{2\pi}{a}$ by the translational vector G which is, in turn, the reverse of the irreducible Brillouin zone at $0 < k < \frac{\pi}{a}$. The dispersion diagram of this structure is presented in figure II.3.2.b, where the modes flatten at the edge of the irreducible Brillouin zone ($k = \frac{\pi}{a}$) and open a photonic Bandgap between two modes. The energy of the upper band mode is mostly concentrated in the low permittivity region. In the case of a PhC created by etching air

holes inside a dielectric membrane, the upper mode is called air mode due to the presence of a large part of its field in the air hole. While the lower one is called a dielectric mode having its large energy part in the high permittivity region (dielectric).

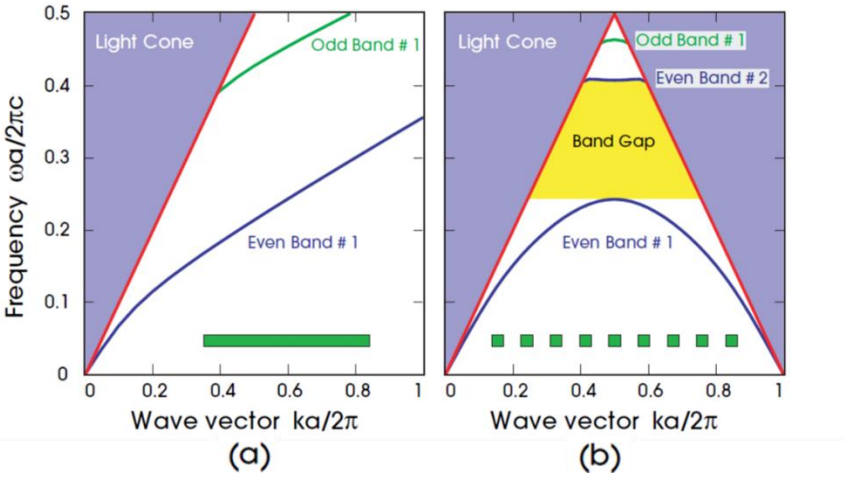

Figure II.3.2 Dispersion band diagram of a) a ridge waveguide b) a photonic crystal with period "a" [19]

After describing the physical and mathematical origin of a band gap we will discuss next the FEM numerical calculation used to optimize the band gap of the proposed PhC design.

II.3.2 Photonic band gap design

As described in the previous part creating a periodic variation of the material permittivity opens a bandgap in the modal band structure. This periodicity can be achieved in several ways; in the proposed design, it is created by etching circular periodic holes inside the core of the HR-Si waveguide presented earlier. For band gap calculations, we used the frequency domain eigenfrequency solver from COMSOL multiphysics 5.2a software[20] which is based on a FEM numerical method. The simulation region contains a one-unit cell of the periodic lattice structure, surrounded by an air box and closed with PML blocks. The cell having the length of one period "a" of the photonic crystal wire is limited by Floquet Bloch periodic conditions from both sides in Z direction with $k_z = \frac{\pi}{a}$. Width (210 µm) and thickness (90 µm) of the cell are the same as the ones corresponding to the previously presented suspended waveguide. We defined in our calculations a real non-dispersive refractive index (n_{Si}=3.4174) for the HR-Silicon and n_{air}=1 for the air medium inside the hole and around the cell. Physics-controlled mesh is used here to set the

mesh size and type. It applies triangular free meshes on the geometry boundaries and free tetrahedral meshes for the intermediate volume.

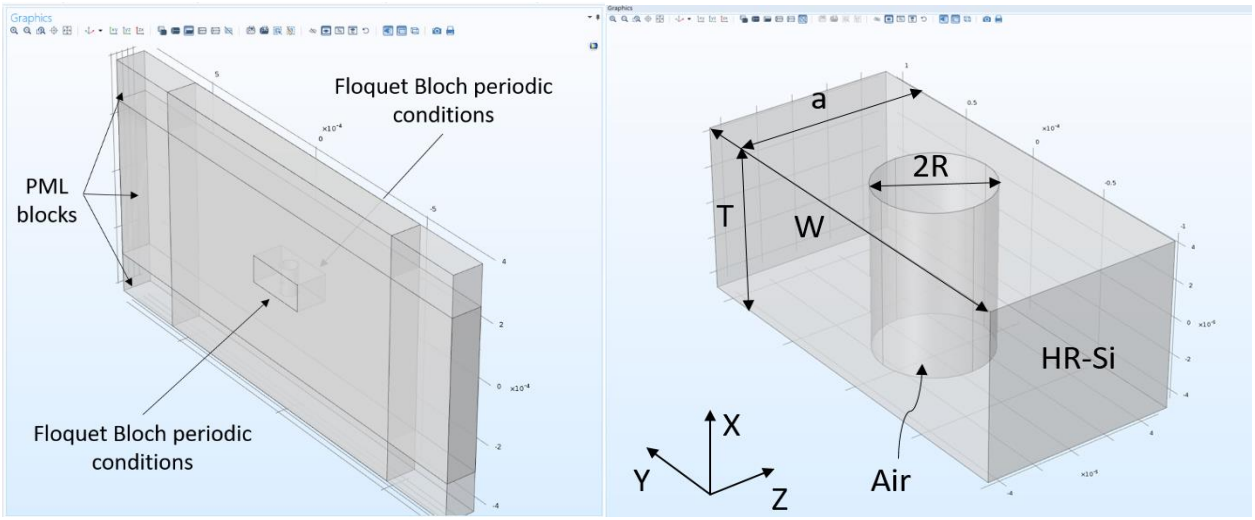

Figure II.3.3 Comsol simulation region on the left. A unit-cell of the periodic structure on the right

The bandgap frequencies are determined by the photonic crystal lattice constant a (period) and the air holes' radius R. The Bragg condition gives the relationship between the period a and the frequency f with $a = \frac{c}{2f n_{Beff}}$, where n_{Beff} correspond to the Bloch mode effective index. Therefore, a Bloch mode with an effective index greater than 1 and less than the effective index of the unpatterned waveguide mode ($1 < n_{Beff} < n_{WGeff} \approx 2.6$ at 600 GHz), corresponds to a PhC period between 95 and 250 µm. To optimize the band gap we made a sweep of the period from a= 90 to 130 µm for three different etching radius R= 27, 28, and 29 µm. Figure II.3.4 plots the eigenfrequencies of the air (red line) and dielectric (black line) modes at the Brillouin zone edge as a function of the lattice constant variation for three different hole radii. These two modes correspond to the splitting of the fundamental E_x^{11} mode in the waveguide with constant permittivity. The fundamental E_y^{11} mode and higher order E_x and E_y modes present also bandgaps at higher frequencies but are not discussed here. The blue line represents the band gap center where the reflectivity achieves its maximum. It is clear from figure II.3.4 how the band gap shifts toward high frequencies by increasing the air hole radius at a constant period (enlarging the low refractive index region) or decreasing the period at a constant air hole radius (reducing the high refractive index region). Figure II.3.5 represents the electric field magnitude of the air mode where the field

is highly localized in the air region and the one of the dielectric mode where it is more confined in the Silicon. The representation of figure II.3.5 corresponds to the band gap edge modes of a PhC structure with a lattice constant a=106.56 µm and an air hole radius R=28µm.

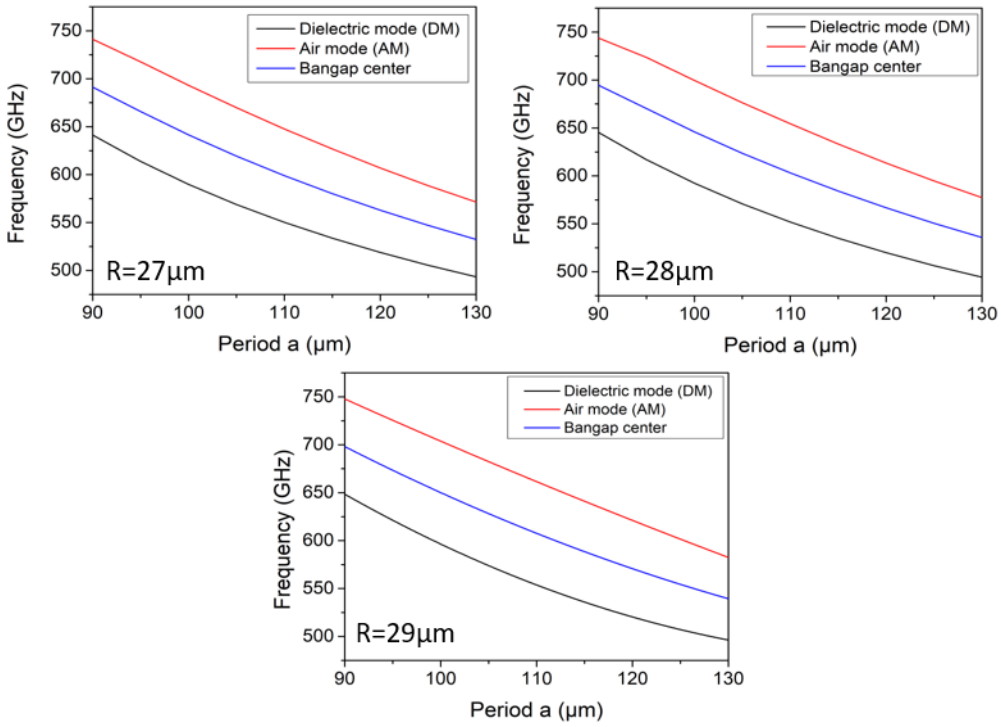

Figure II.3.4 The eigenfrequencies of the air (red line) and dielectric (black line) modes at the Brillouin zone edge as a function of the lattice constant variation for three different hole radii R=27 µm (top left) R=28 µm (top right) and R=29 µm (bottom). The black line represents the bandgap central frequency

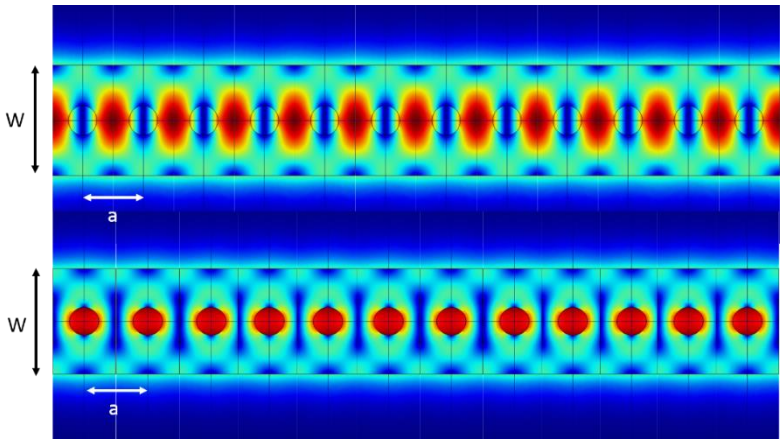

Figure II.3.5 Simulated electric field magnitude of an air mode (bottom) and a dielectric mode (top)

We discussed in this section numerical calculations representing the bandgap adjustments of a PhC structure by controlling its geometrical parameters (lattice constant a, hole radius R). The

parameters corresponding to PhCs with a bandgap in the 600-700 GHz frequency region have been determined. The H_2S molecule considered as a target for the PA gas sensor design has several strong absorption peaks in this frequency region. More details about the strength and absorption frequencies of these molecules are given in chapter V. After the optimization of the bandgap at the frequency region of interest, the design of a high Q resonant cavity at the H_2S absorption frequency will be presented. Before discussing the cavity design we will first introduce two important characteristics of a cavity: its quality factor and mode volume.

II.3.2 Photonic crystal cavity: Quality factor and modal volume

Previously we discussed the designs of perfect photonic crystals, with infinite periodic lattice that creates bandgaps in the photonic band diagram. Once the periodicity of such structure is broken, by removing holes, changing the periodic lattice constant, or even changing the etching radius a defect mode is then created inside this forbidden bandgap. This mode is trapped and confined in the defect region of the PhC, as a resonant mode inside a photonic crystal cavity. If the cavity is ideal and has no losses, the resonant mode would be presented on the frequency spectrum by a narrow discrete peak at the resonant frequency. However, in reality, this is not the case. The confined mode can be dissipated in several ways and thus its resonant peak will broaden assuming a Lorentzian shape. A crucial characteristic of a resonating system is its quality factor which is inversely proportional to the dissipation and losses of the resonant mode. The quality factor Q [19] is a dimensionless term representing the ratio of the energy U stored in the cavity over the lost power P in each cycle:

$$Q = \frac{\omega_0 U}{P} \tag{II.3.8}$$

with $\omega_0 = 2\pi f_0$ corresponds to the angular resonance frequency. It is also expressed sometimes by:

$$Q = \frac{\omega_0}{\Delta\omega} \tag{II.3.9}$$

or

$$Q = \frac{\omega_0 \tau}{2} \tag{II.3.10}$$

where $\Delta\omega$ describe the Lorentzian peak FWHM (full width half maximum) and τ the time constant of the field decay $\left(e^{-\frac{t}{\tau}}\right)$ inside the cavity. In these types of cavities, loss phenomena are divided into two main processes: in-plane and out-of-plane losses. The in-plane losses are governed by mirror strength (reflectivity), material absorption losses, and reflectivity due to the modal mismatch between Bloch's and unpatterned structure modes, while out-of-plane losses refer to the incomplete band gap and coupling to radiative modes (which can also be the result of modal mismatch). Thus we can treat the losses separately by taking:

$$\frac{1}{Q} = \frac{1}{Q_r} + \frac{1}{Q_w} \tag{II.3.11}$$

with Q_w and Q_r the waveguide and radiative quality factor related to the in- and out-of-plane losses respectively. Using HR-Si as the only material in the design helps to reduce the material absorption losses while having a large number of reflective etched holes allows increasing the mirror strength. However, we have to keep in mind that having a very large number of holes would decrease highly the modal transmittance and tends also to increase the modal volumes[21]. The modal volume V corresponds to the geometrical volume occupied by the confined electric field in the real space and represented by:

$$V = \frac{\int \varepsilon \boldsymbol{E}^2 dV}{\max(\varepsilon \boldsymbol{E}^2)} \tag{II.3.12}$$

with E the electric field and ε the permittivity. In some applications such as lasing, it is important to have a low mode volume in addition to the high Q to enhance the spontaneous emission expressed by the Purcell factor which is proportional to Q/V [22]. Therefore, in our design, we chose to have 25 etched holes (N=25), in order to increase Q_w but also to keep a low V. The disadvantage of this kind of wire photonic crystal cavities is their incomplete band gap. Contrarily to 3D photonic crystal cavities with complete bandgap where the trapped mode is confined in the three spatial directions, here the mode is only confined by TIR in one direction and by Bloch's condition in the second. Therefore, the resonant mode can escape the cavity by coupling to radiative modes in the light cone. This phenomenon occurs when the localized electric field inside the cavity has a part of its Fourier transform that falls in the light cone. The advantage of having a fully suspended structure with no material clad is that the light line is pulled up to be far away from the Brillouin zone edges, and thus a smaller part of the electric field in k-space will achieves

the light cone [19], [23]. Radiative losses can be reduced more by gently creating the defect in the structure geometry as explained in[24], [25]. The electric field profile inside the cavity is described by a sinusoidal wave with an envelope determined by the cavity geometry.

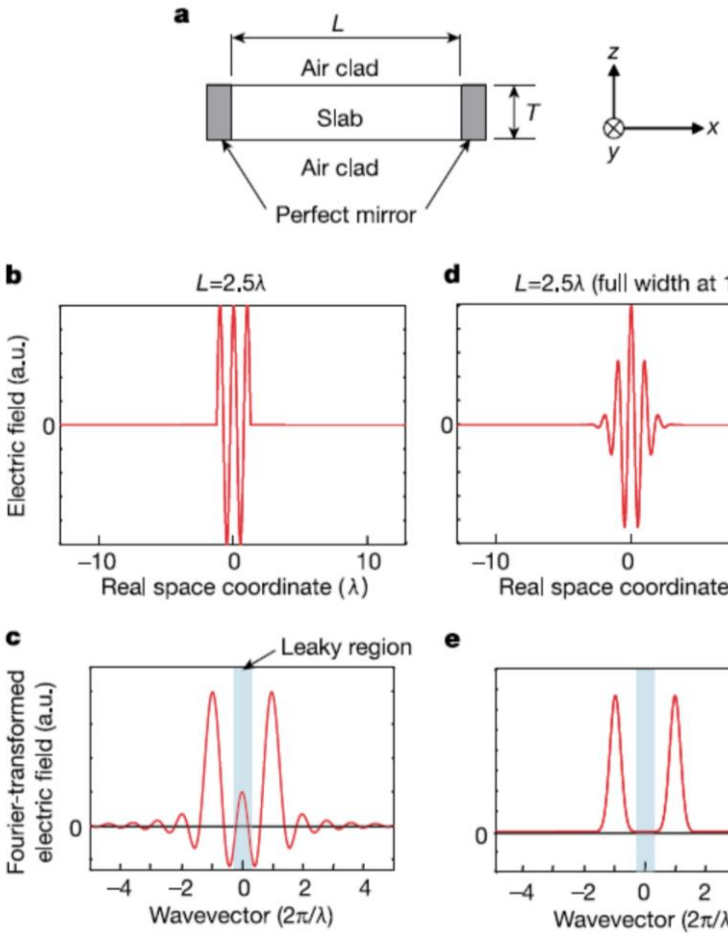

Figure II.3.6. a) Simplified model of a cavity consisting of a dielectric material with thickness T and length L. b, c) The electric field profile inside a cavity with a very short length (2.5λ) and its spatial FT spectra. The leaky region is indicated as a blue area. d, e) The electric field profile with a gentle envelope function (Gaussian curve) and its spatial FT spectrum [26]

The electric field Fourier transform of two different field cavities, one with a rectangular envelope and the other with a Gaussian one are represented in figure II.3.6. It is clear how the function with Gaussian envelope has a Lorentzian shape in k-space with a small part of its tail falling in the leaky region of the lightcone, while the one with rectangular envelope and a Sinc function as Fourier transform obviously leads to substantially stronger leaky wave components. Several mathematical geometrical ways have been proposed to gently create the defect in order to minimize the radiative

loss [23], [27], [28]. In our design, the defect mode was created by applying a parabolic variation of the unit cell period instead of the hole etching radius or waveguide width. Thus the period variation in the design follows the equation below:

$$P_i = P_c + (P_0 - P_c)\left(\frac{i}{\frac{N-1}{2} - 1}\right) \quad \text{(II.3.13)}$$

with P_0 and P_c are respectively the starting and central lattice constant period of the cavity. While P_i corresponds to the varying period between holes, with i going from 0 to $\frac{N-1}{2} - 1$ for a total of N holes with $\frac{N-1}{2}$ periods from both sides of the cavity center.

II.3.3 Photonic crystal cavity design using FEM

The interest in designing a high Q PhC cavity is to confine the THz energy for a long time inside an air hole at the absorption frequencies of the H_2S gas molecule. This THz light trapping for a long time increases the interaction between the light and H_2S molecules and therefore enhances the PA signal detected by the gas sensor. The H_2S is considered an important indicator of food spoilage and it has high absorption peaks at 611.4 and 650.4 GHz. To properly design a PhC cavity with a highly resonant mode that overlaps with the 611 or 650 GHz absorption peak of H_2S, the cavity parameters must be carefully chosen.

As we mentioned previously in this design the defect mode is created by changing the period between the etched holes. In the former case, if the spacing between holes is increased a defect mode is pulled down from the upper band which corresponds to an air mode (see figure II.3.5). Contrarily, by decreasing the spacing a dielectric mode will be pulled up. For gas sensing purposes, we mainly target to confine the mode in the air to favorite the field gas molecules interactions. Therefore, we increased the period following equation II.3.13, symmetrically from the cavity on both sides towards its center. To properly choose the starting and central period, it is important for a photonic crystal with lattice constant P_c, to have an upper air mode at the Brillouin zone edge that overlaps with the frequency of interest of the cavity resonant mode. The central frequency of a band gap has the highest reflectivity, therefore a resonant mode at the band gap center would

have a high Q_w. It is important then to choose a P_0 having a central gap frequency similar to the trapped mode one. Going back to the plots of figure II.3.4 we can extract the proper starting P_0 and central P_c periods of cavities with resonant frequencies at 611 and 650 GHz. A PhC with lattice constant a=106.54 µm (P_0) and an etched hole radius R=28µm presents a band gap with a central frequency of 611 GHz, while the one with a lattice constant of a=120.64 um (P_c) has an air mode at 611 GHz. It should be noted that this interpretation can be done to treat any other design with different P_0, P_c and R and the same target frequency (611 GHz). The dispersion diagrams of these structures are represented in figure II.3.7. These diagrams were calculated using a sweep of the *k* vector in the COMSOL simulation model presented in section II.2.3.

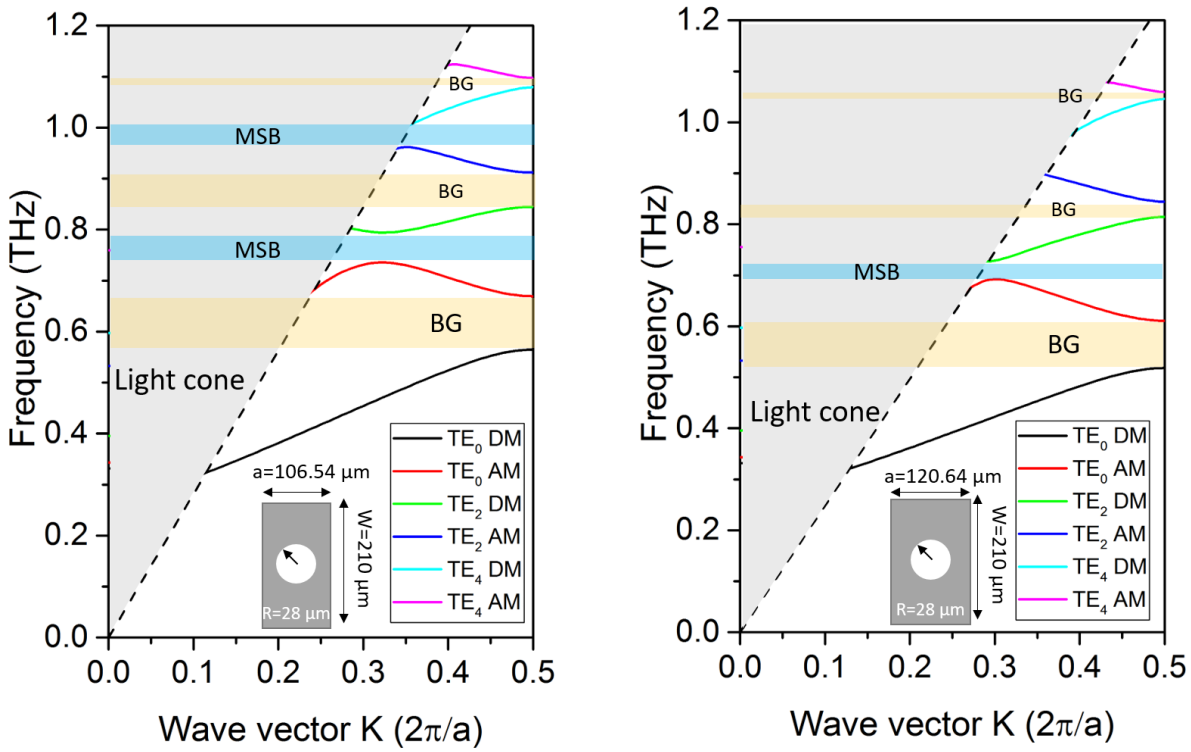

Figure II.3.7 Photonic crystal dispersion diagram for a unit cell structure with a width W=210 µm, thickness T=90 µm, etching hole radius R=28 µm and lattice constant: a=106.54 µm (on the left) and a=120.64 µm (on the right)

However here additional PEC (Perfect Electric Conductor) and PMC (Perfect Magnetic Conductor) boundaries were added to only consider the symmetric E_x modes. Following the same methodology, the parameters of the 650 GHz cavity were also determined. We chose then P_0= 100.1µm and P_c=112.6µm with R=29µm. As shown in figure II.3.4 it is also possible to choose other hole radius and to properly adjust the period in between.

Several bandgaps are observable in the band diagram plots of figure II.3.7. Our interest is concentrated on the bandgap between TE_0 DM and TE_0 AM modes created by the splitting of the fundamental E_x^{11} guided mode. The other bandgaps correspond mainly to higher order modes splitting. As the original waveguide is a multimodal one, additional MSB (Mini Stop Band) is also present and result from the coupling of the fundamental air mode to higher order modes. Such MSB can be interesting in several applications such as bandstop filters with low reflections [29], as the light here is coupled to higher order mode and subsequently to radiative modes instead of being reflected. In our design, this coupling might be an undesired phenomenon as it can potentially introduce additional loss mechanisms. However, these spectral features typical of higher order systems are mostly located at a sufficient frequency spacing removed from the fundamental gap resonance frequency.

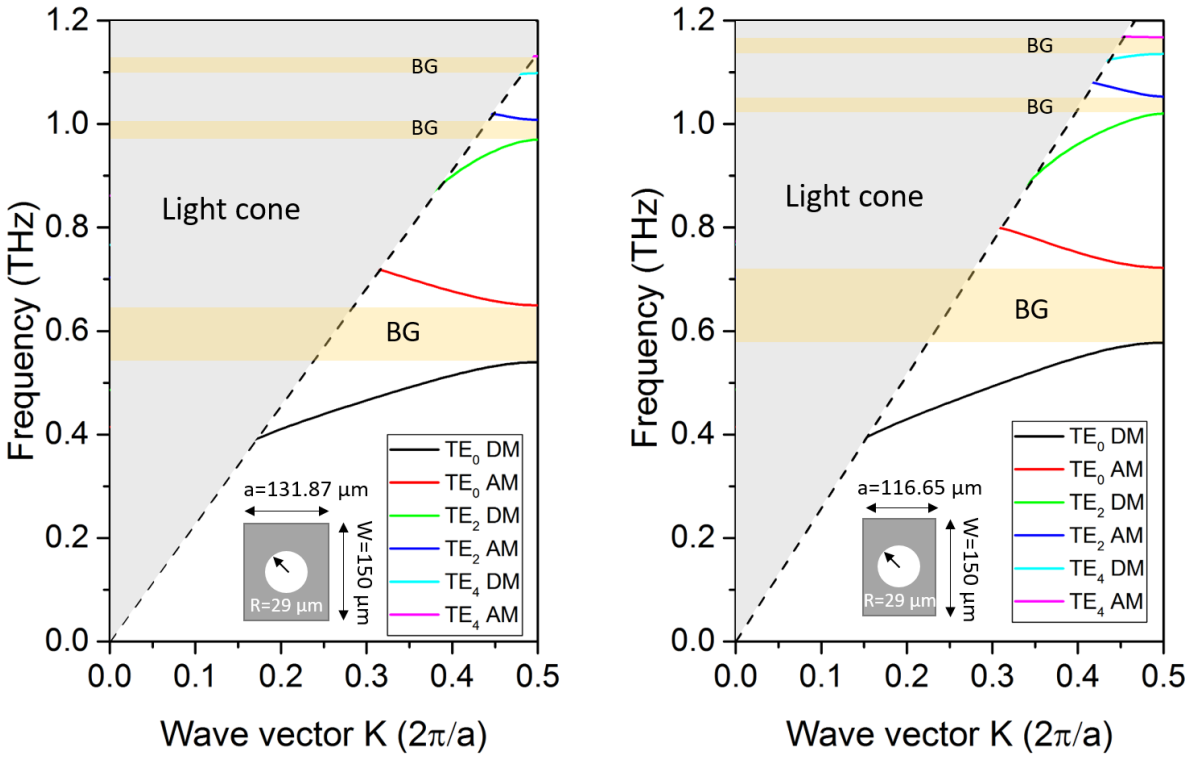

Figure II.3.8 Photonic crystal dispersion diagram for a unit cell structure with a width W=150 µm, thickness T=90 µm, etching hole radius R=29 µm and lattice constant: a=131.87 µm (on the left) and a=116.65 µm (on the right)

To study this coupling effect a similar cavity design with narrower waveguide width that operates in the single mode regime is proposed. To keep on the same HR-SOI wafer with an active region thickness of 90µm, the second design proposed here corresponds to a 90µm thick and 150 µm

large waveguide channel. In a similar way to the previous designs, we found the following parameters for a resonant cavity at 650 GHz: W=150 µm T=90 µm P_0= 116.1µm, P_c= 131.87 µm and R=29µm. Figure II.3.8 represents the dispersion diagram of two PhC with a width of 150µm, hole radius of 29 µm and a lattice constant of 116.65µm and 131.87 µm respectively. The dispersion diagrams of this narrower design are free of MSB. Therefore, no more coupling to higher order mode, however, the light line is closer to the Brillouin zone edge which may increase radiative losses.

3D FDTD simulations are performed and presented in the next section to understand the behavior of the different cavities designs presented in this part.

II.3.3 Photonic crystal cavity design and quality factor calculation using FDTD

The 3D FDTD numerical simulation is a great tool to calculate the resonant frequency and quality factor of the proposed PhC cavities designs. Lumerical FDTD software is used to run these simulations on a cluster computer. The structures are built inside a simulation box with PML boundaries. The PML is set to be far away from the structure in the X, Y direction to prevent the interaction with the field in the cavity, while in the propagation Z direction the cavity wire crosses the PML boundaries to prevent reflections on the edges. A high Q analyzer monitor is used at the cavity central hole to measure the time decay of the electric field. Considering a Q factor in the order of 10^4, the field inside the resonator may take tens or hundreds of ns to totally decay. It is impossible then to measure the Q factor from the frequency domain spectrum because this can take a very long simulation time. Figure II.3.9, represents the time signal decay of the field inside a PhC cavity design with a Q of 47000 for a simulation time of 1ns. A much longer time is required for the field to vanish and thus to be able to calculate the frequency domain spectrum by applying a FT to the simulated time signal. Therefore, this high Q analyzer monitor extracts the quality factor Q from the temporal decay of the field using the formula below:

$$Q = -\frac{2\pi f_R log_{10}(e)}{2m} \qquad \text{(II.3.14)}$$

With f_R the resonance frequency and m the slope of the log of the time signal envelope. This monitor cuts the first part of the measured signal presented by the blue curve of figure II.3.9 which normally corresponds to the source field and measures the slope of the rest (green curve) which is purely describing the cavity mode decay. Dipole electric sources are used to excite the cavity modes within a frequency range of 0.6-0.7 THz. 3 dipoles are arbitrarily placed in the center of the

PhC cavity. A guided mode source, reflecting more closely the experimental conditions, could also be used, however, the calculation error would be higher and a longer simulation time would be required, as the field will take time to get into the cavity due to the high reflective PhC mirror.

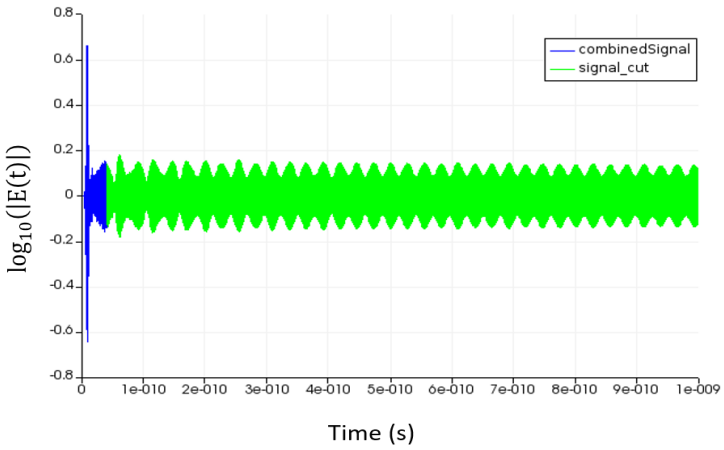

Figure II.3.9 The field decay recorded by the high Q analyzer of Lumerical FDTD (the full recorded signal in green, and the cut source signal in blue)

A 3D modal volume analysis monitor is employed to calculate the cavity mode volume using equation II.3.12. An additional field monitor in the XZ plane is also used to plot the electric field spatial distribution of the confined cavity mode. The calculations were done considering ideal structures with no material loss using n_{Si} =3.4174 and n_{air}=1 and repeated for structures including an imaginary part for the Si refractive index with n_{Si} =3.4174 and $\kappa_{Si}=3\times10^{-5}$ at 650 GHz. The imaginary refractive index was extracted from the measured absorption loss reported in [14] for a HR-Si wafer of 10kΩ resistivity by using the following expression $\kappa_{Si}=\frac{\alpha\lambda_0}{4\pi}$. The numerical errors are governed by the simulation time and mesh size. Therefore, we first run the simulations using a 4µm mesh size in X, Y, and Z directions to reduce the simulation time. However, for the final simulations and to study the convergence of the results, a finer mesh size with 1µm in X, Y and Z was used. The simulation time is always set to 1ns. This time is long enough in order to reduce the numerical errors. Table II.3.1 summarizes the cavity FDTD simulation results with the parameters determined in II.3.2. As represented in Table II.3.1, the resonance frequencies don't correspond to what is expected from the bandgap simulations in II.3.2. In the previous PhC simulations, one lattice constant is considered with infinite periodic conditions. However here the number of periods is set to 24 (25 holes), which explains the blue shift of the resonance frequencies.

Design number	W (µm)	T (µm)	P_0 (µm)	P_c (µm)	R (µm)	N	Material loss (κ_{Si})	f_R (GHz)	Q
1	210	90	106.56	120.65	28	25	0	630	4.7×10^4
1	210	90	106.56	120.65	28	25	3×10^{-5}	630	2.5×10^4
2	210	90	106.56	120.65	29	25	0	636	5.7×10^4
2	210	90	106.56	120.65	29	25	3×10^{-5}	636	3×10^4
3	210	90	100.1	112.6	29	25	0	670	3.7×10^4
3	210	90	100.1	112.6	29	25	3×10^{-5}	670	2.6×10^4
4	150	90	116.65	131.87	29	25	0	669	1.4×10^5
4	150	90	116.65	131.87	29	25	3×10^{-5}	669	4.5×10^4

Table II.3.1 Table representing the quality factors and resonance frequencies obtained by the FDTD simulations for different PhC cavities designs

Using a larger number of holes will give resonance frequencies closer to the expected ones, but this will increase the modal volume, strongly decrease the transmittance, and will also require a very long simulation time. Therefore instead of increasing the number of PhC holes, it is more advisable to shift the bandgap by scaling the periodicities. In our experiments we are using a VDI AMC source with high power in the 630-670 GHz frequency band, thus we focused on optimizing the 650 GHz resonance frequency instead of the 610 GHz one (design 3 and 4). To lower the resonance frequency, the periods between holes should be increased. Therefore, and after several optimizations, we shifted all the periods by 4.10 µm, while keeping the same parabolic variation.

Design number	W (µm)	T (µm)	P_0 (µm)	P_c (µm)	R (µm)	N	Material loss (κ_{Si})	f_R (GHz)	Q	V $\left(\frac{\lambda_0}{n}\right)^3$ $(\mu m)^3$
3.1	210	90	104.2	116.7	29	25	0	650	4.7×10^4	0.76
3.1	210	90	104.2	116.7	29	25	3×10^{-5}	650	2.6×10^4	0.76
4.1	150	90	120.75	135.97	29	25	0	650	1.6×10^5	0.43
4.1	150	90	120.75	135.97	29	25	3×10^{-5}	650	4.7×10^4	0.43

Table II.3.2 Table representing the quality factors and resonance frequencies obtained by the FDTD simulations for the cavities designs with 650 GHz resonant frequency

The results of the 650 GHz resonant cavities are summarized in table II.3.2. Higher order modes also exist at higher frequencies with a lower Q factor. However, here we concentrate on the study of the fundamental mode, as it has the highest Q factor and is highly confined in the cavity center.

Figure II.3.10 represents the electric field magnitude of the fundamental cavity mode for the structure with a width of W=150 µm and W=210 µm respectively.

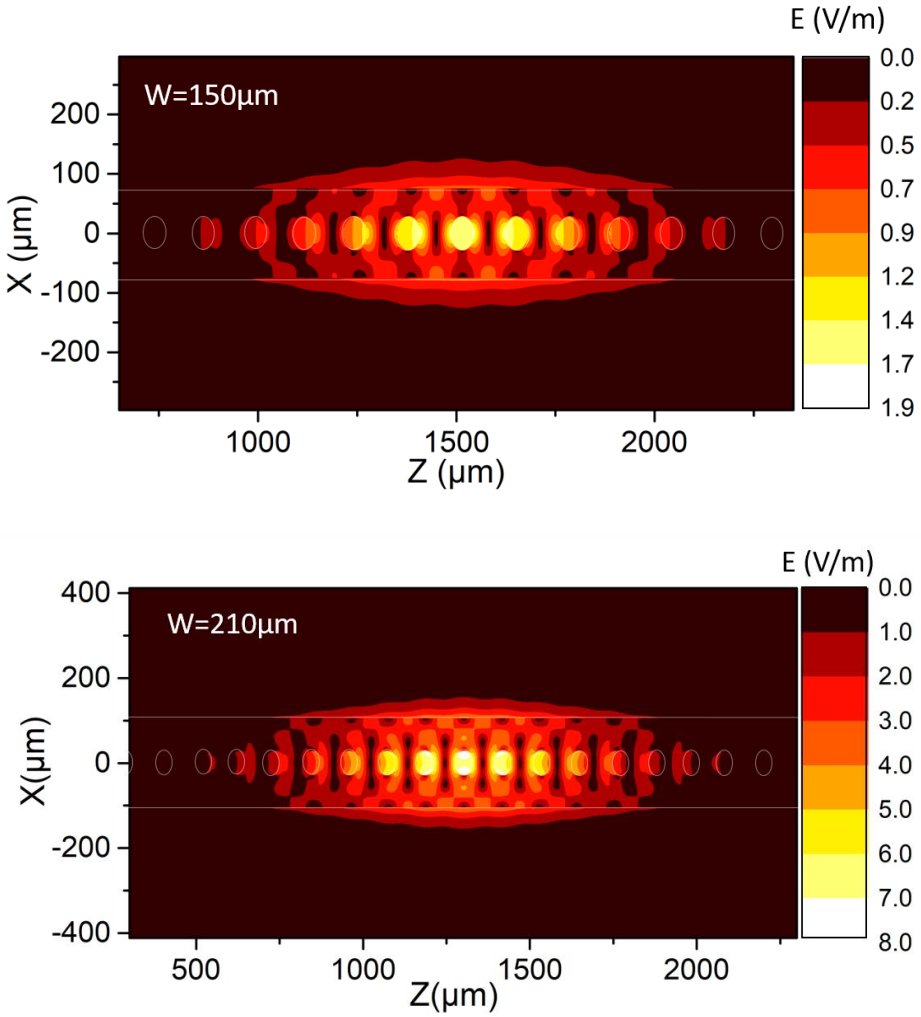

Figure II.3.10 Electric field magnitude of the cavity fundamental mode at 650 GHz for the structure with W= 150µm (top) and W= 210µm (bottom)

II.4. CONCLUSION OF THIS CHAPTER

The design of a PA gas sensor that includes triple resonators to enhance the detected acoustic signal was proposed. The photonic THz part of this sensor is composed of a low loss HR-Si waveguide and a high Q PhC cavity. In this chapter, we concentrate on the numerical calculations of these photonic THz parts. First, the waveguide modal analysis and the simulations of the different sources of losses in the waveguide were calculated. An inverted taper design that feeds the waveguide with very low insertion losses was then presented. In the second part, FEM

numerical method using Comsol multiphysics was used to define the bandgaps of the PhC. Finally, several designs of PhC cavities with resonant frequencies at 611 and 650 GHz and high Q factors in the order of 2×10^4 to 5×10^4were numerically demonstrated. These ultra-high Q factors can be an important added value to improve the light gas molecules' interaction effective length. The experimental results of the waveguide loss extraction and cavities quality factor measurements are reported in chapter IV.

In the next chapter, we will introduce the experimental methods and characterization setups used in chapter IV to characterize the waveguides, PhC cavities, and Poly-Si membrane of the gas sensor design.

II.5. REFERENCES

[1] M. Verstuyft *et al.*, « Proposal for an integrated silicon-photonics terahertz gas detector using photoacoustics », *Opt. Express, OE*, vol. 28, nº 15, p. 22424-22442, juill. 2020, doi: 10.1364/OE.397272.

[2] S. Rienstra et A. Hirschberg, *An Introduction to Acoustics*. 2008.

[3] M. J. Moloney et D. L. Hatten, « Acoustic quality factor and energy losses in cylindrical pipes », *American Journal of Physics*, vol. 69, nº 3, p. 311-314, févr. 2001, doi: 10.1119/1.1308264.

[4] P. M. Morse et K. U. Ingard, *Theoretical Acoustics*. Princeton University Press, 1986.

[5] J. Dai, J. Zhang, W. Zhang, et D. Grischkowsky, « Terahertz time-domain spectroscopy characterization of the far-infrared absorption and index of refraction of high-resistivity, float-zone silicon », *J. Opt. Soc. Am. B, JOSAB*, vol. 21, nº 7, p. 1379-1386, juill. 2004, doi: 10.1364/JOSAB.21.001379.

[6] D. Grischkowsky, S. Keiding, M. van Exter, et C. Fattinger, « Far-infrared time-domain spectroscopy with terahertz beams of dielectrics and semiconductors », *J. Opt. Soc. Am. B, JOSAB*, vol. 7, nº 10, p. 2006-2015, oct. 1990, doi: 10.1364/JOSAB.7.002006.

[7] M. Naftaly et R. E. Miles, « Terahertz Beam Interactions with Amorphous Materials », in *Terahertz Frequency Detection and Identification of Materials and Objects*, Dordrecht, 2007, p. 107-122.

[8] Yasuo KOKUBUN, « High index contrast optical waveguides and their applications to microring filter circuit wavelength selective switch », *IEICE Trans. Electron*, vol. E90-C, nº 5, mai 2007.

[9] C. Pollock et M. Lipson, *Integrated Photonics*. Springer US, 2003.

[10] E. a. J. Marcatili, « Dielectric Rectangular Waveguide and Directional Coupler for Integrated Optics », *Bell System Technical Journal*, vol. 48, nº 7, p. 2071-2102, 1969, doi: 10.1002/j.1538-7305.1969.tb01166.x.

[11] R. M. Knox and P. P. Toulios, « Proceedings of MRI Symposium on Submillimeter Waves, J. Fox, Ed. (Polytechnic Press, Brooklyn, 1970) ».

[12] « High-Performance Photonic Simulation Software - Lumerical ». https://www.lumerical.com/ .

[13] D. Grischkowsky, S. Keiding, M. van Exter, et C. Fattinger, « Far-infrared time-domain spectroscopy with terahertz beams of dielectrics and semiconductors », *J. Opt. Soc. Am. B, JOSAB*, vol. 7, nº 10, p. 2006-2015, oct. 1990, doi: 10.1364/JOSAB.7.002006.

[14] J. Dai, J. Zhang, W. Zhang, et D. Grischkowsky, « Terahertz time-domain spectroscopy characterization of the far-infrared absorption and index of refraction of high-resistivity, float-zone silicon », *J. Opt. Soc. Am. B, JOSAB*, vol. 21, nº 7, p. 1379-1386, juill. 2004, doi: 10.1364/JOSAB.21.001379.

[15] C. Pollock et M. Lipson, *Integrated Photonics*. Springer US, 2003.

[16] G. E. Ponchak, N. I. Dib, et L. P. B. Katehi, « Design and analysis of transitions from rectangular waveguide to layered ridge dielectric waveguide », *IEEE Transactions on Microwave Theory and Techniques*, vol. 44, nº 7, p. 1032-1040, juill. 1996, doi: 10.1109/22.508635.

[17] J. D. Love, W. M. Henry, W. J. Stewart, R. J. Black, S. Lacroix, et F. Gonthier, « Tapered single-mode fibres and devices. I. Adiabaticity criteria », *IEE Proceedings J - Optoelectronics*, vol. 138, nº 5, p. 343-354, oct. 1991, doi: 10.1049/ip-j.1991.0060.
[18] J.-M. Lourtioz, H. Benisty, V. Berger, J.-M. Gerard, D. Maystre, et A. Tchelnokov, *Photonic Crystals: Towards Nanoscale Photonic Devices*, 2e éd. Berlin Heidelberg: Springer-Verlag, 2008.
[19] J. D. Joannopoulos, S. G. Johnson, J. N. Winn, et R. D. Meade, *Photonic Crystals: Molding the Flow of Light - Second Edition*. Princeton University Press, 2011.
[20] « COMSOL: Multiphysics Software for Optimizing Designs », *COMSOL Multiphysics®*. https://www.comsol.fr/ (consulté le mars 05, 2020).
[21] Q. Quan et M. Loncar, « Deterministic design of wavelength scale, ultra-high Q photonic crystal nanobeam cavities », *Opt. Express, OE*, vol. 19, nº 19, p. 18529-18542, sept. 2011, doi: 10.1364/OE.19.018529.
[22] K. J. Vahala, « Optical microcavities », *Nature*, vol. 424, nº 6950, Art. nº 6950, août 2003, doi: 10.1038/nature01939.
[23] E. Kuramochi, H. Taniyama, T. Tanabe, K. Kawasaki, Y.-G. Roh, et M. Notomi, « Ultrahigh-Q one-dimensional photonic crystal nanocavities with modulated mode-gap barriers on SiO_2 claddings and on air claddings », *Opt. Express, OE*, vol. 18, nº 15, p. 15859-15869, juill. 2010, doi: 10.1364/OE.18.015859.
[24] K. Srinivasan et O. Painter, « Momentum space design of high-Q photonic crystal optical cavities », *Opt. Express, OE*, vol. 10, nº 15, p. 670-684, juill. 2002, doi: 10.1364/OE.10.000670.
[25] Y. Akahane, T. Asano, B.-S. Song, et S. Noda, « High- Q photonic nanocavity in a two-dimensional photonic crystal », *Nature*, vol. 425, nº 6961, Art. nº 6961, oct. 2003, doi: 10.1038/nature02063.
[26] Y. Akahane, T. Asano, B.-S. Song, et S. Noda, « High- Q photonic nanocavity in a two-dimensional photonic crystal », *Nature*, vol. 425, nº 6961, Art. nº 6961, oct. 2003, doi: 10.1038/nature02063.
[27] M. Notomi, E. Kuramochi, et H. Taniyama, « Ultrahigh-Q Nanocavity with 1D Photonic Gap », *Opt. Express, OE*, vol. 16, nº 15, p. 11095-11102, juill. 2008, doi: 10.1364/OE.16.011095.
[28] W. Xie *et al.*, « High-Q Photonic Crystal Nanocavities on 300 mm SOI Substrate Fabricated With 193 nm Immersion Lithography », *J. Lightwave Technol., JLT*, vol. 32, nº 8, p. 1457-1462, avr. 2014.
[29] Q. Huang, K. Jie, Q. Liu, Y. Huang, Y. Wang, et J. Xia, « Ultra-compact, broadband tunable optical bandstop filters based on a multimode one-dimensional photonic crystal waveguide », *Opt. Express, OE*, vol. 24, nº 18, p. 20542-20553, sept. 2016, doi: 10.1364/OE.24.020542.

Chapter III:

Experimental setups and methods

CONTENTS

The concept of a new photoacoustic THz gas sensor design based on the implementation of three different resonators was introduced and presented in chapters I and II. In this chapter, the different techniques and experimental setups used for the characterization of the different parts of this sensor will be discussed. The fabrication technique (DRIE etching) and sample preparation are described in a few paragraphs as this work wasn't a part of this thesis. The characterizations of the gas sensor's photonic and acousto-mechanical parts are separately done.

For the THz photonic part, the first step consists in the analysis of the modal behavior of the Si waveguide and the extraction of its propagation losses, insertion losses, … The second step concerns the characterization of the photonic crystal cavities to define their resonance frequencies and quality factors. These measurements have been performed by extracting the S parameters of the different THz components using VNA or by measuring their transmittance with the THz TDS. Other experimental setups based on the use of a THz AMC source and a pyroelectric detector or a bolometric THz camera have also been applied for the same purpose.

Moreover, on the mechanical side, the characterization of the Poly-Si membrane consists of measuring its displacements and resonance frequencies. A commercial Laser Doppler Vibrometer (LDV) (Polytec MSA-500), is used to detect the displacement of the membrane at its resonant frequency. In the absence of gas molecules and photoacoustics, the mechanical resonators (Poly-Si membranes) are actuated by focusing a modulated blue laser on their surfaces. This method is known as the photothermal effect and is quite similar to the photoacoustics. Finally, we also used the Focused Ion Beam (FIB) technique to locally coat the Poly-Si membranes with a metallic reflective layer. This reflective layer is necessary for the optical read-out with the LDV.

All these experimental techniques and setups are described in detail in this chapter.

III.1. FABRICATION PROCESS

The waveguides and cavities fabrication process consists of two etching steps of a high resistivity SOI (Silicon on insulator) wafer. The SOI wafer is composed of 90 µm of HR-Si ($\rho > 10k\Omega.cm$) active layer bonded on a 300 µm thick low resistivity silicon substrate where a 2 µm layer of SiO_2 has been grown by thermal oxidation. The device layer is the guiding channel, which requires one lateral etching to define the waveguide's core width, while its thickness is defined and fixed by

the active layer thickness. The different fabrication steps are represented in figure III.1.1. The wire guide, its anchors, and the PhC crystal holes are etched in a single deep reactive ion etching step (DRIE) with the buried oxide layer as etch stop layer. We used a switched SF_6/C_4F_8 plasma process where etching alternates with passivation, enabling to reach 90 µm depth with a 5 µm resist mask, allowing very good lateral definition for the tiny anchor beams[1]. The process know how has been developed in a joint collaboration between Vmicro and IEMN-NAM6 group. Joint work between Vmicro and IEMN was conducted in the framework of the M-FAB pilot line dedicated to MEMS; this includes the long term recipe development to address the following phenomena in silicon etching:

- Notchless stop of the etching when arriving at the bottom of Device layer
- Management of the Aspect Ration Dependent Etching both on recipes and on the design
- Management of thermal aspects related to processing with high aspect ratio structure, which is far more difficult than standard silicon etching with continuous plasmas at lower thicknesses
- Management of the sidewall slope and low rugosity. These aspects are part of other steps before and after DRIE belonging to Vmicro's know-how.

Typically, the process main feature is the use of fast switching, which enables us to reduce the sidewall roughness down to 50 nm. Using another recipe developed for longer etch times enables backside processing to define the suspended structures (supported by the anchor beams). Once the guiding channel is etched from the top and the back, a final step of HF etching allows to remove the SiO_2 layer. These steps concern the fabrication of the waveguides and PhC cavities, while for the sensor fabrication a step must be added. This step takes place between these two etching processes. After the top side etching that creates the shape of the PhC and guiding channel, we performed a Low Pressure Chemical Vapor Deposition (LPCVD) of Polycrystalline Silicon (Poly-Si), to cover the bottom of the holes with a stretched membrane that represents the mechanical resonator. The Silane gas (SiH_4) concentrations, flow rate, deposition temperature, pressure, and time are adjusted to create a 100 nm of homogeneous Poly-Si stretched membrane with an internal stress $\sigma_i = 50\ MPa$. The Poly-Si membrane deposition is followed by the second etching step to remove the Si and HF etching for SiO_2 release from the backside.

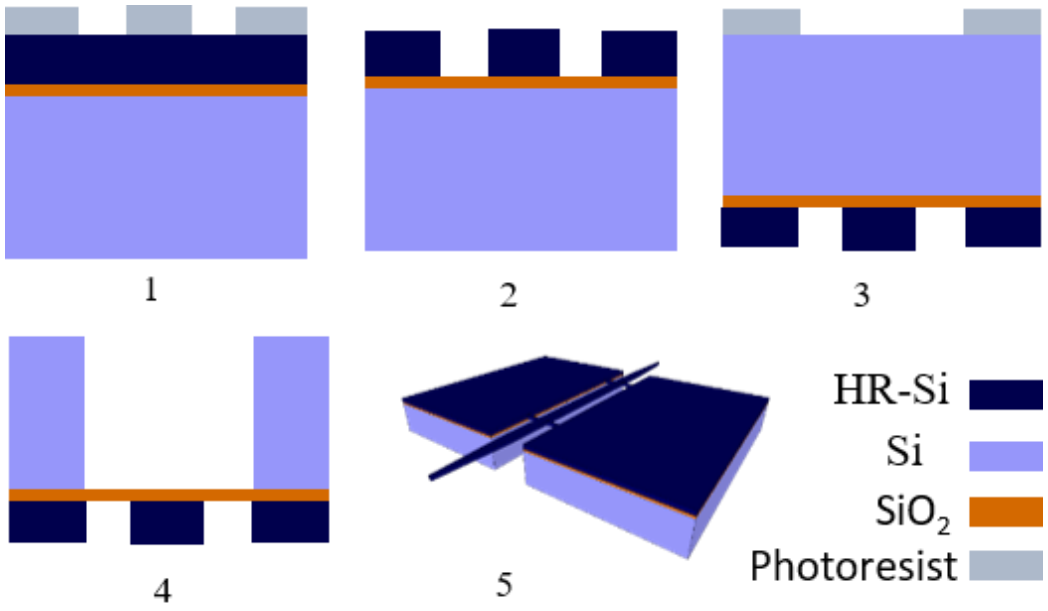

Figure III.1.1 Waveguide and PhC fabrication process steps

The fabricated structures are mounted on a Polylactic acid (PLA) 3D printed holder for easy manipulation and handling in the characterization process. To prevent losses, the plastic holder is grooved under the device's active region. Some of the final results of this process are represented in figure III.1.2, namely: a 38 mm long suspended waveguide with one 90° bend, one photonic crystal cavity, and a 250 mm long waveguide. Figure III.1.3 shows the SEM (Scanning electron microscope) images of the waveguide's tapers and anchors. The SEM images of figure III.1.4 corresponds to the etched holes of the PhC cavities in the presence and absence of the Poly-Si membrane.

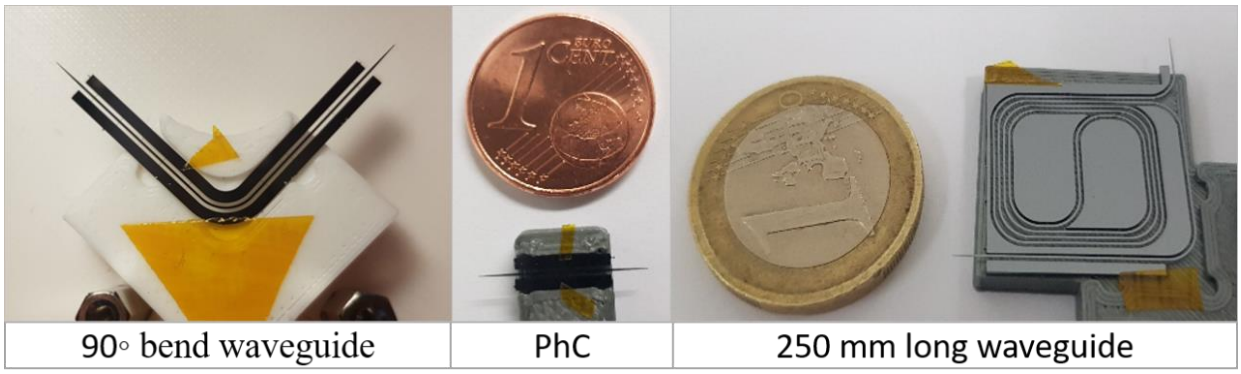

Figure III.1.2 Different structures mounted on plastic holders

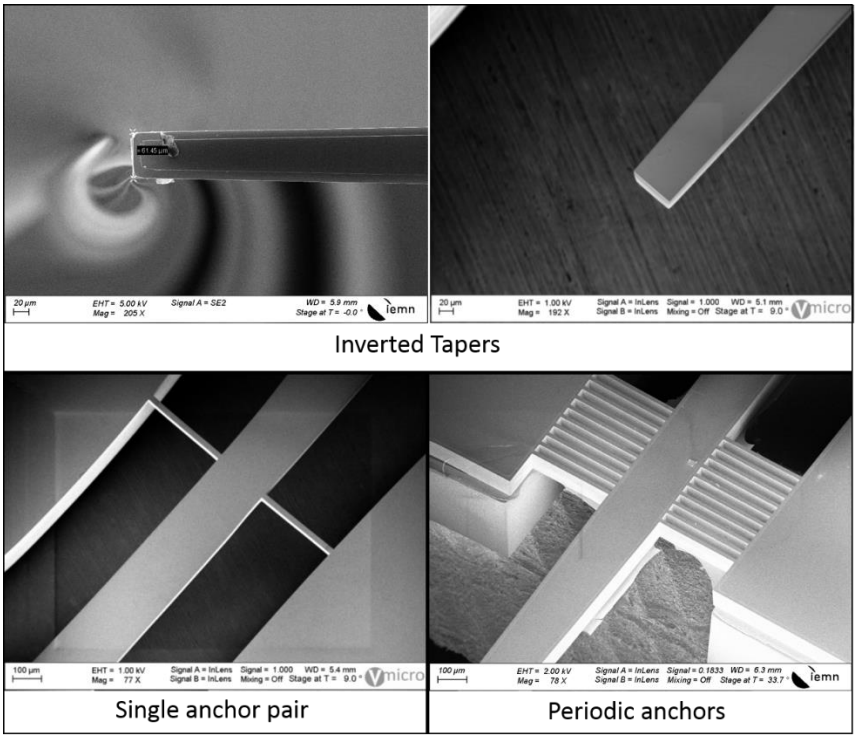

Figure III.1.3 SEM photos of the waveguide's tapers and anchor beams

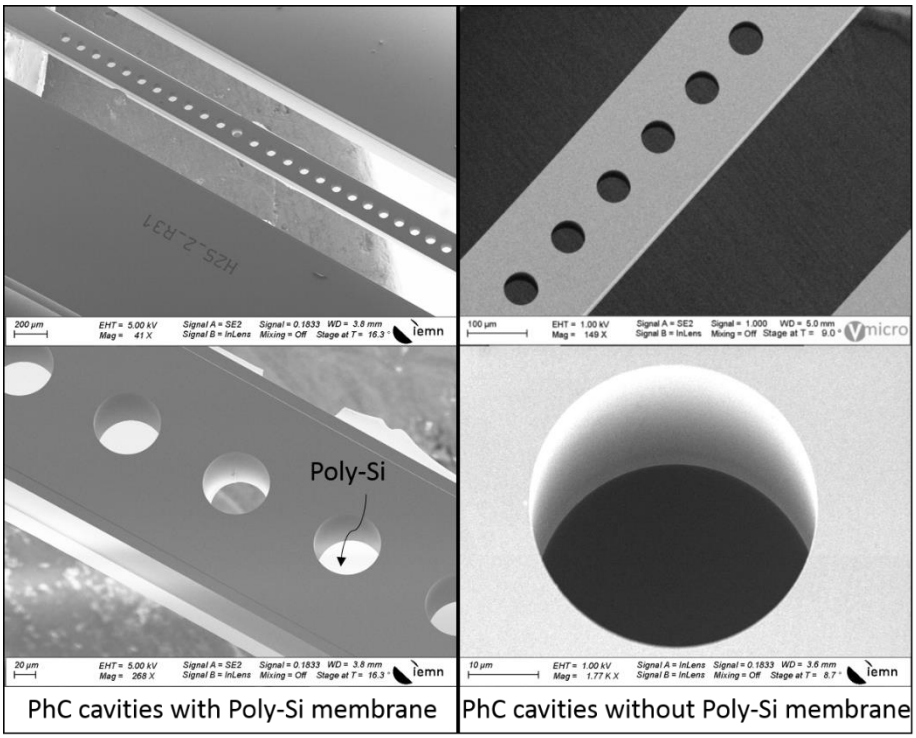

Figure III.1.4 SEM photos of the PhC cavities with and without Poly-Si membrane

III.2. THz ELECTROMAGNETIC CHARACTERIZATION

III.2.1. S parameters extraction using Vector Network Analyzer (VNA)

S parameters are the S-Matrix (scattering matrix) components, that link the different inputs and outputs of any system with N ports. Its scalar equivalent in an optical system is the relationship between the incident reflected and transmitted light passing through a medium. A schematic of a 2 ports S matrix and its optical equivalent is represented in figure III.2.1. Such system is a 2 port system and represented by the expression below:

$$\begin{pmatrix} b_1 \\ b_2 \end{pmatrix} = \begin{pmatrix} S_{11} & S_{12} \\ S_{21} & S_{22} \end{pmatrix} \begin{pmatrix} a_1 \\ a_2 \end{pmatrix} \qquad \text{(III.2.1)}$$

Where a_i and b_i are respectively the complex representations of the incident and reflected wave at the port i.

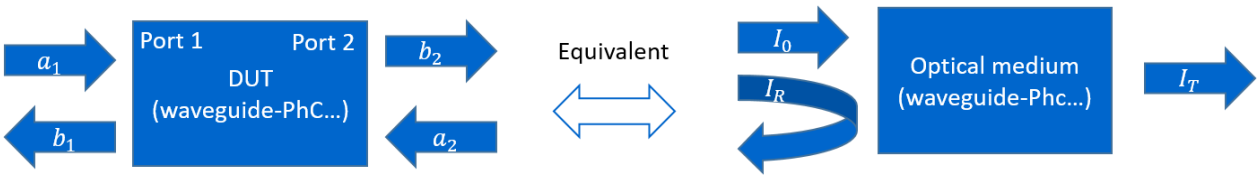

Figure III.2.1 2 ports S parameters model (left) and its scalar equivalent for an optical transmission system (right)

Therefore, the parameters S_{11} and S_{22} represent respectively the complex wave reflections at ports 1 and 2, while S_{21} and S_{12} correspond to the wave transmission from ports 1 to 2 and 2 to 1 sequentially. A vector network analyzer, is a tool allowing to measure both the phase and amplitude of these parameters in the RF and mmW region. Thanks to Vector Network Analyzer extenders (VNAX) those measurements today are possible in the THz region for frequencies up to 1.5 THz [2]. In our experiments, we made 2 ports measurements using a Rohde & Schwarz VNA with two extenders (VNAX) and two metallic waveguide WR-1.5 ports between 500-750 GHz. This technique has several advantages:

- Its large dynamic range (80 dB) allows the measurement of the PhC cavities resonant modes having very low transmission inside the bandgap.
- Its high resolution and fast sweep give the possibility to measure cavities having very high Q factors with a frequency step size of less than 10 MHz in a very short time.

- The VNAX ports are equipped with MWGs at their outputs, making coupling to Silicon waveguides highly efficient with very low insertion losses while conserving the single mode behavior of the Si waveguide (Check section II.2.3).

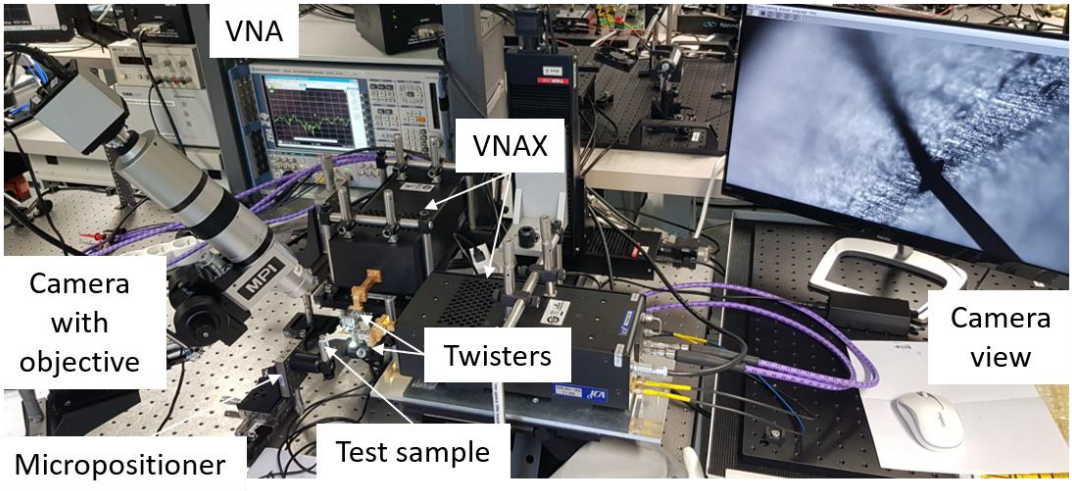

Figure III.2.2 S parameters measurements experimental setup

The experimental setup is represented in figure III.2.2. Polarization twisters are added at the WR-1.5 waveguides ports to match the E_x polarization of the Si waveguides. The measurements are calibrated using a waveguide TRL (Thru, Reflect, Line) method, in the plane of silicon WG injection to correct and remove the impairments from the measurements. As represented in II.2.16, in order to have low insertion losses, the Si waveguide's taper must be inserted for 1 mm inside the WR-1.5 port. For that, we used a camera with an objective or an optical lens with f=50 mm to visualize clearly the input of the WR-1.5 ports. All the samples are mounted on a X, Y, Z micropositioner translational stage to have an accurate control on the sample alignments. This method is highly sensitive and very accurate for waveguide loss extraction and cavities characterizations. However, it is not possible to analyze the modal dispersion of this waveguide using this method, as it has a narrow frequency band and single mode behavior. Therefore, for the waveguide modal analysis, THz-Time Domain Spectroscopy (THz TDS) is a great complementary tool.

III.2.2. THz Time-Domain Spectroscopy (THz-TDS)

THz-TDS is one of the most important spectroscopic tools in the THz region. It is highly used for material characterizations, molecular identifications, and all types of field matter interaction in the THz domain. The TDS usually uses a photoconductive antenna (PCA) or non-linear crystals as a THz emitter and detector. Figure III.2.3 represents the schematic of a TDS where a femtosecond pulsed optical laser, focused on the semiconductor material of the PCA, allows the generation of photocarriers. These photocarriers are accelerated by the DC bias field applied on the dipole antenna and thus a THz pulse is generated. The femtosecond beam is split into two optical paths. While the first part is used to activate the emitter, the second part passes through a mechanical time-delay line toward the detector PCA. The detector illuminated with these femtosecond pulses and receiving the THz pulse allows the measurement of an induced photocurrent at a time t. By changing the position of the translational stage in the delay line path, the THz electric field E(t) profile in the time domain is recorded. Using Fourier transform, the amplitude and phase of the electric field in the frequency domain are determined [3], [4]. The advantage of this technique is its large bandwidth which is defined by the emitter and detector carrier lifetime, and the minimal physical displacement Δx in the delay line. Its coherent nature also provides a high Signal-to-noise (SNR), by detecting only the THz radiation and eliminating the blackbody and other thermal radiations.

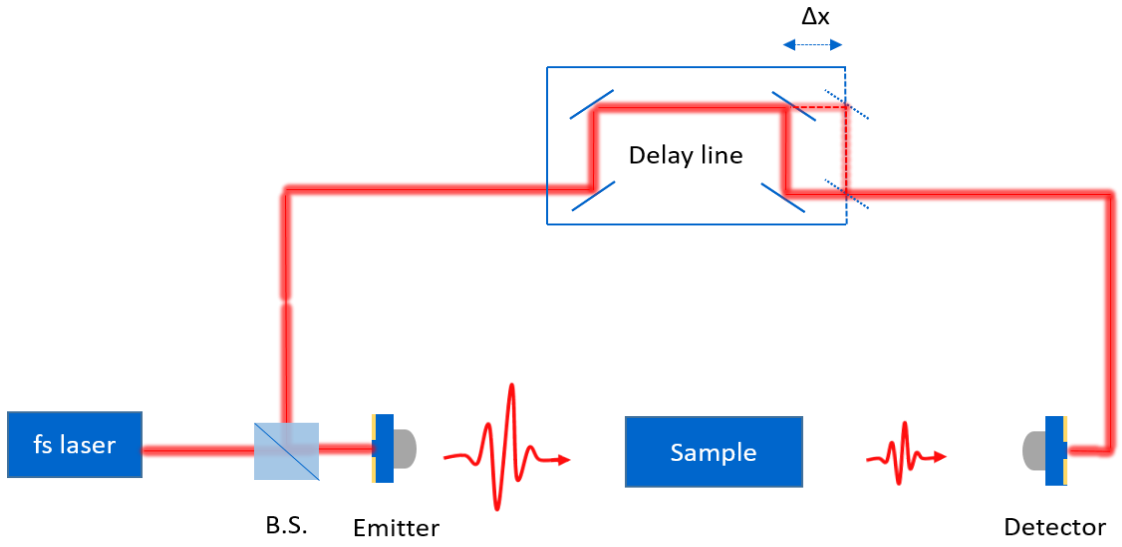

Figure III.2.3 Experimental scheme of a THz-TDS

However, the spectral resolution of this method is limited by the physical length of the delay line. In order to achieve a frequency step size $\Delta f = 10\ MHz$, a very long delay line $l = \frac{c}{\Delta f} = 30\ m$ is necessary. In our measurements, a commercial MenloSystems THz-TDS was used. To couple the THz signal to the waveguides and PhC cavities, a 4 lenses configuration is used in order to focalize the beam at the tapers' ends. Such configuration has higher insertion losses than coupling from a MWG, which makes the VNA a better option for loss extractions. However, the advantage of this free space coupling and large frequency band measurement is that it allows the excitation of higher order modes and gives a clear interpretation of the waveguide multimodal behavior and dispersion. To prevent the detection of the non-guided undesired signal, only 90° bent structures are measured. Figure III.2.4 represents the experimental setup where the emitter, detector, and lenses are mounted on 2 rails with a central rotating connector in between. This will serve to make the beam alignment in a straight configuration, then make a 90° rotation to keep a right angle between the emitter and detector. Further details on the alignments and measurements are discussed in the results and interpretations part (chapter IV).

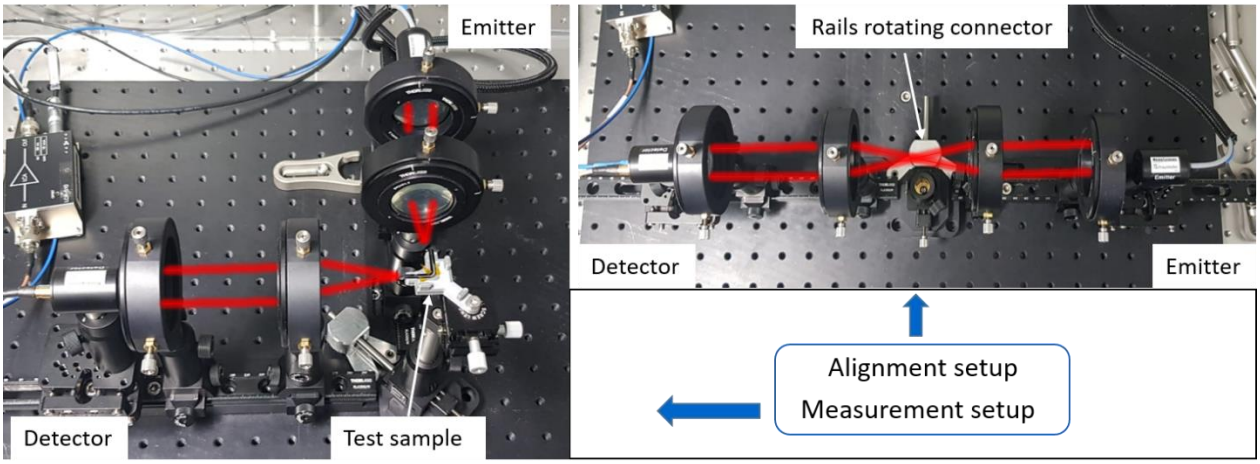

Figure III.2.4 TDS experimental measurement setups used for the beam alignment, and for the measurements

III.2.3. Setups used for THz transmission measurements and mode imaging using AMC VDI source

At some point during the work period of this thesis, a technical problem with the VNAX WR1-.5 port of the VNA has occured. Therefore, it wasn't possible to characterize some of the PhC crystal cavities. The use of the TDS for this purpose wasn't either helpful, due to the lack of resolution

and the complexity of the free space THz coupling (cavities fabricated on straight waveguides). It was then necessary to find a solution, that allows us to measure the cavities resonance frequencies and quality factors. For that we built an S_{21} measurements setup, using a VDI AMC source and synchronized detection by a Pyroelectric detector [5] (THZ10 from SLT) and a lock-in amplifier [6] (HF2LI Zurich instruments).

AMC 643, is an amplifier multiplied electronic chain source fabricated by VDI. This chain is composed of several frequency doublers and a tripler Schottky diodes, that multiply an RF signal by a factor of 48. With the combination of amplifiers, this source provides an output of 1 to 2 mW power at 630-670 GHz frequency band. Despite its tight operational frequency band, this THz source can be very useful since it operates at room temperature with quite high power and compact size. Its WR-1.5 guided output makes it compatible with our integrated sensor design. To prevent the source damage due to high reflections, we added an isolator at an earlier stage of the multiplication chain (WR-5.1 140-220 GHz). A plot representing the measured THz output power of the source as a function of its emission frequency is illustrated in figure III.2.5(a). This plot is measured after the addition of the isolator in the electronic chain. Figure III.2.5(b) shows a photograph of this VDI AMC source. A TTL amplitude modulation feature is also available for this source, which makes the synchronized detection possible without the necessity of external modulation. This source isn't only used for the S_{21} measurements, but it serves for several experiments and mainly to feed the photoacoustic gas sensor.

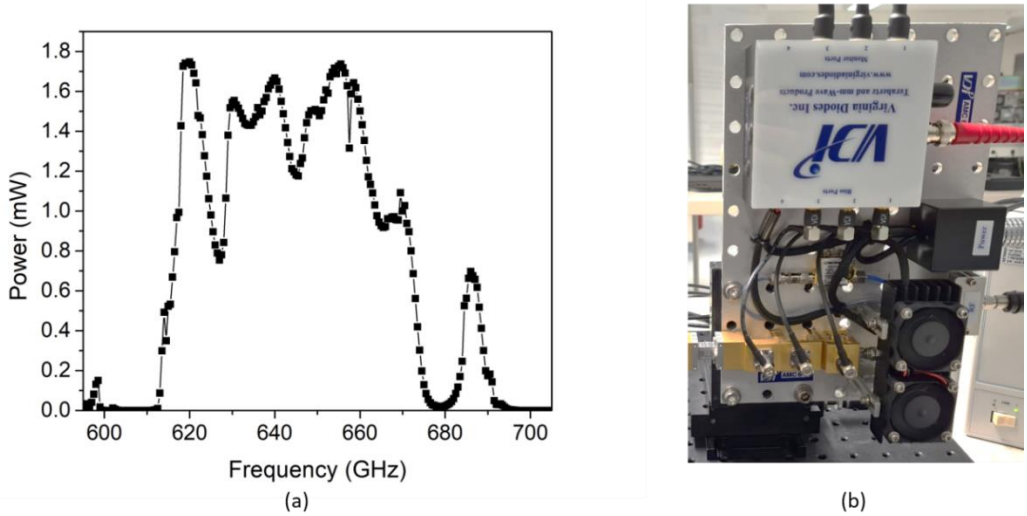

Figure III.2.5 (a) A plot of the VDI AMC source THz output power as a function of its emission frequency. (b) Photograph of the VDI AMC source

The use of a pyroelectric membrane for the THz detection has several advantages such as: working at room temperature, large bandwidth, synchronized detection that eliminates the background, and the most important is its large active area that allows collecting the signal without the need of beam focusing. The main issue with these detectors is the thermal detection principle that makes them highly sensitive to thermal fluctuations and acoustical waves (microphone effect). Such detectors can have a fast response, however, to increase the SNR the detection system must be coupled to an amplifier (LPF) with a very small bandwidth. Therefore, a long integration time is necessary. Figure III.2.6 represents the experimental setup. A waveform generator is used to apply a 0-3.5 V square waves on the TTL port of the THz source which is modulated electronically. The modulation frequency is set to 13 Hz, at which the pyroelectric membrane is highly sensitive. A lock-in amplifier is used to synchronize the detection, by using an external reference from the same waveform generator used to modulate the THz source. The current variation detected by the Pyroelectric detector is converted into a voltage signal through an amplifier (OAP), which is sent to the lock-in input. The lock-in amplifier multiplies the input and reference signal, then extracts the phase and amplitude of the detected signal by phase sensitive detection PSD. As mentioned previously the advantage of such synchronized detection is that it extracts information from a noisy signal by using a relative defined reference signal at the same frequency. The source RF input signal is generated by a Synthesizer at 13.13-13.96 GHz with a 0 dBm power.

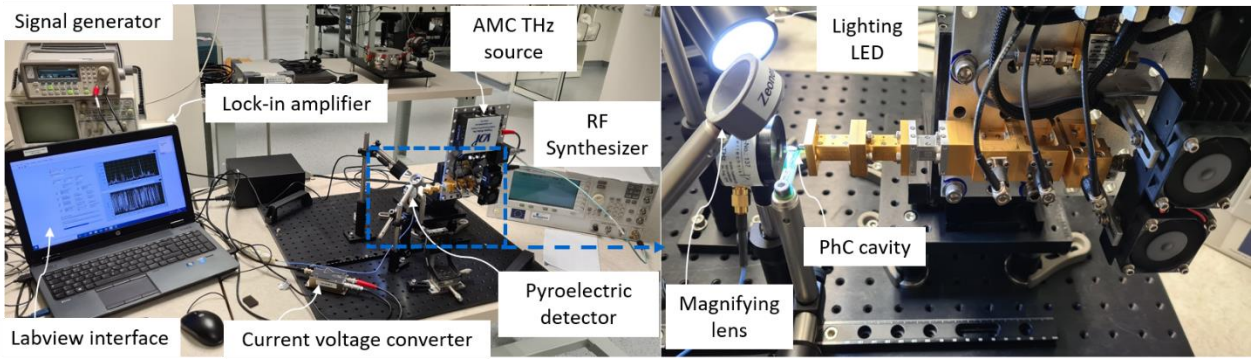

Figure III.2.6 S21 measurements experimental setup using AMC source and pyroelectric detector

The full setup is controlled with a LabVIEW [7] interface. It allows to sweep the Synthesizer RF frequency and thus the THz AMC source frequency by defining a frequency bandwidth and stepsize. At each frequency step, the LabVIEW software waits for a time t, before importing the demodulated phase and amplitude by the lock-in. This time t is controlled and defined by the integration time (τ) or lock-in LPF cut-off frequency (f_c). The waiting time t must be longer than

the integration time $\tau = \frac{1}{2\pi f_c}$. Therefore, for highly sensitive detection of some µV power, very long measurements time (up to 5s/measured point) is required. Similar to the VNA measurements, the alignments are made using a magnifying lens and a microcontroller stage. This technique has proven to be useful and efficient for S_{21} measurements, however, for high SNR it is largely time consuming.

In another experimental setup, instead of using the pyroelectric detector for the S_{21} measurements, a THz bolometric camera developed by I2S [8] is used to image the waveguide output mode and to qualitatively verify the insertion loss simulated in II.2.3. Without modulation and at room temperature, this camera, whose sensitive area is composed of an antenna-coupled micro-bolometer array detects and plots the THz field with a resolution of 320x240 pixels.

III.3. MECHANICAL CHARACTERIZATION

III.3.1. Laser Doppler Vibrometer (LDV)

The sensor response to gas detection is defined by the Poly-Si membrane displacement. Therefore, to determine the concentration of the detected gas, a sensitive vibration read-out system is necessary. A commercial laser doppler vibrometer (LDV) (MSA-500 Polytec) is used for this purpose. The advantage of this detection technique is its non-contact and non-destructive method, which consists in the determination of the Doppler frequency shift of a laser beam reflected on the movable object under test (Poly-Si membrane). When a laser beam hits the object in movement (membrane), it scatters and reflects back with a frequency shift known as the Doppler effect. The frequency shift $f_d = 2\frac{v}{\lambda}$ is proportional to the velocity v of the object in movement, where $\lambda = 630\ nm$ corresponds to the laser beam wavelength. Therefore, it is possible to measure the object displacement by simply measuring this frequency shift f_d. To detect this frequency shift, LDV uses a photodetector that measures the intensity I of the signal resulting from the interference between the reflected beam and a reference beam with the respective intensities I_1 and I_2.

The detected intensity I is represented by:

$$I = I_1 + I_2 + 2\sqrt{I_1 I_2 \cos 2\pi\left(\frac{r_1 - r_2}{\lambda}\right)} \qquad \text{(III.3.1)}$$

The third term (interference term) depends on the two beams' optical path difference which is related to the displacement of the object under test.

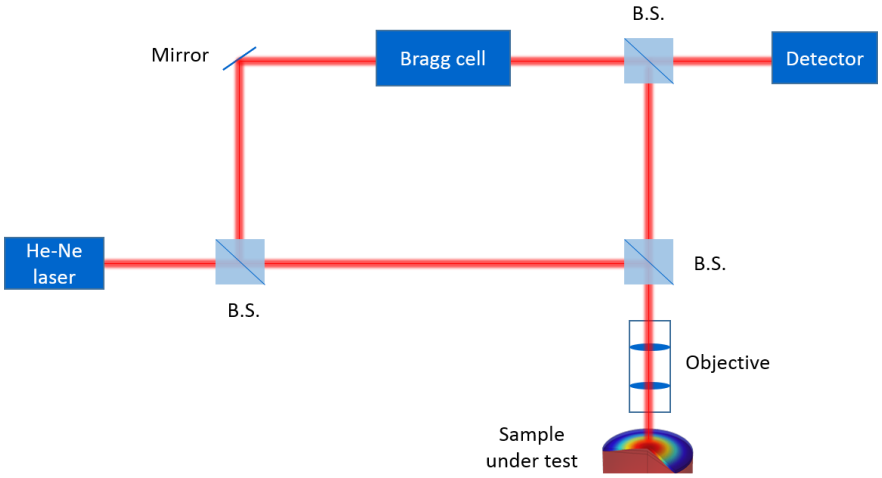

Figure III.3.1 LDV optical setup

The measurement and reference beams of the LDV optical setup are represented in figure III.3.1. To determine the displacement direction, additional frequency modulation is added to the reference beam using an acousto-optical modulator (Bragg cell). This vibrometer has several optical objectives with different magnifications (x5 x10 x100) that provide a microscopic view of the sample and focus the measuring laser beam to very small diameters (< 1 µm). It has a very high displacement resolution (< 0.4 $pm/\sqrt{Hz}$) at working frequencies up to 2 MHz. High frequencies measurements up to 24 MHz with high sensitivity (< 0.1 $pm/\sqrt{Hz}$) are also possible.

III.3.2. Modulated blue laser for membrane's mechanical modes optical excitation

The mechanical characterization process is represented by the actuation of the Poly-Si membranes and the detection of the resonant frequencies of their eigenmodes. Several techniques have been used in the past years for MEMS and NEMS actuation. Piezoacoustics is the most common. It consists of using a piezoelectric material in contact with the resonator. Thanks to optics, other non-contact, non-destructive, and high frequencies operational techniques have been demonstrated. The use of a modulated light beam for the mechanical excitation of a circular thin membrane was reported in 1981 by [9]. This technique is based on the photothermal (PT) effect. The latter is well known and quite similar to photoacoustics (PA) which is the main topic of this thesis. From

equations, I.4.4 and I.4.11 represented in chapter I, a modulated laser beam absorbed by a material is followed by the generation of periodic heat. The generated heat is expressed by a thermal gradient inside the material followed by a bending moment. The PT effect was used in the excitation of monolayer mechanical resonators such as membranes or cantilevers [9]–[12]. It has a higher impact on the excitation of bilayer resonators [13], [14], where the bimorph bending effect is dominant due to the difference in thermal expansion between the two layers of different materials. Because of the several advantages cited here, the PT technique is applied for the actuation of the Poly-Si membranes in the mechanical characterization experiments. A modulated fibered blue laser diode (λ=405 nm) is used for this purpose. The choice of this laser is due to the high absorbance of the Poly-Si at this wavelength compared to longer ones [15]. A comparison of the performance between a red and blue laser used in the PT excitation of a single-crystalline Si cantilever was reported in [12]. Higher mechanical bendings were observed with the blue laser compared to the red one. The fibered blue laser output is collimated then modulated in a free space electro-optic amplitude modulator. This modulator is composed of two Lithium Niobate crystals that employ the Pockels effect. The crystal's birefringence is proportional to the applied voltage. Therefore, the light polarization variation traversing these crystals is proportional to the modulation of the applied electric field. By adding two polarizers at the input and output of the modulator, the polarization variation results in amplitude modulation of the laser beam. A full amplitude modulation corresponds to a π phase shift of the light beam. In order to produce this phase shift, a high half-wave voltage V_π up to 120 V (for λ=405 nm) must be applied to the EO crystals. The applied voltage is generated by a Zurich lock-in amplifier, then amplified using a high voltage amplifier (HVA). This lock-in is also used for the synchronized detection of the MEMS displacements detected by the LDV. The EOM permits the modulation from DC up to 100 MHz, however, the upper-frequency level is limited by the bandwidth (DC to >500 kHz) and slew rate (400V/µs) of the HVA. After modulation, the laser beam is collected using a collimator then injected inside a SM fiber. The fiber allows guiding the beam toward the test sample placed on a stage in the transversal plane under the LDV. A collimator is connected to the fiber end followed by an achromatic doublet lens with a focal length f=43.4mm. This optical lenses system converges the beam waist into a small spot size with a diameter < 10µm, while keeping a long working distance. As the LDV laser beam has a normal incidence, the blue laser fiber is inclined with an incidence angle of 45 and 60 °.

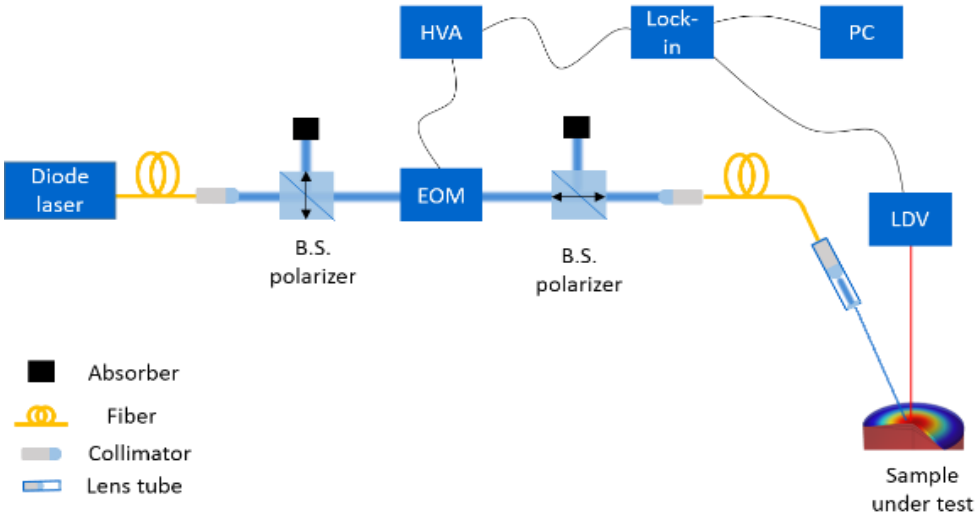

Figure III.3.2 Schematic of the PT excitation and LDV detection setup

Figures III.3.2 and III.3.3 represent a schematic and a photograph of the photothermal optical excitation and LDV setup. After passing through all these optical components, only 0.7 mW of the 10 mW optical power generated by the laser source reaches the sample under test. However, this 0.7 mW is highly enough to excite the membranes or any other MEMS such as Si cantilevers.

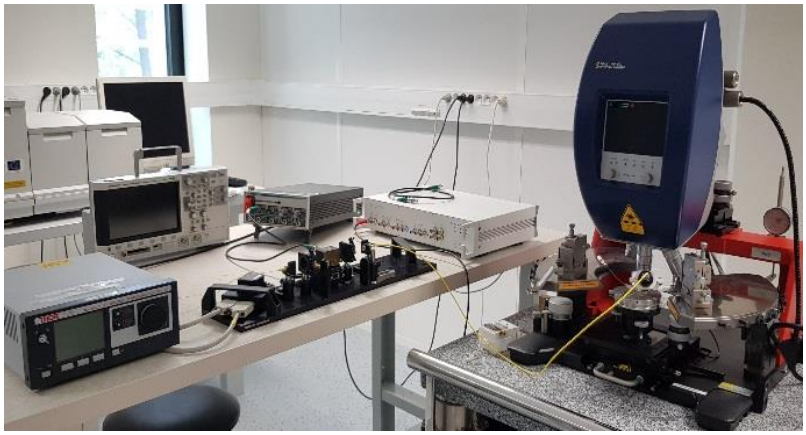

Figure III.3.3 Photograph of the PT excitation and LDV detection setup

III.3.3. Focused Ion Beam (FIB) and Scanning Electron Beam (SEM)

Since the optical non-contact methods used for vibrometry such as LDV retrieve the displacement information from the reflected and scattered laser beam on the surface of a movable object, therefore the object under test must be reflective at the laser's wavelength. The LDV used for the characterization of the Poly-Si membranes is equipped with a He-Ne laser (λ=630 nm). At this wavelength, a very thin layer of Poly-Si (100 nm) is transparent [16]. Therefore, in order to

measure the displacement of the membrane with this LDV, an additive reflective metallic layer is necessary. Several metallic deposition techniques such as Chemical Vapor Deposition (CVD), Molecular Beam Epitaxy (MBE), Physical Vapor Deposition (PVD) could be used for this purpose. However, with these techniques, all the structure is covered with the metal layer and not only the mechanical resonator. The presence of a metallic layer on the THz guiding channel is undesired, as it can lead to high ohmic losses. Therefore, a local metal deposition only on the surface of the Poly-Si resonator is necessary. Using the previously cited techniques for this purpose is complicated and requires additional lithographic steps. To avoid this, a local deposition using the Focused Ion Beam (FIB) is useful [17]. Quite similar to a Scanning Electron Beam (SEM), a FIB uses an accelerated focused ion beam instead of an electron beam to generate secondary electrons after the interaction with a sample in a way to image its surface. This imaging process is possible while using a low ions current, however for higher current and since ions are heavier than electrons, they sputter atoms from the sample surface, resulting in an etching phenomenon. In presence of a precursor gas such as Tungsten hexacarbonyl ($W(CO)_6$) or trimethylplatinum ($C_9H_{16}Pt$), ions react with the gas molecules and decompose them leading to a deposition of a metallic layer such as Tungsten (W) or Platinum (Pt) in presence of $W(CO)_6$ or $C_9H_{16}Pt$ respectively. In our experiments we used the FEI-STRATA DB235 FIB/SEM shown in figure III.3.3 to make a Pt deposition. It combines a FIB with an SEM and a gas injection system (GIS) inside a vacuum chamber. The ion beam gun is inclined making an angle of 52° with the vertical SEM column. It contains a tungsten needle with a liquid metal Gallium (Ga) inside. The needle is heated at the melting point temperature (29.8°C) of the Ga allowing the Ga^+ ions generation. Ions are accelerated through a voltage applied between the needle tip and an extraction electrode.

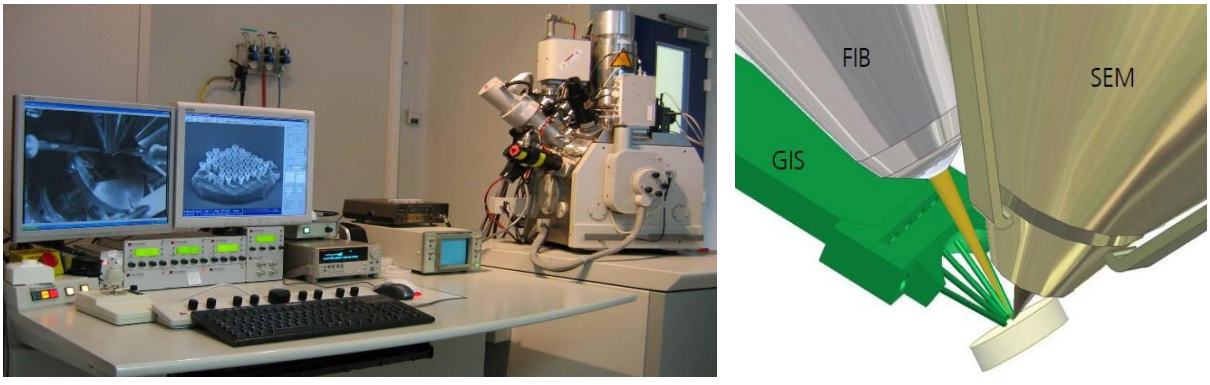

Figure III.3.4 FIB/SEM photo at IEMN cleanroom on the left and schematic representing the position of the FIB,SEM and GIS inside the vacuum chamber on the right [18]

This needle is followed by a beam focalization system, that allow to achieve very small spot diameters of some nm. The advantage of this technique is that it can go close to the surface and locally metalize very small regions by scanning the ion spot over the surface of interest, and without any necessity for lithographic steps. However, this method has a non-uniform and inhomogeneous deposition behavior. The deposed metal layer can also contain some organic residues which make it less pure than the ones grown with other techniques such as CVD and PVD. Several parameters such as dwelltime, beam intensity, deposition surface, deposition time, and overlap play a role in growth control and layer dimensions determination. In all our depositions the dwell time (time of the ion beam stay at each scanning point) is fixed to 0.2µs and the overlap (overlap between scanning points described by the relation $\frac{d-a}{d}$ where d represents the spot diameter and a the distance between scanning point) to -200%, while the rest of the parameters are adjusted in a way to control the Pt layer dimensions. After the metallization with the FIB, microscopic images (similar to the one presented in figures III.1.3 and III.1.4) of the structures were taken using the SEM.

III.4. CONCLUSION OF THIS CHAPTER

This chapter presented the different experimental setups dedicated to the characterization of the waveguides and PhCs cavities designs proposed in this work. In the first part, we briefly described the technological process used by Vmicro (our collaborator in the Terafood project) for the fabrication of these THz components and the final gas sensor design. We then presented the different measurement techniques used to extract the propagation losses of the waveguide, analyze its modal behavior and define the resonant frequencies and quality factors of the PhC cavities.

In the final part, the steps of the mechanical characterization of the Poly-Si membrane are illustrated. It starts with a description of the method applied for the mechanical excitation of the Poly-Si resonators, followed by the optical system that allows to detect their mechanical motions. Finally, the FIB metallization technique used to coat the Poly-Si membranes with Pt metal layer is introduced. The results of the measurements based on these experimental setups and techniques are presented in chapter IV.

III.5. REFERENCES

[1] F. Laermer and A. Schilp, “Method of anisotropically etching silicon,” US5501893A, Mar. 26, 1996.
[2] “Vector Network Analyzer Extension Modules (VNAX).” https://www.vadiodes.com/en/spectrum-analyzer-extension-modules-sax.
[3] J. Neu and C. A. Schmuttenmaer, “Tutorial: An introduction to terahertz time domain spectroscopy (THz-TDS),” *J. Appl. Phys.*, vol. 124, no. 23, p. 231101, Dec. 2018, doi: 10.1063/1.5047659.
[4] N. M. Burford and M. O. El-Shenawee, “Review of terahertz photoconductive antenna technology,” *Opt. Eng.*, vol. 56, no. 1, p. 010901, Jan. 2017, doi: 10.1117/1.OE.56.1.010901.
[5] pyrosensor de Redaktionsteam, “THZ10.” https://www.pyrosensor.de/Standard-924644.html.
[6] “50 MHz Lock-in Amplifier | Zurich Instruments.” https://www.zhinst.com/europe/en/products/hf2li-lock-amplifier.
[7] “LabVIEW 2020.” https://www.ni.com/fr-fr/shop/labview/labview-details.html.
[8] “TZcam the camera intégrating Terahertz Imaging sensor designed by i2S - i2S.” https://www.i2s.fr/en/imaging-solutions/specific-cameras-for-the-visible-and-invisible/tzcam.
[9] E. Dieulesaint, D. Royer, and C. Bonnefoy, “Mechanical Excitation of a Membrane by an Optical Beam.,” in *1981 Ultrasonics Symposium*, Oct. 1981, pp. 802–805, doi: 10.1109/ULTSYM.1981.197733.
[10] R. J. Dolleman *et al.*, “Optomechanics for thermal characteri-zation of suspended graphene,” *Phys. Rev. B*, vol. 96, no. 16, p. 165421, Oct. 2017, doi: 10.1103/PhysRevB.96.165421.
[11] D. Miller and B. Alemán, “Spatially resolved optical excitation of mechanical modes in graphene NEMS,” *Appl. Phys. Lett.*, vol. 115, no. 19, p. 193102, Nov. 2019, doi: 10.1063/1.5111755.
[12] S. Nishida, D. Kobayashi, H. Kawakatsu, and Y. Nishimori, “Photothermal excitation of a single-crystalline silicon cantilever for higher vibration modes in liquid,” *J. Vac. Sci. Technol. B Microelectron. Nanometer Struct. Process. Meas. Phenom.*, vol. 27, no. 2, pp. 964–968, Mar. 2009, doi: 10.1116/1.3077487.
[13] G. C. Ratcliff, D. A. Erie, and R. Superfine, “Photothermal modulation for oscillating mode atomic force microscopy in solution,” *Appl. Phys. Lett.*, vol. 72, no. 15, pp. 1911–1913, Apr. 1998, doi: 10.1063/1.121224.
[14] D. Kiracofe, K. Kobayashi, A. Labuda, A. Raman, and H. Yamada, “High efficiency laser photothermal excitation of microcantilever vibrations in air and liquids,” *Rev. Sci. Instrum.*, vol. 82, no. 1, p. 013702, Jan. 2011, doi: 10.1063/1.3518965.
[15] D. P. Poenar and R. F. Wolffenbuttel, “Optical properties of thin-film silicon-compatible materials,” *Appl. Opt.*, vol. 36, no. 21, p. 5122, Jul. 1997, doi: 10.1364/AO.36.005122.
[16] D. Ho, M. O. Noor, U. J. Krull, G. Gulak, and R. Genov, “CMOS Tunable-Wavelength Multi-Color Photogate Sensor,” *IEEE Trans. Biomed. Circuits Syst.*, vol. 7, no. 6, pp. 805–819, Dec. 2013, doi: 10.1109/TBCAS.2013.2243727.
[17] M. Manoccio, M. Esposito, A. Passaseo, M. Cuscunà, and V. Tasco, “Focused Ion Beam Processing for 3D Chiral Photonics Nanostructures,” *Micromachines*, vol. 12, no. 1, Art. no. 1, Jan. 2021, doi: 10.3390/mi12010006.
[18] “What is FIB - Orsay Physics.” https://www.orsayphysics.com/what-is-fib

Chapter IV:

Experimental characterization results

CONTENTS

This Chapter presents the experimental characterization results of the photonic and mechanical parts of the gas sensor separately. The first part is devoted to the discussion of the measurements of the designed THz waveguide, tapers, and PhC cavities mentioned in chapter II. It starts with the demonstration of low propagation and insertion losses of the waveguide, followed by a multimodal analysis and finishes with a full experimental discussion on the PhC cavities resonance frequencies and quality factors.

The second part focuses on studying the acousto-mechanical resonator of the gas sensor. It presents the metallization of the Poly-Si membranes with the FIB technique, and their mechanical resonance measurements with the LDV at different pressure levels.

Part I: THz photonic characterization

IV.1. WAVEGUIDE PROPAGATION LOSS

IV.1.1 Cut-back method for total propagation losses extraction

The detection limit of the gas sensor is directly proportional to the THz power interacting with molecules. Since the generation of high THz powers at room temperatures remain quite complicated, it is necessary to build this sensor on an ultra-low loss integrated platform. This loss value is quantified by the extraction of the propagation losses of the THz waveguide designed in chapter II. Therefore, two ports S parameters measurements are done using VNA with frequency extenders VNAX in the 500-750 GHz frequency band. Since losses in a waveguide proportionally increase with its lengths augmentation, it is possible then to extract the propagation losses from the linear dependence between waveguide losses and lengths. This is known by the cut-back method. Hence five waveguides with 3.8, 10.9, 14.9, 19.1, 25.1 cm respective lengths are measured with the VNA. Figure IV.1.1 shows the photograph of these structures. The guiding channels are twisted with 90° bends to form a compact spiral shape that fits a 3" diameter wafer. To easily handle these structures, a PLA (Polylactic acid) 3D printed holder was used. An additional 1 mm air space is ensured by etching the plastic under the guiding channel. As presented in chapter II (Figure II.2.4) the E_x fundamental mode electric field is highly confined inside the Si, thus this 1 mm air space is large enough to prevent the absorption of the field by the plastic holder. Despite

the very low insertion losses demonstrated by the simulation in chapter II (part II.2.3), we chose to keep a right angle between the in- and output tapers to prevent the detection of non-guided energy.

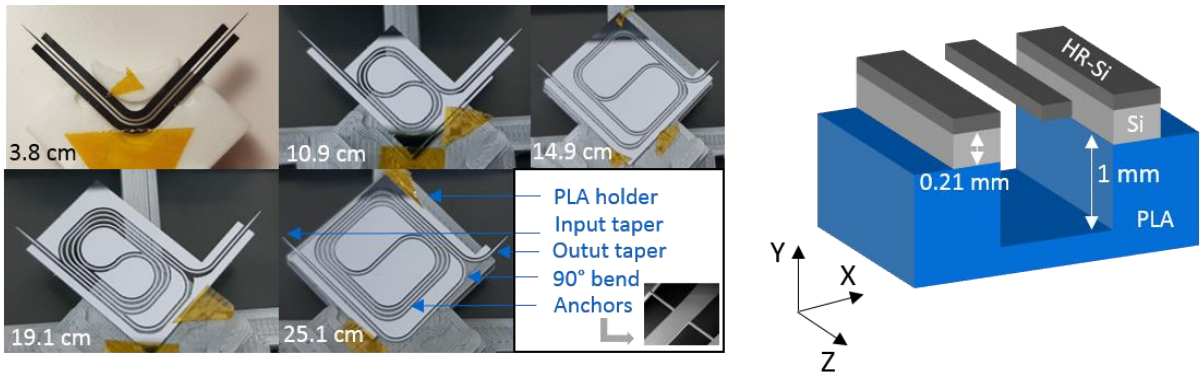

Figure IV.1.1 Photos of waveguides with different lengths on the left, and schematic representing the waveguide on a plastic holder on the right

The sample under test is mounted on an X, Y, and Z translational micrometer stage with 2µm sensitivity for precise alignment. A camera with an objective is used to enlarge the visualization at the MWG input of port 1. The waveguide taper is then introduced by 1 mm inside the port and aligned by controlling its central position in the XY plane. The second port is itself mounted on a translational stage that allows to align it with the second taper. S_{21} and S_{12} represent the transmitted normalized power in dB scale from port 1 to 2 and 2 to 1 respectively. These two parameters are fundamentally equal and can be written as:

$$S_{21} = 10\log_{10}\frac{I_{Transmitted}}{I_0} \quad \text{(IV.1.1)}$$

Similarly, the reflected normalized power S_{11} or S_{22} are represented by:

$$S_{11} = 10\log_{10}\frac{I_{reflected}}{I_0} \quad \text{(IV.1.2)}$$

where $I_{Transmitted}$, and $I_{reflected}$ correspond respectively to the transmitted and reflected intensity, and I_0 the incident one. Figure IV.1.2 represents the S_{21} and S_{11} parameters of the waveguides with different lengths. It is clear how the transmittance (S_{21}) decreased as the length was increased. While the reflectance (S_{11}) remains below -10 dB which confirms the low insertion losses simulated in chapter II. The behavior of S_{21} is also quite similar to the one simulated in II.2.3 for

a taper position at 1 mm inside the MWG. As expected from simulation the insertion losses are higher at low frequencies.

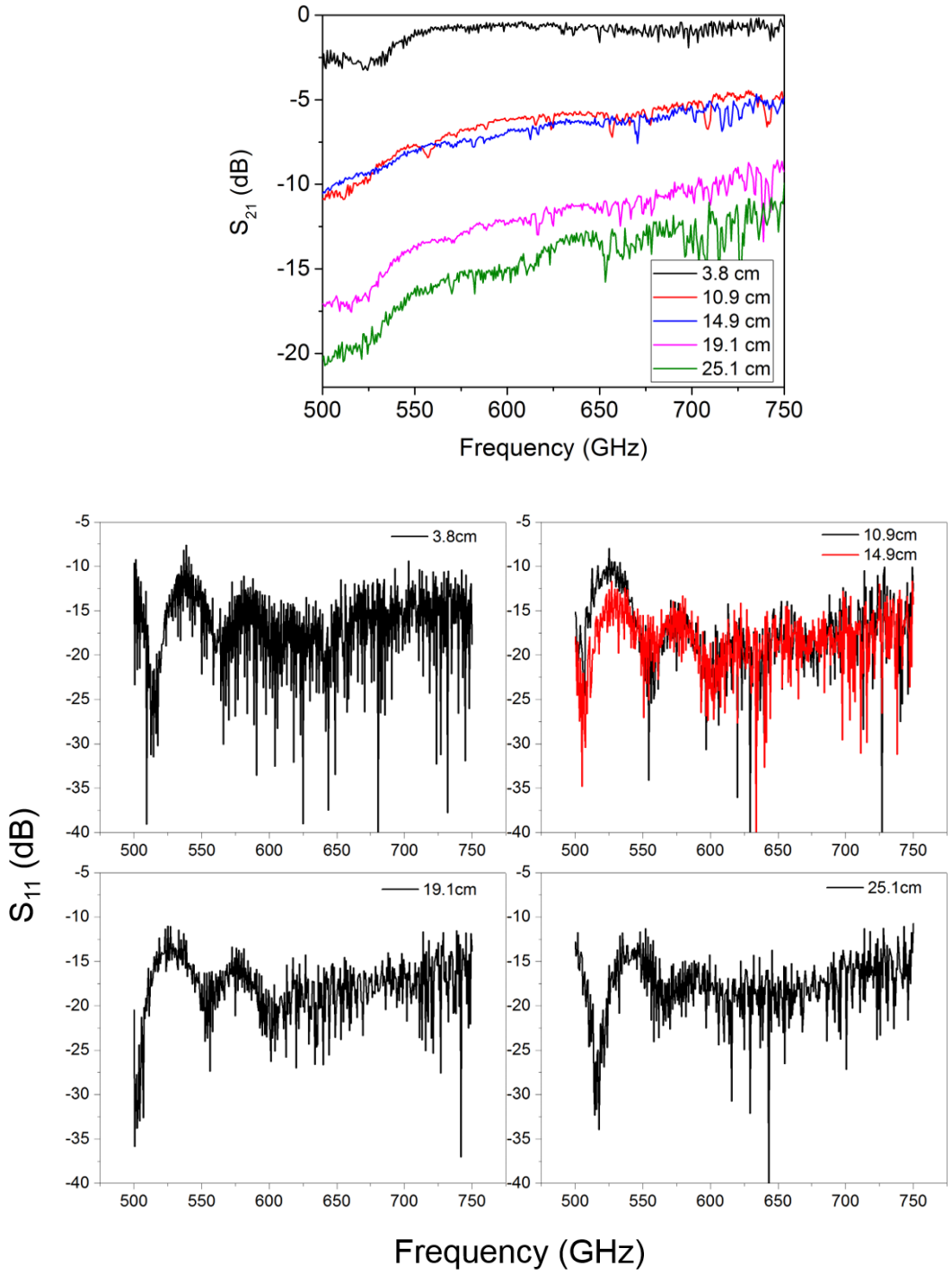

Figure IV.1.2 Measured S parameters of the waveguides with different lengths. On the top the magnitude of S_{21} in dB and the S_{11} one on the bottom

Therefore, by comparing these results to the simulations, we can confirm the low insertion losses, and we can assume that the coupling conditions are nearly identical and have a very low error impact on the measurement results. We believe the extra loss peaks appearing in some measurements to be the result of misalignments as observed in the simulations in figure II.2.17. A linear dependence is observable between transmittance and length except for the structure with 14.9 cm. This exception is probably due to the variation of parameters other than just the length in the (such as number of anchors and bends). To confirm the linearity of the loss dependence between the structures we used the Inverse Fast Fourier Transformation (IFFT), to convert the frequency domain data into the time domain. Since S parameters allow to extract the amplitude and phase, it is possible to reconstruct the complex form of the electric field which is expressed by:

$$\boldsymbol{E}(\omega) = |E(\omega)|e^{j\varphi(\omega)} \tag{IV.1.3}$$

With

$$|E(\omega)| = 10^{\frac{S_{21}}{20}} \tag{IV.1.4}$$

and $\varphi(\omega)$ the measured phase in radians. Therefore, the temporal electric field spectrum is obtained by the Fourier transformation of IV.1.3:

$$E(t) = \frac{1}{2\pi}\int_{-\infty}^{+\infty} e^{-i\omega t}\boldsymbol{E}(\omega)d\omega \tag{IV.1.5}$$

where $\omega = 2\pi f$ the angular frequency and t the time variable. The experimental frequency step size δf determines the mathematical temporal sampling interval T which corresponds to the scanning time in a time domain measurement:

$$T = \frac{1}{\delta f} \tag{IV.1.6}$$

The temporal resolution is determined by the frequency bandwidth Δf of the measured spectrum

$$\delta t = \frac{1}{\Delta f} \tag{IV.1.7}$$

The spectrum frequency bandwidth here is limited by the single mode behavior of the WR-1.5 waveguide at the output ports of the VNAX. It corresponds to 250 GHz, going from 500 to 750 GHz. Therefore, the finest achievable temporal spectral resolution corresponds to 4 ps. Those measurements are done using a calibration of the full frequency bandwidth with 401 points and

thus a $\delta f = 623.44$ MHz. In the time domain, this corresponds to a t =1.6 ns scanning time. This time is not sufficient for the wave to travel through long waveguides. It was impossible then to extract the time signal form of waves traveling structures with length > 10.9 cm using this calibration. Therefore, another calibration with narrower frequency bandwidth (620-650 GHz) and smaller frequency step size $\delta f = 24.98$ MHz is used for long structures measurements. This results in a lower temporal spectral resolution (33 ps) for the 14.9, 19.1, and 25.1 cm long structures, compared to the shortest ones with 3.8-10.9 cm length and 4 ps spectral resolution (see figure IV.1.3(a)).

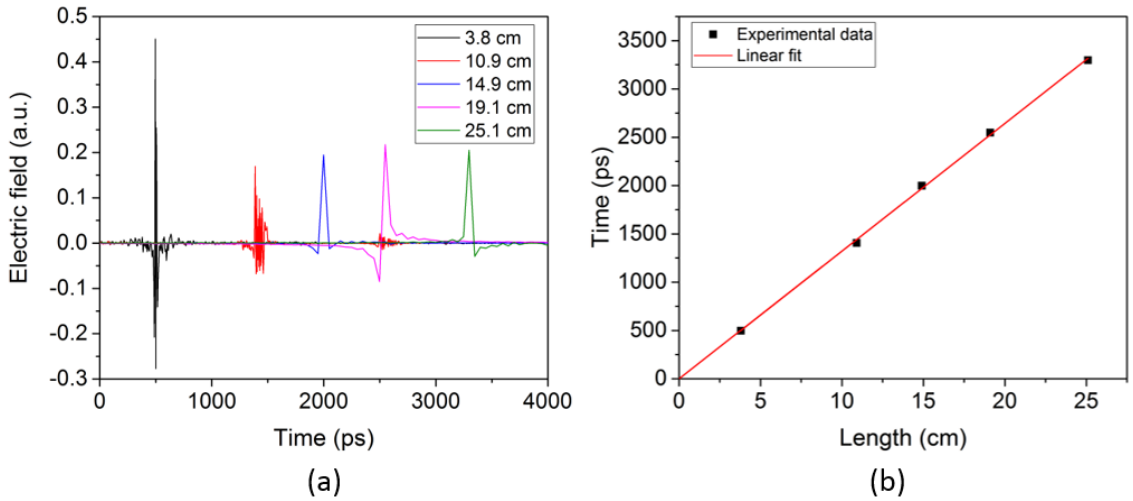

Figure IV.1.3 Time signal calculated from the experimental frequency spectrum inverse Fourier transformation of each waveguide on the left (a) and linear variation of the time delay with propagation length increasing on the right (b)

It is possible to increase the spectral resolution and scanning time by using another calibration of the full band with a smaller frequency step size. However, the main purpose of these analyses is to determine the linear behavior of the propagating energy inside the waveguide. Figure IV.1.3(b) shows this linear dependency between the time delay and the physical length of the structure. Table IV.1.1 summarizes the different characteristics and parameters of each structure.

Length	Bends	Anchors (pair) (N)
3.8 cm	1	8
10.9 cm	11	15
14.9 cm	11	20
19.1 cm	19	22
25.1 cm	19	35

Table IV.1.1 Table representing the length, number of bends, and pair of anchor for the different measured structure

To extract an upper limit of the propagation loss that includes all loss mechanisms (bend radiation, anchors scattering and material absorption loss), we have to consider the structures with different lengths and the same approximate number of bends and anchor pairs variation. Therefore, for that purpose, we eliminate the 14.9 cm structure from the linear loss fitting.

Reflections are excluded from the calculated total loss expressed by:

$$loss = -10\log_{10}\left(\frac{T}{1-R}\right) \quad \text{(IV.1.8)}$$

where T and R are respectively the linear power transmittance and reflectance represented by:

$$T = 10^{\frac{S_{21}}{10}} \quad \text{(IV.1.9)}$$

$$R = 10^{\frac{S_{11}}{10}} \quad \text{(IV.1.10)}$$

Losses in dB scale are represented in figure IV.1.4 for the structures with 3.8,10.9,19.1 and 25.1 cm.

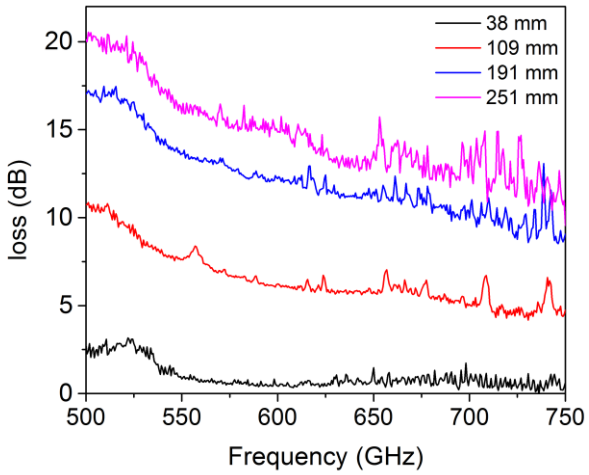

Figure IV.1.4 Total propagation losses for structures with different lengths

A linear fit of the calculated loss function of waveguide length at two arbitrarily chosen frequencies 600 and 700 GHz is represented in figure IV.1.5. The slopes of these fitting lines are directly related to the total propagation loss coefficient which is α=0.068 and α=0.058 dB/mm respectively. Figure IV.1.6 represents the propagation loss coefficient calculated from the fitted slope at each frequency point over the entire band (500-750 GHz). It can be stated that this novel integrated THz waveguide platform based on suspended HR-Si dielectric wire waveguides, exhibits propagation

losses that vary between 0.045 and 0.085 dB/mm with an average of 0.065 dB/mm. This average loss is equivalent to 0.032 dB/λ_0. Contrarily to other work, here the extracted value includes all the losses phenomena such as bend loss, and despite that this value remains the lowest among several other THz silicon waveguides [1]–[4]. For the first time over a large frequency band (250 GHz) extending up to 750 GHz, a very low propagation loss (including bend, material, and scattering loss) is demonstrated.

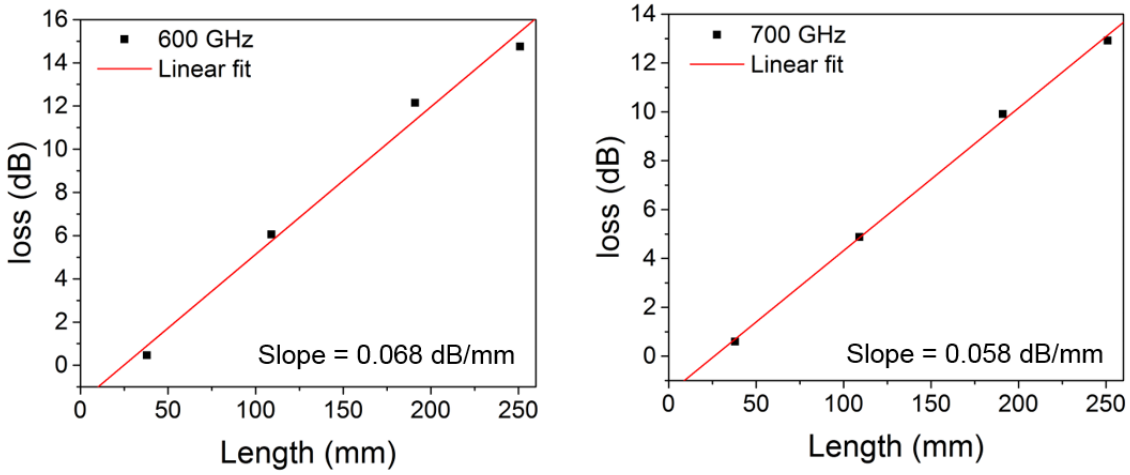

Figure IV.1.5 Linear fit of the total propagation loss at two particular frequencies 600 GHz on the left and 700 GHz on the right

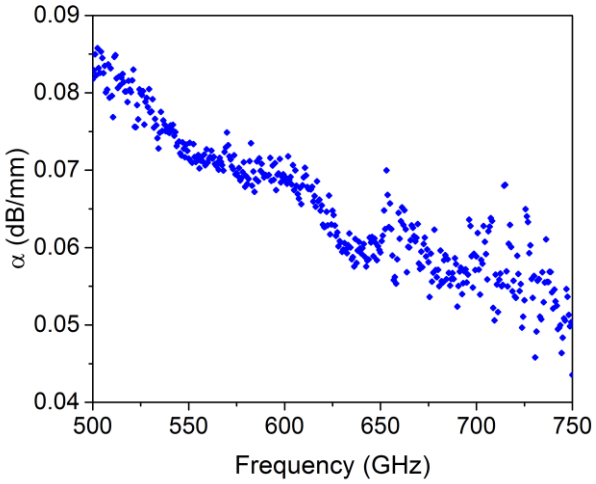

Figure IV.1.6 Extracted propagation loss in the suspended waveguide structure

IV.1.2 Anchors, bends, and material loss

In the previous part, we extracted an upper limit of the propagation losses. However, it was remarkable that the 14.9 cm structure is in disagreement with the loss-length linear dependency. It is also clear that the 10.9 and 14.9 cm has almost the same loss value and even less loss for the longer waveguide at low frequencies (see figure IV.1.2). Therefore, the 4 extra centimeters of propagation length and the 5 additional pairs, have an insignificant impact on the loss variation. This could explain the fact that the material absorption losses are quite low. The higher losses for the shorter waveguide at low frequencies could be attributed to a coupling difference between the two measurements and hence higher insertion losses. To separate the different loss phenomena, we first measured experimentally the anchor losses simulated in II.2.2.1. For that, another structure of 3.8 cm length with a doubled number of anchor pairs (16 instead of 8) was also measured. Figure IV.1.7 represents the measured S_{21} and S_{11} of the two structures. The high reflectance and low transmittance at low frequencies for the 16 pairs structure might be attributed to a non-optimized coupling. This can increase the error of the calculated scattered loss per anchor pair.

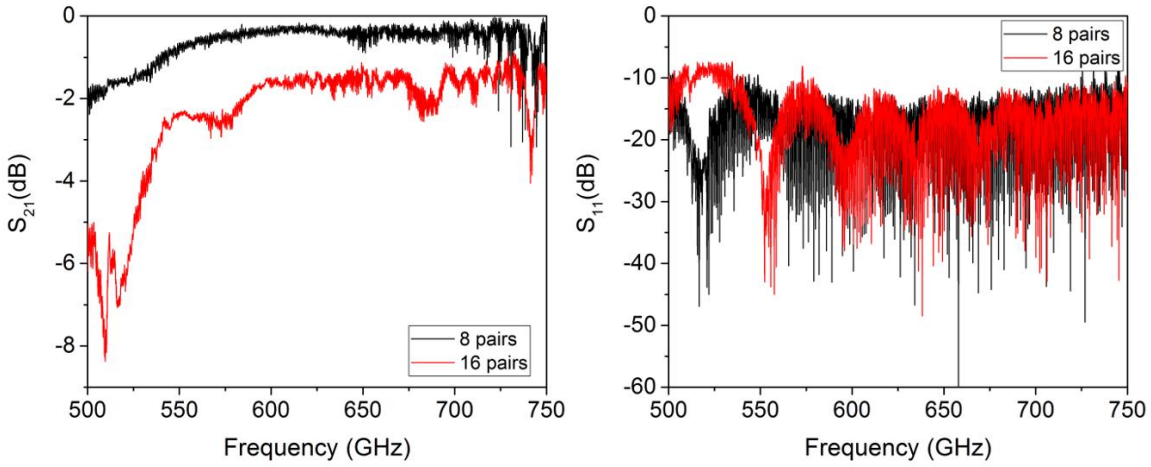

Figure IV.1.7 Measured S parameters of structures with 8 and 16 pairs of anchor

Using the same reasoning as previously the loss in each structure was calculated. Then the loss per anchor pair was determined as follow:

$$loss_{anchor\ pair} = \frac{loss_{16} - loss_{8}}{8} \qquad \text{(IV.1.11)}$$

Where $loss_{16}$ and $loss_8$ are respectively the measured loss for structures with 16 and 8 pairs of anchor. 8 is the number of the anchor pairs difference between the two structures. Figure IV.1.8 represents the measured loss per pair of anchor over the full frequency band. These values are higher than the ones expected from simulations. However, the measurements and interpretation of such low loss amounts (0.1 dB) are limited by the experimental errors. The extracted anchor loss is then subtracted from the spirals measured loss as follows:

$$Corrected\ loss = loss - N \times loss_{anchor\ pair} \tag{IV.1.12}$$

where N corresponds to the number of anchor pairs in each structure as presented in table IV.1.1.

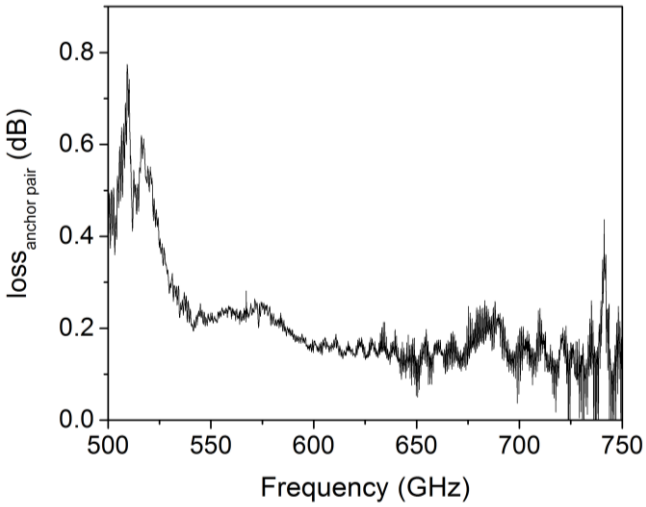

Figure IV.1.8 Measured loss per pair of anchor

These corrected losses are represented in figure IV.1.9. The error in this calculation is quite high leading to a nonphysical negative loss for the 3.8 cm waveguide. However, it gives an approximation of the anchors, material, and bends loss separately. An overlap between structures with the same number of bends is observable in figure IV.1.9. Thus, this confirms an ultra-low level of material absorption loss (less than 0.1 dB/cm). This value is very close to what has been measured by Grischkowsky et al.[5] and Dai et al.[6] for HR-Si with resistivity ≥ 10 kΩ.

The loss level offset between structures with different numbers of bends is related to the bend loss. It is possible then to extract an estimated value of loss per bend from the offsets difference divided by the bends variation number. Despite the system complexity and the low loss values dominated

by the experimental errors, we can extract approximate loss amounts for: bends (0.5-0.6 dB/bend), anchors (0.1-0.2 dB/anchor pair), and material absorption (< 0.1 dB/cm).

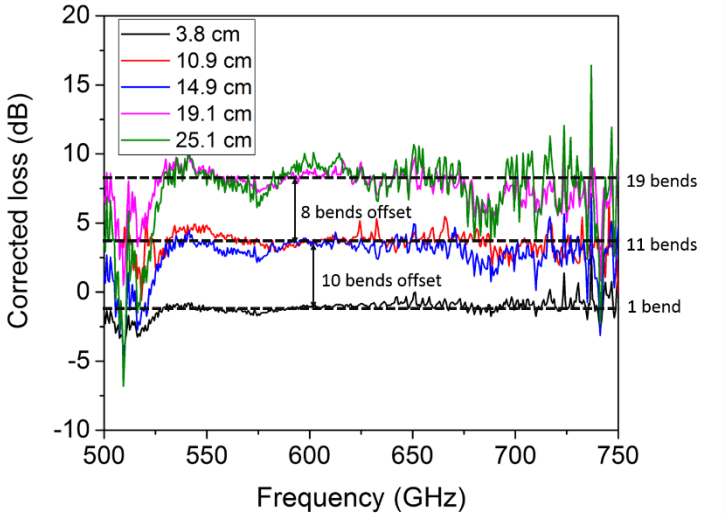

Figure IV.1.9 Measured loss after the extraction of anchor loss

IV.1.4 Insertion losses: Metallic waveguide/Si taper transition

The previous S_{21} measurements confirm the simulated low insertion losses represented in chapter II.2.3 with an inverted taper of 65x90x3000 µm dimension, at 1 mm inside the MWG. Therefore, this inverted taper is highly efficient for Metallic-Si waveguide transition, but it requires a complex alignment to insert the taper inside the MWG. Contrarily to an inverted taper, a horn (see figure IV.1.10) has an adiabatic reduced width rather than increased.

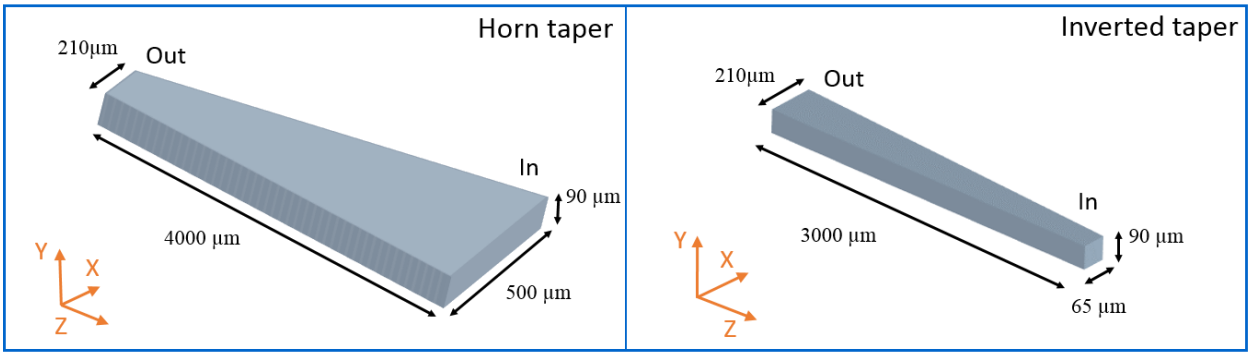

Figure IV.1.10 Schematic representing the different tapered ends

The Horn taper has a large input width (500 µm), which couldn't be inserted inside the MWG (cross-section 191 x 381 µm). Therefore, feeding the structure with a horn taper might be easier in the manipulation. To compare the efficiency of these two different tapers we measured the S parameters of two similar structures with different tapered ends. For both measurements, the tapers were aligned at the two ports sides with the MWG center to ensure a perfect butt-coupling. We also measured the structure with an inverted taper at 1 mm inside MWG from both sides. The S_{21} and S_{11} modulus of each measurement are represented in Figure IV.1.11.

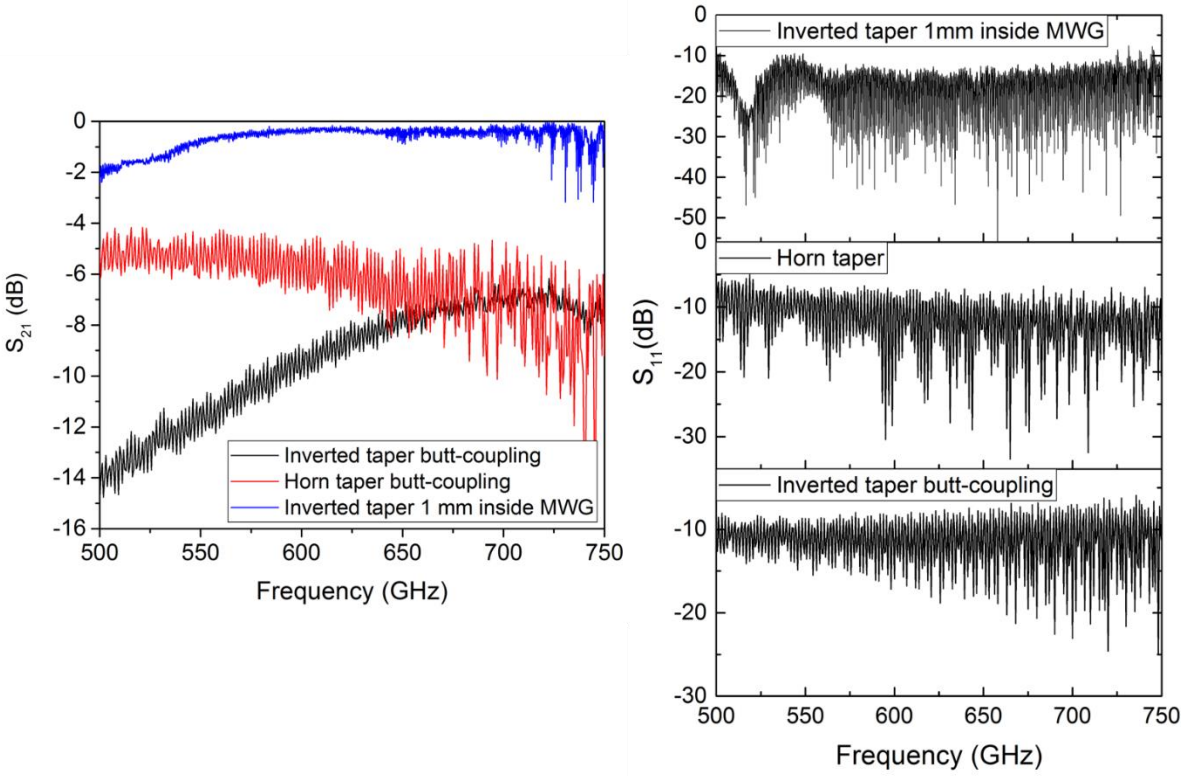

Figure IV.1.11 S parameters measurements for structure with horn and inverted tapers at different coupling positions. On the left the magnitude of S_{21} and the S_{11} on the right

As expected from simulation, for a perfect butt-coupling position, the inverted taper is less efficient due to the small modal overlap. Since at the transition point the horn taper has stronger modal confinement and better overlap, losses are lower, especially at low frequencies. However, the main reason for the non-negligible insertion losses with the horn taper (5 dB) is the high impedance mismatch presented by the high reflectivity (S_{11} < 10 dB at low frequencies). From these measurements, we can conclude that despite the complexity of manipulating an inverted taper

inside the MWG, such alignment is necessary as it has at least one order magnitude less insertions losses compared to any other taper or alignment configuration.

While in the first part of this section, S parameters measurements were used to present the inverted taper with low insertion losses, in the next, a different experimental demonstration using a VDI AMC THz source and an antenna-coupled micro-bolometric uncooled THz camera is also reported. The experimental setup is presented in figure IV.1.12. A 90° bended waveguide with two tapered ends (inverted tapers) is mounted on a microcontroller stage to optimize its position inside the source MWG. The camera is equipped with an objective composed of two HR-Si lenses, that allow focusing the divergent THz beam on its sensor surface. It is placed in front of the second taper end at the objective focal length (f =196 mm). A TTL trigger signal is generated by the camera and received by the source, allowing the camera to detect a reference background while the source is turned off.

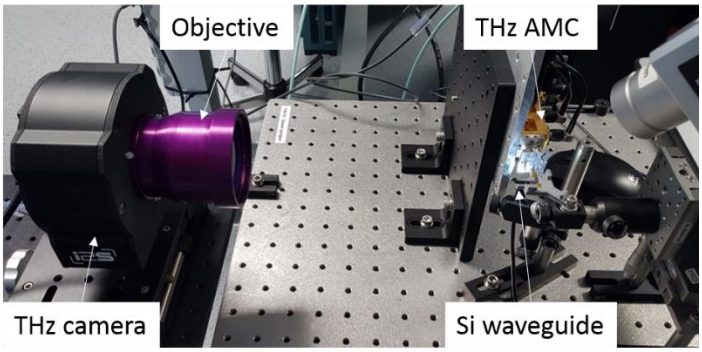

Figure IV.1.12 Mode imaging experimental setup

Figure IV.1.13, shows the Si waveguide placed in front of the MWG at a butt-coupling position. Two spots are observable on the camera interfaces. The central spot corresponds to the guided energy collected at the edge of the output taper. While the second spot might be related to the non-coupled radiative energy at the transition between the MWG and the Si taper. To confirm that a metallic object (ruler) was placed in front of the transition area to block the radiative field from reaching the camera. In presence of the metallic object, the camera detects only one spot that corresponds clearly to the guided mode in the Si channel. Once the detected spots are well defined, the waveguide taper was then introduced inside the MWG to improve the coupling. Figure IV.1.14 represents the THz camera response at different positions of the taper inside the waveguide. During these measurements, the camera position was adjusted so that the MWG-Si taper transition point

is at the focal length of the camera objective lens. Hence the detection of a more intense radiative focused beam compared to the guided one, at the butt-coupling position of figure IV.1.14.

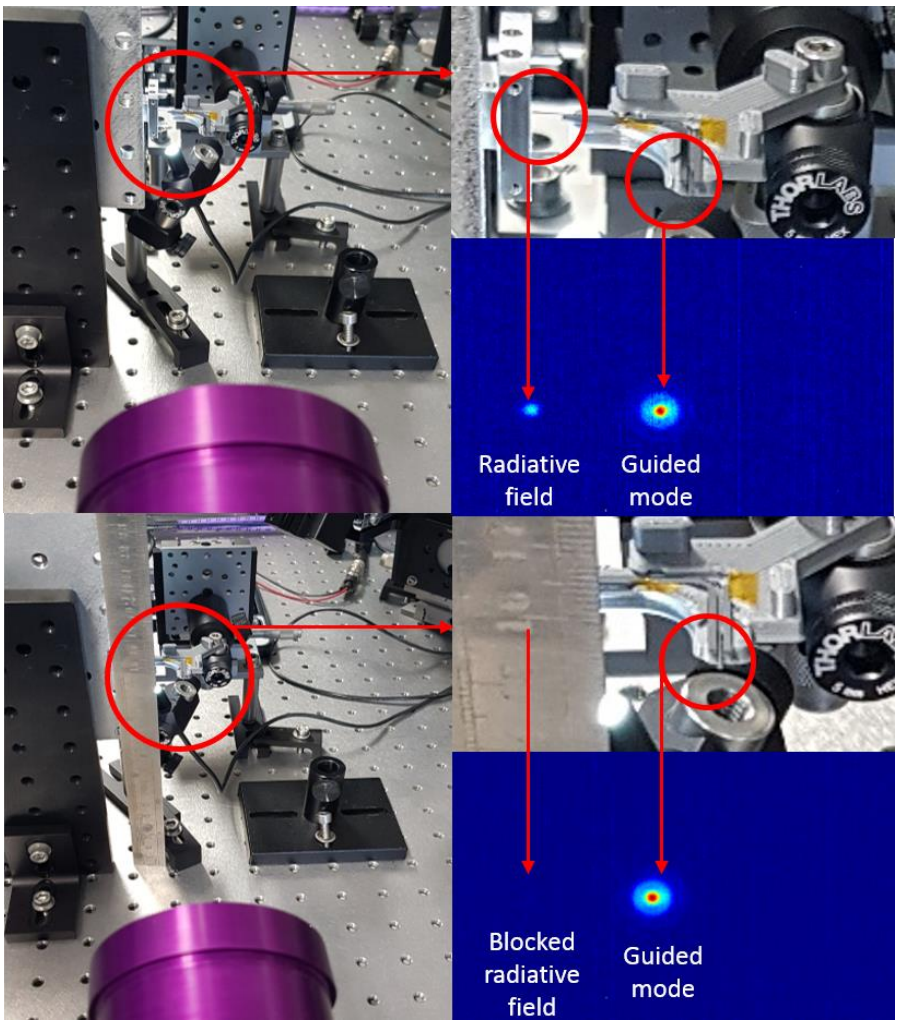

Figure IV.1.13 Camera detection at the butt-coupling position, with blocking the radiative field (on the bottom) and without (on the top)

However, for a position of the taper at 500 µm inside the MWG, the radiative spot intensity starts to decrease while the guided one increases, until the total disappearance of the radiative spot when the taper is inserted for 1 mm inside the MWG. This demonstration confirms the previously presented S parameters measurements and the simulated results in chapter II, which illustrate the insertion losses variation with taper position inside the MWG.

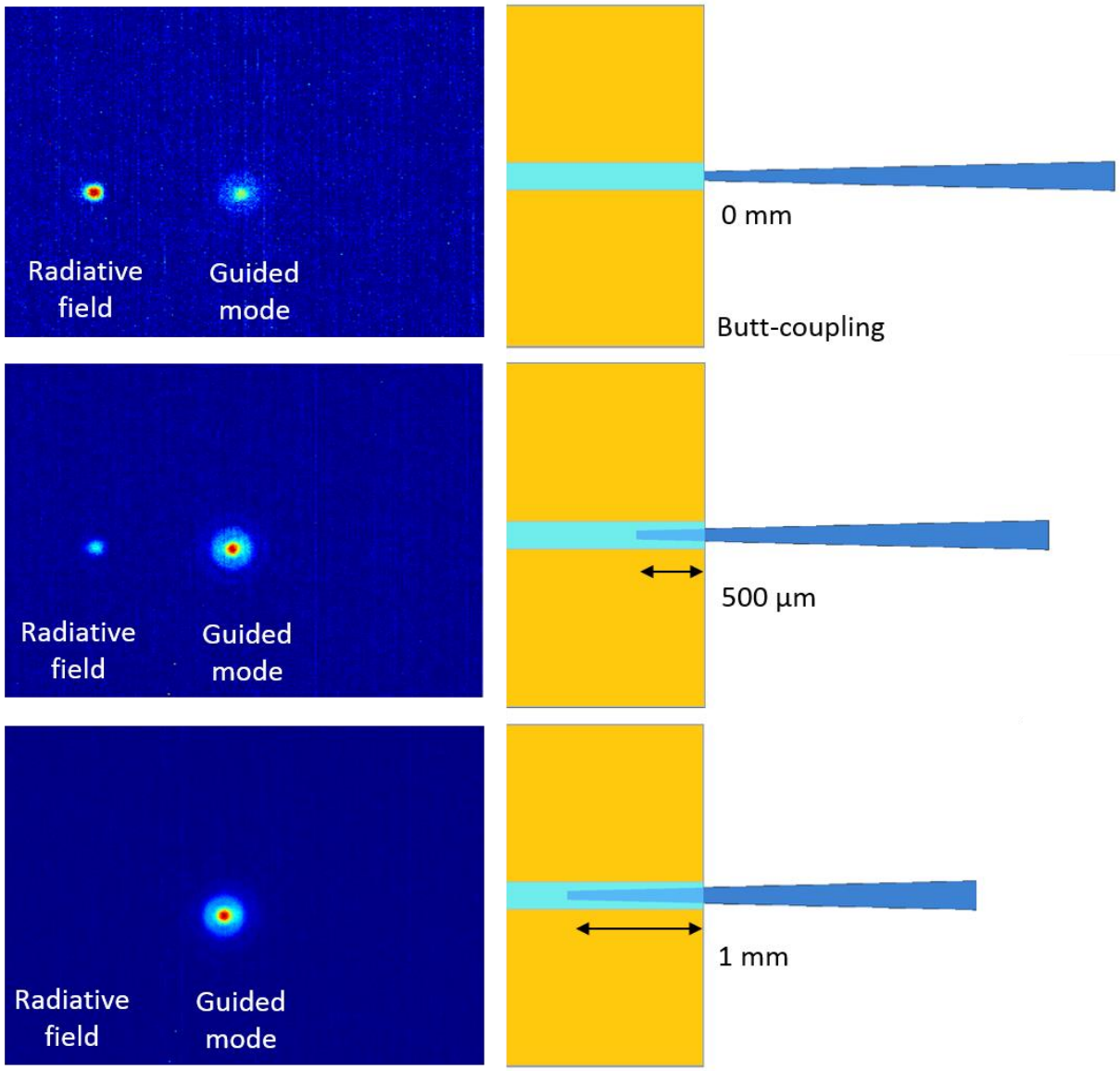

Figure IV.1.14 THz camera detection at several coupling positions

IV.2. WAVEGUIDE MULTIMODAL ANALYSIS (TDS MEASUREMENTS)

Up to now we only discussed the single-mode regime of this waveguide. However, as represented in chapter II, the designed waveguide supports higher-order modes that are not excited with the VNA due to their symmetry and polarization nature at low frequencies below 650 GHz. At higher frequencies E_x even modes exist and have a good overlap with Gaussian beam. The experimental misalignments in a free space configuration are much more important than inside a MWG port. Therefore, odd anti-symmetric modes are more likely to be excited by a Gaussian beam. Thus, a

Gaussian beam of a broadband source such as a dipole antenna of a TDS is easily coupled into several modes inside the Si guiding channel. To analyze the intermodal dispersion, we measured using a TDS the transmission of a THz pulse traveling a 90° bent waveguide of 3.8 cm length. The TDS emitter and receiver are mounted on a rotatable rail with 4 lenses to focus the THz beam spot. The lenses used have a diameter and a focal length of 50 mm. These dimensions correspond to a numerical aperture of 0.5 identical to that of the waveguide's taper to maximize the energy coupling. The THz beam was first focused at the central point between the two middle lenses where the sample will be mounted later. The reference pulse was recorded by averaging 1000 scans. This number of scans is fixed for all measurements to reduce the noise level.

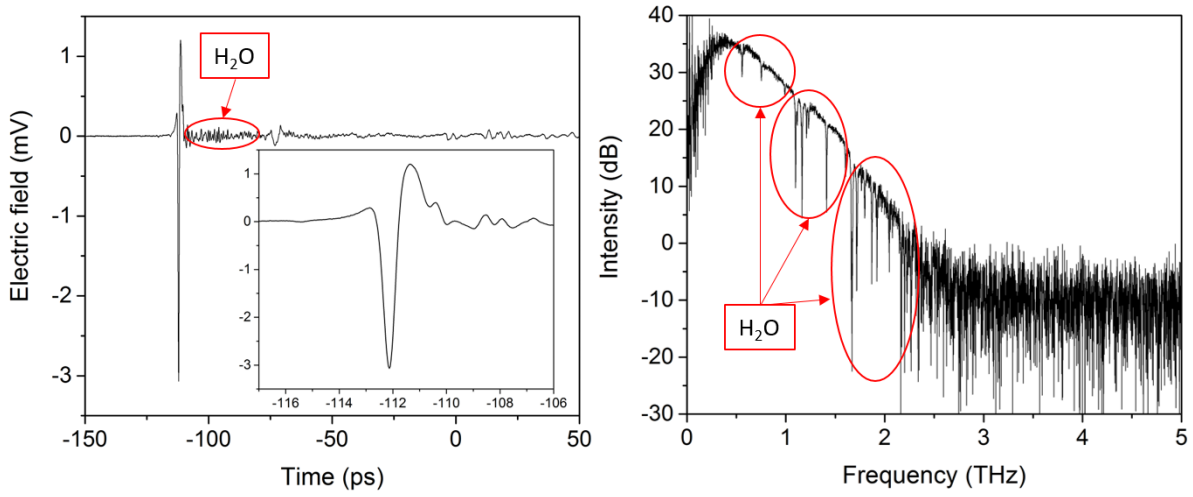

Figure IV.2.1 Measured THz reference pulse on the left and its FFT on the right. The inset on the left: Enlargement of THz reference pulse

Figure IV.2.1 represents the reference time pulse and its FFT calculated using Matlab. The reference pulse signal is distorted by the water vapor absorption [7]. This impact is also observed through strong peaks in the frequency domain spectrum. It is possible to purge with Nitrogen the medium inside the box containing the setup to prevent water vapor absorption. Since the pulse will be guided inside the Si and less affected by the water absorption, measurements were done without purging. To couple the pulse inside the bent waveguide, the rails were rotated to maintain a right angle between the emitter with the first two lenses on one side and the receiver with the other two lenses on the second side. The waveguide is mounted on a micropositioner at the rails rotational axis center. The two lenses close to the waveguide were moved back 1.9 cm each to keep the

taper's edges near the lens's focal point. The right angle between emitter and receiver ensures the detection of guided waves only. Figure IV.2.2 represents the measured transmitted pulse through the waveguide and its FFT. The incoming reference pulse is delayed, stretched, and chirped after traveling inside the waveguide. The time delay between the reference and transmitted pulses is represented by:

$$\Delta t = (n_g - 1)\frac{l}{c} \qquad \text{(IV.2.1)}$$

Where n_g represents the excited mode group index, $l = 3.8 \times 10^{-2}\ m$ the waveguide length and $c = 3 \times 10^8\ m/s$ the speed of light in vacuum.

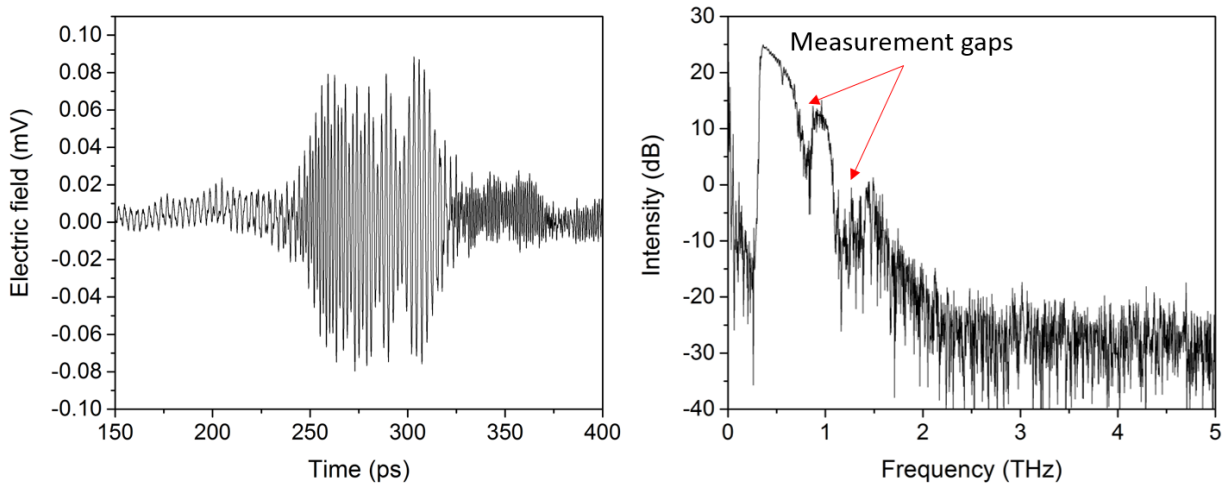

Figure IV.2.2 Measured THz pulse transmitted through the waveguide on the left and its FFT on the right

The pulse is delayed by almost 400 ps and stretched to more than 250 ps, with a positive and negative chirp. This large stretching of the pulse is related to the dispersion of different modes in the waveguide[8], [9]. The group index dispersion of the modes propagating through this chirped pulse varies from n_g = 3.07 to 5.04. These values are extracted using equation IV.2.1. The frequency spectrum represents a sharp cut-off around 0.31-0.33 THz. This corresponds to the frequencies were the fundamental mode is weakly confined and easily couple to the radiative modes after travelling through the bended section. However, two unusual gaps appear in the spectrum at higher frequencies (0.7-0.86 THz and 1.05-1.4 THz). To understand these two gaps, we present in figure IV.2.3 the simulated group index modal dispersion of the waveguide. Only E_x modes are considered in this plot since the TDS PC antenna are horizontally polarized.

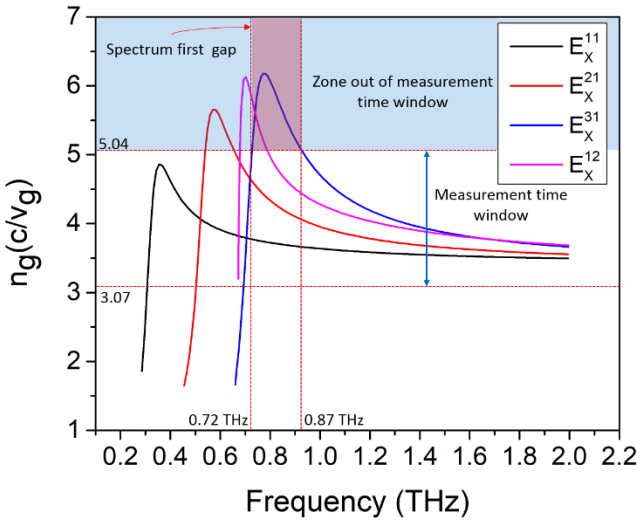

Figure IV.2.3 Simulated group index modal dispersion of the first 4 E_x modes

As represented in figure IV.2.3 the blue highlighted zone corresponds to a time longer than the one measured in our experiments. Therefore, due to the short measurement time, several modes with slow group velocities aren't detected, resulting in a measurement gap in the spectrum. Since the receiver of the TDS is a PC antenna, anti-symmetric modes are not detected due to the zero overlap integral [10]. Thus the only detected modes presented in figure IV.2.3 are the symmetric ones (E_x^{11} and E_x^{31}). While the scanning time was long enough to detect the E_x^{11}, some slow frequencies of the E_x^{31} mode aren't detected, giving the origin of the first measurement gap (0.7-0.86 THz). Similarly, the other gap is related to unmeasured higher order symmetric modes. The multimodal regime of the waveguide and the high modal dispersion explain the large pulse stretching. We can also conclude from the negative and positive group velocity dispersion ($GVD = \frac{\partial}{\partial\omega}\frac{1}{v_g}$) at high and low frequencies respectively, the reason behind the pulse negative and positive chirp (Figure IV.2.2). Figure IV.2.4 represents the 3 different measured pulses: the reference pulse, the one transmitted through the waveguide in the multimode regime, and the last one extracted from the IFFT of the S parameter measurement with the VNA which corresponds to the waveguide single mode regime. In the single mode regime, the dispersion is limited by the waveguide geometry and material dispersion, and therefore the pulse is less stretched compared to the multimode regime where intermodal dispersion takes place. The difference in delay times between the measured TDS pulse and the one calculated using the phase and amplitude extracted from the

VNA measurement is due to the shifted reference pulse (-112 ps) in the TDS measurement. Furthermore, in a TDS measurement, the time delay expressed by the equation IV.2.1 represents the time difference between the propagation in the waveguide and the same propagation distance in air. To define the propagation time in the waveguide using the TDS, an additional time must be considered that corresponds to the propagation in air for a distance equivalent to that of the waveguide.

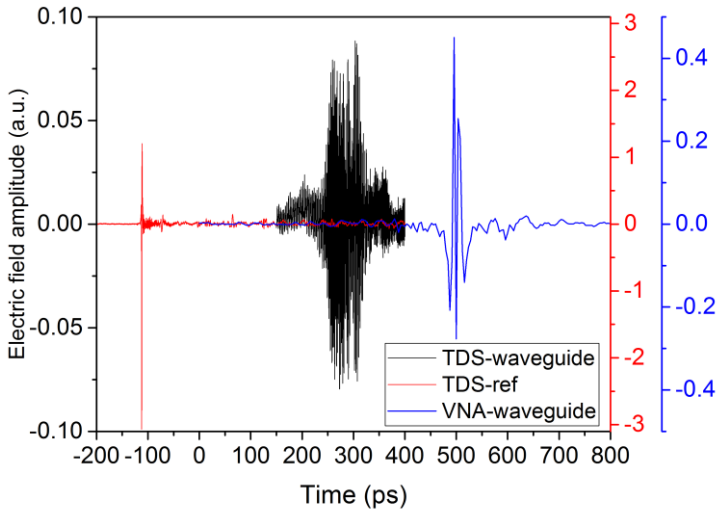

Figure IV.2.4 Comparison between the THz TDS reference pulse, THz TDS pulse transmitted through the waveguide, and IFFT of the S_{21} parameter measured with VNA

IV.3. PHOTONIC CRYSTALS

IV.3.1 Bragg reflectors and bandgaps

The previously mentioned results have provided information about the upper and lower limit of the HR-Si platform used for the fabrication of waveguides, PhC cavities, and finally the photoacoustic gas sensor. This section presents the experimental results of the PhCs and PhC cavities designs mentioned in chapter II. We first discuss the photonic band gaps at the Brillouin zones edges of the Bragg reflectors simulated in II.3.2 and II.3.3. Therefore, we measured the S parameters of two PhC Bragg mirrors with 60 holes of 29 µm radius each: one with a lattice constant a=106.56 µm and a second one with a=120.65 µm. These specific parameters represent the starting and ending periods (lattice constants) of the apodized cavities discussed in the following section. For these measurements, we used the same VNA measurement setup used for

loss extraction. A full band calibration (500-750 GHz) with frequency step size $\delta f = 125$ MHz is used in order to visualize the full bandgap. The simulated modal dispersion of these two structures, together with the measured transmittance and reflectivity are represented in figure IV.3.1. In both configurations, the bandgap is convincingly observed, as the region of combined low S_{21} transmittance (-30dB down to -50dB) and high S_{11} reflectivity (up to -0.5dB or 90% power reflection). For the former Bragg mirror (a=106.5 6µm) we observe a bandgap from 566 to 675.4 GHz, while for the latter (a=120.65 µm) the gap appears from 518.4 to 616.4 GHz.

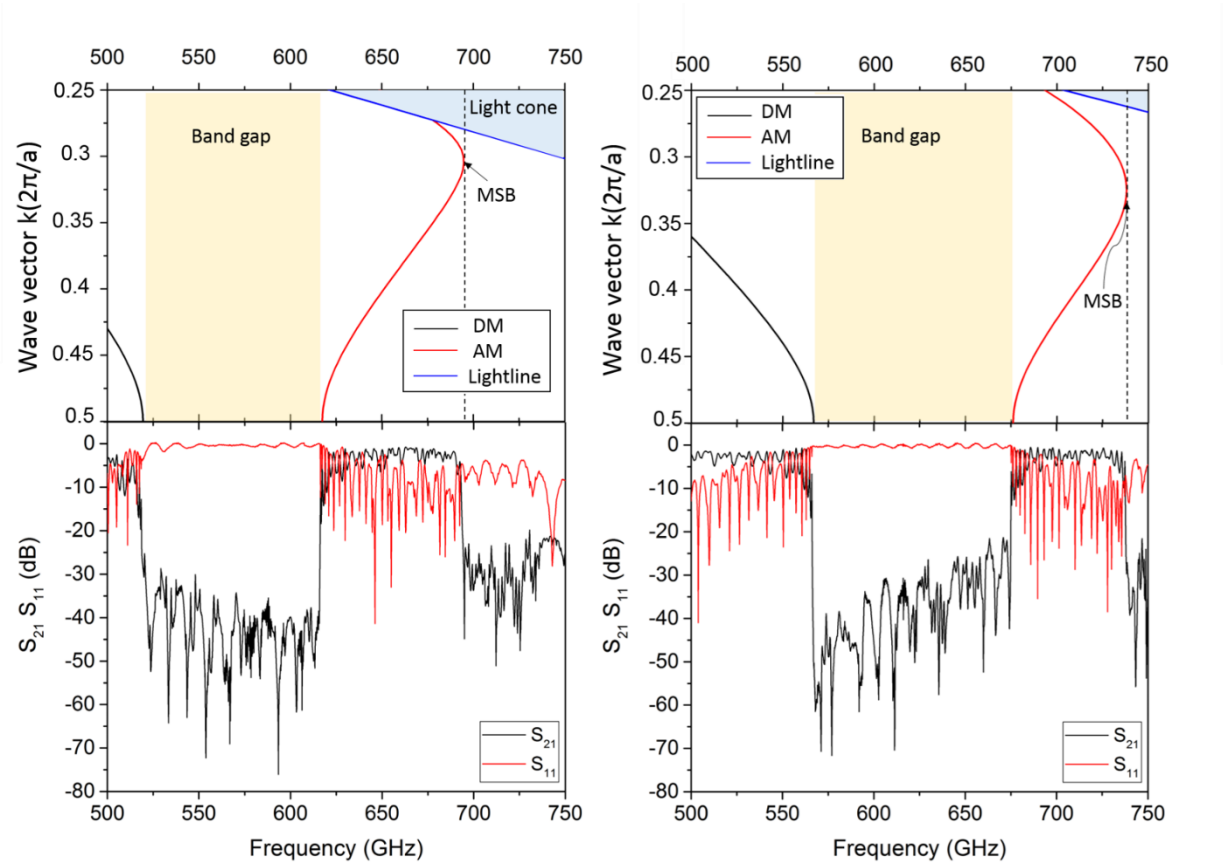

Figure IV.3.1 On the bottom the S parameters measurements representing the photonic band gaps of two Bragg reflectors with 60 holes of radius R=29µm and a lattice constant a=120.65 µm on the left and a=106.56 µm on the right. On the top the simulated modal dispersion representing the band gaps at the Brillouin zone edges of these reflectors

As represented in figure IV.3.1 the measured and numerical predictions of the band gaps edge frequencies are in very close agreement with less than 0.1% error. It is also observed that within the allowed bands a reasonable -2 dB S_{21} transmittance is observed, implying only 63% power transfer, while the S_{11} reflections back to the VNA port are still non-negligible as 10-30% (-5 to -10 dB). This is to be understood as the result of the impedance mismatch at the transition between

the unpatterned suspended wire guides and the etched PhC part in the suspended guide. Together with the extra small scatter losses induced by the etched holes, this also accounts for the remaining scatter losses of about 10-25%. We also observe a gap at higher frequencies for both structures. Contrarily to the photonic bandgap where the light is mainly reflected instead of transmitted, in these gaps the transmittance decrease (S_{21} = -30 -40 dB) while the reflectance remains also low (S_{11} = -5 -10 dB). The frequencies at which these gaps are observed correspond to the ones at which the air modes slow down and fold back in the simulated dispersion diagram. Therefore, these gaps correspond to mini stopbands and occur when the fundamental air mode is coupled to higher order symmetric dielectric modes in the region of the Brillouin zone far away from the edge.

IV.3.2 High-Quality factor cavities

We proposed in chapter II the designs of several PhC cavities with resonant frequencies at 630-636 GHz and 650 GHz respectively. In this section, we discuss the experimental results of the 630-636 GHz cavities referred to as designs number 1 and 2 in Chapter II. However, the 650 GHz cavities are dedicated to gas sensing and will be discussed later. These structures were also characterized with the VNA by extracting their S_{21} and S_{11} parameters. However, for these measurements, an additional finer calibration on limited bandwidth (630-650GHz) with $\delta f = 8$ MHz is used to resolve potential high Q resonances. Figure IV.3.1 represents the photos of two PhC cavities with similar parameters that correspond to the same design (design number 2, R=29µm). Both cavities were created by etching the core of a suspended waveguide. However, the first waveguide presented on the left side of figure IV.3.2 has a length of 3.8 cm including a bend, while the second one shown on the right side of the same figure is a 1.7 cm long straight waveguide.

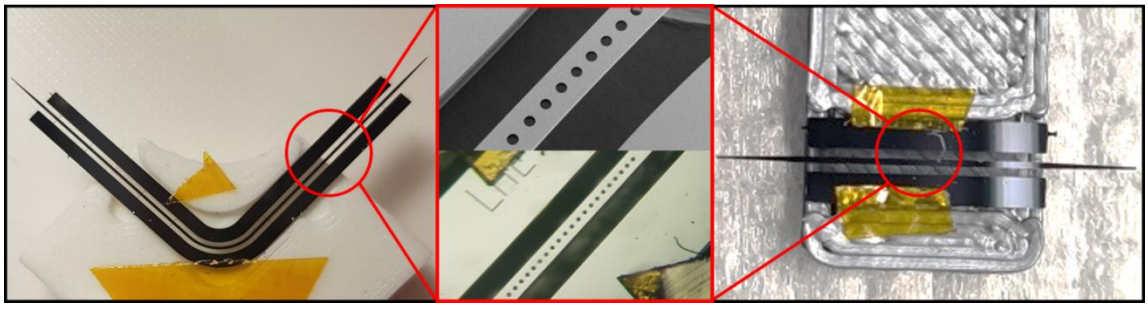

Figure IV.3.2 A photograph of a PhC cavity on top of a 90° bended waveguide on the left and a straight waveguide on the right. At the center microscopic (SEM and optical) images of the PhC

The two were fabricated on two different wafers following the same technological process. Samples are all mounted similarly on the same plastic holder used to suspend the waveguides presented in figure IV.1.1. Figure IV.3.3 presents the large frequency range S parameters of two bended structures PhC cavities. The two designs have the same lattice constant variation but different hole radius with 28 µm (design 1) and 29 µm (design 2) respectively. The right-hand side plot of figure IV.3.3 corresponds to the 28 µm hole radius structure, while the 29 µm one is illustrated by the plot on the left-hand side. As expected from simulations a large bandgap with high reflectance (S_{11}= -2 dB) and low transmittance (S_{21}= -50 dB) appears in the frequency region between 530 and 680 GHz. The 29µm hole radius cavity has a 2 to 6 GHz blue shifted gap compared to the 28 µm one. Resonant fundamental and higher order defect modes arise in the forbidden regions. The frequencies of these defect resonant modes also drift with the gap shifting. It is therefore possible to adjust and tune the cavities resonance frequencies by simply changing the radius of their etched hole. In this work, we focus on studying the fundamental resonant mode behavior, due to its high confinement in the cavity center and its large overlap with acousto-mechanical cavity of the integrated gas sensor.

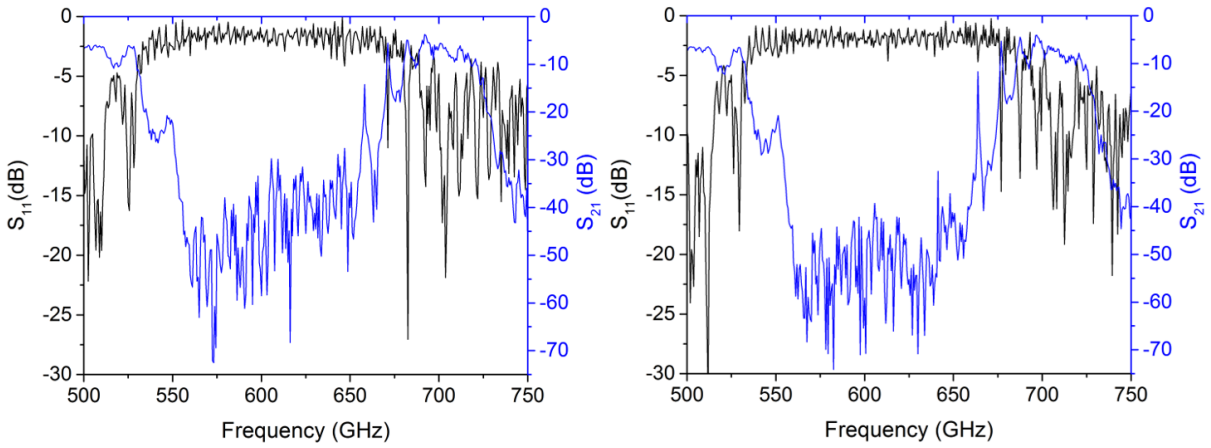

Figure IV.3.3 S_{21} and S_{11} measurements representing the bandgaps and resonance frequencies of two bent structure PhC cavities with the same lattice constant and radius R=28µm (design 1) on the left and R=29µm (design 2) on the right

Figure IV.3.4 plots the S_{21} of the fundamental defect modes, in linear (inset) and logarithmic scale, measured by the finer calibration of the VNA with 8 MHz step size for both structures. The linear scale represents a clear Lorentzian shape of the resonant peaks.

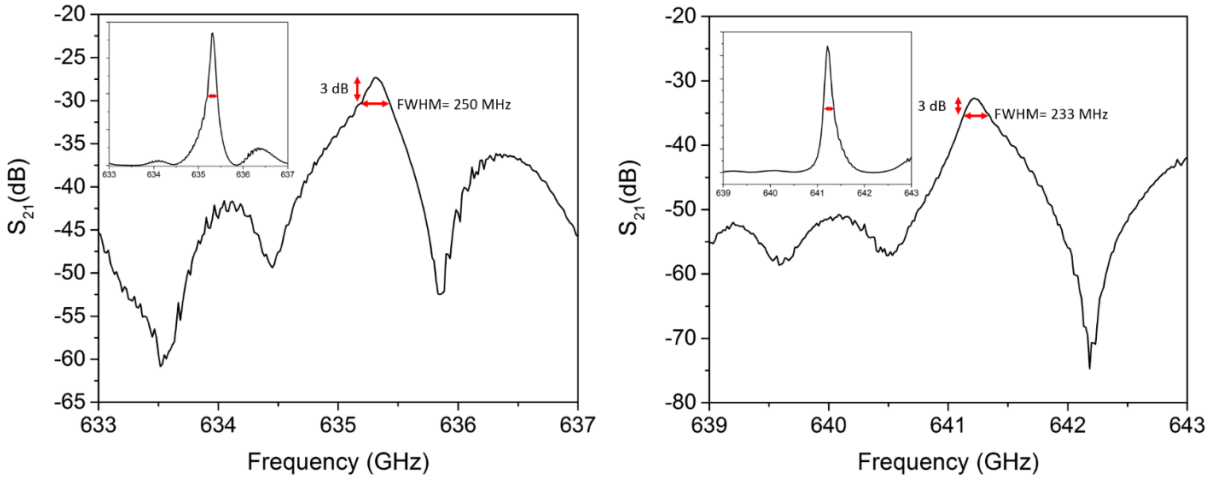

Figure IV.3.4 S_{21} measurements representing the resonance frequencies of two bent structure PhC cavities with same lattice constant variation and radius R=28µm (design 1) on the left and R29=µm (design 2) on the right

The measured resonance frequencies correspond to 635.3 and 641.2 GHz for the sample with hole radii of 28 and 29 µm respectively. These values are blue shifted compared to the numerically calculated ones in chapter II. This discrepancy between experimental and numerical results is mainly due to the radii size error in the fabrication process. The SEM photo of figure IV.3.5 shows the experimental diameter hole size of the structure with a theoretical radius of 29 µm. The experimental radius of this structure is 0.8 µm larger than the design. Therefore the fabrication error is estimated to be less than 3%. However, this error varies from one sample to another. In the next processes, the sizes on the fabrication masks were optimized to reduce this error. To calculate the resonance frequency quality factor we used the following definition:

$$Q = \frac{f_R}{\Delta f} \qquad \text{(IV.3.1)}$$

with f_R the peak resonance frequency, and Δf the resonance width at -3 dB or the FWHM (Full Width Half Maximum). The FWHM of the 28 and 29 µm radii structure are respectively 250 and 230 MHz, giving a Q of 2500 and 2750. These values are much lower than the simulated one shown in table II.3.1 for an HR-Si with an extinction coefficient of $\kappa_{Si}= 3 \times 10^{-5}$. Therefore, the loss value used in the numerical calculations is underestimated. By separating the material losses from other losses phenomenon, we can write the measured inverse quality factor as follows:

$$\frac{1}{Q_{Measured}} = \frac{1}{Q_{Simulated}} + \frac{1}{Q_{Material}} \qquad \text{(IV.3.2)}$$

where $Q_{Measured}$ represents the measured quality factor that includes all type of losses, while $Q_{Simulated}$ is the one calculated numerically in absence of material loss (refractive index imaginary part $\kappa_{Si} = 0$) and $Q_{Material}$ is the quality factor describing the material absorption losses. Using the numerical results of chapter II (table II.3.1) and the one measured here, we can extract a $Q_{Material}$ of 2600 and 2900, equivalent to a decay time constant $\tau = \frac{2Q}{\omega_0} = 1.33 \times 10^{-9}$ and 1.43×10^{-9} s for the 28 and 29 µm radii structure respectievly.

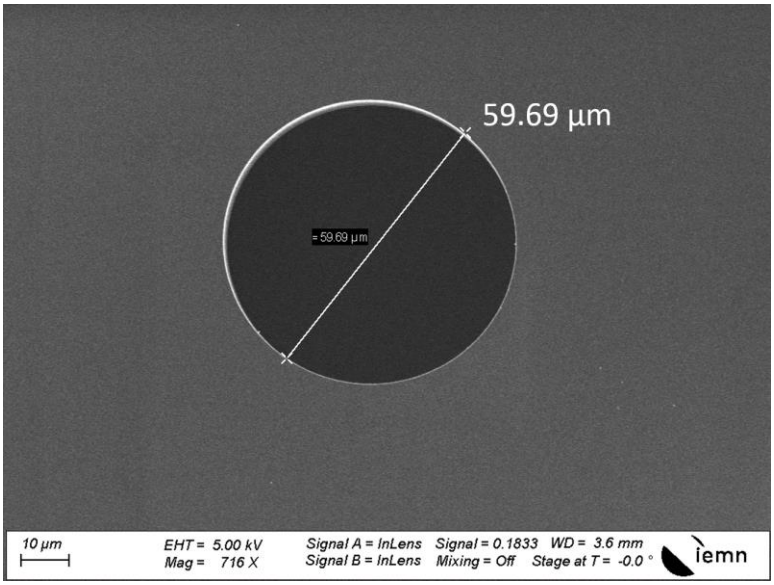

Figure IV.3.5 SEM photo showing the measured diameter of one hole of the PhC cavity design with R=29µm (design number 2)

The simulated results represented in table II.3-1, shows that an extinction coefficient $\kappa_{Si} = 3\times 10^{-5}$, correspond to a $Q_{Material} = 6.7\times 10^{4}$ equivalent to τ=3.4×$10^{-8}s$. Thus by analogy, we can define the material extinction coefficient that corresponds to the previously extracted $Q_{Material}$. The absorption and extinction coefficient are related by:

$$\alpha = \frac{4\pi\kappa_{Si} f}{c} \qquad \text{(IV.3.3)}$$

with f the frequency and c the vacuum speed of light. Following these calculations, we obtain an estimation of the absorption coefficient of the HR-Si wafer used in the technological process. The estimated value corresponds to an α =0.19-0.2 cm^{-1}. This value is a bit high and corresponds to Si resistivity lower than 10 kΩcm. Figure IV.3.6 shows the variation in the absorption coefficient

of the Si as a function of its resistivity, based on the results shown in [11]–[16]. Thus, the HR-Si wafer used in this process might have a resistivity of 1000 kΩcm.

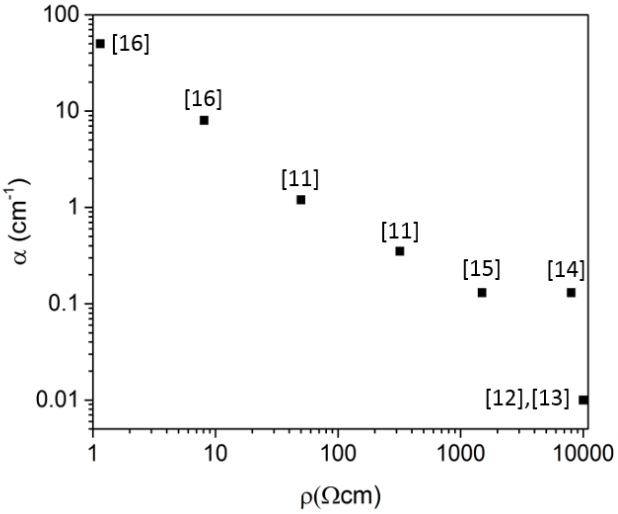

Figure IV.3.6 Plot representing the dependence of the Si absorption coefficient on the material resistivity extracted from [11]–[16]

All the previously presented results belong to cavities fabricated on bent waveguide. Thanks to the taper's ultra-low insertion losses, it is then possible to fabricate and characterize cavities on straight waveguides. Following the same previous measurement steps, we characterized the cavity design with R=29 µm built on top of the straight waveguide. The frequency of the fundamental resonant mode is observed at 640.25 GHz. This frequency value is also blue shifted, but closer to the expectation which explains the lower hole size error. The measurements presented here are done with a butt-coupling configuration (check section IV.1.4), which explains the very low transmission of the resonant mode (-25 dB). This low transmission isn't only limited by the insertion loss but it's the result of the high reflective mirror consisting of 25 etched holes. The high ripples present in the S_{11} measurements are also caused by the bad coupling and the high insertion losses. This cavity presents an ultra-high Q factor of 18800 with a FWHM of 34 MHz. At THz frequencies, a similar design for 100 and 200 GHz frequencies with Q= 11900 and 2200 respectively was demonstrated by [17]. Aside from [17], 1D photonic crystal cavities were very little investigated in the THz region. Other dielectric cavities such as ring resonators and 2D PhC cavities with high-quality factors up to 15000 have been reported [18]–[24]. Therefore, such a Q factor for air confined PhC cavities at THz frequencies is the highest among several and is

measured for the first time. This very high Q is the result of several parameters such as mirrors high reflectivity, gentle Gaussian apodization, and most importantly the very low material absorption loss. Following the same previous calculation steps, we can extract the material absorption loss that corresponds to an absorption coefficient of 0.019 cm^{-1}. Such a low loss value is very close to the one of a 10 kΩcm HR-Si represented in figure IV.3.6. Table IV.3.1 summarizes the experimental and simulated results of the different designs followed by the HR-Si wafers extracted absorption loss values.

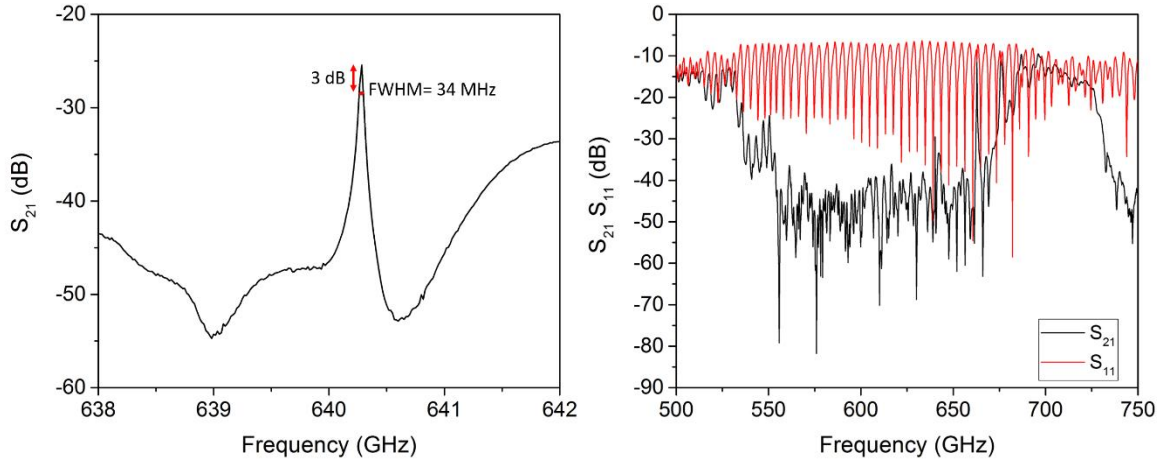

Figure IV.3.7 S_{21} measurement using the fine calibration representing the resonance frequency of the straight waveguide cavity with R=29µm on the left. S parameters representing the bandgap of the same cavity using the large band calibration

Design number	R (µm)	Simulated Q	Simulated f_R (GHz)	Measured f_R (GHz)	Measured Q	Extinction coefficient κ_{Si} (at f_R)	Absorption coefficient α (cm^{-1})
1 (BW)	28	4.7×10^4	630	635.3	2.5×10^3	7.52×10^{-4}	0.20
2 (BW)	29	5.7×10^4	636	641.2	2.7×10^3	7.08×10^{-4}	0.19
2 (SW)	29	5.7×10^4	636	640.25	1.8×10^4	7.08×10^{-5}	0.019

Table IV.3.1 Table summarizing the simulated and experimental results of the PhC cavities with hole radius 28 and 29µm on top of bended waveguide (BW) and straight waveguide (SW). The absorption and extinction coefficients are the ones extracted from the calculations.

IV.3.3 High transmittance cavities

In the previous section, we presented the result of ultra-high Q cavity that may be useful in many applications. More especially for the proposed gas sensor design, this cavity allows to enhance the light molecules interaction and therefore a higher photoacoustic signal is generated and detected. However, some other application beyond the photoacoustic requires detection of the THz signal and therefore for such applications higher transmission is necessary. We propose in this section the measurements of cavities with high Q factors and high transmittance. The main reason for having low transmittance in the previous design is the highly reflective mirror with a large number of etched holes (N=25). Therefore, we produced the same design with a fewer number of holes to reduce the mirror reflectivity and thus increase the defect mode transmittance. The S parameters measurements of two 29µm hole radii structures with 21 and 17 total number of etched holes are represented in figure IV.3.8. As expected the Lorentzian peak of these resonant modes is wider than the previous one. Thus the quality factor is decreasing from 1.88×10^4 for N=25 to 7×10^3 and 1.5×10^3 respectively for cavities with N=21 and 17.

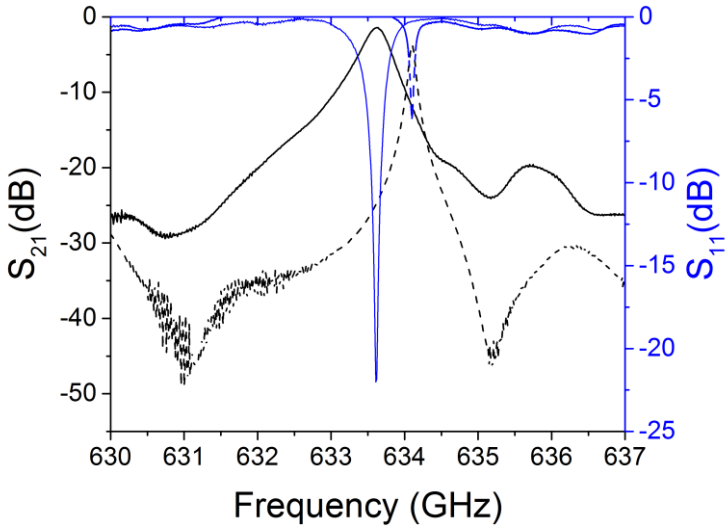

Figure IV.3.8 Resonance frequencies at f_R = 634.1 and 633.63 GHz, for cavities with N=21 (dashed lines) and 17 (solid lines) hole respectively

The resonance frequencies are red shifted with respect to the one with N=25. For the cavity with N=21, the resonance frequency is observed at 634.1 GHz while the one with N=17 is at 633.63GHz. However, the transmission is increasing, to reach up to 72% of transmittance (-1.4

dB) for N=17, while the mode is almost not reflected with less than 1% of reflectance (-22 dB). Similarly, for the cavity with 21 holes, S_{21}= -3.7 dB (42%) and S_{11}= -6.2 dB (24%). Despite the low mirror reflectance in these designs, their measured quality factor remains higher and comparable to the one fabricated on wafers with lower resistivity.

IV.3.4 650 GHz cavities

The concept behind designing these types of high Q cavities is to have a highly confined electric field at the THz absorption frequency of a polar gas molecule, in order to increase the gas sensor detection limit. In this gas sensor design we target the H_2S gas, and notably the 650.37 GHz spectral line. This gas is an important food spoilage indicator, and its 650.37 GHz spectral line is the strongest among all the others in the THz AMC source frequency range (620-680 GHz). Therefore, in chapter II several adjusted designs with resonant defect mode frequencies around 650 GHz were proposed. In this section, the measurements of design number 3.1 are discussed. The measurements were done with two different methods. The first one using a synchronized detection with a Pyroelectric detector and an AMC THz source (check III.2.3). While the second method is the one used previously which consists of the extraction of S parameters with VNA.

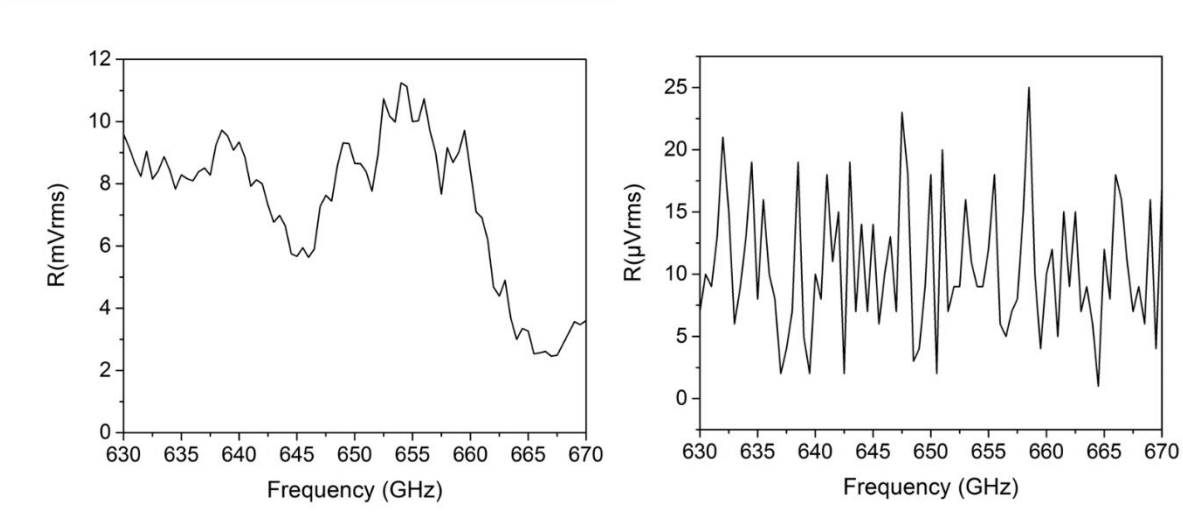

Figure IV.3.9 AMC source power on the left and noise floor on the right detected with a pyroelectric detector

The left-handed side of figure IV.3.9 represents the AMC source signal detected directly with the pyroelectric detector, while the right-handed side corresponds to the measured noise floor with an integration time of 23 ms. This method then provides a SNR_{dB} of 40-60 dB. The disadvantage of

this technique is that it requires a long integration time and it's highly impacted by the environmental thermal and acoustical fluctuations. The measured transmission of the cavity design with 650 GHz resonant frequency (design number 3.1) is represented in figure IV.3.10. No resonance is observable and the measured signal is close to the noise level. The two wide peaks appearing in the spectrum correspond to the source AMC power variation versus its output frequency and can be eliminated by normalization.

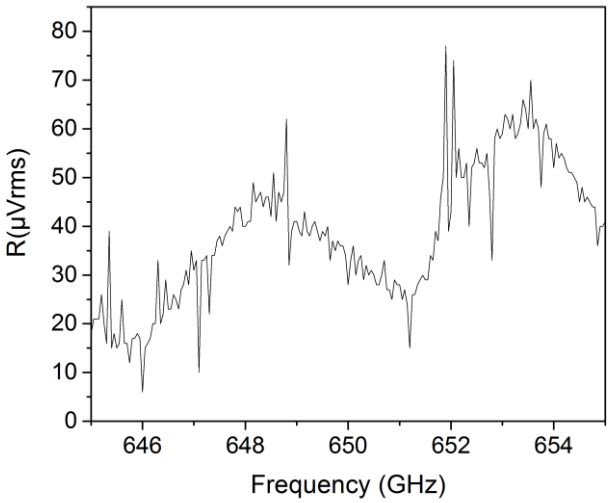

Figure IV.3.10 Detected signal of the 650 GHz PhC cavity using the synchronized detection with the AMC source and pyroelectric detector

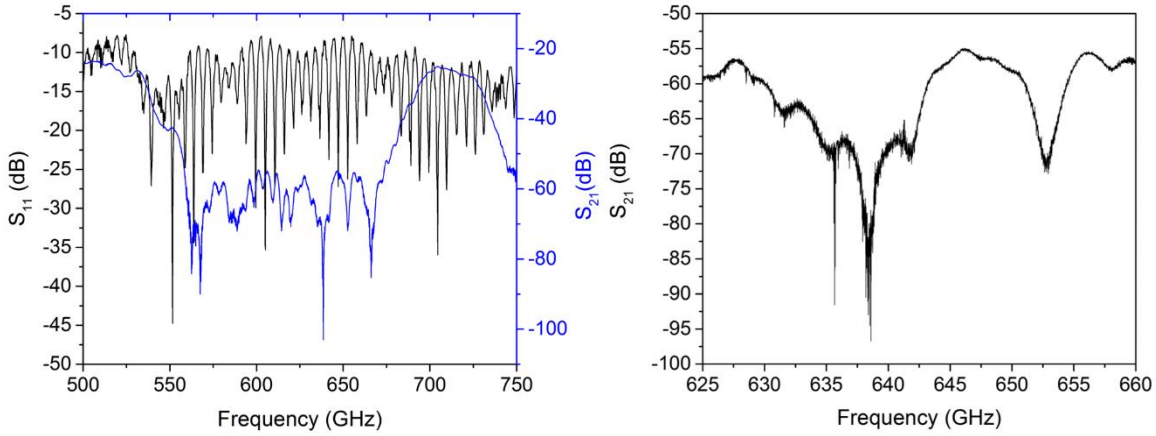

Figure IV.3.11 S parameters of the 650 GHz PhC cavity with the full band calibration on the left and the finer calibration on the right

Since no resonance is detected with this technique, the same structure was then characterized with the VNA that offers a larger dynamic range and higher sensitivity. The measured S parameters presented in figure IV.3.11 are in agreement with the previous measurements. No resonance peak is detected between 625 and 660 GHz. While in the large frequency band, a large bandgap is observable only through the transmission. While for the S_{11} measurements, strong ripples with a reflection upper level of -10 dB are observable. The highest transmitted power in the allowed conduction band is below -25 dB. Such very low transmittance is the result of huge losses. Hence the total dissipation of the defect resonant mode. To understand the origin of losses, unpatterned straight, and bended waveguides fabricated on the same wafer process as the 650 GHz cavities designs were measured using the VNA. Figure IV.3.12 represents the photos of the measured structures on the left and the plot of their S_{21} magnitudes on the right. The three measured structures correspond to one straight waveguide of 2.75 cm length, a 10.6 cm long waveguide including 4 bends of 400 µm radius each, and finally the third one with 40 bends and a total length of 3.26 cm. As expected the propagation losses are important and increase with the length of the waveguide. Almost 18 dB of the power at 600 GHz is lost after traveling 2.75 cm inside the Silicon. These huge loss values could only be attributed to the Si absorption since the waveguide is fully suspended in the air. It is quite complicated to extract an exact value of the propagation loss in dB/cm due to the lack of structure length variation and the different number of bends in each measured structure.

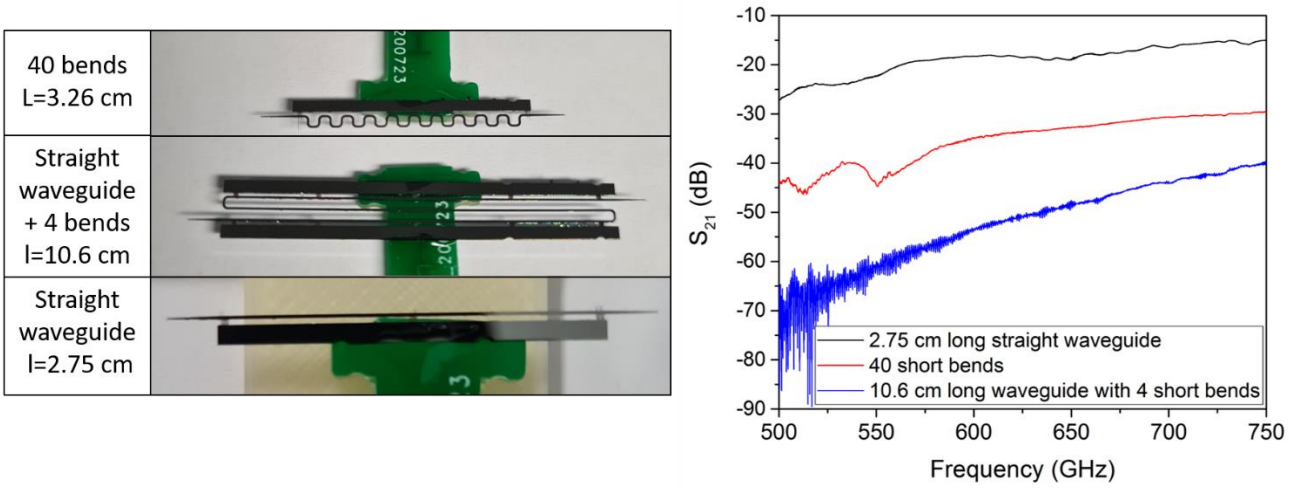

Figure IV.3.12 Photos of the measured structure on the left and their S_{21} plot on the right

Considering the bend radiation and material absorption losses as the only source of loss, it is possible then to express the measured loss as follows:

$$loss = l\alpha + N\alpha_B \quad \text{(IV.3.4)}$$

With loss representing the measured S_{21} in dB, l the structure total length in cm, α the propagation loss (or material absorption loss) in dB/cm, N the number of bends and α_B the bend radiative loss in dB/bend. By this is we obtain a system of three equations with two unknowns (α and α_B). Solving this system of equations gives an approximate value of propagation loss α=5-6 dB/cm (at 600 GHz) and bend loss α_B=0.3-0.5 dB/bend. As represented in figure IV.3.4, this value of propagation loss α=5-6 dB/cm belongs to a Si wafer with 10's Ωcm of resistivity. All the fabrication processes in this work were done on an SOI wafer with 90 µm of HR-Si active region bonded on a 300 µm thick ordinary Si substrate with 2 µm of SiO_2. We discussed earlier in this work the impact of the active region resistivity on the propagation losses and cavities quality factor. However, for this last process, we believe that the active region and substrate material of the SOI wafer were inverted and thus are the result of an error with the manufacturer. This is under further investigation.

We presented in the first part of this chapter, the different characterization results of the THz waveguide and cavities. Waveguide with low propagation losses was reported with an extracted upper limit of 0.9 dB/cm. PhC cavities with tunable resonance frequency were presented. Cavities with high Q factors and high transmittance were also demonstrated thanks to the very low loss of the HR-Si platform. We also discussed the measurements of the gas sensor optimized cavities designs, with 650 GHz resonant frequency. These measurements were dominated by the huge losses of the Si wafer.

Even though the final demonstration of the THz resonant cavity at the H_2S absorption peak wasn't achieved, the presented results are highly promising and validate the concept of the sensor's THz optical cavity.

The next part of this chapter is dedicated to the characterization of the gas sensor acousto-mechanical part.

Part II: Mechanical characterization

In chapter II we presented the concept and design of the proposed photoacoustic gas sensor. To remind, this sensor is composed of three main parts: the THz cavity, acoustic cavity, and finally the mechanical resonator. The first part of this chapter was dedicated to present the promising results on the THz high Q cavity and the low THz losses of the sensor's guiding platform.

The THz cavity created by etching air holes in the core of a Si waveguide is itself the acoustical cavity. One etched hole of 29 µm radius and 90 µm height represents an acoustic cylinder or pipe. The bottom ends of these cylinders are covered by a 100 nm thick stretched Poly-Si membrane, which represents the mechanical resonator. In this part, we present the characterization results of the Si acoustic cylinder and the Poly-Si membrane.

IV.4. Pt layer deposition on Poly-Si membranes

The acousto-mechanical characterization process consists of detecting the resonance frequencies and quality factors of the mechanical membrane and acoustic cylinder. The LDV is used to detect optically the displacement of the Poly-Si membrane and thus its resonance frequency. The laser beam of the vibrometer experiences a Doppler shift upon reflection on the movable surface of the membrane, and thus a displacement is extracted from the detected reflected beam. However, the LDV laser beam of 630 nm wavelength is transmitted through the 100 nm thick membrane [25], [26]. Therefore, an additive metal layer is necessary to ensure the reflection of the laser. The presence of metals on the Si guiding channel is undesired, as it might increase the THz propagation losses. A local metal coating only on the Poly-Si membrane surface is therefore crucial. To prevent additional lithographic and technological processes, the FIB is used to locally coat the Poly-Si membrane with platinum metal. In presence of metals, the membrane has a different effective mass and stress. Thus, the mechanical resonance frequency and quality factors of the membrane will highly depend on the properties of the added metal layer (thickness, deposition surface, mass…). To understand the effect of the added metal film on the resonator, several Pt depositions were applied on different membranes of a 29 µm radius.

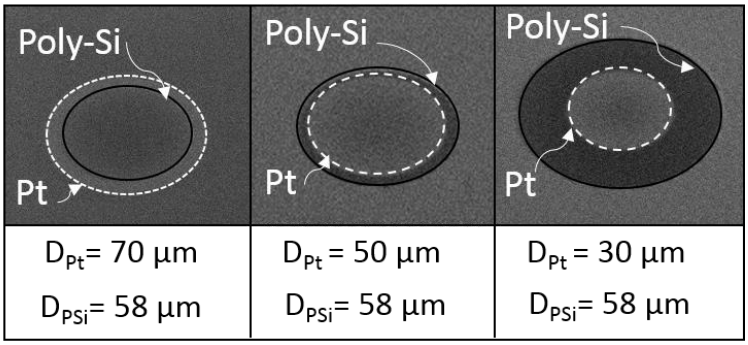

Figure IV.4.1 SEM images of Poly-Si membranes of 29µm radii size with three coated Pt layer of different sizes

Figure IV.4.1 shows SEM images of three Poly-Si membranes coated by three different sizes of Pt layer. The Pt layers selected sizes represent:

1- A layer with a diameter of 70 µm, larger than the Poly-Si membrane size, and extended to the Si cylinder border.
2- The 50 µm Pt layer almost fully covers the Poly-Si membrane without masking the edges.
3- And finally, the third layer of 30µm represent a local mass on the center of the Poly-Si membrane.

Each of these metal layers was reproduced multiple times with different thicknesses. All these metal coatings were done on the same waveguide and with the same deposition parameters (dwell time= 0.2µs, overlap -200%, and ion beam intensity of 3nA) (see chapter III, section III.3.3). The only changing parameter is the deposition time that controls the thickness of the layer. The 70 µm Pt layer was produced four times with respective deposition times: 60, 90, 120, and 150 s. Similarly, five and three different thicknesses were applied for the membranes with 50 and 30µm Pt layers respectively. The deposition time of these structures is respectively 20, 40, 60, 80, and 100s with 50 µm diameter and 10, 20, and 30 s for the 30 µm one. To measure the thickness of the added metal, reference layers with the same deposition parameters as the one added on the Poly-Si membranes were coated nearby on the Si guiding channel. Three reference layers corresponding to the 60 and 100 s deposition time of the 50 µm Pt layer and the 30 s related to the 30 µm one were added. The thicknesses of these reference layers were measured using a profilometer. Figure IV.4.2 represents SEM images showing the different coated metal layers and the three others used as references for the thickness measurements. In the same figure, schematics illustrating the profiles of the layers measured with the profilometer are shown. The edges of these layers are

thicker than their centers. Therefore, the metallization process is not uniform. This phenomenon is also observable in the SEM photos that show a contrast between the center and the edges of the metalized zones.

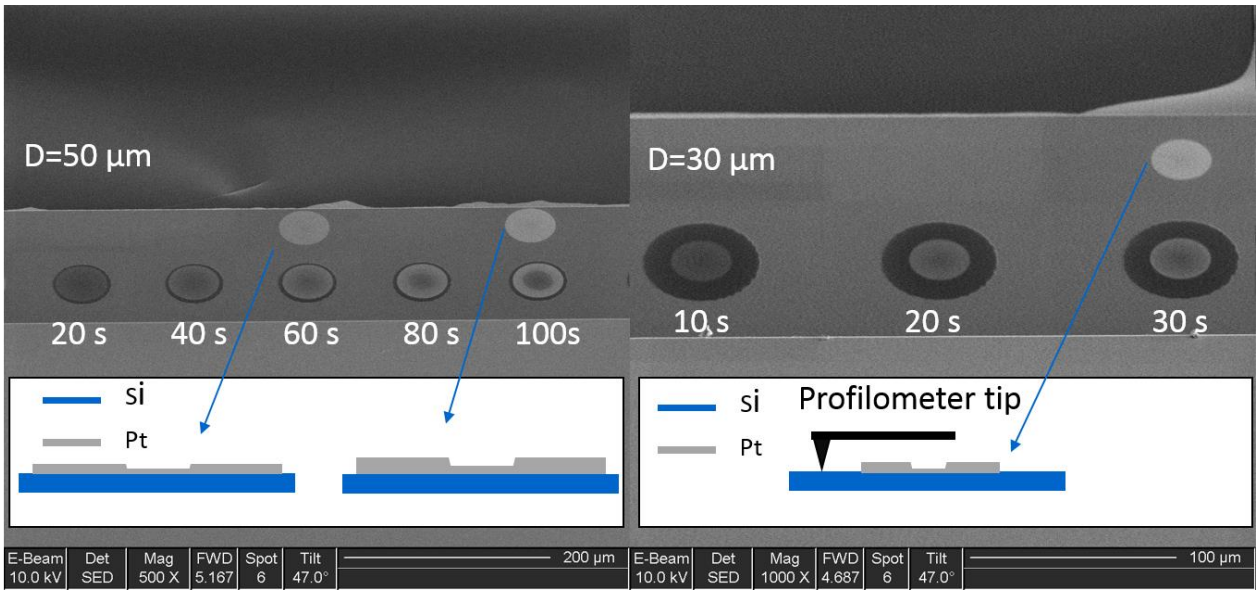

Figure IV.4.2 SEM images representing the reference coated layer and a schematic representing the measurements of their thicknesses with the profilometer

Pt layer diameter	Deposition time (s)	Estimated edges thickness (nm)	Estimated center thickness (nm)
70 µm	60	26	20
	90	39	30
	120	51	40
	150	64	50
50 µm	20	17	13
	40	33	26
	60	50 (measured 53 nm)	40 (measured 45 nm)
	80	67	53
	100	84 (measured 83 nm)	66 (measured 65 nm)
30 µm	10	23	18
	20	46	37
	30	70 (measured 68 nm)	55 (measured 55 nm)

Table IV.4.1 Table representing the estimated thicknesses of the different deposited Pt layers

Since the thickness is directly proportional to the deposition surface and time, we can then extract from the three measured reference layers an approximate deposition rate of 1.64 $\mu m^3/s$ for the edges and 1.3 $\mu m^3/s$ at the center. Table IV.4.1 represents the approximate extracted thicknesses of the different Pt depositions. The real values of the measured reference thicknesses are very close to the ones estimated from the approximate defined deposition rate. Figure IV.4.3 shows the size of the metals deposed on the 50 and 30µm surfaces using an optical microscopic image. The experimental dimensions of the metalized surfaces are very close to those targeted, with an error of less than 4%. Finally, it can be stated that the FIB technique is a great tool for the direct growth of local thin metal layers. However, it suffers from the metals' impure qualities and inhomogeneous depositions. We observed more metal growth at the edges of the films than in the center. For thin layers, this level discrepancy effect remains small, but it becomes more important for thicker layers.

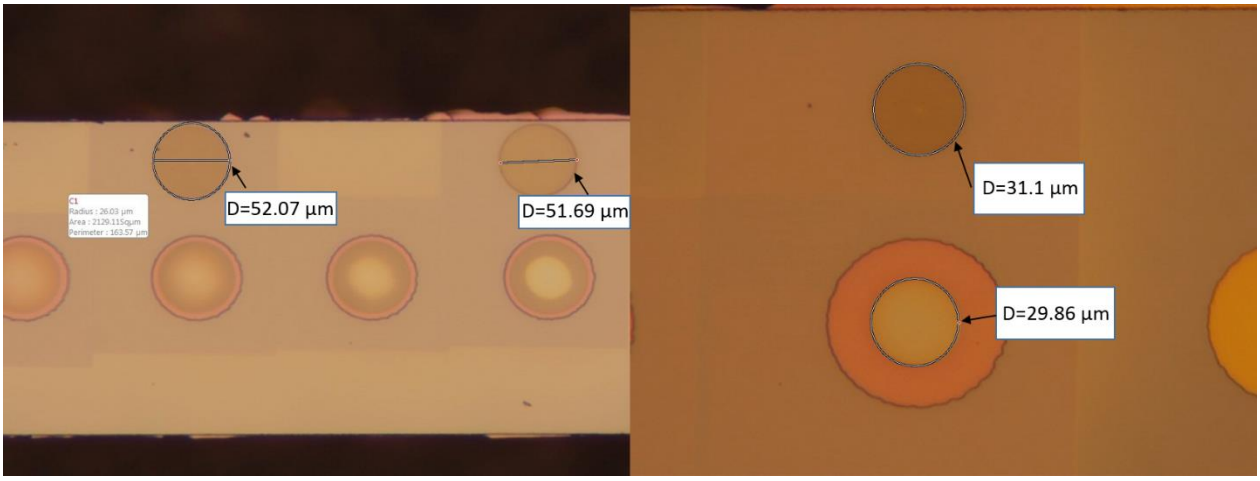

Figure IV.4.3 Optical microscopic image representing the measured size of the 50 µm Pt deposition reference layers on the left and the 30 µm one on the right

IV.5. POLY-SI MEMBRANE RESONANCE FREQUENCY AT ATMOSPHERIC PRESSURE

In the previous section, we discussed the metallization of the Poly-Si membrane with several Pt layers of different dimensions and thicknesses. This part presents the measurements of these membranes at the atmospheric conditions and discusses the impact of the added metals. While the displacement of the membrane is detected by the LDV, another optical setup is used to drive the membranes by a photothermal effect. An amplitude modulated blue laser beam is focused on the

surface of the membrane. The modulated light absorbed by the membrane is transformed into a thermal wave, and thus a mechanical motion of the membrane at the modulation frequency of the laser. However, this effect could be limited to hundreds of kHz due to the low thermal conductivity κ (149 W/m/k) and high specific heat c_p (703 J/Kg/k) of the Poly-Si membrane. Thanks to the presence of the platinum layer, the thermal expansion coefficient differences between the two materials lead to an additional bending stress that improves the membrane's mechanical motion. The blue laser is focused with a spot size in the order of 5 to 10 µm on the center of the membrane to overlap with the fundamental mechanical mode of the membrane. The output power reaching the membrane was fixed to 450 µw with a 30 to 50% of modulation depth. The modulation frequency of the laser is swept from 100 kHz up to 2 MHz through an internal oscillator of the lock-in. The amplitude and phase are measured with the vibrometer and then decoded by the lock-in. Once the resonance frequency is detected, a tighter sweeping frequency BW is used to record the signal.

Figure IV.5.1 shows the amplitude of the resonant frequencies related to the membranes with 50µm Pt layer and different thicknesses. The resonance frequency highly depends on the thickness of the metal layer. For thicker metal layers the resonance is shifting to the higher frequencies except for the thickest layer of 66 nm. This exception could be attributed to the inhomogeneous metal layer.

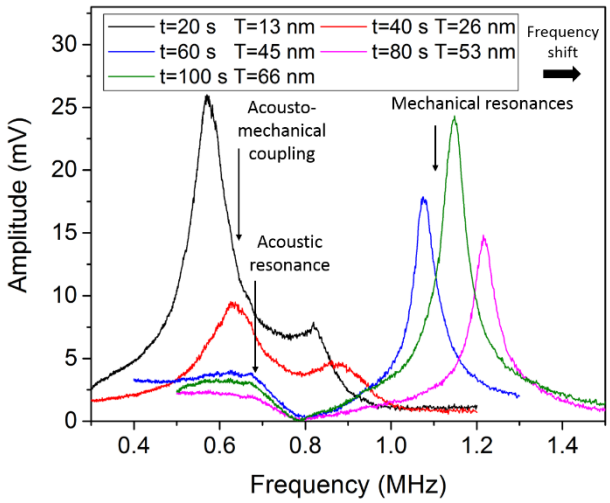

Figure IV.5.1 The measured mechanical resonance frequencies of the membranes with 50µm metal layers and different thicknesses

The measurements of the membranes with 45, 53, and 66 nm thick metal layers show Lorentzian peaks at the respect frequencies 1.07, 1.21, and 1.15 MHz with a quality factor $Q = \frac{f_0}{\Delta f}$ = 14±1. The low-quality factor is the result of the high drag losses in the viscous regime at the atmospheric pressure level. Smaller and wider peaks are barely seen at the lower frequencies between 670 and 690 kHz. We believe that these small peaks might correspond to the resonance frequency of the acoustical cylinder expected at 710 kHz.The other two membranes with thinner metal layers (13 and 26 nm) present double peaks at 570-820 kHz and 630-870 kHz respectively. These double peaks are attributed to the acousto-mechanical strong coupling between the mechanical and acoustical resonators. This coupling occurs when the metal load shifts the Poly-Si mechanical resonant frequency to overlap with the acoustical one resulting in a frequency splitting. The coupling strength is defined by the relative-frequency splitting which corresponds to 250 and 240 kHz for the membranes with respectively 13 and 26 nm thick metal layer. Therefore, it can be stated that this coupling is in the strong coupling regime. This coupling was expected from the simulation presented in figure 6 of [27]. The strong coupling of Graphene-SiN membranes mechanical resonators was presented in [28], [29], while in [30] the intermodal hybridization of a MoS_2 membrane was reported. We present here a first observation of a mechanical Poly-Si membrane and a Si cylinder resonators coupling. However, the validation of the strong coupling demonstration requires additional observations and further research work.

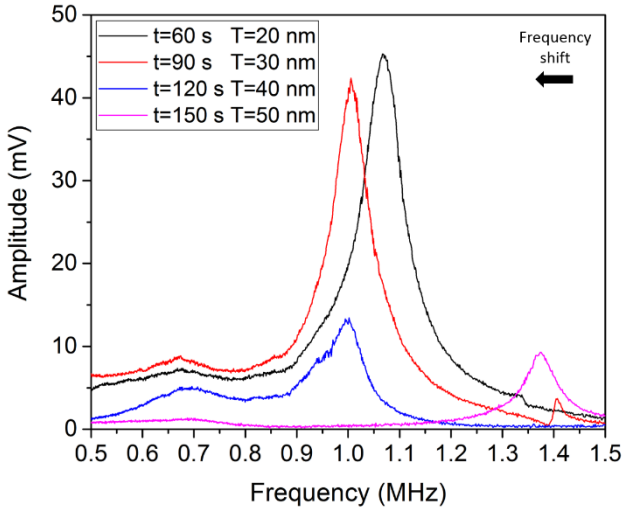

Figure IV.5.2 The measured mechanical resonance frequencies of the membranes with 70µm metal layers and different thicknesses

The measurements of the 70 µm Pt layer are represented in figure IV.5.2. Contrarily to the membranes with 50 µm of metalized surfaces, the resonance frequency is red shifting for thicker metal layers. Therefore, the added metal is increasing the membrane's effective mass. Since the 70 µm, Pt layer is reaching the Si cylinder borders, it has a lower impact on the stress of the membrane. The small peaks attributed to the acoustical resonance are also observed around 690 kHz. The resonant frequencies of the fundamental mechanical modes for the membranes with 20,30 and 40 nm thick metal layer are 1.07, 1.01, and 1 MHz respectively. The measured quality factor (Q= 9±1) of these peaks is slightly lower than the ones with smaller metal surfaces. This effect of the metal covering entirely the surface on the quality factor is clearly observed and discussed in [31]. The membrane with the thickest metal layer shows a resonant mode at 1.38 MHz with a Q=16±1. This is a higher order mode, while the fundamental mode isn't detected, which could be due to bad positioning of the blue actuating laser.

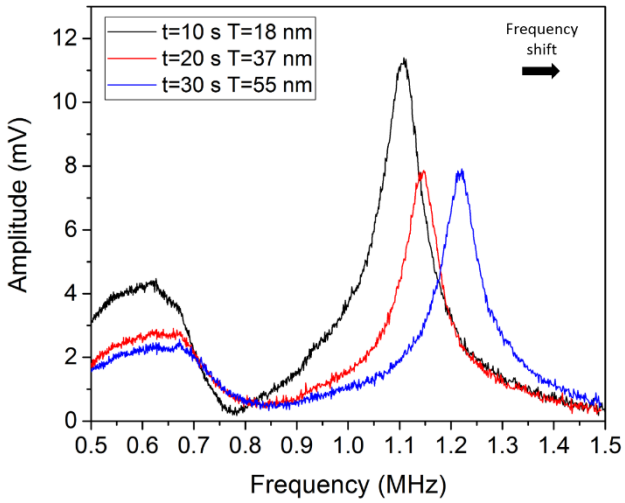

Figure IV.5.3 The measured mechanical resonance frequencies of the membranes with 30µm metal layers and different thicknesses

As shown in chapter II (II.1) the resonance frequency of a membrane mechanical resonator is proportional to $\sqrt{\frac{\sigma_i}{\rho}}$, where σ_i are the internal stress of the membrane and ρ its mass density. Therefore, for the structures with a 30 µm metalized surface, the change in membrane stress is dominant over the variation in mass, leading to higher resonant frequencies for the increased metal thicknesses in figure IV.5.3. The mechanical resonance frequency shifts from 1.1, to 1.14 and then 1.21 MHz by increasing the thickness of the Pt film from 18 to 37 and 55 nm respectively. The quality factor of these modes is Q=12 ±1.

We observed in this part the several effects of metals on the mechanical resonance frequency of the Poly-Si membrane. It is possible to control the position of the resonance frequency by 100's of kHz by adjusting the parameters of the added metal layer. This mechanical frequency tuning shows the avoided crossing and coupling with the acoustical resonance. Finally, at the atmospheric pressure level, the losses due to the added metal layer are negligible and the quality factor is limited by the medium viscosity. In the following section, we present the experimental measurements at low pressure levels where the drag losses are eliminated.

IV.6. POLY-SI MEMBRANE RESONANCE FREQUENCY AT LOW PRESSURES

The gas sensor is designed to detect gas molecules at different pressure levels. Therefore, it necessary to characterize the behavior of the acousto-mechanical resonators at low pressures. In this section, we present the measurements of the membranes with different metallization at several pressure levels. The characterization setup is the same as that used to measure the resonant frequencies at atmospheric pressure level. However, for these experiments, the samples were mounted inside a vacuum chamber to control the pressure (see figure IV.6.1). The vacuum chamber is initially designed to be used in gas measurement experiments and its details will, therefore, be introduced in the next chapter.

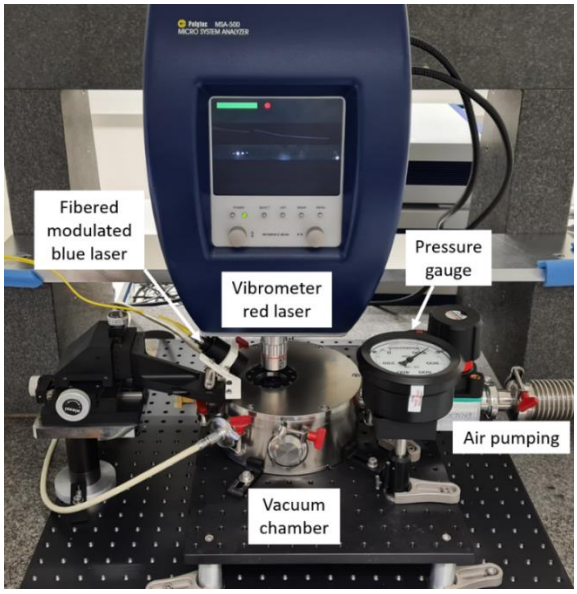

Figure IV.6.1 Experimental setup of the mechanical characterization at low pressures

Figure IV.6.2 represents the resonant frequency measurement of the membrane with a metal surface of 70 µm diameter and a thickness of 40 nm. The pressure inside the chamber is changing from 40 mbar up to 1 bar (atmospheric pressure level). The blue laser power is fixed at 400 µw with a 30 to 50% of modulation depth. At the atmospheric pressure, the mechanical resonant frequency is observed at 1.055 MHz. This value is 55 kHz higher than the one presented in the previous section for the same structure at the same atmospheric conditions but with a higher actuating laser power of 450 µw. Therefore, this small shift is due to the heating of the membrane. At lower pressure, the mechanical resonance peak becomes finer without any remarkable frequency shift. Below the atmospheric pressure level, the Lorentzian shape of the resonance is distorted by strong fluctuations of the signal amplitude. It is then complicated to extract the quality factors at low pressures.

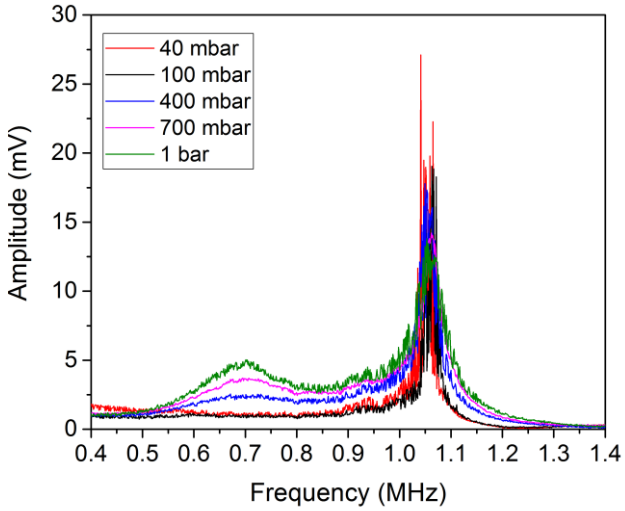

Figure IV.6.2 The dependence of the resonant frequency on the pressure for the membrane with a 70 µm metal layer diameter and a thickness of 40 nm

A gradual disappearance of the peak near 690 kHz is also observed with the decreasing of the pressure. To understand this, we have to introduce the Knudsen number Kn. The Knudsen number, Kn, is the ratio between the molecular mean free path and the relevant physical length defined in this case by the acoustical cylinder radius. This ratio can be written as follows:

$$k_n = \frac{k_B T}{\sqrt{2}\pi d^2 P R} \qquad \text{(IV.6.1)}$$

Where $k_B = 1.38064852 \times 10^{-23}$ m^2kg/ s^2K, T=298 K the working temperature, d the gas molecule collisional diameter, for air d= 4.9×10^{-10}m for the air [32], P the pressure in Pa and R=29×10^{-6} µm the cylinder radius. The Knudsen number is inversely proportional to the pressure and used to determine the gas rarefaction. At high pressure and for a low $K_n < 0.01$ the air is considered as a continuum flow, while for lower pressure and a $K_n > 10$ the gas is considered as free molecules [33]. At pressures below 130 mbar (Kn > 0.01), the air inside the acoustical cylinder is no more considered as a continuum viscous fluid and the peak near 690 kHz totally vanishes. Therefore, it can be confirmed that the natural origin of this peak belongs well to the acoustical resonance.

In the previous section, an acousto-mechanical coupling was observed in the measurements of the membrane with 50 µm large and 13 nm thick Pt layer. In this section, the impact of the pressure variation on this coupling is discussed and presented in figure IV.6.3. These measurements were also achieved by fixing the blue laser beam at the center of the membrane with a modulation depth between 30 and 50 % and a power of 400 µw. As expected at low pressures and in the absence of air acoustic resonance only one peak appears at 740 and 715 kHz for the respective pressures of 50 and 100 mbar. The mechanical resonance is shifting to the lower frequencies due to the increased effective mass exerted by the fluid on the membrane. The distorted Lorentzian shape of the peak at low pressures might be the result of nonlinear vibration. This nonlinearity is the result of the change in the restoring force due to the large vibration amplitude at low pressures[34].

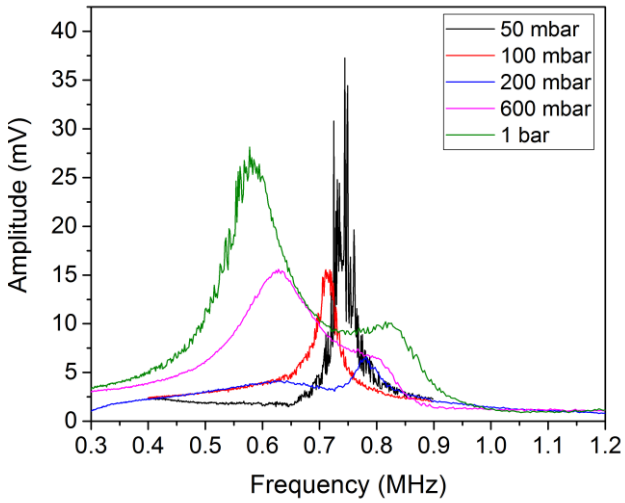

Figure IV.6.3 The dependence of the resonance frequency on the pressure for the membrane with a 50 µm metal layer diameter and a thickness of 13 nm

At higher pressure levels, the mechanical resonance continues shifting to the lower frequencies where it couples with the acoustical resonance and splits into two peaks. The coupling strength depends on the position of the mechanical resonance and its overlap with the acoustical one. At 1 Bar and in agreement with the previous measurements, the hybridized modes appear at 570 and 820 kHz.

The last structures are the ones with a 30 µm of metal surface. The measurements result of this membrane with an 18 nm Pt thick layer are shown in figure IV.6.4.

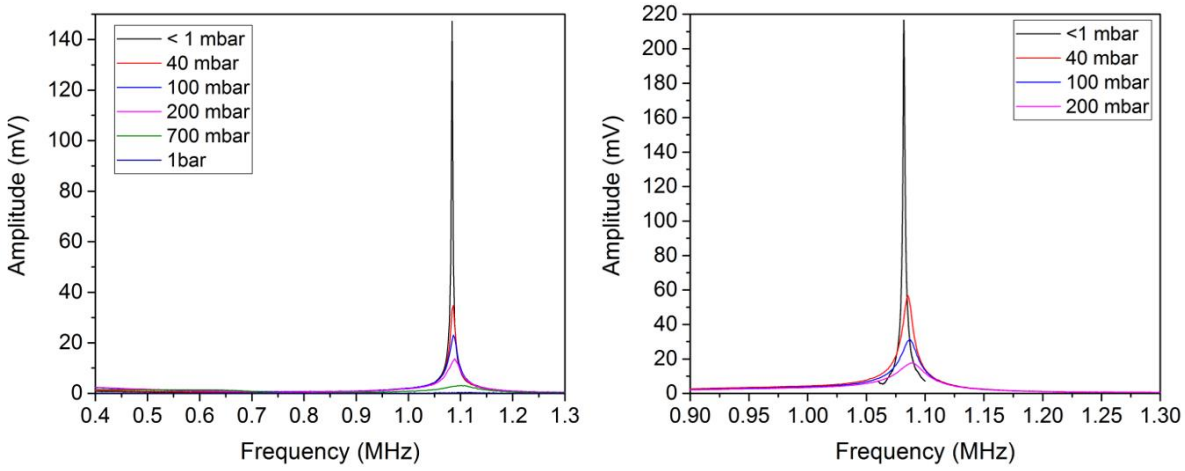

Figure IV.6.4 The dependence of the resonance frequency on the pressure for the membrane with a 30 µm metal layer diameter and a thickness of 18 nm on the left. The right side represents the resonant frequencies at low pressure with a tighter frequency BW

This structure has a very different behavior compared to the previous one. Contrarily to the structure with a Pt diameter of 50µm, the resonance frequency is blue shifted from vacuum to atmospheric pressure. However, this shift is very low less than 30Hz/mbar in the viscous regime (between 200 and 1000 mbar) and almost negligible in the molecular regime (< 200 mbar). The Lorentzian shape of the peak is conserved even at vacuum pressures below 1 mbar. Thus, in contrast to the other membranes, this structure represents a linear vibration. The quality factor of the resonance increases from 10 to 50 with the pressure variation going from atmospheric to 100 mbar. This higher quality factor is due to the elimination of the air drag losses. In the molecular regime, where the losses are induced by the membrane-molecules collision, higher quality factors up to 80 at 40 mbar and 550 at pressures below < 1 mbar are measured. It might be possible to measure highest quality factor at lower pressure where the mechanical dissipation is limited by

intrinsic losses. However, this wasn't measured here since it has no importance for food quality control gas sensing application.

The measurements of the same 30µm metalized membrane with thicker metal layer of 37 nm are illustrated in Figure IV.6.5. For thicker metal, the frequency shifting is more important. It is possible to extract large quality factors up to 80 at 60 mbar. However, at lower pressure (below 1 mbar) a nonlinear effect appears. Therefore, this nonlinearity might be attributed to geometrical effect related to the surface and thickness of the added metal.

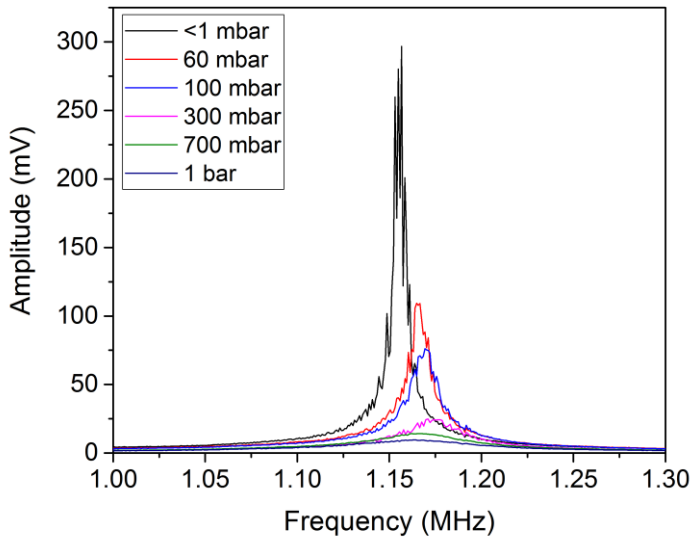

Figure IV.6.5 The dependence of the resonance frequency on the pressure for the membrane with a 30 µm metal layer diameter and a thickness of 37 nm on the left

Figure IV.6.6 shows a comparison of the thermal effect on the behavior of the mechanical resonance between the two membranes of 30µm metal layer with a thickness of 18 and 37 nm respectively. These two measurements were done at a pressure below 1 mbar. The power of the actuating laser is changing from 100 to 450 µw. The membrane with a Lorentzian peak and linear vibration shows an increase in vibration amplitude while its resonant frequency remains unchanged for higher laser power (figure IV.6.6 (a)). Therefore, all the heat energy created by the absorption of the light is transformed into a mechanical displacement of the membrane. However, for the membrane with a thicker Pt layer (37 nm), in addition to the increase in amplitude, a frequency drift is observed due to thermal effects. By increasing the laser power, some of the thermal energy induces a softening of the membrane leading to a red shifting of the resonant frequency. Therefore, it can be concluded that the added non-uniform metal layer has a significant impact on the mechanical resonance of the membrane. Nonlinear vibrations and spring softening

and hardening due to thermal effects increase for thicker and larger metal layers. It is then necessary to reduce the size and the thickness of the metal layer covering the center of the membrane.

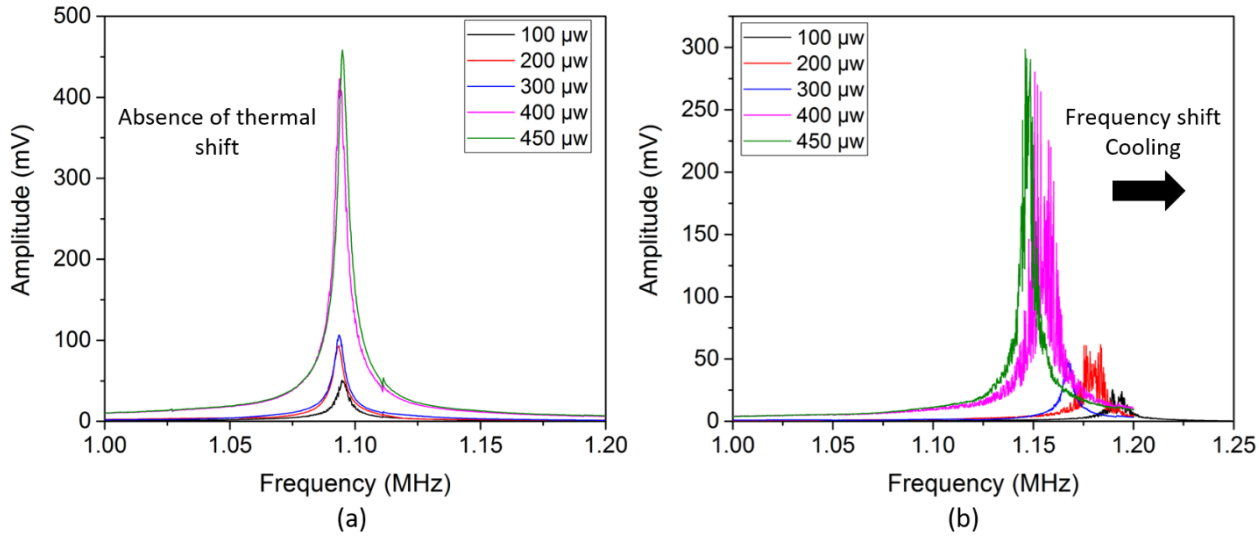

Figure IV.6.6 The dependence of the resonance frequency on the actuating laser power for the membrane with 30µm metal layer diameter and a thickness of:18 nm (a), 37 nm (b)

In the last part of the mechanical characterization, we measured the profile of the fundamental mode of the membrane covered by a 30 µm diameter and 18 nm thick Pt layer. The LDV red laser was mapped on the surface of the membrane to measure the displacement at the resonant frequency at different points of the membrane. Figure IV.6.7 shows the image of the experimental mode on the left compared to a simulated one on the right. The experimental mode with a central maximum is quite similar to the one observed in the simulation. The simulation was done by using the simple example of a vibrating membrane based on an analytical approach with COMSOL multiphysics.

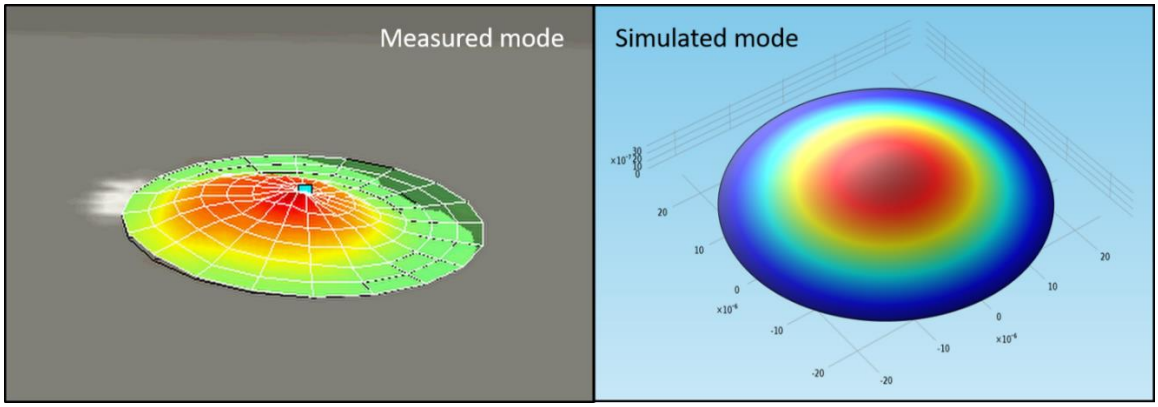

Figure IV.6.7 On the left: the measured profile of the fundamental mechanical mode for the membrane with 30 µm diameter metal layer and a thickness of 18 nm at a pressure < 1mbar. On the right: a COMSOL multiphysics simulated fundamental mode of a single poly-Si membrane with no metal layer

IV.7. CONCLUSION OF THIS CHAPTER

This chapter summarizes the experimental characterization results of the different parts of the gas sensor. In the first part, we presented the measurements related to the THz electromagnetic part of the design. An average propagation loss of 0.065 dB/mm for the HR-Si guiding channel was extracted. We demonstrated very low insertion losses below 0.5 dB for a transition of the THz energy from a WR-1.5 metallic waveguide to the Si waveguide through an inverted taper. A multimodal analysis of the Si waveguide was also reported. We showed the measurements of an ultra-high Q THz cavity at 640 GHz. Such demonstration is a promising result towards the integration of a THz cavity in the gas sensor at the gas molecule absorption peak (i.e. at 650 GHz for the H_2S). Other PhC cavities and Bragg reflector were also reported.

In the second part, we discussed the characterization results of the mechanical part. We demonstrated the possibility of tuning the mechanical resonance frequency by adjusting the parameter of an additional metal layer. The acousto-mechanical coupling between the Poly-Si membrane and the Si acoustical cylinder has been experimentally proven. We presented the effect of the pressure variation on the frequency shifting and mechanical quality factors. We also measured a good mechanical quality factor of about 550. The higher Q factors of the purely mechanical modes compared to the hybrid acousto-mechanical ones show the low efficiency of the acoustical resonator which may be avoided in the PA application.

We have therefore demonstrated in this chapter the great performance of the photonic and mechanical parts of the sensor. However, the assembly of these parts to form the gas sensor has not yet been realized. A PA detection using a mechanical membrane will be presented in chapter 5 as a preliminary demonstration of the H_2S PA sensing.

IV.8. REFERENCES

[1] N. Ranjkesh, M. Basha, A. Taeb, A. Zandieh, S. Gigoyan, et S. Safavi-Naeini, « Silicon-on-Glass Dielectric Waveguide—Part I: For Millimeter-Wave Integrated Circuits », *IEEE Transactions on Terahertz Science and Technology*, vol. 5, nº 2, p. 268-279, mars 2015, doi: 10.1109/TTHZ.2015.2399693.

[2] N. Ranjkesh, M. Basha, A. Taeb, et S. Safavi-Naeini, « Silicon-on-Glass Dielectric Waveguide—Part II: For THz Applications », *IEEE Transactions on Terahertz Science and Technology*, vol. 5, nº 2, p. 280-287, mars 2015, doi: 10.1109/TTHZ.2015.2397279.

[3] K. Tsuruda, M. Fujita, et T. Nagatsuma, « Extremely low-loss terahertz waveguide based on silicon photonic-crystal slab », *Opt. Express, OE*, vol. 23, nº 25, p. 31977-31990, déc. 2015, doi: 10.1364/OE.23.031977.

[4] H. Amarloo et S. Safavi-Naeini, « Terahertz Line Defect Waveguide Based on Silicon-on-Glass Technology », *IEEE Transactions on Terahertz Science and Technology*, vol. 7, nº 4, p. 433-439, juill. 2017, doi: 10.1109/TTHZ.2017.2708505.
[5] D. Grischkowsky, S. Keiding, M. van Exter, et C. Fattinger, « Far-infrared time-domain spectroscopy with terahertz beams of dielectrics and semiconductors », *J. Opt. Soc. Am. B, JOSAB*, vol. 7, nº 10, p. 2006-2015, oct. 1990, doi: 10.1364/JOSAB.7.002006.
[6] J. Dai, J. Zhang, W. Zhang, et D. Grischkowsky, « Terahertz time-domain spectroscopy characterization of the far-infrared absorption and index of refraction of high-resistivity, float-zone silicon », *J. Opt. Soc. Am. B, JOSAB*, vol. 21, nº 7, p. 1379-1386, juill. 2004, doi: 10.1364/JOSAB.21.001379.
[7] D. M. Mittleman, R. H. Jacobsen, R. Neelamani, R. G. Baraniuk, et M. C. Nuss, « Gas Sensing using Terahertz Time-Domain Spectroscopy », *Applied Physics B*, vol. 67, nº 3, p. 379-390, janv. 1998, doi: http://dx.doi.org/10.1007/s003400050520.
[8] D. R. Grischkowsky, « Optoelectronic characterization of transmission lines and waveguides by terahertz time-domain spectroscopy », *IEEE Journal of Selected Topics in Quantum Electronics*, vol. 6, nº 6, p. 1122-1135, nov. 2000, doi: 10.1109/2944.902161.
[9] E. S. Lee, J. S. Jang, S. H. Kim, et Y. B. J. and T.-I. Jeon, « Propagation of Single-Mode and Multi-Mode Terahertz Radiation Through a Parallel-Plate Waveguide », *Journal of the Korean Physical Society*, vol. 53, nº 4, p. 1891-1896, oct. 2008, doi: 10.3938/jkps.53.1891.
[10] D. R. Grischkowsky, « Optoelectronic characterization of transmission lines and waveguides by terahertz time-domain spectroscopy », *IEEE Journal of Selected Topics in Quantum Electronics*, vol. 6, nº 6, p. 1122-1135, nov. 2000, doi: 10.1109/2944.902161.
[11] T.-I. Jeon et D. Grischkowsky, « Observation of a Cole–Davidson type complex conductivity in the limit of very low carrier densities in doped silicon », *Appl. Phys. Lett.*, vol. 72, nº 18, p. 2259-2261, avr. 1998, doi: 10.1063/1.121271.
[12] J. Dai, J. Zhang, W. Zhang, et D. Grischkowsky, « Terahertz time-domain spectroscopy characterization of the far-infrared absorption and index of refraction of high-resistivity, float-zone silicon », *J. Opt. Soc. Am. B, JOSAB*, vol. 21, nº 7, p. 1379-1386, juill. 2004, doi: 10.1364/JOSAB.21.001379.
[13] D. Grischkowsky, S. Keiding, M. van Exter, et C. Fattinger, « Far-infrared time-domain spectroscopy with terahertz beams of dielectrics and semiconductors », *J. Opt. Soc. Am. B, JOSAB*, vol. 7, nº 10, p. 2006-2015, oct. 1990, doi: 10.1364/JOSAB.7.002006.
[14] M. N. Afsar, « Dielectric Measurements of Millimeter-Wave Materials », *IEEE Transactions on Microwave Theory and Techniques*, vol. 32, nº 12, p. 1598-1609, déc. 1984, doi: 10.1109/TMTT.1984.1132899.
[15] J. M. Dutta, C. R. Jones, et H. Dave, « Complex Dielectric Constants for Selected Near-Millimeter-Wave Materials at 245 GHz », *IEEE Transactions on Microwave Theory and Techniques*, vol. 34, nº 9, p. 932-936, sept. 1986, doi: 10.1109/TMTT.1986.1133473.
[16] M. van Exter et D. Grischkowsky, « Carrier dynamics of electrons and holes in moderately doped silicon », *Phys. Rev. B*, vol. 41, nº 17, p. 12140-12149, juin 1990, doi: 10.1103/PhysRevB.41.12140.
[17] S. M. Hanham, M. M. Ahmad, S. Lucyszyn, et N. Klein, « LED-Switchable High-Q Packaged THz Microbeam Resonators », *IEEE Transactions on Terahertz Science and Technology*, vol. 7, nº 2, p. 199-208, mars 2017, doi: 10.1109/TTHZ.2016.2634547.
[18] A. L. Bingham et D. Grischkowsky, « Terahertz two-dimensional high-Q photonic crystal waveguide cavities », *Optics Letters*, vol. 33, nº 4, p. 348, févr. 2008, doi: 10.1364/OL.33.000348.
[19] Y. Miyamoto, H. Kanaoka, et S. Kirihara, « Terahertz wave localization at a three-dimensional ceramic fractal cavity in photonic crystals », *Journal of Applied Physics*, vol. 103, nº 10, p. 103106, mai 2008, doi: 10.1063/1.2924327.
[20] J. Xie, X. Zhu, X. Zang, Q. Cheng, L. Chen, et Y. Zhu, « Terahertz integrated device: high-Q silicon dielectric resonators », *Optical Materials Express*, vol. 8, nº 1, p. 50, janv. 2018, doi: 10.1364/OME.8.000050.
[21] C. M. Yee et M. S. Sherwin, « High-Q terahertz microcavities in silicon photonic crystal slabs », *Applied Physics Letters*, vol. 94, nº 15, p. 154104, avr. 2009, doi: 10.1063/1.3118579.
[22] W. J. Otter, S. M. Hanham, N. M. Ridler, G. Marino, N. Klein, et S. Lucyszyn, « 100GHz ultra-high Q-factor photonic crystal resonators », *Sensors and Actuators A: Physical*, vol. 217, p. 151-159, sept. 2014, doi: 10.1016/j.sna.2014.06.022.
[23] K. Okamoto, K. Tsuruda, S. Diebold, S. Hisatake, M. Fujita, et T. Nagatsuma, « Terahertz Sensor Using Photonic Crystal Cavity and Resonant Tunneling Diodes », *J Infrared Milli Terahz Waves*, vol. 38, nº 9, p. 1085-1097, sept. 2017, doi: 10.1007/s10762-017-0391-0.

[24] S. M. Hanham, C. Watts, W. J. Otter, S. Lucyszyn, et N. Klein, « Dielectric measurements of nanoliter liquids with a photonic crystal resonator at terahertz frequencies », *Appl. Phys. Lett.*, vol. 107, nº 3, p. 032903, juill. 2015, doi: 10.1063/1.4927242.
[25] D. Ho, M. O. Noor, U. J. Krull, G. Gulak, et R. Genov, « CMOS Tunable-Wavelength Multi-Color Photogate Sensor », *IEEE Transactions on Biomedical Circuits and Systems*, vol. 7, nº 6, p. 805-819, déc. 2013, doi: 10.1109/TBCAS.2013.2243727.
[26] D. P. Poenar et R. F. Wolffenbuttel, « Optical properties of thin-film silicon-compatible materials », *Appl. Opt., AO*, vol. 36, nº 21, p. 5122-5128, juill. 1997, doi: 10.1364/AO.36.005122.
[27] M. Verstuyft *et al.*, « Proposal for an integrated silicon-photonics terahertz gas detector using photoacoustics », *Opt. Express*, vol. 28, nº 15, p. 22424, juill. 2020, doi: 10.1364/OE.397272.
[28] R. Singh, R. J. T. Nicholl, K. I. Bolotin, et S. Ghosh, « Motion Transduction with Thermo-mechanically Squeezed Graphene Resonator Modes », *Nano Lett.*, vol. 18, nº 11, p. 6719-6724, nov. 2018, doi: 10.1021/acs.nanolett.8b02293.
[29] C. Schwarz *et al.*, « Deviation from the Normal Mode Expansion in a Coupled Graphene-Nanomechanical System », *Phys. Rev. Applied*, vol. 6, nº 6, p. 064021, déc. 2016, doi: 10.1103/PhysRevApplied.6.064021.
[30] C.-H. Liu, I. S. Kim, et L. J. Lauhon, « Optical Control of Mechanical Mode-Coupling within a MoS2 Resonator in the Strong-Coupling Regime », *Nano Lett.*, vol. 15, nº 10, p. 6727-6731, oct. 2015, doi: 10.1021/acs.nanolett.5b02586.
[31] P.-L. Yu, T. P. Purdy, et C. A. Regal, « Control of Material Damping in High-Q Membrane Microresonators », *Phys. Rev. Lett.*, vol. 108, nº 8, p. 083603, févr. 2012, doi: 10.1103/PhysRevLett.108.083603.
[32] M. J. Martin, B. H. Houston, J. W. Baldwin, et M. K. Zalalutdinov, « Damping Models for Microcantilevers, Bridges, and Torsional Resonators in the Free-Molecular-Flow Regime », *Journal of Microelectromechanical Systems*, vol. 17, nº 2, p. 503-511, avr. 2008, doi: 10.1109/JMEMS.2008.916321.
[33] G. Karniadakis, A. Beskok, N. Aluru, S. S. Antman, J. E. Marsden, et L. Sirovich, Éd., « Basic Concepts and Technologies », in *Microflows and Nanoflows: Fundamentals and Simulation*, New York, NY: Springer, 2005, p. 1-48.
[34] Eunki Hong, S. Trolier-McKinstry, R. Smith, S. V. Krishnaswamy, et C. B. Freidhoff, « Vibration of micromachined circular piezoelectric diaphragms », *IEEE Transactions on Ultrasonics, Ferroelectrics, and Frequency Control*, vol. 53, nº 4, p. 697-706, avr. 2006, doi: 10.1109/TUFFC.2006.1621496.

Chapter V:

H_2S photoacoustic detection with a poly-Si membrane

CONTENTS

The motivation of this thesis work is to detect low concentrations of gas molecules present in food packaging, to control the freshness of the food, and to ensure the safety of its consumption.

The advantage of using the photoacoustic spectroscopy technique for this purpose was illustrated in chapter I. A new concept of an integrated PA gas sensor design was proposed in chapter II. In chapters III and IV, we presented the experimental methods and characterization results of the different parts of this gas sensor. The assembly of these different parts is not accomplished yet. Therefore, it isn't possible to present the gas measurements with a fully integrated sensor.

However, in this chapter, we present the PA detection of H_2S gas molecules with a suspended Poly-Si membrane. In these measurements, the THz light is focused near the membrane instead of being confined inside the PhC cavity. Therefore, the signal enhancement due to the increased light molecules interaction inside the THz cavity is not considered here.

In the first part, we introduce the design of a vacuum chamber used for the PA gas experiments. A low loss guided THz transition to the gas cell interior with low leakage is also presented. In the second part, two different THz alignments were used to excite the molecules. The performance and PA results of the two alignments were then discussed and compared. The measurements of H_2S gas molecules at different concentrations and pressure levels were also reported. Finally, we show the minimum detection limit (MDL) achieved with the Poly-Si membrane as PA microphone.

V.1. GAS CELL DESIGN

A schematic of the experimental setup for the photoacoustic gas sensing is presented in figure V.1.1. It is composed of an AMC electronic THz source, an LDV, and a gas chamber with a pumping and gas injection system. The electronic source is used to feed the sensor with THz modulated power while the LDV allows detecting the mechanical response of the sensor. The gas cell is a customized circular chamber with an internal diameter of 19 cm and a height of 7 cm made from stainless steel by MDC [1]. It is equipped with 6 KF-25 flanges ports distributed on its walls. The chamber lid contains a BK7 glass window of 4 cm diameter and a thickness of 2 mm. This window is used to visualize the gas sensor inside the chamber, and to detect the displacement of

the membrane with the laser of the vibrometer. Inside the chamber, we mounted an aluminum breadboard with M2 threaded holes to fix the piezoelectric stages and optical components. Figure V.1.2 shows a schematic of the gas chamber. Two ports of the KF-25 flanges are used to pump the air in the chamber and to inject the gas. Three others allow access to the electrical cables and metallic waveguide inside the chamber. And finally, the last one is for the THz beam output.

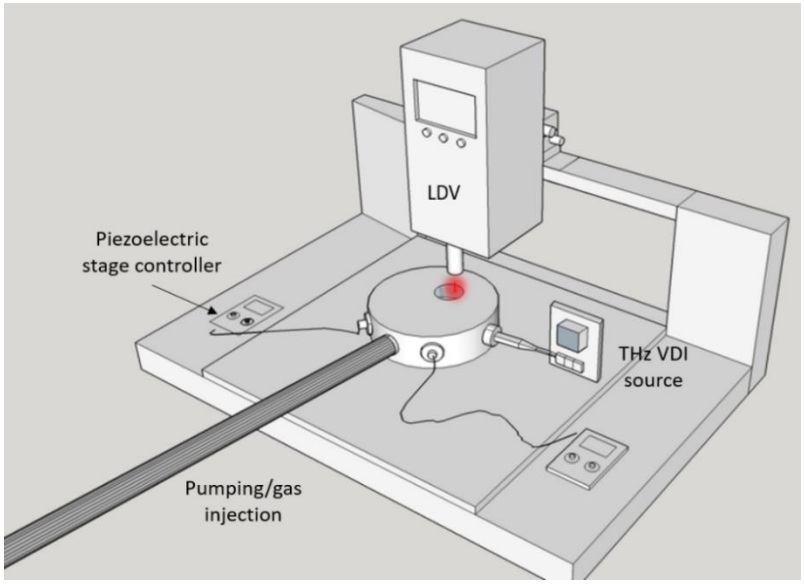

Figure V.1.1 Schematic of the gas sensing experimental setup

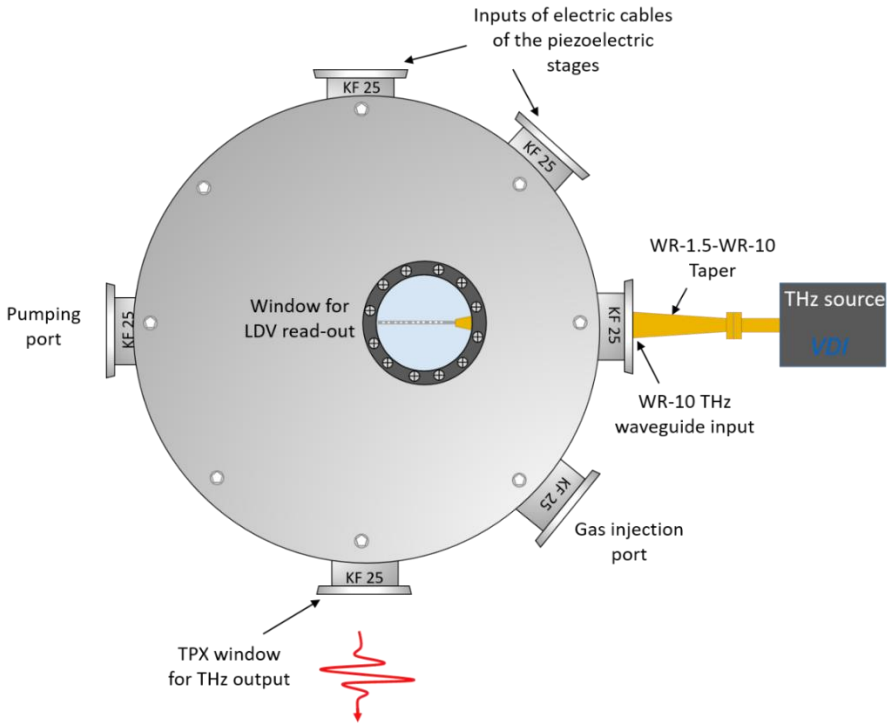

Figure V.1.2 Schematic of the gas chamber

KF-25 blank flange caps are drilled and tapped to screw in the electrical cable connectors of the piezoelectric stages (SmarAct). Another flange cap is drilled to form a frame for the THz output window. A TPX lens with a diameter of 2 cm is then glued to this flange frame with vacuum epoxy glue. The two flange caps including the TPX window and the electrical cable connector are shown in figure V.1.3. A leakage test was applied for both flange caps by closing a KF-25 flanged tee with these two caps and pumping the tube to pressure levels of 10^{-7} mbar. To insert the THz wave into the chamber, we have specially designed a hermetically sealed THz metallic waveguide transition that will be presented in the following paragraph. The top optic window is fitted inside the chamber lid to ensure that the distance from the sensor position inside the chamber to the outer surface of the window is less than the focal length of the LDV objective lens.

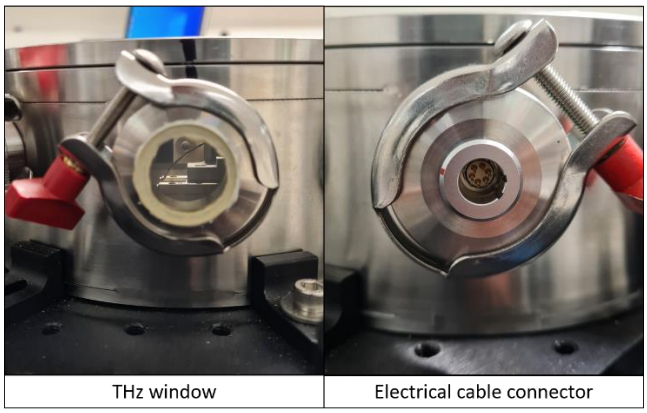

Figure V.1.3 Photograph of the THz window (on the left) and the electrical cable connector (on the right) caps clamped on the KF-25 flanges of the gas chamber

V.1.1 Sealed THz guided transition

We presented in chapters II and IV the low insertion losses from a MWG to the Si waveguide of the sensor. A free-space coupling is more lossy and complicated. Therefore, it's important to have a MWG inside the gas chamber to feed the sensor with low insertion losses. Figure V.1.4 shows the schematic of a THz metallic waveguide transition allowing to guide the THz waves inside the gas chamber with a low level of leaks. A WR-10 copper waveguide is welded to a Brass KF-25 flange cap milled to the shape of a WR-10 MWG flange. The welding process is possible thanks to the large cross-section (2.54 x 1.27 mm) of a WR-10 MWG. Moreover, such waveguides are available as long tubings that can be cut to the desired length. However, it becomes complicated for a WR-1.5 waveguide with a cross-section of 381x191 µm. In this case, only the split-block

approach is used to fabricate such waveguides, which complicates the hermetic gas-tight sealing. Therefore, two WR-1.5-WR-10 tapers are used to couple the THz waves from the VDI source to the WR-10 multimode waveguide and then to the Si gas sensor. Finally, to prevent gas leakage we added a sealing window between the welded WR-10 waveguide with the KF-25 flange and a second commercial one (see figure V.1.4).

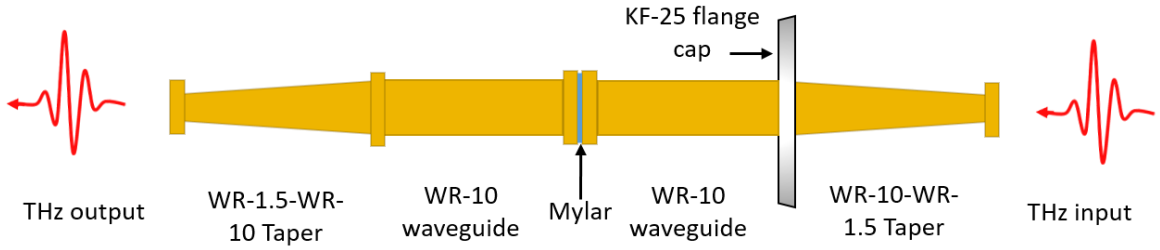

Figure V.1.4 Schematic of the THz metallic waveguide sealed transition

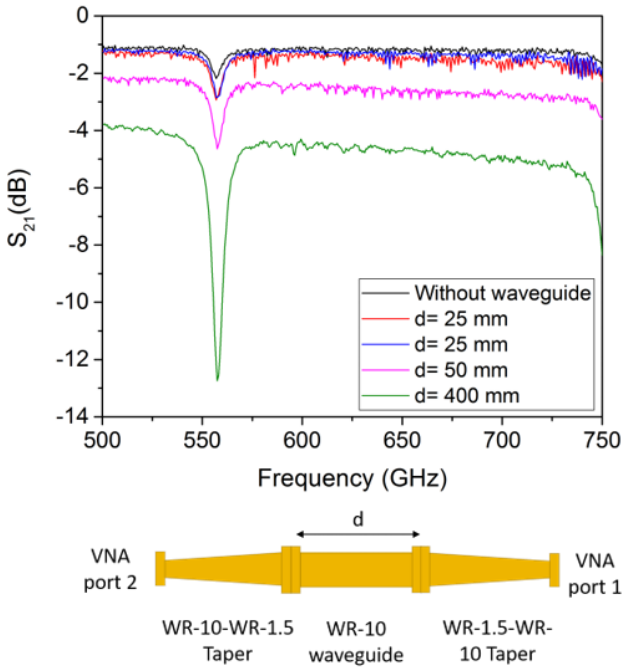

Figure V.1.5 Top: The measured propagation losses inside a structure with two WR-1.5-WR-10 tapers and a WR-10 MWG with different lengths in between. Bottom: A schematic of the measured structures presented in the top graphic

This transition could be highly efficient for guiding the THz waves inside the gas chamber but it also has propagation losses. These losses arise from the propagation in the tapers and waveguides, but also from the absorption, reflections, and radiation at the separative sealing window. The losses quantification was treated separately, first to optimize the length of the WR-10 MWG and then to

identify the material and thickness of the best sealing window. Figure V.1.5 shows the S_{21} measurements and the schematic of a structure with two WR-1.5-WR-10 tapers and a WR-10 MWG of different lengths in between. The two tapers propagation loss is around 1 dB while the propagation loss inside the WR-10 MWG increases by 0.01-0.02 dB/mm (depends on the waveguide quality). In the 500-750 GHz band, the WR-10 waveguide is overmoded, but the taper excites only the TE_{01} mode which explains the observed low propagation losses and the absence of high loss peaks attribute to the "trapped mode" and higher-order modes [2], [3]. A 5cm long waveguide (WR-10) in addition to the 5.08 cm length of the two tapers is then sufficient to transmit the THz waves to the gas chamber center with less than 3dB of loss.

The next step is to define the best material with high sealing performance and low THz losses to be used as a sealing separative window. Several materials with different thicknesses are proposed and measured with the VNA. The tested polymer windows are the following: 30 and 80 µm thick Polyethylene (PE), 47 µm of Polypropylene (PP), 60µm of Kapton, and a 3.5 µm thick Mylar. The film under test is placed and clamped between two WR-1.5-WR-10 tapers connected to the VNAX ports.

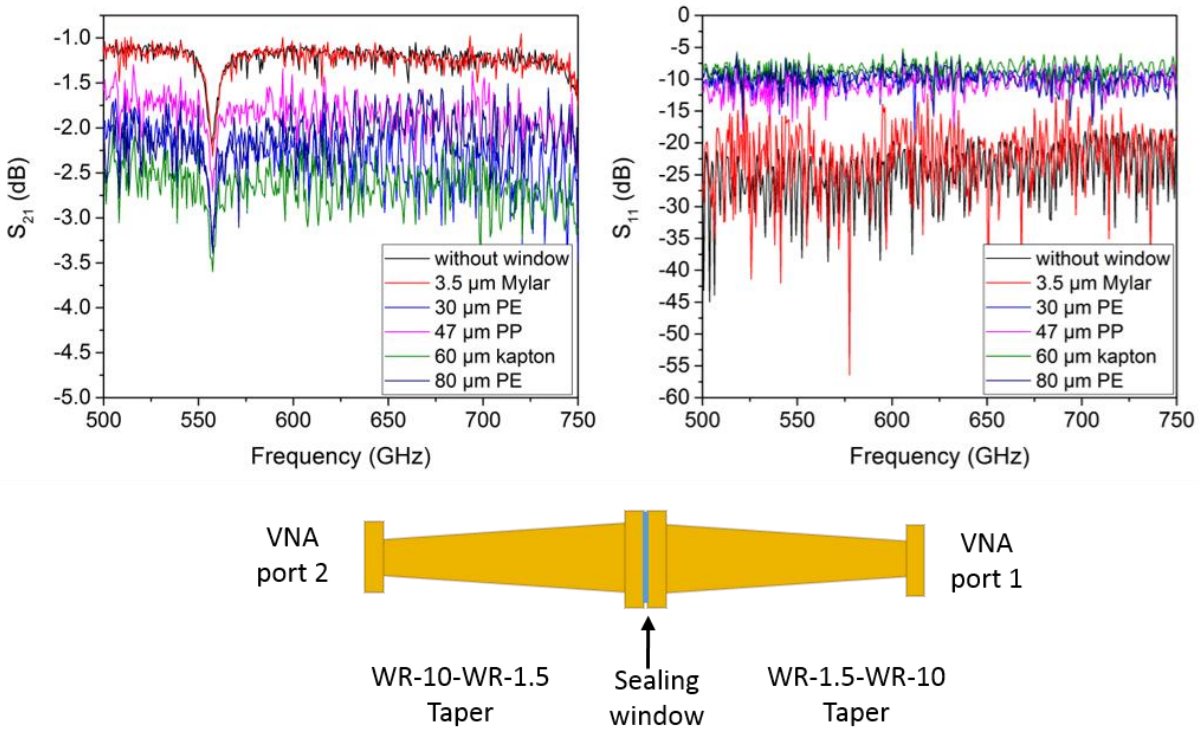

Figure V.1.6 Top: Measured S parameters of a structure with two WR-1.5-WR-10 tapers and different types of sealing windows with several thicknesses in between. Bottom: A schematic of the measured structure

The reflection (S_{11}) and transmission (S_{21}) measurements of the different films are presented in figure V.1.6. The 3.5 µm Mylar has negligible losses and its S_{21} measurement almost overlaps with the one in absence of any separative window. It also presents very low reflections (S_{11}< -15, -20 dB). Other materials such as PP has also acceptable losses of almost 1 dB for a film thickness of 47 µm. However, the thicker layers tend to increase the reflection (S_{11} >10 dB). Losses higher than 2 dB are observable for the Kapton and PE films.

After the demonstration of the Mylar's low losses, we then tested its mechanical resistance to the 1 bar pressure difference. A leakage of 0.5 µbar/second was observed with the 3.5 µm thick Mylar at low pressure and the film showed some sign of damage after disassembly. A thicker Mylar of 12 µm thickness shows better performance with a leakage rate of less than 80 nbar/second.

Finally, we built the full guided transition with two tapers, a KF-25 cap waveguide (WR-10), a commercial WR-10 waveguide, and a 12 µm thick Mylar in between. The structure total loss presented in figure V.1.7 (b) was extracted from the one port S parameter measurement done with the VNA. Figure V.1.7 (a), shows the photograph of the structure connected to the VNA port and closed on the second side by a short circuit to ensure the wave total reflection.

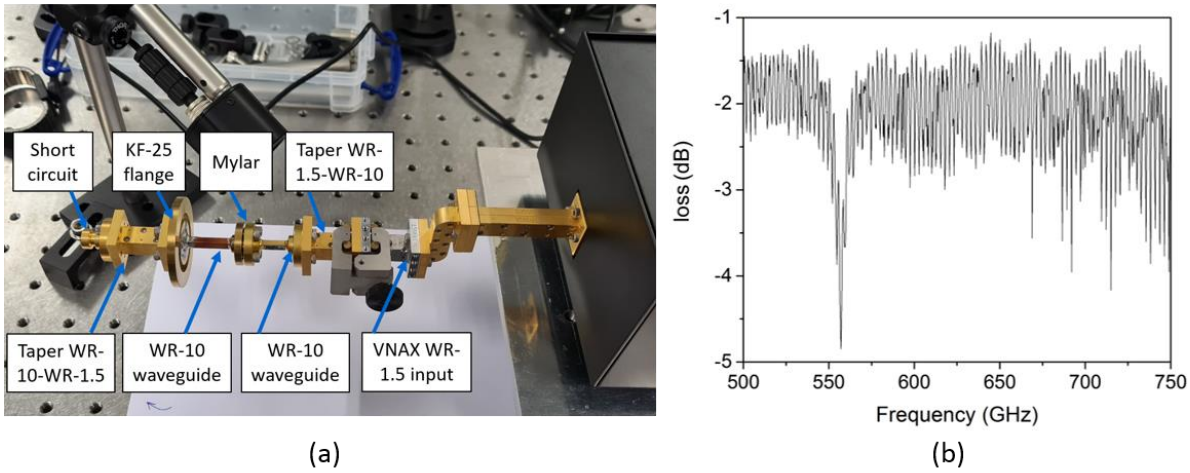

Figure V.1.7 (a) Photograph of the sealed guided THz transition connected to the VNAX port. (b) The measured total loss of the guided transition presented in (a).

The total measured losses of this hermetically sealed THz guided transition are lower than 2.5 dB. This value remains much lower than the insertion losses from an external free-space Gaussian beam (estimated to be > 5 dB).

V.2. EXPERIMENTAL SETUP

In this chapter, we present the PA detection of H_2S gas molecules. As mentioned earlier, the fabrication of the fully integrated gas sensor has not yet been completed. Therefore, these measurements were done with a Poly-Si membrane PA microphone only and without considering the confinement of the THz light inside the high Q THz cavity.

Figure V.2.1 shows the schematic of the experimental setup for the PA detection based on the original concept of the sensor. The THz light is coupled to the Si waveguide through an inverted taper placed inside the MWG transition. The light is then trapped and confined inside a PhC cavity at the absorption peak of the target gas. The effective propagation length of the light inside the cavity is multiplied by a factor proportional to its quality factor Q. Therefore, the gas molecules-light interaction is highly increased leading to a strong acoustical signal. The acoustical signal is then amplified inside the acoustical cylinder and finally detected with the mechanical vibration of the Poly-Si membrane.

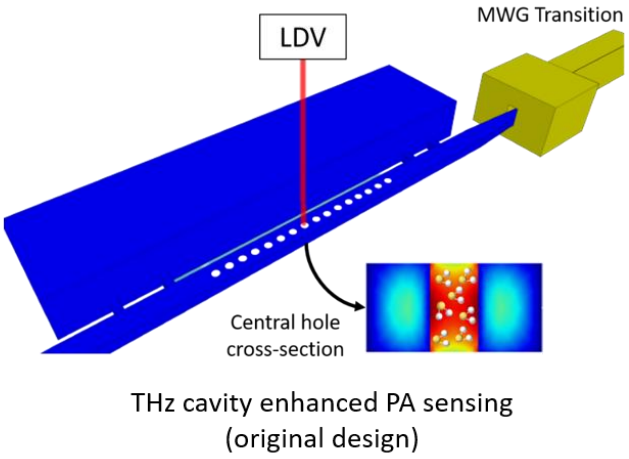

Figure V.2.1 Schematic showing the experimental setup of the PA gas detection with the THz light guided inside the Si waveguide and confined inside the cavity at the gas molecules absorption frequency (the original working principle of the designed gas sensor).

Since up to now there is no available THz cavity resonant at any absorption frequency of the H_2S target gas (611, 626, 650, 665, 687, 689, … GHz), we used alternative methods to excite the gas molecules and detect the PA response with the Poly-Si membrane. Figure V.2.2 shows two different alignment setups used during these measurements. In these experiments, a WR-1.5 horn antenna is connected to the end of the MWG transition. The THz beam is collimated with an off-axis parabolic mirror of an EFL (Effective Focal Length) and a diameter of ¼". In the first

configuration (Figure V.2.2 (a)), the Poly-Si membrane is placed parallel to the propagating beam at a distance of 12.7 mm. The gas molecules-light interaction extends over a length of 15 cm, from the sealing Mylar window inside the MWG transition to the TPX window at the THz output port of the gas chamber. However, only a small part of the sound generated by this interaction overlaps with the mechanical mode of the Poly-Si membrane.

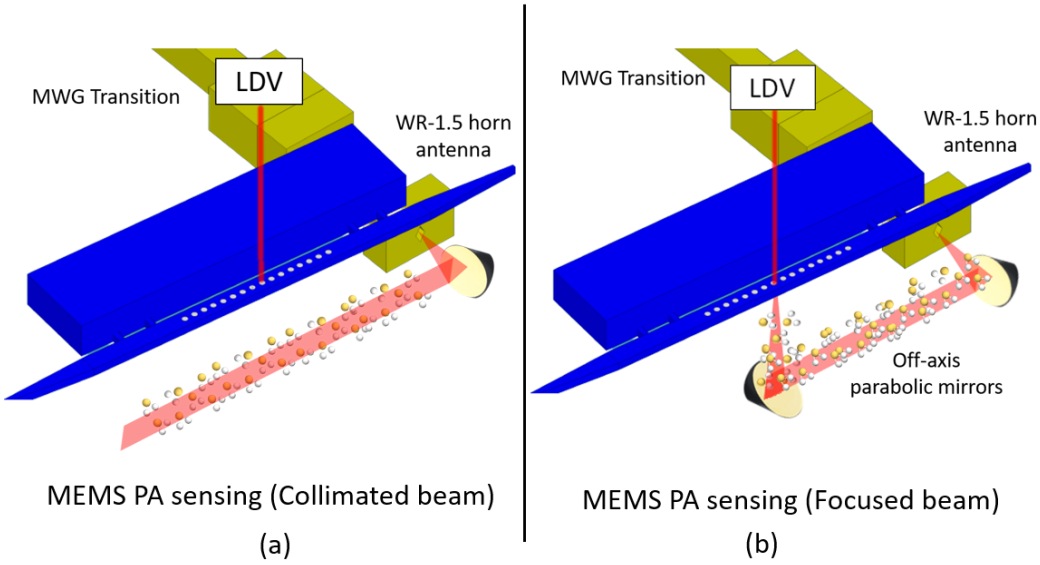

Figure V.2.2 Schematic showing the experimental setup of the PA gas detection with: (a) The THz light collimated under the Poly-Si membrane, (b) the THz focused on the membrane

The second THz alignment configuration shown in figure V.2.2 (b) uses a second off-axis parabolic mirror of an EFL (Effective Focal Length) and diameter of ½" to focus the THz beam on the Poly-Si membrane. A smaller light-molecules interaction length of 7 cm is achieved. However, the overlap between the acoustical wave and the mechanical resonator is more important.

The THz signal is generated with a VDI AMC THz source. The RF signal input to the VDI source is provided by a Rohde & Schwarz SMA 100B RF and microwave signal generator. Amplitude modulation of the RF signal at the frequency of the Poly-Si membrane is applied internally with a sinusoidal wave. The THz source emits a signal at frequencies between 620 and 670 GHz. It also presents an emission peak between 685 and 690 GHz. The THz power at the horn antenna output is frequency-dependent and varies between 400µw and 1.1 mW. At 650 GHz the approximate THz power corresponds to 800 µW. We created a Labview interface to control the source parameters (modulation frequency, emission frequency) and to collect the measured data. An MSA-500

Polytec laser Doppler vibrometer (LDV) is used to detect the displacement of the Poly-Si membrane. The measured signal is sent to a lock-in amplifier (HF2LI Zurich instruments). The amplitude modulation signal generated by the SMA signal generator is also used as a reference for the lock-in amplifier. The synchronized phase and amplitude of the mechanical signal are then detected by the lock-in. To align the collimated THz beam an antenna-coupled micro-bolometric uncooled THz camera (I2S) is placed in front of the TPX output window. The camera is then inclined with a 45˚angle above the structure to detect and optimize the focused THz beam on the membrane. The first mirror position is controlled manually with a translational stage and two clamped optical posts. The second mirror and the Poly-Si membrane are mounted on piezoelectric stages for precise alignment (see figure V.2.3).

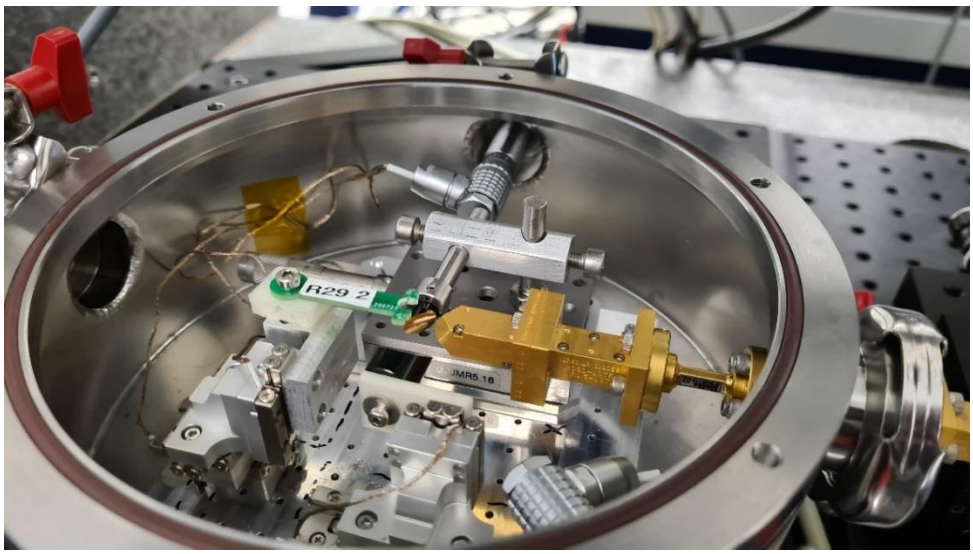

Figure V.2.3 Photograph of the gas chamber interior

The air inside the chamber is pumped with a turbomolecular pump (Edwards T-Station 85). A needle valve is used to control the flow of the injected gas. To pump out the H_2S and to avoid the spreading of such toxic gas in the lab room, a zeolite sorption pump is used to adsorb the gas molecules. This pump is cooled with liquid nitrogen. Two different gauges are used to measure precisely the low (< 10 mbar) and high pressure (>10 mbar) of the gas inside the chamber. The full experimental setup is presented in figure V.2.4 (The Pumps, gas cylinder, PC, lock-in, and RF signal generator aren't shown in the photo). An enlarged photo of the aligned membrane with the two off-axis parabolic mirrors, the THz horn antenna, and the vibrometer red laser is also shown in figure V.2.4.

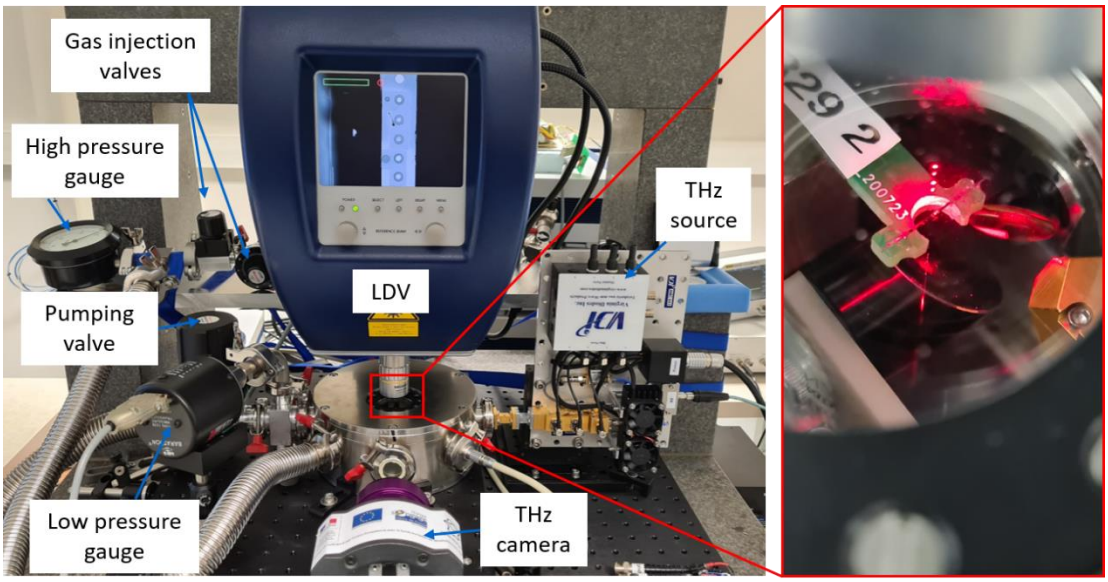

Figure V.2.4 A photograph of the experimental setup on the left hand side. An enlarged photo of the membrane inside the chamber on the right hand side

V.3. POLY-SI MEMBRANE DYNAMICS

The detection of the highest PA signal occurs when the THz light is modulated at the resonance frequency of the Poly-Si membrane. In chapter IV, we presented the dynamics of the Poly-Si membrane with a radius of 29 µm, a thickness of 100 nm, and different metal layer dimensions. The fundamental mode resonant frequencies of these membranes vary between 500 kHz and 1.4 MHz depending on the added metal layer. The amplitude of the RF input signal connected to the THz source is fully modulated at frequencies up to 1 MHz. An external mixer coupled to a spectrum analyzer was used to measure the modulation depth of the THz source output. The THz signal amplitude is fully modulated at the modulation frequencies below 100 kHz. However, for higher modulation frequencies, the modulation depth starts to decrease and vanishes at frequencies beyond 500 kHz. A possible explanation is that the automatic bias circuit of the varactor diodes of the THz chain source compensates for the fast modulation of the RF signal. Therefore, it is impossible to modulate this VDI source at the resonance frequency of the previously presented Poly-Si membranes.

As shown in chapter II (equation II.1.7), the mechanical resonance frequency depends on the geometrical dimensions of the membrane. Therefore, to reduce the modulation frequency, an adjusted larger design of the membrane with lower resonance frequency is proposed and used for

the following gas measurements. The new dimensions of the single suspended Poly-Si membrane correspond to a radius of 250 μm and a thickness of 750 nm. The membrane is coated by 10 nm of chromium (Cr) and 70 nm of gold (Au).

The mechanical resonance frequency of the membrane is determined by measuring its Brownian motion displacement at several air pressure levels. The membrane is placed inside the vacuum chamber, where the air inside is pumped to pressures below 1 mbar. A valve is then opened to inject air inside the chamber and gradually increase the pressure. The vibrometer's laser spot is aligned on the membrane center using the x5 magnification objective. The signal measured by the vibrometer is sent to the lock-in. An internal oscillator of the lock-in is used as a reference to determine the phase and amplitude of the input signal. The oscillation frequency of the reference signal is first swept from 30 to 40 kHz. High signal amplitude with a Lorentzian shape is observed at frequencies near 36.5 kHz for low pressures. A frequency sweep with a 2 Hz step size is then applied on a tighter bandwidth (BW) between 36 and 37 kHz with an integration time of 6 ms to measure the precise position of the membrane's resonance frequency. For broader resonances at high pressures, the measurements were done with a frequency sweep between 34.5 and 37 kHz with 2.5 Hz step size and the same integration time.

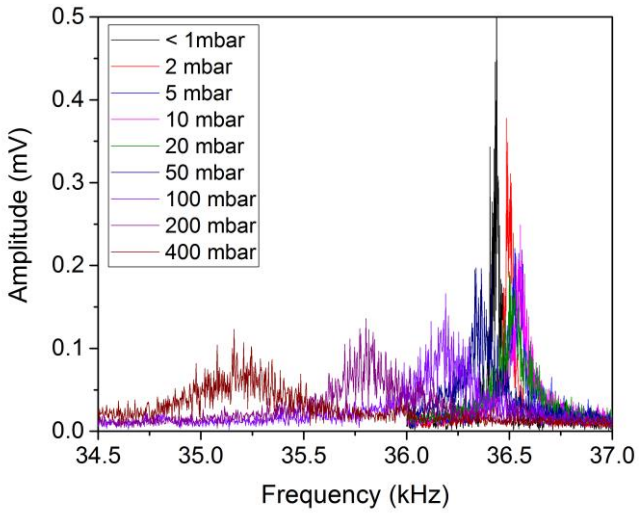

Figure V.3.1 The measured amplitude of the mechanical resonance of the Poly-Si membrane driven by the thermal noise at different air pressure levels

Figure V.3.1 shows the averaged amplitude of three recorded scans at different pressures. At very low pressures (below 1 mbar) the resonance peak appears at 36.45 kHz. A spring hardening is

observed at low-pressure variations (below 10 mbar) leading to a small shift in the resonance frequency up to 36.55 kHz at 10 mbar. This is followed by a spring softening and larger frequency shifts toward lower frequencies at high pressures. Similar behavior of the resonance frequency shifting was also reported in [4]. The increase of frequency at the low pressures of the molecular regime could be attributed to an additional stiffness caused by the penetration of the air molecules inside the membrane's material. At higher pressures, the air starts to behave like a mass load and leads to a decreasing in the resonance frequency. The impact of the air damping on the broadening of the peak is also clearly visible. This is reflected in a decrease of the quality factor at high pressures. A Lorentzian fitting of the measured peaks at the pressure levels of 100, 10 mbar, and the one below 1 mbar shows a broadening of 350,120 and 50 Hz. These frequency broadenings correspond respectively to the quality factors of 700, 300, and 100.

These measurements show that the resonance frequency of the membrane and its quality factor are sensitive to the pressure variation. Therefore, for the highest sensitivity of the PA detection, a tuning of the modulation frequency is necessary to match with the mechanical resonance.

V.4. DETECTION OF PURE H_2S WITH TWO DIFFERENT THZ ALIGNMENTS

H_2S gas is a toxic deadly molecule present in natural gas, oil, water, … It is also emitted by the bacterial growth in food which is responsible for food spoilage. Thus, H_2S is a great indicator of food spoilage, and monitoring its concentrations to control the food quality has been the subject of much research [5]–[11]. For a cheddar cheese, the concentration of H_2S should be lower than 50 ppb [10], while for fresh beef meat conserved at 25 °C for 48 hours the H_2S concentration has evolved from 480 ppb to 7.16 ppm [11]. The detection of small H_2S concentrations in the order of sub-ppm is then necessary to ensure the safety of food consumption.

In addition to being an excellent food spoilage indicator, the other advantage of detecting the H_2S gas molecules is its high-intensity rotational transition in the THz region. Figure V.4.1 shows the intensities of the different absorption lines of the H_2S molecules without any broadening effect in the 620-690 GHz frequency range. This range corresponds to the emission BW of the THz VDI source and it's a range free of water vapor strong absorption lines. Five peaks with high intensities are present in this range. The THz cavity of the integrated gas sensor is initially designed to target

the 650.374186 GHz transition. Therefore, in the first measurements, we focused on this specific absorption line.

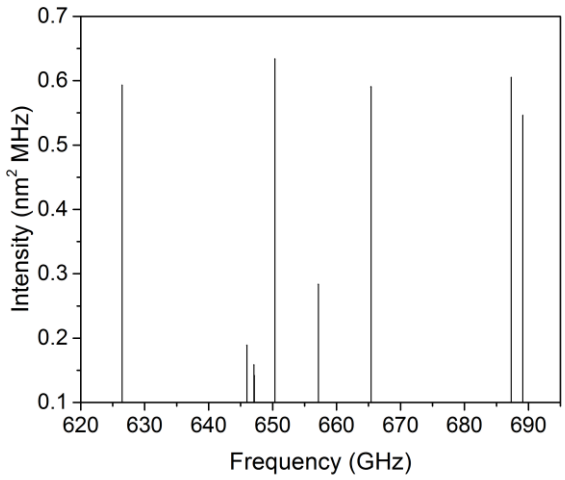

Figure V.4.1 Plot showing the intensities of several H_2S absorption peaks (without broadening effect) in the frequency range 620-690 GHz extracted from the JPL molecular spectroscopy database [12]

This part shows the results of the PA detection of pure H_2S gas with two different THz beam alignments. The setup schematics are presented earlier in figure V.2.2. The RF signal frequency is fixed at 13.549462 GHz for a THz emission at the center of the 650.374186 GHz molecular absorption line.

In the first trial, the THz collimated beam was propagating longitudinally under the membrane at a distance of 12.7 mm (figure V.2.2 (a)). The beam is detected by a THz camera placed outside the chamber. The air inside the chamber was first pumped to vacuum levels. 500 µbar of pure H_2S was then injected inside the chamber. The THz spot detected by the camera is attenuated then totally disappears after the gas injection which confirms the H_2S high absorption.

In the absence of THz emission, the noise floor and the mechanical resonance frequency of the membrane were measured by sweeping the frequency of the lock-in oscillator and detecting the membrane's displacement with the LDV. Figure V.4.2 (a) represents in black square dots the average of 3 successive scans of the thermal noise, and its Lorentzian fit in the red line. The peak of the Lorentzian fit corresponds to a resonance at a frequency of 36.57 kHz. The off-resonance noise level amplitude is lower than 5µV, equivalent to a mechanical displacement of less than 0.1 fm. At the resonance, the noise is slightly higher with 100 µV of amplitude representing a displacement of 2 fm. The modulation frequency of the THz source is then fixed at 36.57 kHz for

a resonant detection of the PA signal. The lock-in integration time was set to 6 ms. This time t should be larger than the microphone response time which is expressed by [13]:

$$t > \tau = \frac{Q}{\pi f_R} \qquad \text{(V.4.1)}$$

where Q the Poly-Si membrane quality factor and f_R its resonance frequency. The used integration time corresponds then to quality factors of the mechanical resonator below 700. This quality factor value was measured in the previous part at pressure levels below 1 mbar. Therefore, working at lower pressure levels requires longer integration times. However, in all the presented measurements the integration time was fixed to 6 ms.

The detected PA signal at the resonance frequency is presented by the black square dots in figure V.4.2 (b). Its Lorentzian fitted curve has an amplitude of 11.4 mV. Therefore, an 0.23 pm of central displacement of the Poly-Si membrane is measured by the LDV. The Signal to Noise Ratio (SNR) is the ratio between the resonance peak amplitude in presence of the THz signal, and the peak amplitude while the THz source is turned off. This ratio is an indicator of the system sensitivity and the lowest detectable gas concentration. An SNR of 114 is measured at a pressure level of 0.5 µbar. The Lorentzian fitted curves have quality factors of 570 and 1200 for the measured noise and signal peaks respectively.

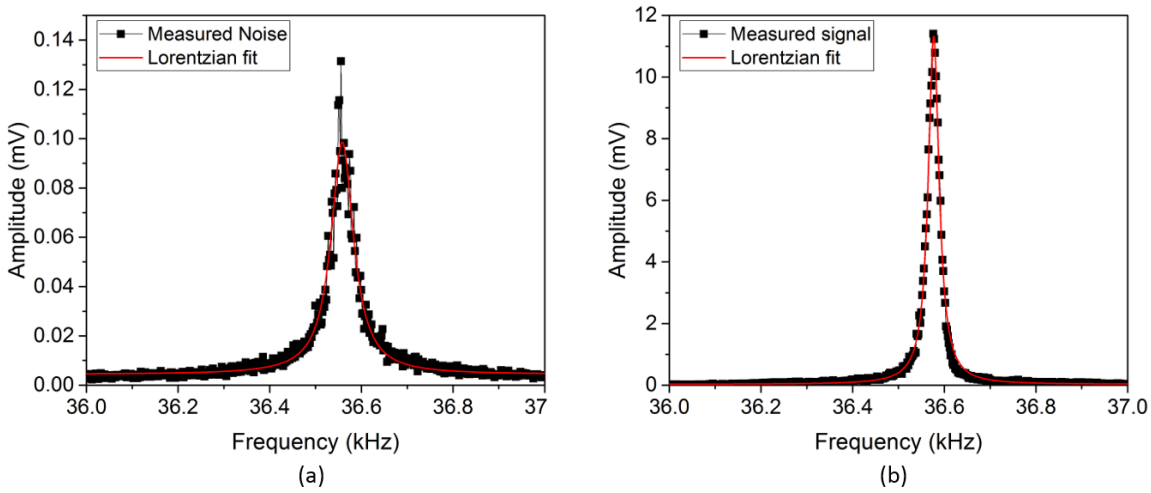

Figure V.4.2 The measured mechanical resonance frequency of the membrane in the presence of 500 µbar pure H_2S:
(a) in absence of THz light (noise level), and (b) in the presence of THz light (signal level)

The same measurements were done at different pressures of pure H_2S inside the chamber. Figure V.4.3 shows the measured noise and PA signal at the 100 µbar, 1 and 10 mbar H_2S pressure levels

respectively. The noise level remains almost constant at the different pressures below 10 mbar with an approximate amplitude of 100 µV at the resonant peak (Figure V.4.3 (a) and (c)). At 10 mbar the noise is slightly lower with an amplitude of 70 µV (Figure V.4.3 (e)). The decrease of the Brownian motion amplitude (noise amplitude) is due to the increase of damping at higher pressure. The resonance frequency shifting is negligible with a measured peak at 36.49 kHz for the H_2S pressures of 100 µbar and 10 mbar, and 36.5 kHz for the 1 mbar pressure level. The observed frequency positions and small shifting values are in great agreement with the one presented in figure V.3.1, contrary to the one measured earlier at a pressure of 500 µbar which represents a shifted resonance frequency. This is due to the different positions of the LDV laser spot on the membrane surface. For the measurements, at 500 µbar the laser spot wasn't perfectly centered on the membrane. A shifting of the detected frequency was observed by moving the position of the laser. Such an effect was also observed in [14]. This discrepancy can also be related to thermal effects since the temperature is not controlled during the experiments. The quality factors of the measured Brownian motion peaks in the presence of H_2S are also in good agreement with the one presented in figure V.3.1 for the Brownian motion in an air medium. The quality factors at 100 µbar, 1, and 10 mbar pressure levels correspond respectively to 700, 500, and 300. However, and similar to what was observed in figure V.4.2 at 500 µbar pressure level, the quality factor for the peak measured in the presence of the PA signal is larger and corresponds to a value of 1200 at the different pressure levels. The higher quality factor in presence of the PA signal compared to that measured with Brownian motion is an interesting phenomenon that needs to be observed in more detail. While the saturation of the measured quality factor at 1200 can be related to the short integration time of 6 ms. The PA signal increases at higher pressures from 5.3 to 28 and 37 mV at 100 µbar, 1 and 10 mbar gas pressures, respectively. Equations I.4.30 and I.3.5 show the dependence of the acoustical signal amplitude on gas concentrations, confirming the increase of the PA signal with higher gas concentrations (higher pressures). This dependency is non-linear and it also depends on the quality factor of the mechanical resonator that decreases at higher pressures. The noise level is quite low and decreases slightly with higher pressures, while the PA signal starts to saturate. The SNR is then increasing from 50 to 600 with higher pressure of H_2S. The advantage of this THz alignment is its low impact on the noise level (the THz beam does not illuminate directly the membrane). However, the overlap between the generated sound from the

light molecules interaction and the mechanical mode of the membrane is low in this configuration. From equation I.4.27, this low overlap results in smaller PA signal amplitudes.

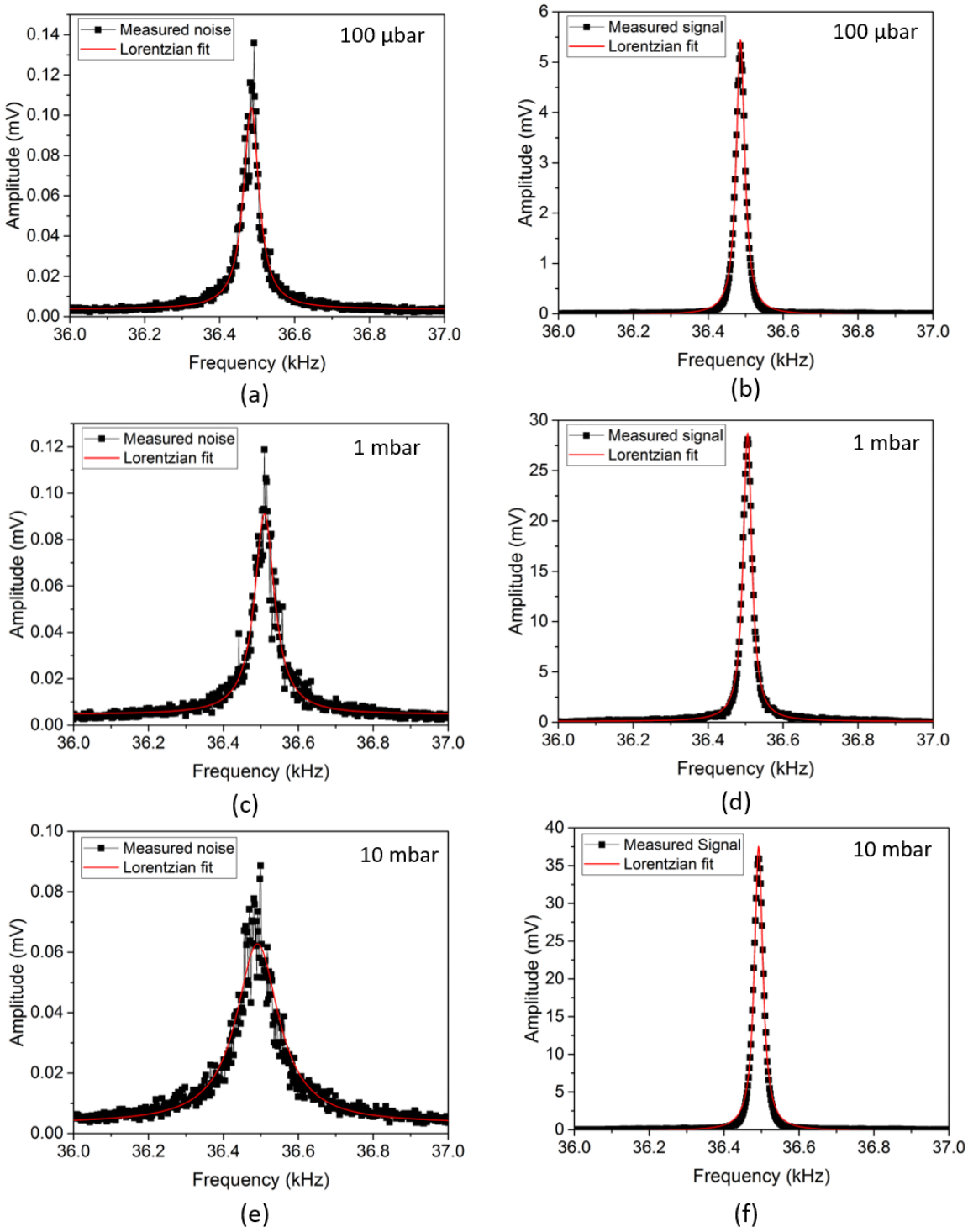

Figure V.4.3 The measured noise (a-c-e) and PA signal (b-d-f) at different pressures of pure H_2S

The benefit of modulating the THz source at the mechanical resonance frequency of the membrane is to enhance the detected acoustical signal by a factor proportional to the mechanical resonator quality factor. Figure V.4.4 shows a comparison between a resonant and an off-resonance PA detection. The detected signal amplitude is 10 times stronger at the resonance frequency of the membrane compared to the off-resonance measurement, while the SNR is slightly higher by a factor of 1.4. However, the modulation frequency (36.57 kHz) used for the off-resonance measurement presented here remains close to the mechanical resonance (36.49 kHz). At a modulation frequency far away from the resonance, the measured signal and SNR would be much weaker than the ones detected at the resonance frequency.

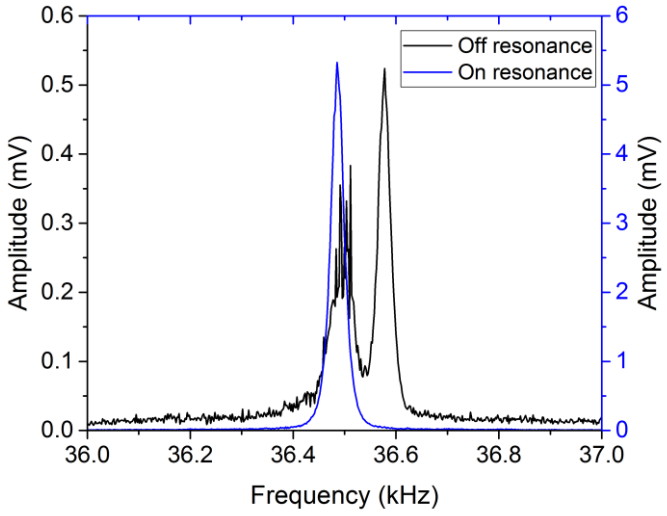

Figure V.4.4 Comparison between the resonant and off-resonance PA signal for the detection of 100 µbar of pure H_2S

For the second alignment the collimated THz light is focused on the surface of the membrane (see figure V.2.2 (b)). In this configuration, an additional signal is detected which is due to the PT effect caused by the THz beam on the Poly-Si membrane. This signal is not related to the gas absorption and therefore, it is almost independent of the THz frequency. This THz direct detection effect also adds extra noise to the measurements. To measure and quantify this parasitic signal level, the air inside the chamber is pumped down to 500 µbar pressure level. The THz light amplitude is then modulated at a frequency of 36.5 kHz and the membrane displacement signal is recorded with 6 ms of lock-in integration time. The measured THz signal and its Lorentzian fit are represented in figure V.4.5 (a). It is quite complicated to extract the noise level from this measured signal, since the noise is dominated by the high parasitic signal of the THz beam. After these measurements,

the air inside the chamber is pumped to the high vacuum levels. 500 µbar of pure H_2S is then introduced into the chamber. The recorded PA signal is presented in figure V.4.5 (b). At the same pressure (500 µbar) and concentration (pure H_2S) levels as the one measured with a collimated beam, a 4 times larger signal with an amplitude of 50 mV is detected with the focused THz beam.

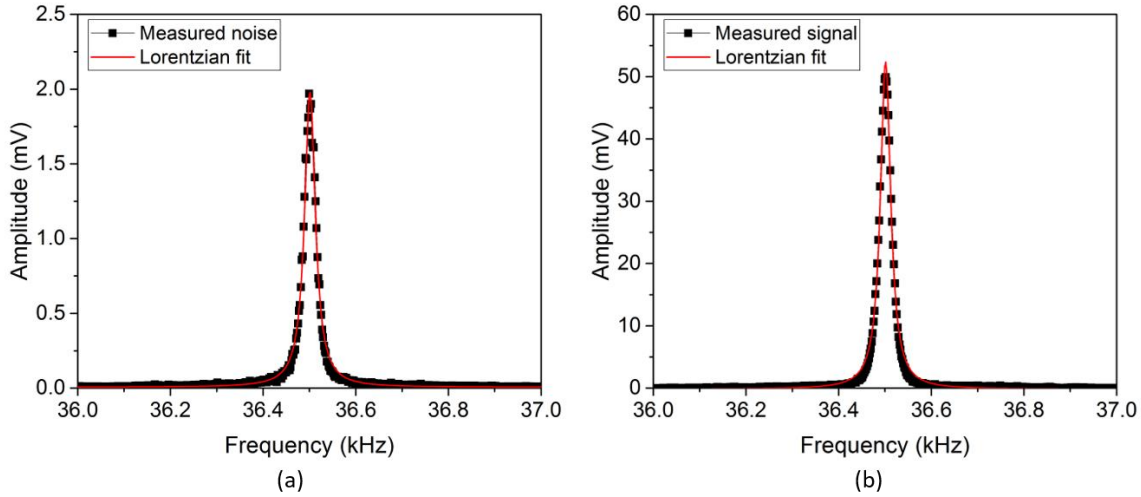

Figure V.4.5 The measured mechanical resonance with the THz beam focused on the membrane in presence of: (a) 500 µbar of air (noise level), and (b) 500 µbar of pure H_2S (signal level)

This high PA signal amplitude is the result of a large overlap between the generated acoustical waves and the mechanical resonant mode of the membrane. The net displacement of the membrane caused by the heat generated from the gas molecule's absorption is 960 fm. While for the collimated THz beam, the same gas concentration leads to a smaller displacement of only 230 fm.

In this part, the PA detection of the H_2S molecules at its 650.37 GHz absorption line using a Poly-Si membrane as a microphone was successfully demonstrated. The PA measurements with two different alignments of the THz light were reported. The impact of the parasitic signal caused by the THz light was also discussed. We finally presented the advantage of a resonant detection over the off-resonance one. In the next part, the spectrum of the strong absorption lines of H_2S between 620 and 690 GHz is presented at different pressures and concentrations using the PA detection with a focused THz beam on the Poly-Si membrane.

V.5. THE H_2S ABSORPTION SPECTRUM IN THE RANGE 620-690 GHZ

In the previous measurements, the PA signal was detected by measuring the mechanical resonance of the membrane. The THz emission frequency was fixed at the 650.37 GHz molecular absorption line and a sweeping of the lock-in oscillator frequency was applied to detect the response of the membrane. In this part, we present the measurements of the 5 strongest absorption lines of the H_2S in the spectral region between 620 and 690 GHz. For the highest PA signal detection, the amplitude of the THz radiation is modulated at the resonant frequency of the membrane. A Labview interface is used to sweep the emitted THz frequency and to collect the PA signal from the vibrometer through the lock-in amplifier. The air was pumped out, and 500 µbar of pure H_2S was injected inside the chamber. The source emission frequency was swept around the different absorption peaks of the H_2S molecule with a frequency step size of 150 and 250 kHz (depends on the measured absorption line). The PA signal is detected with a sampling time of 6 ms and a waiting time of 100 ms between each scan point. Five of the strongest absorption lines of H_2S in the 620-690 GHz frequency spectral range are measured and presented in figure V.5.1. Ideally in the absence of broadening the molecular absorptions lines would be presented as straight fine lines similar to the simulated ones without broadening presented in figure V.4.1. However, in reality, this is not the case and the absorption line is broadened. The line shape broadening is described by three different processes: natural line broadening, collisional broadening, and Doppler broadening. At the THz frequencies and for the vibrational and rotational energies states the natural line broadening is neglected. The collisional broadening is caused by the collisions between molecules and, or with air molecules. These collisions lead to an enlargement of the absorption line, resulting in a peak with a Lorentzian shape of a FWHM inversely proportional to the meantime collisions $\tau_{collision}$ between molecules. The meantime collisions are defined by:

$$\tau_{collision} \sim \frac{1}{\sigma_S P}\left(\frac{\pi m k_B T}{8}\right)^{\frac{1}{2}} \qquad \text{(V.5.1)}$$

where σ_S (m^2) is the collision cross-section, P (Pa) the pressure, m (kg) the mass, k_B =1.38x10^{-23} J/K Boltzmann constant, and T(K) the temperature. At a constant temperature, the collision time increases with the pressure decreasing, and thus at low pressure, collisional broadening becomes negligible and the broadening is dominated by the Doppler effect. The Doppler broadening is due to the free random motion of the molecules and results in a Gaussian lineshape. In the absence of

collisions between molecules at low pressure, the distribution of velocity induces a distribution of frequencies. Therefore, at low pressure the lineshape of the absorption lines follows the Doppler broadening and is represented by a Gaussian peak with a FWHM expressed by:

$$\mathrm{FWHM} = \Delta f = \frac{f_0}{c}\sqrt{\frac{8RTln2}{M}} \qquad \text{(V.5.2)}$$

Where f_0 corresponds to the central frequency of the molecular absorption peak, c the speed of light, R the perfect gas constant (R=8.3144 J/K.mol) T the temperature, and M the molar mass of the molecule (M_{H2S} =34.1 g/mol). The Doppler broadening of the 650.37 GHz absorption line of the H_2S molecule corresponds then to a $\Delta f = 1.36\ MHz$.

The black dot squares presented in figure V.5.1 correspond to the measured PA signal at the membrane's resonant frequency. The measured peaks look more like a Gaussian than a Lorentzian. Thus the red line of figure V.5.1 represents the Gaussian fit of the measured data points.

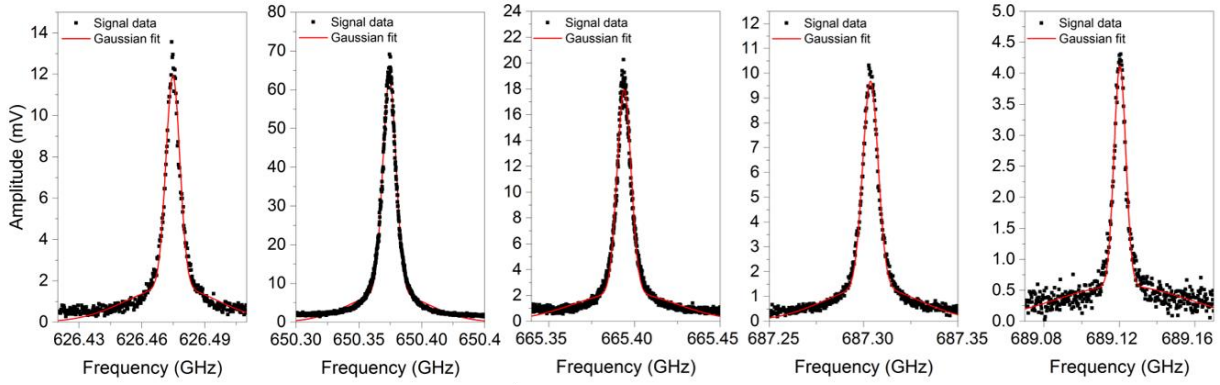

Figure V.5.1 The strong absorption peaks of pure H_2S between 620 and 690 GHz at a pressure of 500µbar

The measured central frequencies of the Gaussian fits are in perfect agreement with the spectral line frequencies extracted from the JPL molecular spectroscopy database [12]. The comparison between these values is presented in table V.5.1.

JPL database frequency (MHz)	626474.6250	650374.1860	665393.738	687303.4680	689120.17
Measured frequency (MHz)	626474.7	650374.3	665393.9	687303.6	689120.3

Table V.5.1 Table representing the different measured absorption lines frequencies compared to the one extracted from the JPL molecular spectroscopy database

Despite the Gaussian shape of the peaks, the Doppler regime is not yet reached at a pressure of 500 µbar. This can be observed in the measured broadening of the peaks which corresponds to a Δf of 8, 13, 10, 10 and 8 MHz for the respective lines with a central frequency of 626.47, 650.37, 665.39, 687.3 and 689. These values remain higher than the theoretical broadening of 1.36 MHz value expected in the Doppler regime. Furthermore, these extracted broadening coefficients are slightly higher than those measured in the Terafood project by [15] using absorption spectroscopy. The PA signal amplitude depends on the linestrength intensity but also on the THz source power which is highly dependent on the frequency. The difference in the PA signal amplitude between the different lines is mainly due to the variation of the THz power (presented in figure III.2.5 (a)) since the lines have almost the same intensities (see figure V.4.1).

The gas inside the chamber is then pumped with the sorption pump. After achieving the vacuum level, 2 mbar of pure H_2S are injected followed by a 98 mbar of air. This results in a H_2S concentration of 2% diluted with 98% of air. The same previous experimental setup is used to measure the absorption lines of the 2% diluted H_2S at a pressure level of 100 mbar. The square black dots in figure V.5.2 represent the measured PA signal. The collisions between H_2S molecules at high pressure (100 mbar), and their collisions with the air molecules result in a Lorentzian-shape broadening of the absorption peak presented by the Lorentzian fit illustrated by a red line in figure V.5.2. This large broadening leads to an overlap between the two close lines at 687.3 and 689.12 GHz.

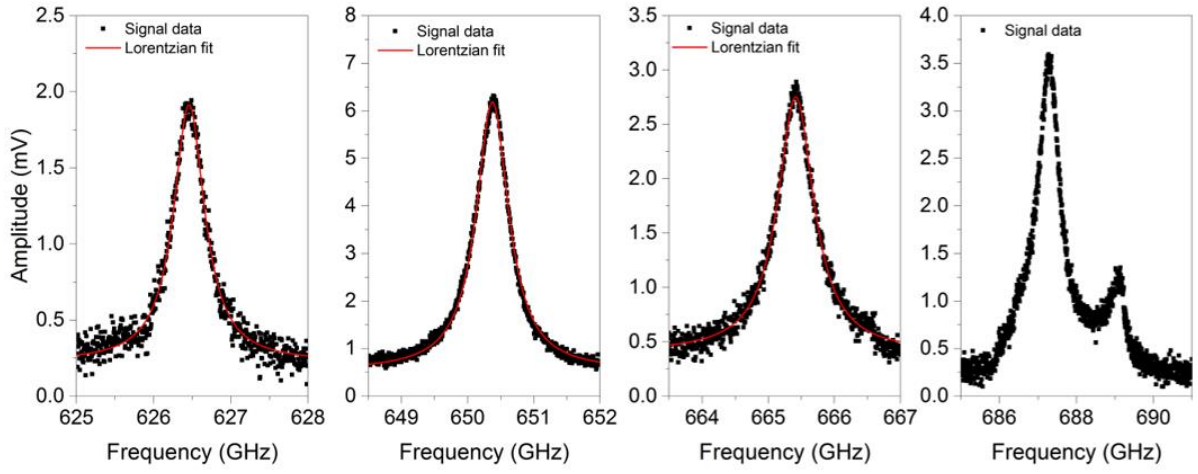

Figure V.5.2 The strong absorption peaks of 2% diluted H_2S between 620 and 690 GHz at a total pressure of 100 mbar

The lower PA signal compared to previous measurements is due to the lower gas concentrations since the signal is directly proportional to the gas concentrations. However, this is not the only reason, as the quality factor of the mechanical resonator also decreases with increasing the pressure. Finally, figure V.5.3 shows a great agreement between the measured and simulated absorption lines for a H_2S gas concentration of 2% at a pressure of 100 mbar. The simulated spectrum was obtained from Spectraplot [16] based on the HITRAN database [17] by using the same experimental parameters and a 10 cm long gas cell.

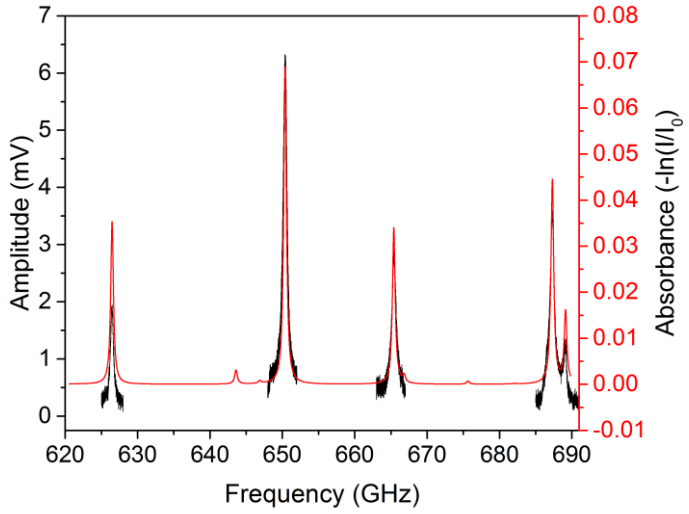

Figure V.5.3 The measured (black line) and simulated (using Spectraplot *[16]*) (red line) spectral lines of 2% diluted H_2S at a pressure of 100 mbar

V.6. DETECTION LIMIT

A gas sensor is characterized by its sensitivity and lower limit of detectable concentration. To define the sensitivity of this system, different H_2S concentrations were measured. A certified gas mixture of 1% of H_2S in pure Nitrogen (N_2) was first used. For lower concentrations, the mixture was produced manually by injecting 1 mbar of the 1% H_2S:N_2 gas mixture inside the chamber and then adding a 9 mbar of air to achieve a 1‰ final concentration of H_2S. The same dillution process was also applied for lower concentrations down to 100 ppm. All the measurements were done at a total pressure of 10 mbar inside the chamber. The THz modulation frequency was fixed at the Poly-Si resonance frequency, and the PA signal was detected with an integration time of 6 ms while sweeping the THz emission frequency. The black line in figure V.6.1 represents the

measured PA signal at different concentrations of H_2S. At a pressure of 10 mbar the collisional broadening effect is dominant and a Lorentzian shape fits the best with the data. The fitted curve is represented by the red line in figure V.6.1.

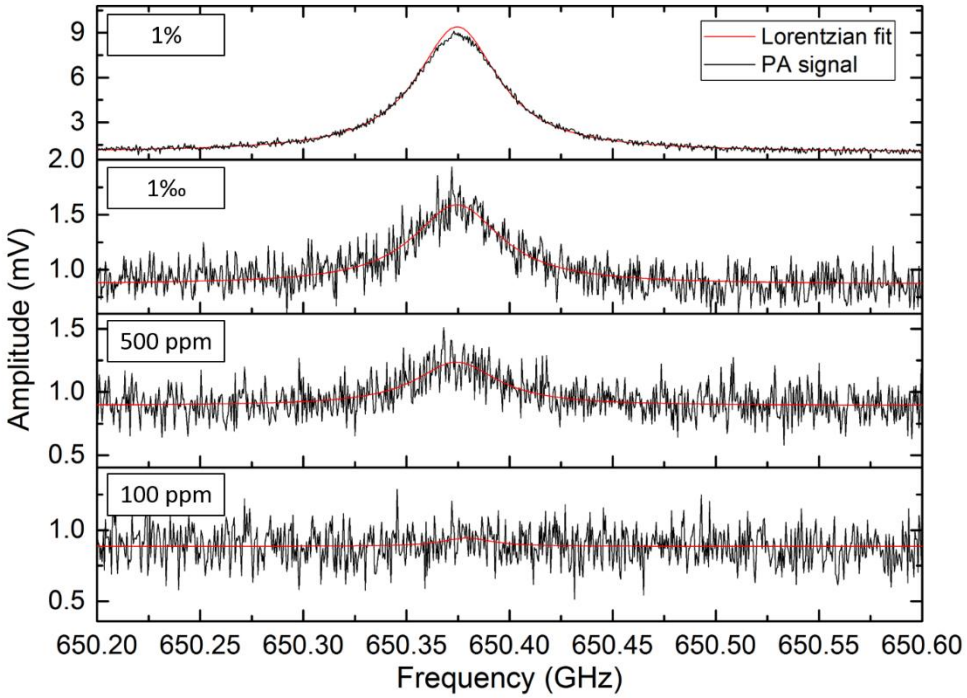

Figure V.6.1 The measured photoacoustic signal and the Lorentzian fit of the 650.37 GHz H_2S spectral line at different concentrations down to 100 ppm and a fixed pressure of 10 mbar

A signal of 9 mV is detected at the absorption line's peak for a pressure of 10 mbar and an H_2S gas concentration of 1%. This signal corresponds to the PA but also to the direct THz detection. The direct THz detection is represented by the signal offset measured at frequencies far away from the molecular absorption line. This undesired offset can be calculated and subtracted to define the pure PA signal. The offset level is determined by the Lorentzian fit tails extended to frequencies beyond the absorption line. It corresponds to 1 mV for a concentration of 1% of H_2S and 0.89 mV for lower concentrations. Therefore the measured PA signal for a concentration of 1% of H_2S corresponds to an amplitude of 8 mV. The noise level was measured at a frequency far away from the absorption line peak by calculating the RMS (Root Mean Square) of 100 scanning points after the subtraction of the offset signal. The calculated noise corresponds to 120 µV. This noise value is slightly higher than the one presented in section V.4 for the collimated THz alignment with a noise level of 70 µV at 10 mbar (where the THz beam doesn't touch the membrane). Therefore,

this extra noise of 30 µV is the result of the PT effect caused by the focused THz beam on the Poly-Si membrane. However, this noise value is negligible with respect to the high signal gain achieved with this THz alignment. The SNR in this measurement corresponds then to 66. A comparison of the SNR between different THz alignment will be discussed in the next section. For lower H_2S concentrations of 1 ‰, 500 ppm, and 100 ppm diluted by air a PA signal of 0.7, 0.3, and 0.06 mV were respectively measured. Comparing these values to the calculated noise results in a SNR of 5.8, 2.5, and 0.5 for the respective concentrations of 1 ‰, 500 ppm, and 100 ppm. At 100 ppm the signal is dominated by the noise and therefore the measurement of such concentration exceeds the minimum detection limit (MDL) of this system. The minimum detection limit (MDL) is defined as the lowest detected concentration with an SNR=1. The black dot squares in figure V.6.2 represent the measured SNR at the different H_2S concentrations. The linear fit presented by the red line confirms the proportionality between the PA signal amplitude and the gas concentrations. This linear dependence was also expected from the relationship between the PA signal amplitude and gas concentration found by combining equations I.3.5 and I.4.30. The horizontal black dashed line corresponds to an SNR =1. The blue dot intersection between this SNR unity line and the linear fitting of the measured data indicates the MDL of the system. Therefore an MDL of 200 ppm can be achieved by using the Poly-Si membrane as a PA microphone.

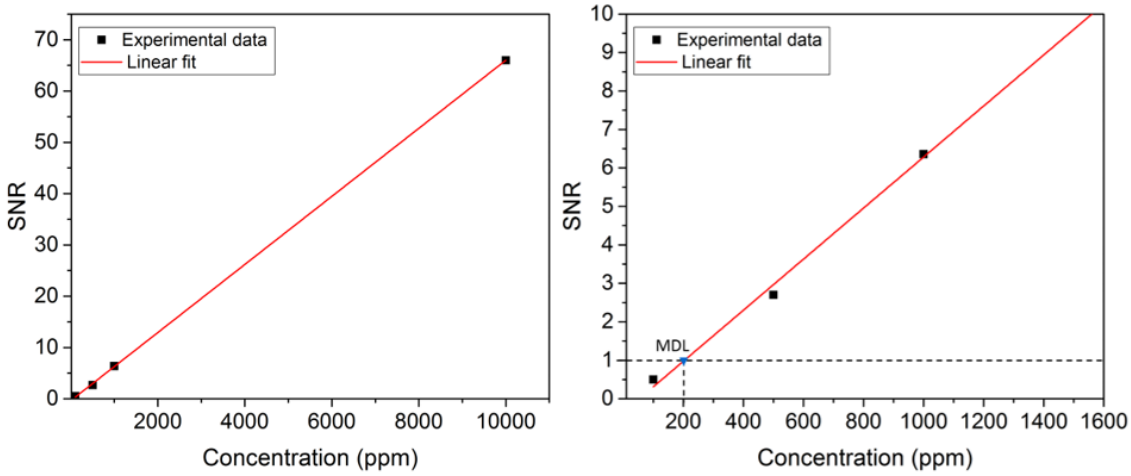

Figure V.6.2 Left: Plot of the PA SNR versus the H_2S gas concentration at a pressure of 10 mbar. Right: A zoom on the low SNR levels of the plot on the left. The black horizontal dashed line indicate the SNR=1 level, the blue dot corresponds to the MDL of the used gas sensing system.

This MDL value is in the same order as other PA techniques based on the cantilever enhanced photoacoustic spectroscopy (CEPAS) for the detection of CH_3CN [18],[19]. Other techniques that use quartz enhanced photoacoustic spectroscopy (QEPAS) presents higher sensitivity with an MDL of 7 ppm for the detection of CH_3OH [20]. This same technique (QEPAS) was also used for the detection of 30 ppm[21] and 360 ppt [22] of H_2S. However, the disadvantage of this method remains in the necessity of a very long integration time due to the very large Q factors of the tuning fork, and it's also based on the use of QCL that needs to be cooled at cryogenic temperature levels. This demonstration of the low MDL is only representing the sensitivity of the Poly-Si membrane as a PA microphone. The enhancement of the THz cavity is not considered here. By integrating the Poly-Si membrane with the THz PhC cavity demonstrated in chapter IV, the effective gas molecules-THz light interaction length would be increased by a factor proportional to the THz cavity quality factor. The dependence of the detected concentration on the interaction length is presented in equation I.3.6 based on the Lambert-Beer law. Therefore, the MDL would be enhanced by a factor proportional to the THz cavity quality factor. In [23] we present a relationship between the gas concentration and the THz cavity quality factor. Using the following equations referred to as equation (9,13 and 14) in [23]:

$$P_{abs} = \frac{Q_0}{Q_{gas}} P_{THz} \tag{V.6.1}$$

$$\frac{1}{Q_{gas}} = a\kappa_{gas} \tag{V.6.2}$$

$$\kappa_{gas} = AC \tag{V.6.3}$$

where P_{abs} correspond to the THz absorbed power by the molecules, Q_0 the THz quality factor =18000 presented in chapter IV and [24], P_{THz} = 800µW the THz output power, Q_{gas} the quality factor resulting from the gas absorption, κ_{gas} the gas absorbance or imaginary refractive index in the simulation, C the gas concentration, A and a constants, the gas concentration C could be written by:

$$C = \frac{P_{abs}}{nQ_0 P_{THz}} \tag{V.6.4}$$

with n a constant. Equation V.6.4 shows the increased response of the gas sensor with the THz cavity quality factor. Similar demonstrations based on the use of optical cavities in the MIR to

increase the interaction effective length and improve the detected signal have been reported in [25]–[27]. In this work, we expect to achieve an MDL of 10's of ppb by coupling for the first time an integrated THz high Q cavity with a Poly-Si microphone similar to the one presented in this chapter.

V.7. SNR OF THREE DIFFERENT THZ ALIGNMENTS

The sensitivity is also defined by the noise equivalent absorption (NNEA) coefficient. The NNEA is expressed by:

$$NNEA = \alpha_{min} P_0 \sqrt{t} \tag{V.7.1}$$

where P_0= 800µw corresponds to the THz source emitted power, t the integration time and α_{min} the minimal absorption coefficient represented by:

$$\alpha_{min} = \frac{\alpha_{peak}}{SNR} \tag{V.7.2}$$

with α_{peak} the absorption coefficient simulated using Spectraplot for a light molecules interaction length of 7cm. The system NNEA is equivalent to 2.32×10^{-7} W. $cm^{-1}/\sqrt{Hz}$. To improve the sensitivity of this system it is then necessary to improve the SNR. We presented in section V.4 a comparison between the PA signal detected while the THz beam is focused on the membrane and the one where the beam is collimated at a distance of 12.7 mm away from the membrane. In this part, the SNR of these two different alignments and an additional one where the membrane is placed longitudinally in the collimated beam are discussed and compared. The measured PA signal of a 1% H_2S concentration at a pressure of 10 mbar with the three different alignments is presented in figure V.7.1. For both configurations where the THz beam is collimated the offset signal is absent, contrary to what was observed for the focused THz beam on the Poly-Si membrane. For the configuration where the membrane is placed longitudinally in the propagation direction of the collimated beam, a high PA signal is detected. This higher signal compared to the configuration where the membrane was placed at 12.7mm away from the THz beam is due to the largest overlap between the membrane and the sound waves. Moreover, the noise level remains low without being impacted by the PT effect of the THz beam. This gives an SNR of 46. The two other configurations present an SNR of 66 for the focused beam and 16 for the collimated one respectively. Therefore

the advantage of placing the membrane longitudinally in the propagation direction is that it shows a high SNR without being impacted by the parasitic signal and additional noise caused by the THz beam. This configuration is the closest to the final gas sensor design, where the THz beam is highly concentrated and propagating longitudinally through the membrane.

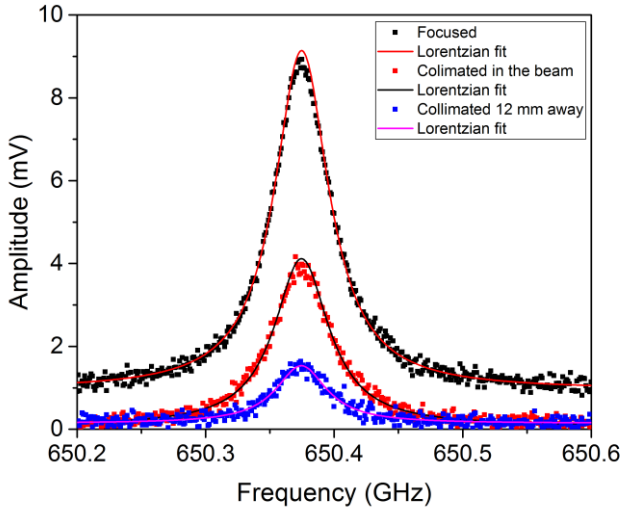

Figure V.7.1 Measured PA signal of 1% H_2S gas concentration at a pressure of 10 mbar for three different THz alignments

V.8. CONCLUSION OF THIS CHAPTER

The objective of this chapter is to validate the concept of PA detection using a Poly-Si membrane as a microphone. This demonstration is the first step toward the PA gas detection with the fully integrated THz gas sensor design discussed in this thesis.

In the first part, the design of a customized gas chamber for the THz PA spectroscopy was presented. A THz low loss and hermetically sealed transition metallic waveguide was fabricated, tested, and successfully used for guiding the THz light into the gas chamber.

In the second part, we presented the detection of H_2S gas molecules which is considered a great indicator of food spoilage using a single Poly-Si membrane as a PA microphone. Before that, a study of the dynamic behavior of the membrane and the shift of its resonance frequency with the pressure variation was performed.

Different alignments of the THz beam were used to excite the gas molecules and detect the PA signal of the Poly-Si membrane. A comparison of the sensitivity and detection performance between the different THz alignments is then reported. An approach between these different alignments and the original concept of the gas sensor is also illustrated.

Several absorption lines of the H_2S molecules in the 620-690 GHz frequency range were measured at different pressure levels. These measurements show the pressure impact on the absorption lines broadening. An MDL of 200 ppm was demonstrated and compared to the sensitivity of other PA THz techniques. Such an important demonstration gives an approximate estimation of the sensitivity of the fully integrated sensor with the Poly-Si membrane coupled to the THz cavity. A sensitivity of 10's of ppb is then expected for the detection of H_2S molecules with the fully integrated gas sensor proposed in this thesis.

Finally, this demonstration of a very sensitive PA gas detection at the THz frequencies using a MEMS microphone is, to my knowledge, the first in the world. It also gives high hopes for the development of fully integrated gas sensors with ultra-high sensitivity and a detection limit of some ppb.

V.9. REFERENCES

[1] « MDC Vacuum Products LLC ». http://www.mdcvacuumproductsllc.com/ (consulté le mars 29, 2021).

[2] H. Soekmadji, S.-L. Liao, et R. J. Vernon, « Trapped Mode Phenomena in a Weakly Overmoded Waveguiding Structure of Rectangular Cross Section », *Journal of Electromagnetic Waves and Applications*, vol. 22, nº 1, p. 143‑157, janv. 2008, doi: 10.1163/156939308783122706.

[3] G. A. Ediss, « Measurements and Simulations of Overmoded Waveguide Components at 70-118 GHz, 220-330 GHz and 610-720 GHz », p. 10.

[4] K. B. Gavan, J. van der Heijden, E. W. J. M. van der Drift, et H. S. J. van der Zant, « Effect of pressure on the Q factor and the resonance frequency of SiN microcantilevers », in *2009 4th IEEE International Conference on Nano/Micro Engineered and Molecular Systems*, janv. 2009, p. 380‑384, doi: 10.1109/NEMS.2009.5068600.

[5] M. O. Hanna, J. W. Savell, G. C. Smith, D. E. Purser, F. A. Gardner, et C. Vanderzant, « Effect of Growth of Individual Meat Bacteria on pH, Color and Odor of Aseptically Prepared Vacuum-Packaged Round Steaks », *Journal of Food Protection*, vol. 46, nº 3, p. 216‑221, mars 1983, doi: 10.4315/0362-028X-46.3.216.

[6] B. H. Lee et R. E. Simard, « Evaluation of Methods for Detecting the Production of H2S, Volatile Sulfides, and Greening by Lactobacilli », *Journal of Food Science*, vol. 49, nº 4, p. 981 ‑ 983, 1984, doi: https://doi.org/10.1111/j.1365-2621.1984.tb10374.x.

[7] A. F. Egan, B. J. Shay, et P. J. Rogers, « Factors affecting the production of hydrogen sulphide by Lactobacillus sake L13 growing on vacuum-packaged beef », *Journal of Applied Bacteriology*, vol. 67, nº 3, p. 255‑262, 1989, doi: https://doi.org/10.1111/j.1365-2672.1989.tb02493.x.

[8] B. J. Shay et A. F. Egan, « Hydrogen sulphide production and spoilage of vacuum-packaged beef by a Lactobacillus », *Psychrotrophic microorganisms in spoilage and pathogenicity / edited by T.A. Roberts ... [et al.]*, 1981.
[9] W.-Y. Chung, G. T. Le, T. V. Tran, et N. H. Nguyen, « Novel proximal fish freshness monitoring using batteryless smart sensor tag », *Sensors and Actuators B: Chemical*, vol. 248, p. 910‑916, sept. 2017, doi: 10.1016/j.snb.2017.01.134.
[10] T. Kristoffersen et F. E. Nelson, « The Relationship of Serine Deamination and Hydrogen Sulfide Production by Lactobacillus casei to Cheddar Cheese Flavor », *Journal of Dairy Science*, vol. 38, nº 12, p. 1319‑1325, déc. 1955, doi: 10.3168/jds.S0022-0302(55)95114-6.
[11] L. H. Almy, « A METHOD FOR THE ESTIMATION OF HYDROGEN SULFIDE IN PROTEINACEOUS FOOD PRODUCTS [1] », *J. Am. Chem. Soc.*, vol. 47, nº 5, p. 1381‑1390, mai 1925, doi: 10.1021/ja01682a024.
[12] https://spec.jpl.nasa.gov/ftp/pub/catalog/catform.html.
[13] L. Dong, A. A. Kosterev, D. Thomazy, et F. K. Tittel, « QEPAS spectrophones: design, optimization, and performance », *Appl. Phys. B*, vol. 100, nº 3, p. 627‑635, sept. 2010, doi: 10.1007/s00340-010-4072-0.
[14] C. Yang *et al.*, « Effect of laser deflection on resonant cantilever sensors », in *2009 IEEE SENSORS*, oct. 2009, p. 869‑872, doi: 10.1109/ICSENS.2009.5398240.
[15] M. Mouelhi, « Analyse de profils de raies rotationnelles de composés d'intérêt atmosphérique sondés dans le domaine Térahertz », These en préparation, Littoral, 2017.
[16] « SpectraPlot.com - Absorption spectroscopy simulator ». https://www.spectraplot.com/absorption.
[17] I. E. Gordon *et al.*, « The HITRAN2016 molecular spectroscopic database », *Journal of Quantitative Spectroscopy and Radiative Transfer*, vol. 203, p. 3‑69, déc. 2017, doi: 10.1016/j.jqsrt.2017.06.038.
[18] N. E. Glauvitz, R. A. Coutu, I. R. Medvedev, et D. T. Petkie, « Terahertz Photoacoustic Spectroscopy Using an MEMS Cantilever Sensor », *Journal of Microelectromechanical Systems*, vol. 24, nº 1, p. 216‑223, févr. 2015, doi: 10.1109/JMEMS.2014.2327916.
[19] R. A. Coutu, I. R. Medvedev, et D. T. Petkie, « Improved Sensitivity MEMS Cantilever Sensor for Terahertz Photoacoustic Spectroscopy », *Sensors*, vol. 16, nº 2, Art. nº 2, févr. 2016, doi: 10.3390/s16020251.
[20] P. Patimisco *et al.*, « A quartz enhanced photo-acoustic gas sensor based on a custom tuning fork and a terahertz quantum cascade laser », *Analyst*, vol. 139, nº 9, p. 2079‑2087, avr. 2014, doi: 10.1039/C3AN01219K.
[21] V. Spagnolo *et al.*, « THz Quartz-enhanced photoacoustic sensor for H_2S trace gas detection », *Opt. Express, OE*, vol. 23, nº 6, p. 7574‑7582, mars 2015, doi: 10.1364/OE.23.007574.
[22] A. Sampaolo *et al.*, « H2S quartz-enhanced photoacoustic spectroscopy sensor employing a liquid-nitrogen-cooled THz quantum cascade laser operating in pulsed mode », *Photoacoustics*, vol. 21, p. 100219, mars 2021, doi: 10.1016/j.pacs.2020.100219.
[23] M. Verstuyft *et al.*, « Proposal for an integrated silicon-photonics terahertz gas detector using photoacoustics », *Opt. Express, OE*, vol. 28, nº 15, p. 22424‑22442, juill. 2020, doi: 10.1364/OE.397272.
[24] E. Akiki *et al.*, « High-Q THz Photonic Crystal Cavity on a Low-Loss Suspended Silicon Platform », *IEEE Transactions on Terahertz Science and Technology*, vol. 11, nº 1, p. 42 ‑ 53, janv. 2021, doi: 10.1109/TTHZ.2020.3019928.
[25] S. Borri *et al.*, « Intracavity quartz-enhanced photoacoustic sensor », *Appl. Phys. Lett.*, vol. 104, nº 9, p. 091114, mars 2014, doi: 10.1063/1.4867268.
[26] P. Patimisco *et al.*, « High finesse optical cavity coupled with a quartz-enhanced photoacoustic spectroscopic sensor », *Analyst*, vol. 140, nº 3, p. 736‑743, 2015, doi: 10.1039/C4AN01158A.
[27] T. Tomberg, T. Hieta, M. Vainio, et L. Halonen, « Cavity-enhanced cantilever-enhanced photo-acoustic spectroscopy », *Analyst*, vol. 144, nº 7, p. 2291‑2296, 2019, doi: 10.1039/C9AN00058E.

Conclusion and perspectives

In this thesis, we presented the design of a novel THz photoacoustic gas sensor used for the detection of gas molecules inside food packaging. The H_2S molecule is one of many gases that can be considered as an indicator of spoilage in packaged foods. The detection of this molecule at concentration levels of 100s of ppb is necessary to ensure the safe consumption of a packaged food. To increase the sensitivity of the gas sensor and detect ppb levels, the proposed sensor design combines three resonators [1]: a THz photonic crystal cavity, an acoustic pipe, and a thin mechanical membrane. These different parts are integrated on an HR-Si platform represented by a suspended waveguide. Each part of this sensor has been treated independently in this work. The achieved results related to these different parts and the PA gas measurements are summarized in these paragraphs.

Waveguides with compact sizes are necessary for transmitting electromagnetic energy over long distances with low losses. Such components may be required for any application in the THz domain. In this work, a low-loss HR-Si waveguide was demonstrated and used to feed the integrated gas sensor. Both single and multimode waveguides were numerically analyzed in the 500-750 GHz frequency range. The core of the waveguide is formed of HR-Si surrounded by air to form the cladding. The use of thin Si anchor beams to suspend the floating guide channel was numerically proven to be nearly lossless with a loss value of 0.04 dB per pair of anchors. Bended waveguides with a theoretical loss value of 0.1 dB/bend were also designed to facilitate incorporation into compact integrated circuits. A highly efficient transition between this Si waveguide and a commercial metallic waveguide was achieved by properly designing inverted tapers. It results in 0.2 dB of total insertion losses. Long waveguides (up to 25 cm) fitted on compact surfaces were measured experimentally. The measured propagation loss of a long waveguide that includes bends varies between 0.045 and 0.085 dB/mm corresponding to an average of 0.065 dB/mm for the 500-750 GHz frequency range. This average loss is equivalent to 0.032 dB/λ_0 [2]. Such a value is the lowest among several other THz silicon waveguides [3]–[6]. For the first time over a large frequency band (250 GHz) extending up to 750 GHz, a very low propagation loss (including bend, material, and scattering loss) is demonstrated.

The **photonic crystal cavity** represents the THz photonic resonator of the gas sensor that increases the interaction length between gas molecules and THz light and thus improves the sensor's sensitivity. Several numerical calculations were performed to define appropriate parameters for photonic crystal cavity designs with high Q resonant modes in the 600-700 GHz frequency range. The numerical results present cavity modes with quality factors between 25000 and 47000. Such high Q-factors at THz frequencies have never been reported [7]–[14]. In order to put this in perspective, rescaling this to the NIR region would (at equal photon lifetimes) imply a cavity with Q up to 10^7, or in other words among the strongest reported. A record quality factor of 18000 has been measured experimentally [2] for a THz resonant mode strongly confined in a subwavelength air hole of a 1D wire photonic crystal cavity. Similar cavities with lower reflectivity resulting in lower quality factors of 7000 and 1500 and higher transmittance of 42 and 72% respectively have also been demonstrated.

The **Acousto-mechanical resonator** of the gas sensor is defined by a central hole of the PhC cavity which is covered by a stressed thin membrane of Poly-Si. The cylindrical hole corresponds to the acoustic resonator and the stressed membrane represents the mechanical one. The fundamental mechanical resonant mode of the poly-Si membrane with a quality factor of 550 was measured at a pressure below 1 mbar. An acouto-mechanical coupling between the acoustic pipe and mechanical membrane was experimentally observed at high pressures.

Photoacoustic detection of H_2S molecules was demonstrated by simply using a stressed Poly-Si membrane as a resonant mechanical microphone. This demonstration doesn't include the effect of the THz cavity or the acoustic resonator. Five of the strongest absorption lines of the H_2S in the frequency range between 620 and 690 GHz were measured with this technique. These measurements are in great agreement with the simulated data of the H_2S spectral lines extracted from the HITRAN database. A minimum detection limit of 200 ppm was reported for the detection of H_2S at a pressure of 10 mbar. The sensitivity of this system is comparable to other sensors based on the CEPAS [15], [16] and slightly higher than the one using QEPAS [17]–[19]. The next step of this work will focus on the fabrication of the designed PhC cavity resonant at 650 GHz to match with the absorption peak of the H_2S. This demonstration will allow the combination of the triple resonators and take advantage of the improved light-molecule interaction to increase the sensitivity

of the gas sensor. A THz resonant cavity with a quality factor in the order of 18000 can reduce the MDL to an estimated value in the order of 10s of ppb.

Finally, we also presented in this work the design of a gas chamber with a sealed THz metallic waveguide transition. It guides the THz energy into the chamber while maintaining the tightness and pressure level inside the chamber with low THz losses below 2.5 dB.

The different scientific demonstrations presented in this thesis corresponds to multidisciplinary work. The proposed THz photonics and mechanical components can be used for several applications and are necessary for some. The photonic crystal cavities and waveguides can be adjusted to fit any other frequency of interest. Additional work is required to understand the behavior of MEMS under the impact of metal layer loads.

In this work, we continue to develop the proposed integrated THz gas sensor toward the detection of sub ppb of H_2S concentrations. The design under developpement targets the 650.37 GHz absorption line of the H_2S. It can also be adjusted to detect different absorption lines of H_2S or any other gas molecules by tuning the resonant frequency of the PhC cavity. The integration of multiple PhC cavities with different resonant frequencies on the same wire waveguide or on parallel waveguides is also possible. This allows monitoring several gas molecules at the same time. Such a system increases the accuracy of the food freshness analysis. It can also be used for any other applications, notably biomedical for the detection of viruses.

Instead of using MEMS for the acoustical signal detection, it is also possible to couple the PhC cavity with a Quartz tuning fork. The very high Q factors of these resonators increase the detection sensitivity. Despite their high sensitivity, tuning forks suffer from the small spacing (0.3, 0.8 mm) between the prongs, which is comparable to the wavelength of the THz beam(≈0.5 mm). The PhC cavity provides sub-wavelength confinement of the THz energy in very small volumes. Therefore, placing a PhC cavity between the tuning fork prongs increases the interaction length between the THz light and molecules, but also prevents the THz beam from contacting the tuning fork prongs.

The proposed gas sensor is integrated on-chip with a very compact size of 17x0.2x0.09 mm compatible to fit inside food packages. However, the THz power source and the optical read-out system (LDV) that currently drive the sensor are bulky in size. A miniaturized LDV integrated on an SOI chip has been reported in recent years [20]–[22]. Demonstration of an uncooled on-chip

THz source is still lacking. It is possible to design grating couplers at THz frequencies to externally feed the gas sensor with the available THz sources. The realization of these different demonstrations can be useful for the complete integration of the gas sensor to operate inside the food packaging.

[1] M. Verstuyft *et al.*, "Proposal for an integrated silicon-photonics terahertz gas detector using photoacoustics," *Opt. Express*, vol. 28, no. 15, pp. 22424–22442, Jul. 2020, doi: 10.1364/OE.397272.

[2] E. Akiki *et al.*, "High Q THz photonic crystal cavity on a low loss suspended Silicon platform," *IEEE Trans. Terahertz Sci. Technol.*, pp. 1–1, 2020, doi: 10.1109/TTHZ.2020.3019928.

[3] N. Ranjkesh, M. Basha, A. Taeb, A. Zandieh, S. Gigoyan, and S. Safavi-Naeini, "Silicon-on-Glass Dielectric Waveguide—Part I: For Millimeter-Wave Integrated Circuits," *IEEE Trans. Terahertz Sci. Technol.*, vol. 5, no. 2, pp. 268–279, Mar. 2015, doi: 10.1109/TTHZ.2015.2399693.

[4] N. Ranjkesh, M. Basha, A. Taeb, and S. Safavi-Naeini, "Silicon-on-Glass Dielectric Waveguide—Part II: For THz Applications," *IEEE Trans. Terahertz Sci. Technol.*, vol. 5, no. 2, pp. 280–287, Mar. 2015, doi: 10.1109/TTHZ.2015.2397279.

[5] H. Amarloo and S. Safavi-Naeini, "Terahertz Line Defect Waveguide Based on Silicon-on-Glass Technology," *IEEE Trans. Terahertz Sci. Technol.*, vol. 7, no. 4, pp. 433–439, Jul. 2017, doi: 10.1109/TTHZ.2017.2708505.

[6] K. Tsuruda, M. Fujita, and T. Nagatsuma, "Extremely low-loss terahertz waveguide based on silicon photonic-crystal slab," *Opt. Express*, vol. 23, no. 25, pp. 31977–31990, Dec. 2015, doi: 10.1364/OE.23.031977.

[7] A. L. Bingham and D. Grischkowsky, "Terahertz two-dimensional high-Q photonic crystal waveguide cavities," *Opt. Lett.*, vol. 33, no. 4, p. 348, Feb. 2008, doi: 10.1364/OL.33.000348.

[8] Y. Miyamoto, H. Kanaoka, and S. Kirihara, "Terahertz wave localization at a three-dimensional ceramic fractal cavity in photonic crystals," *J. Appl. Phys.*, vol. 103, no. 10, p. 103106, May 2008, doi: 10.1063/1.2924327.

[9] J. Xie, X. Zhu, X. Zang, Q. Cheng, L. Chen, and Y. Zhu, "Terahertz integrated device: high-Q silicon dielectric resonators," *Opt. Mater. Express*, vol. 8, no. 1, p. 50, Jan. 2018, doi: 10.1364/OME.8.000050.

[10] C. M. Yee and M. S. Sherwin, "High-Q terahertz microcavities in silicon photonic crystal slabs," *Appl. Phys. Lett.*, vol. 94, no. 15, p. 154104, Apr. 2009, doi: 10.1063/1.3118579.

[11] W. J. Otter, S. M. Hanham, N. M. Ridler, G. Marino, N. Klein, and S. Lucyszyn, "100GHz ultra-high Q-factor photonic crystal resonators," *Sens. Actuators Phys.*, vol. 217, pp. 151–159, Sep. 2014, doi: 10.1016/j.sna.2014.06.022.

[12] K. Okamoto, K. Tsuruda, S. Diebold, S. Hisatake, M. Fujita, and T. Nagatsuma, "Terahertz Sensor Using Photonic Crystal Cavity and Resonant Tunneling Diodes," *J. Infrared Millim. Terahertz Waves*, vol. 38, no. 9, pp. 1085–1097, Sep. 2017, doi: 10.1007/s10762-017-0391-0.

[13] S. M. Hanham, C. Watts, W. J. Otter, S. Lucyszyn, and N. Klein, "Dielectric measurements of nanoliter liquids with a photonic crystal resonator at terahertz frequencies," *Appl. Phys. Lett.*, vol. 107, no. 3, p. 032903, Jul. 2015, doi: 10.1063/1.4927242.

[14] S. M. Hanham, M. M. Ahmad, S. Lucyszyn, and N. Klein, "LED-Switchable High-Q Packaged THz Microbeam Resonators," *IEEE Trans. Terahertz Sci. Technol.*, vol. 7, no. 2, pp. 199–208, Mar. 2017, doi: 10.1109/TTHZ.2016.2634547.

[15] N. E. Glauvitz, R. A. Coutu, I. R. Medvedev, and D. T. Petkie, "Terahertz Photoacoustic Spectroscopy Using an MEMS Cantilever Sensor," *J. Microelectromechanical Syst.*, vol. 24, no. 1, pp. 216–223, Feb. 2015, doi: 10.1109/JMEMS.2014.2327916.

[16] R. A. Coutu, I. R. Medvedev, and D. T. Petkie, "Improved Sensitivity MEMS Cantilever Sensor for Terahertz Photoacoustic Spectroscopy," *Sensors*, vol. 16, no. 2, Art. no. 2, Feb. 2016, doi: 10.3390/s16020251.

[17] P. Patimisco *et al.*, "A quartz enhanced photo-acoustic gas sensor based on a custom tuning fork and a terahertz quantum cascade laser," *Analyst*, vol. 139, no. 9, pp. 2079–2087, Apr. 2014, doi: 10.1039/C3AN01219K.

[18] V. Spagnolo *et al.*, "THz Quartz-enhanced photoacoustic sensor for H_2S trace gas detection," *Opt. Express*, vol. 23, no. 6, pp. 7574–7582, Mar. 2015, doi: 10.1364/OE.23.007574.

[19] A. Sampaolo *et al.*, "H2S quartz-enhanced photoacoustic spectroscopy sensor employing a liquid-nitrogen-cooled THz quantum cascade laser operating in pulsed mode," *Photoacoustics*, vol. 21, p. 100219, Mar. 2021, doi: 10.1016/j.pacs.2020.100219.

[20] Y. Li, P. Segers, J. Dirckx, and R. Baets, "On-chip laser Doppler vibrometer for arterial pulse wave velocity measurement," *Biomed. Opt. Express*, vol. 4, no. 7, p. 1229, Jul. 2013, doi: 10.1364/BOE.4.001229.

[21] Y. Li and R. Baets, “Homodyne laser Doppler vibrometer on silicon-on-insulator with integrated 90 degree optical hybrids,” *Opt. Express*, vol. 21, no. 11, pp. 13342–13350, Jun. 2013, doi: 10.1364/OE.21.013342.
[22] Y. Li *et al.*, “Six-beam homodyne laser Doppler vibrometry based on silicon photonics technology,” *Opt. Express*, vol. 26, no. 3, pp. 3638–3645, Feb. 2018, doi: 10.1364/OE.26.003638.

List of publications

JOURNAL PUBLICATIONS

- **Integrated THz photoacoustic gas sensor for the detection of H_2S molecules applied for food quality control, Photoacoustics Elsevier** (In preparation)
  E. Akiki, M-H. Mammez, G. Ducournau, B. walter, F. Bavedila, E. Lebouvier, M. Faucher G. Mouret, J-F. Lampin, M. Vanwolleghem
- **High Q THz photonic crystal cavity on a low loss suspended Silicon platform, IEEE Transactions on Terahertz Science and Technology 2021, 11 (1), 42-53**
  E. Akiki, M. Verstuyft, B. Kuyken, B.Walter, M. Faucher, J-F. Lampin, G. Ducournau, M.Vanwolleghem
- **Proposal for an integrated silicon-photonics terahertz gas detector using photoacoustics, Optics Express 2020 28 (15), 22424-22442**
  M. Verstuyft, **E. Akiki,** B.Walter, M. Faucher, J-F. Lampin, M.Vanwolleghem, B. Kuyken

ORAL PRESENTATIONS AND POSTERS

- **H_2S photoacoustic detection with an integrated THz gas sensor for food quality control** (IRMMW-THz 2021) – keynote presentation
  E. Akiki, M-H. Mammez, G. Ducournau, B. walter, F. Bavedila, E. Lebouvier, M. Faucher G. Mouret, J-F. Lampin, M. Vanwolleghem
- **Spectromérie photo-acoustique THz du H_2S pour le suivi de l'état de fraicheur des aliments** (Congrès Optique Dijon 2021)
  M-H. Mammez, **E. Akiki**, G. Ducournau, B. Walter, M. Faucher, J-F. Lampin, S. Eliet, A. Cuisset, F. Hindle, R. Bocquet, G. Mouret, M. Vanwolleghem
- **High Q factor and high transmittance suspended membrane THz PhC cavity: experimental demonstration for sensing applications** (IRMMW-THz 2020)
  E. Akiki, M. Verstuyft, G. Ducournau, B.Walter, M. Faucher, B. Kuyken, J-F. Lampin, M.Vanwolleghem
- **A Suspended Silicon Terahertz platform with low loss waveguide and high Q Photonic Crystal cavities**
  (IRMMW-THz 2019)
  E. Akiki, M. Verstuyft, B. Kuyken, B.Walter, M. Faucher, J-F. Lampin, G. Ducournau, M.Vanwolleghem
- **An Integrated Photoacoustic Terahertz Gas Sensor** (IRMMW-THz 2019)
  M. Verstuyft, **E. Akiki,** B.Walter, M. Faucher, M.Vanwolleghem, B. Kuyken
- **Low loss Suspended Silicom waveguide and photonic crystal for THz regime** (CLEO EUROPE 2019)
  E. Akiki, M. Verstuyft, G. Ducournau, B.Walter, E. Mairiaux, M. Faucher, J-F. Lampin, M.Vanwolleghem, B. Kuyken

- **Integrated high Q optical cavity on a low loss Si suspended waveguide for THz application** (FGTC 2019)
  E. Akiki, M. Verstuyft, G. Ducournau, B.Walter, E. Mairiaux, M. Faucher, J-F. Lampin, B. Kuyken, M.Vanwolleghem
- **Terahertz photoacoustic gas sensor (**GDR NanoTeraMIR annual days, 2019)
  E. Akiki, M. Verstuyft, G. Ducournau, E. Mairiaux, B.Walter, M. Faucher, J-F. Lampin, M.Vanwolleghem, B. Kuyken

Abstract:

In this thesis work, a photoacoustic THz gas sensor (operating in the 620-690 GHz band) used for monitoring Volatile Organic compounds (VOCs) in food packages is presented. This gas sensor is fabricated on low-loss THz High resistivity Silicon (HR-Si) waveguides. The design, modal analysis, and propagation losses of the suspended Si waveguide are discussed in detail. Highly competitive losses not exceeding 0.6 dB/cm in this band have been measured. Three different resonators: photonic, acoustic, and mechanical are at the origin of the gas sensor designs. They allow to triply enhance the detected photoacoustic signal and to reduce the minimum detection limit of the gas sensor. Photonic crystal (PhC) cavities representing the THz photonic resonator are created on top of the Si waveguide. The design optimization and experimental characterizations of several THz PhC cavities are presented in this work. This has led to a resonant PhC cavity at 640 GHz with a record Q factor of 18000. A central hole of the PhC cavity behaves as an acoustical resonator. It is covered by a stressed polycrystalline silicon (Poly-Si) membrane that corresponds to the mechanical resonator. Analytical analysis and experimental characterization measurements are performed to study these acousto-mechanical resonators. The combination of the above realizations has allowed us to demonstrate the first THz photoacoustic detection of low concentrations (200 ppm) of H_2S molecules on an integratable platform. H_2S being a crucial indicator of food spoilage, this work is therefore an important first step towards a real-time compact sensor technology, both for food quality control applications as well as environmental and biomedical ones.

Résumé:

Ce travail de thèse présente un capteur de gaz photoacoustique aux fréquences THz utilisé pour surveiller les composés organiques volatils (COV) dans les emballages alimentaires. Ce capteur de gaz est fabriqué sur un guide d'onde THz à faible perte en silicium à haute résistivité (HR-Si). La conception, l'analyse modale et les pertes de propagation du guide d'onde Si suspendu sont discutées en détail. Des pertes très compétitives ne dépassant pas 0,6 dB/cm dans cette bande ont été mesurées. Trois résonateurs différents : photonique, acoustique et mécanique sont à l'origine de la conception des capteurs de gaz. Ils permettent d'amplifier le signal photoacoustique détecté et de réduire la limite de détection minimale du capteur de gaz. Des cavités cristaux photoniques (PhC) représentant le résonateur photonique THz sont créées au-dessus du guide d'onde Si. L'optimisation du design et les caractérisations expérimentales de plusieurs cavités PhC THz sont présentées dans ce travail. Cela a conduit à une cavité PhC à 640 GHz avec un facteur Q record de 18000.Un trou central de la cavité PhC se comporte comme un résonateur acoustique. Il est recouvert d'une membrane de silicium polycristallin (Poly-Si) sous contrainte qui correspond au résonateur mécanique. Une analyse analytique et des mesures de caractérisation expérimentales sont effectuées pour étudier ces résonateurs acoustomécaniques. La combinaison des réalisations ci-dessus nous a permis de démontrer la première détection photoacoustique THz de faibles concentrations (200 ppm) de molécules H_2S sur une plateforme intégrable. Le H_2S étant un indicateur crucial de la dégradation alimentaire, ce travail est donc un premier pas important vers une technologie de capteur compact, temps réel, à la fois pour des applications de contrôle de qualité alimentaire et des applications environnementales et biomédicales.